APPENDIX D STOCHASTIC POINT SOURCE GROUND MOTION MODEL

D.1 Background

The stochastic point source model may be termed a spectral model in that it fundamentally describes the Fourier amplitude spectral density at the surface of a half-space (Hanks and McGuire, 1981). The model uses a Brune (1970, 1971) omega-squared description of the earthquake source Fourier amplitude spectral density. This model is easily the most widely used and qualitatively validated source description available. Seismic sources ranging from **M** = -6 (hydrofracture) to **M** = 8 have been interpreted in terms of the Brune omega-squared model in dozens of papers over the last 30 years. The general conclusion is that it provides a reasonable and consistent representation of crustal sources, particularly for tectonically active regions such as plate margins. A unique phase spectrum can be associated with the Brune source amplitude spectrum to produce a complex spectrum that can be propagated using either exact or approximate (1-, 2- or 3-D) wave propagation algorithms to produce single or multiple component time histories. In this context the model is not stochastic, it is decidedly deterministic and as exact and rigorous as one chooses. A two-dimensional array of such point sources may be appropriately located on a fault surface (area) and fired with suitable delays to simulate rupture propagation on an extended rupture plane. As with the single-point source, any degree of rigor may be used in the wave propagation algorithm to produce multiple-component or average horizontal-component time histories. The result is a kinematic[1] finite-source model that has as its basis a source time history defined as a Brune pulse whose Fourier amplitude spectrum follows an omega-squared model. This finite-fault model would be very similar to that used in published inversions for slip models if the 1-D propagation were treated using a reflectivity algorithm (Aki and Richards, 1980). This algorithm is a complete solution to the wave equation from static offsets (near-field terms) to an arbitrarily selected high frequency cutoff (generally 1-2 Hz).

Alternatively, to model the wave propagation more accurately, recordings of small earthquakes at the site of interest (with source locations distributed along the fault of interest) may be used as empirical Green functions (Hartzell, 1978). To model the design earthquake, the empirical Green's functions are delayed and summed in a manner to simulate rupture propagation (Hartzell, 1978). Provided (a) sufficient small earthquakes are recorded at the site of interest, (b) the source locations adequately cover the expected rupture surface, and (c) sufficient low frequency energy is present in the Green's functions, this would be the most appropriate procedure to use if nonlinear site response is not an issue. With this approach the wave propagation is, in principle, exactly represented from each Green's function source to the site. However, nonlinear site response is not treated unless Green's function motions are recorded at a nearby rock outcrop with dynamic material properties similar to the rock underlying the soils at the site, or recordings are made at depth within the site soil column. These motions may then be used as input to either total or effective stress site response codes to model nonlinear effects. Important issues associated with this approach include the availability of an appropriate nearby (1 to 2 km) rock outcrop and, for the downhole recordings, the necessity to

---

[1]Kinematic source model is one whose slip (displacement) is defined (imposed) while in a dynamic source model forces (stress) are defined (see Aki and Richards 1980 for a complete description).

remove all downgoing energy from the at-depth soil recordings. The downgoing energy must be removed from the downhole Green's functions (recordings) prior to generating the control motions (summing) as only the upgoing wavefields are used as input to the nonlinear site response analyses. Removal of the downgoing energy from each recording requires multiple site response analyses that model uncertainty in the Green's functions resulting from uncertainty in dynamic material properties and from the numerical site response model used to separate the upgoing and downgoing wavefields.

To alleviate these difficulties one can use recordings widely distributed in azimuth at close distances to a small earthquake and correct the recordings back to the source by removing wave propagation effects using a simple approximation (say 1/R or generalized rays plus a constant for crustal amplification and radiation pattern), to obtain an empirical source function. This source function can be used to replace the Brune pulse to introduce some natural (although source, path, and site specific) variation into the dislocation time history. If this is coupled to an approximate wave propagation algorithm (asymptotic ray theory) that includes the direct rays and those that have undergone a single reflection, the result is the empirical source function method (EPRI, 1993). Combining the reflectivity propagation (which is generally limited to frequencies $\leq$ 1-2 Hz due to computational demands) with the empirical source function approach (appropriate for frequencies $\geq$ 1 Hz; EPRI, 1993) results in a broad band simulation procedure. This method is strictly deterministic at low frequencies (where an analytical source function is used) and incorporates some natural variation at high frequencies through the use of an empirical source function (Somerville et al., 1995).

All of these techniques are fundamentally similar, well founded in seismic source and wave propagation physics, and importantly, they are *all* approximate. Simply put, all models are inexact and the single essential element in selecting a model is to incorporate the appropriate degree of rigor, commensurate with uncertainties and variabilities in crustal structure and site effects, through extensive validation exercises. It is generally felt that more complicated models produce more accurate results. However, the implication that is often overlooked is that more sophisticated models require an increased number of parameters that must be specified. This is not too serious a consequence in modeling past earthquakes since a reasonable range in parameter space can be explored to give the "best" results. For future predictions, however, this increased rigor may carry undesirable baggage in increased parametric variability (Roblee et al., 1996). The effects of lack of knowledge (epistemic uncertainty; EPRI, 1993) regarding parameter values for future occurrences results in uncertainty or variability in ground motion predictions. It may easily be the case that a very simple model such as the point source model can have comparable, or even smaller, total variability (modeling plus parametric) than a much more rigorous model with an increased number of parameters (EPRI, 1993). What is desired in a model is sufficient sophistication that it captures the dominant and stable features of source, distance, and site dependencies observed in strong ground motions. It is these considerations that led to the development of the stochastic point source model and, in part, leads to the stochastic element of the models.

The stochastic nature of the point source RVT model is simply the assumption made about the character of ground motion time histories that permits stable estimates of peak parameters (e.g. acceleration, velocity, strain, stress, oscillator response) to be made without computing detailed time histories (Hanks and McGuire, 1981; Boore, 1983). This process uses random vibration theory to relate a time domain peak value to the time history root-mean-square (RMS) value (Boore, 1983).

An important assumption is that the process is normally distributed random noise and stationary (its statistics do not change with time) over its duration. A visual examination of any time history quickly reveals that this is clearly not the case: time histories (acceleration, velocity, stress, strain, oscillator) start, build up, and then diminish with time. However, during the critical strong-motion part of the shaking, the assumption is accurate enough to permit the approach to work surprisingly well, as numerous comparisons with recorded motions and both qualitative and quantitative validations have shown (Hanks and McGuire, 1981; Boore, 1983, 1986; McGuire et al., 1984; Boore and Atkinson, 1987, Silva and Lee, 1987; Toro and McGuire, 1987; Silva et al., 1990; EPRI, 1993; Schneider et al., 1993; Silva and Darragh, 1995). Corrections to RVT are available to accommodate different distributions as well as non-stationarity and are usually applied to the estimation of peak oscillator response in the calculated response spectra (Boore and Joyner, 1984; Toro, 1985).

D.2 Point Source Model Description

The conventional stochastic ground motion model uses an ω-squared source model (Brune, 1970, 1971) with a single-corner frequency and a constant stress drop (Boore, 1983; Atkinson, 1984). Random vibration theory is used to relate RMS (root-mean-square) values to peak values of acceleration (Boore, 1983), and oscillator response (Boore and Joyner, 1984; Toro, 1985; Silva and Lee, 1987) computed from the power spectra to expected peak time domain values (Boore, 1983).

The shape of the Fourier amplitude spectrum of acceleration FA(f), is given by

$$FA(f) = C \frac{f^2}{1+(\frac{f}{f_0})^2} \frac{M_0}{R} P(f)\, A(f)\, e^{-\frac{\pi f R}{\beta_0 Q(f)}} \qquad \text{(D-1)}$$

where

$$C = (\frac{1}{\rho_0 \beta_0^3}) \cdot (2) \cdot (0.55) \cdot (\frac{1}{\sqrt{2}}) \cdot \pi.$$

M_0 = seismic moment,
R = hypocentral distance,
β_0 = shear-wave velocity at the source,
ρ_0 = crustal density at the source
Q(f) = frequency dependent quality factor (crustal damping),
A(f) = crustal amplification,
P(f) = high-frequency truncation filter,
f_0 = source corner frequency.

C is a constant that contains source region density (ρ_0) and shear-wave velocity (β_0) terms and accounts for the free-surface effect (factor of 2), the source radiation pattern averaged over a sphere (0.55) (Boore, 1986), and the partition of energy into two horizontal components ($1/\sqrt{2}$).

Source scaling is provided by specifying two independent parameters, the seismic moment (M_0) and the high-frequency stress parameter or stress drop ($\Delta\sigma$). The seismic moment is related to magnitude through the definition of moment magnitude **M** by the relation

$$\log M_0 = 1.5\ \mathbf{M} + 16.05 \qquad \text{(Hanks and Kanamori, 1979)} \qquad \text{(D-2)}$$

The stress drop ($\Delta\sigma$) relates the corner frequency f_0 to M_0 through the relation

$$f_0 = \beta_0\ (\Delta\sigma/8.44\ M_0)^{1/3} \qquad \text{(Brune; 1970, 1971)} \qquad \text{(D-3)}$$

The stress drop is sometimes referred to as the high frequency stress parameter (Boore, 1983) (or simply the stress parameter) since it directly scales the Fourier amplitude spectrum for frequencies above the corner frequency (Silva, 1991; Silva and Darragh 1995). High (> 1 Hz) frequency model predictions are very sensitive to this parameter (Silva, 1991; EPRI, 1993) and the interpretation of it being a stress drop or simply a scaling parameter depends upon how well real earthquake sources (on average) obey the omega-squared scaling (Equation D-3) and how well they are fit by the single-corner-frequency model. If earthquakes truly have single-corner-frequency omega-squared sources, the stress drop in Equation D-3 is a physical parameter and its values have a physical interpretation of the forces (stresses) accelerating the relative slip across the rupture surface. High stress drop sources result from a smaller fault rupture area (for the same **M**) than low stress drop sources (Brune, 1970). Less physically, stress drop can be viewed as simply a high frequency scaling or fitting parameter.

The spectral shape of the single-corner-frequency ω-squared source model is then described by the two free parameters M_0 and $\Delta\sigma$. The corner frequency increases with the shear-wave velocity and with increasing stress drop, both of which may be region dependent.

Crustal amplification accounts for the increase in wave amplitude as seismic energy travels through lower-velocity crustal materials from the source to the surface. The amplification depends on average crustal and near surface shear-wave velocity and density (Boore, 1986).

The P(f) filter in equation (D-1) is used in an attempt to model the observation that acceleration spectral density appears to fall off rapidly beyond some region- or site-dependent maximum frequency (Hanks, 1982; Silva and Darragh, 1995). This observed phenomenon truncates the high frequency portion of the spectrum and is responsible for the band-limited nature of the stochastic model. The band limits are the source corner frequency at low frequency and the high frequency spectral attenuation. This spectral fall-off at high frequency has been attributed to near-site attenuation (Hanks, 1982; Anderson and Hough, 1984) or to source processes (Papageorgiou and Aki, 1983) and perhaps results from both effects. In the Anderson and Hough (1984) attenuation model, adopted here, the form of the P(f) filter is taken as

$$P(f, r) = e^{-\pi\kappa(r)f} \qquad \text{(D-4)}$$

$\kappa(r)$ in Equation D-4 is a site- and distance-dependent parameter that represents the effect of intrinsic attenuation upon the wavefield as it propagates through the crust from source to receiver.

κ (r) depends on epicentral distance (r) and on both the shear-wave velocity (β) and quality factor (Q_S) averaged over a depth of H beneath the site (Hough et al., 1988;). At zero epicentral distance kappa (κ) is given by

$$\kappa(0) = \frac{H}{\overline{\beta}\ \overline{Q_S}} \qquad \text{(D-5)}$$

and is referred to as simply κ.

The bars in Equation D-5 represents an average of β and Q_s over a depth H. The value of κ at zero epicentral distance is attributed to attenuation in the very shallow crust directly below the site (Hough and Anderson, 1988; Silva and Darragh, 1995). The intrinsic attenuation along this part of the path is not thought to be frequency dependent and is modeled as a frequency independent, (although site- and crustal-region dependent) constant value of κ (Hough et al., 1988; Rovelli et al., 1988). This zero epicentral distance κ is the model implemented in this study.

The crustal path attenuation from the source to just below the site is modeled with the frequency-dependent quality factor Q(f). Thus the distance component of the original κ(r) (Equation D-4) is accommodated by Q(f) and R in the last term of Equation D-1:

$$\kappa(r) = \frac{H}{\overline{\beta}\ \overline{Q_S}} + \frac{R}{\beta_0\ Q(f)} \qquad \text{(D-6)}$$

The Fourier amplitude spectrum, FA(f), given by Equation D-1 represents the stochastic ground motion model employing a Brune source spectrum that is characterized by a single corner frequency. It is a point source and models direct shear-waves in a homogeneous half-space (with effects of a velocity gradient captured by the A(f) filter, Equation D-1). For horizontal motions, vertically propagating shear-waves are assumed. Validations using incident inclined SH-waves accompanied with raytracing to find appropriate incidence angles leaving the source showed little reduction in uncertainty compared to results using vertically propagating shear-waves. For vertical motions, P/SV propagators are used in addition to raytracing to model incident inclined plane waves (Appendix K and EPRI, 1993). This approach has been validated with recordings from the 1989 M 6.9 Loma Prieta earthquake (EPRI, 1993).

Equation D-1 represents an elegant ground motion model that accommodates source and wave propagation physics as well as propagation path and site effects with an attractive simplicity. The model is appropriate for an engineering characterization of ground motion since it captures the general features of strong ground motion in terms of peak acceleration and spectral composition with a minimum of free parameters (Boore, 1983; McGuire et al., 1984; Boore, 1986; Silva and Green, 1988; Silva et al., 1988; Schneider et al., 1993; Silva and Darragh, 1995). An additional important aspect of the stochastic model employing a simple source description is that the region-dependent parameters may be evaluated by observations of small local or regional earthquakes. Region-specific seismic hazard evaluations can then be made for areas with sparse strong motion data with relatively simple spectral analyses of weak motion (Silva, 1992).

In order to compute peak time-domain values, i.e. peak acceleration and oscillator response, RVT is used to relate RMS computations to peak value estimates. Boore (1983) and Boore and Joyner (1984) present an excellent development of the RVT methodology as applied to the stochastic ground motion model. The procedure involves computing the RMS value by integrating the power spectrum from zero frequency to the Nyquist frequency and applying Parseval's relation. Extreme value theory is then used to estimate the expected ratio of the peak value to the RMS value of a specified duration of the stochastic time history. The duration is generally taken as the inverse of the source corner frequency plus a term that increases with distance (Boore, 1983).

Factors that affect strong ground motions such as surface topography, finite and propagating seismic sources, laterally varying near-surface velocity and Q gradients, and random inhomogeneities along the propagation path are not included in the model. While some or all of these factors are generally present in any observation of ground motion and may exert controlling influences in some cases, the simple stochastic point source model appears to be robust in predicting median or average properties of ground motion (Boore 1983, 1986; Schneider et al., 1993; Silva, 1993). For this reason it represents a powerful predictive and interpretative tool for engineering characterization of strong ground motion.

D.3 Site Effects Model

To model soil and soft rock response, an RVT-based equivalent-linear approach is used by propagating either the point source outcrop power spectral density through a one-dimensional column. RVT is used to predict peak time domain values of shear-strain based upon the shear-strain power spectrum. In this sense, the procedure is analogous to the program SHAKE (Schnabel et al., 1972) except that peak shear strains in SHAKE are measured in the time domain. The purely frequency domain approach obviates a time domain control motion and, perhaps just as significantly, eliminates the need for a suite of analyses based on different input motions. This arises because each time domain analysis may be viewed as one realization of a random process. In this case, several realizations of the random process must be sampled to have a statistically stable estimate of site response. The realizations are usually performed by employing different control motions whose response spectrum matches a specified target. In the frequency-domain approach, the estimates of peak shear strains and oscillator response are, as a result of the RVT, fundamentally probabilistic in nature. Stable estimates of site response can then be rapidly computed permitting statistically significant estimates of uncertainties based on parametric variations.

The parameters that influence computed response include the shear-wave velocity profile and the strain dependencies of both the shear modulus and shear-wave damping.

D.4 Partition and Assessment of Ground Motion Variability

An essential requirement of any numerical modeling approach, particularly one that is implemented in the process of defining design ground motions, is a quantitative assessment of prediction accuracy. This means that one must characterize the variability associated with model predictions. For a ground motion model, prediction variability is comprised of two components: modeling variability and parametric variability. Modeling variability is a measure of how well the model works (how

accurately it predicts ground motions) when specific parameter values are known. Modeling variability is measured by misfits of model predictions to recorded motions through validation exercises and results from unaccounted components in the source, path, and site models (e.g. a point source cannot model the effects of directivity, and linear site response cannot accommodate nonlinear effects). Parametric variability results from a range of values for model parameters (i.e. slip distribution, soil profile, G/G_{max} and hysteretic damping curves). It is the sensitivity of a model to a range of values for model parameters. The total variability, modeling plus parametric, represents the variance associated with the ground motion prediction and, because it is a necessary component in estimating fractile levels, may be regarded as important as median predictions.

Both the modeling and parametric variabilities may have components of randomness and uncertainty. Table D-1 summarizes the four components of total variability in the context of ground motion predictions. Uncertainty is that portion of both modeling and parametric variability that, in principle, can be reduced as additional information becomes available, whereas randomness represents the intrinsic or irreducible component of variability for a given model or parameter. Randomness is that component of variability that is intrinsic or irreducible *for a given model.* The uncertainty component reflects a lack of knowledge and may be reduced as more data are analyzed. For example, in the point source model, stress drop is generally taken to be independent of source mechanism and tectonic region, and is found to have a standard error of about 0.7 (natural log) (EPRI, 1993). This variation or uncertainty plus randomness in $\Delta\sigma$ results in a variability in ground motion predictions for future earthquakes. If, for example, it is found that normal faulting earthquakes have generally lower stress drops than strike-slip events, which are, in turn, lower than reverse mechanism events, perhaps much of the variability in $\Delta\sigma$ may be reduced. In extensional regimes, where normal faulting earthquakes are most likely to occur, this new information may provide a reduction in variability (uncertainty component) for stress drop, say to 0.3 or 0.4 resulting in less ground motion variation due to a lack of knowledge of the mean stress drop. There is, however, a component of this stress drop variability that can *never* be reduced in the context of the Brune model. This results simply from the heterogeneity of the earthquake dynamics, which is not accounted for in the model and which results in the randomness component of parametric variability in stress drop. A more sophisticated model may be able to accommodate or model more accurately the source dynamics but, at the expense of a larger number of parameters and increased parametric uncertainty (i.e. finite-fault with slip model and nucleation point as unknown parameters for future earthquakes). That is, more complex models typically seek to reduce modeling randomness by more closely modeling physical phenomena. However, such models often require more comprehensive sets of observed data to constrain additional model parameters, which generally leads to increased parametric variability. If the increased parametric variability is primarily in the form of uncertainty, it is possible to reduce total variability, but only at the additional expense of constraining the additional parameters. Therefore, existing knowledge and/or available resources may limit the ability of more complex models to reduce total variability.

The distinction of randomness and uncertainty is model driven and somewhat arbitrary. The allocation is only important in the context of probabilistic seismic hazard analyses, because uncertainty is treated using alternative hypotheses in logic trees while randomness is integrated over in the hazard calculation (Cornell, 1968). For example, the uncertainty component in stress drop may be treated by using a discrete representation of the stress drop distribution and assigning weights and

specific values. A reasonable three point approximation to a normal distribution is given by weights of 0.2, 0.6, 0.2 for 5%, mean, and 95% values of stress drop respectively. If the distribution of uncertainty in stress drop were such that the 5%, mean, and 95% values were 50, 100, and 200 bars respectively, the stress drop values would be 50 and 200 bars with weights of 0.2, and 100 bars with a weight of 0.6. The randomness component in stress drop variability would then be formally integrated over in the hazard calculation.

D.4.1 Assessment of Modeling Variability

Modeling variability (uncertainty plus randomness) is usually evaluated by comparing response spectra computed from recordings to predicted spectra. The modeling variability is defined as the standard error of the residuals of the log of the average horizontal component (or vertical component) response spectra. The residual is defined as the difference of the logarithms of the observed average 5% damped acceleration response spectra and the predicted response spectra. At each period, the residuals are squared and summed over the total number of sites for one or all earthquakes modeled. Dividing the resultant sum by the number of sites (provided they are statistically independent) results in an estimate of the model variance. Any model bias (average offset) that exists may be estimated in the process (Abrahamson et al., 1990; EPRI, 1993) and used to correct (lower) the variance (and to adjust the median as well). In this approach, the modeling variability can be separated into randomness and uncertainty where the bias-corrected variability represents randomness and the total variability represents randomness plus uncertainty. The uncertainty is captured in the model bias as this may be reduced in the future by refining the model. The remaining variability (randomness) remains irreducible for *this* model. In computing the variance and bias estimates only the frequency range between processing filters at each site (minimum of the 2 components) is used. The causal butterworth filter corners are listed for each site (and component) in the Strong Motion Catalogue (Appendix B).

D.4.2 Assessment of Parametric Variability

Parametric variability, or the variation in ground motion predictions due to uncertainty and randomness in model parameters is difficult to assess. Formally it is straightforward: a Monte Carlo approach may be used with each parameter randomly sampled about its mean (or median) value either individually for sensitivity analyses (Silva, 1992; Roblee et al., 1996) or in combination to estimate the total parametric variability (Silva, 1992; EPRI, 1993). In reality, however, there are two complicating factors.

The first factor involves the specific parameters kept fixed with all earthquakes, paths, and sites when computing the modeling variability. These parameters are then implicitly included in modeling variability provided the data sample a sufficiently wide range in source, path, and site conditions. The parameters that are varied during the assessment of modeling variation should have a degree of uncertainty and randomness associated with them for the next earthquake. Any ground motion prediction should then have a variation reflecting this lack of knowledge and randomness in the free parameters.

An important adjunct to fixed and free parameters is the issue of parameters that may vary but by fixed rules. For example, source rise time is magnitude dependent and is specified by an empirical relation (Silva et al., 1997) in the stochastic finite-source model. In evaluating the modeling variability with different magnitude earthquakes, rise time is varied, but because it follows a strict rule, any variability associated with rise time variation is counted as modeling variability. This is strictly true only if the sample of earthquakes has adequately spanned the space of magnitude, source mechanism, and other factors that may affect rise time. Also, the earthquake to be modeled must be within that validation space. As a result, the validation or assessment of model variation should be done on as large a number of earthquakes of varying sizes and mechanisms as possible.

The second, more obvious factor in assessing parametric variability is a knowledge of the appropriate distributions for the parameters (assuming correct values for median or mean estimates are known). In general, for the stochastic models, median parameter values and uncertainties are based, to the extent possible, on evaluating the parameters derived from previous earthquakes (Silva, 1992; EPRI, 1993).

The parametric variability is site, path, and source dependent and must be evaluated for each application (Roblee et al., 1996). For example, at large source-to-site distances, crustal path damping may control short-period motions. At close distances to a large fault, both the site and finite-source (asperity location and nucleation point) may dominate, and depending upon site characteristics, the source or site may control different frequency ranges (Silva, 1992; Roblee et al., 1996).

In combining modeling and parametric variance, independence is assumed (covariance is zero) and the variances are simply added to give the total variance.

$$\sigma^2_T = \sigma^2_M + \sigma^2_P{}^2 \qquad \text{(D-7)},$$

where

σ^2_M = modeling variance,

σ^2_P = parametric variance.

D.4.3 Model Bias And Variance Estimates For The Point Source Model

Results presented here are from a validation exercise sponsored by the Department of Energy. It was begun in 1994 and completed in 1997 (Silva et al., 1997) and included the stochastic finite-source model as well. In this exercise, regional crustal models (for each earthquake) were used along with generic rock and soil profiles (one each) and generic (region specific) G/G_{max} and hysteric damping curves. Region and earthquake specific inversions were done for Q(f) models and point source stress drops. Bias and variance estimates were computed over 16 earthquakes, 503 sites, reflecting the magnitude range of **M** 5.3 (Imperial Valley aftershock) to **M** 7.4 and a site distance range of 1 to 218 km (460 km for CEUS). CEUS data include both the Saguenay and Nahanni earthquakes. This

[2]Strong ground motions are generally considered to be log normally distributed.

represents a comprehensive data set and provides a statistically robust assessment of prediction accuracy for the point source model.

Model bias and variability estimates are shown in Figures D-1, D-2, and D-3. Over all the sites, Figure D-1, the bias is slightly positive for frequencies greater than about 10 Hz and is near zero from about 10 Hz to 1 Hz. Below 1 Hz, a stable point source overprediction is reflected in the negative bias. The analyses are considered reliable down to about 0.3 Hz where the model shows about a 40% overprediction.

The model variability is low, about 0.5 above about 3 to 4 Hz and increases with decreasing frequency to near 1 at 0.3 Hz. Above 1 Hz, there is little difference between the total variability (uncertainty plus randomness) and randomness (bias corrected variability) reflecting the near zero bias estimates. Below 1 Hz there is considerable uncertainty contributing to the total variability suggesting that the model can be measurably improved, as its predictions tend to be consistently high at very low frequencies ($\leq$ 1 Hz). This stable misfit may be interpreted as the presence of a second corner frequency for WNA sources (Atkinson and Silva, 1997).

For the soil sites, Figure D-2 shows a slight improvement at 1 Hz and above in both the bias and variability estimates. This indicates that the rock sites must reflect the converse and Figure D-3 does show larger bias and variability estimates than the results for all the sites. Soil sites are modeled more accurately than rock sites. This suggests that strong ground motions at rock sites are more variable than motions at soil sites and that the model is not capturing the increased site-to-site variation. This is consistent with the trend seen in the individual earthquake analyses: soil sites are modeled more accurately than rock sites because they have less intra-event variability. The larger rock site bias above 20 Hz suggests a small stable underprediction possibly from the use of a single smooth rock profile rather than randomizing the profile and using a mean spectrum.

In general, for frequencies of about 1 Hz and higher, the point source bias estimates are small (near zero) and the variabilities range from about 0.5 to 0.6. These estimates are low considering that high frequency ground motion variance decreases with increasing magnitude, particularly above **M** 6.5 (Youngs et al., 1995), and these validations are based on a data set comprised of several earthquakes with **M** less than **M** 6.5 (288 of 513 sites). Because generic site parameters were used, the model variability (mean = 0) contains the total uncertainty and randomness contribution for the site. The parametric variability due to uncertainty and randomness in site parameters: shear-wave velocity, profile depth, G/G_{max} and hysteretic damping curves need not be added to the model variability estimates. It is useful to perform parametric variations to assess site parameter sensitivities on the ground motions, but only source and path damping Q(f) parametric variabilities require assessment on a site-specific basis for addition to the model variability. The uncertainty and randomness for the point source is contained in the stress drop for the single-corner frequency model as well as source depth. For applications to the CEUS, additional uncertainty may be appropriate to accommodate the likelihood of a double corner source, that is, to include epistemic uncertainty in the shape of the source spectrum. Alternatively, composite source spectra could be used based on weighted averages of the single- and double-corner models.

References

Abrahamson, N.A., P.G. Somerville, and C.A. Cornell (1990). "Uncertainty in numerical strong motion predictions" *Proc. Fourth U.S. Nat. Conf. Earth. Engin.*, Palm Springs, CA., 1, 407-416.

Aki, K. and P. G. Richards. (1980). *"Quantitative seismology."* W. H. Freeman and Co., San Francisco, California.

Anderson, J. G. and S. E. Hough (1984). "A Model for the Shape of the Fourier Amplitude Spectrum of Acceleration at High Frequencies." *Bull. Seism. Soc. Am.*, 74(5), 1969-1993.

Atkinson, G.M and W.J. Silva (1997). "An empirical study of earthquake source spectra for California earthquakes." *Bull. Seism. Soc. Am.* 87(1), 97-113.

Atkinson, G.M. (1984). "Attenuation of strong ground motion in Canada from a random vibrations approach." *Bull. Seism. Soc. Am.*, 74(5), 2629-2653.

Boore, D.M., and G.M. Atkinson (1987). "Stochastic prediction of ground motion and spectral response parameters at hard-rock sites in eastern North America." *Bull. Seism. Soc. Am.*, 77(2), 440-467.

Boore, D.M. and W.B. Joyner (1984). "A note on the use of random vibration theory to predict peak amplitudes of transient signals." *Bull. Seism. Soc. Am.*, 74, 2035-2039.

Boore, D.M. (1986). "Short-period P- and S-wave radiation from large earthquakes: implications for spectral scaling relations." *Bull. Seism. Soc. Am.*, 76(1) 43-64.

Boore, D.M. (1983). "Stochastic simulation of high-frequency ground motions based on seismological models of the radiated spectra." *Bull. Seism. Soc. Am.*, 73(6), 1865-1894.

Brune, J.N. (1971). "Correction." *J. Geophys. Res.* 76, 5002.

Brune, J.N. (1970). "Tectonic stress and the spectra of seismic shear waves from earthquakes." *J. Geophys. Res.* 75, 4997-5009.

Electric Power Research Institute (1993). "Guidelines for determining design basis ground motions." Palo Alto, Calif: Electric Power Research Institute, vol. 1-5, EPRI TR-102293.

vol. 1: Methodology and guidelines for estimating earthquake ground motion in eastern North America.

vol. 2: Appendices for ground motion estimation.

vol. 3: Appendices for field investigations.

vol. 4: Appendices for laboratory investigations.

vol. 5: Quantification of seismic source effects.

Hanks, T.C. (1982). "f_{max}." *Bull. Seism. Soc. Am.*, 72, 1867-1879.

Hanks, T.C., and R.K. McGuire (1981). "The character of high-frequency strong ground motion." *Bull. Seism. Soc. Am.*, 71(6), 2071-2095.

Hanks, T.C., and H. Kanamori (1979). "A moment magnitude scale." *J. Geophys. Res.*, 84, 2348-2350.

Hartzell, S.H. (1978). "Earthquake aftershocks as Green's functions." *Geophys. Res. Letters*, 5, 1-4.

McGuire, R. K., A. M. Becker, and N. C. Donovan (1984). "Spectral Estimates of Seismic Shear Waves." *Bull. Seism. Soc. Am.*, 74(4), 1427-1440.

Hough, S. E. and J. G. Anderson (1988). "High-Frequency Spectra Observed at Anza, California: Implications for Q Structure." *Bull. Seism. Soc. Am.*, 78(2), 692-707.

Hough, S.E., J.G. Anderson, J. Brune, F. Vernon III, J. Berger, J. Fletcher, L. Haar, T. Hanks, and L. Baker (1988). "Attenuation near Anza, California." *Bull. Seism. Soc. Am.*, 78(2), 672-691.

Papageorgiou, A.S., and K. Aki (1983). "A specific barrier model for the quantitative description of inhomogeneous faulting and the prediction of strong ground motion, part I, Description of the model." *Bull. Seism. Soc. Am.*, 73(4), 693-722.

Roblee, C.J., W.J. Silva, G.R. Toro and N. Abrahamson (1996). "Variability in site-specific seismic ground-motion design predictions." in press.

Rovelli, A., O. Bonamassa, M. Cocco, M. Di Bona and S. Mazza (1988). "Scaling laws and spectral parameters of the ground motion in active extensional areas in Italy." *Bull. Seism. Soc. Am.*, 78(2), 530-560.

Schneider, J.F., W.J. Silva, and C.L. Stark (1993). "Ground motion model for the 1989 **M** 6.9 Loma Prieta earthquake including effects of source, path and site." *Earthquake Spectra*, 9(2), 251-287.

Silva, W.J., N. Abrahamson, G. Toro, C. Costantino (1997). "Description and validation of the stochastic ground motion model." Submitted to Brookhaven National Laboratory, Associated Universities, Inc. Upton, New York.

Silva, W.J., and R. Darragh (1995). "Engineering characterization of earthquake strong ground motion recorded at rock sites." Palo Alto, Calif:Electric Power Research Institute.

Silva, W.J. (1993) "Factors controlling strong ground motions and their associated uncertainties." *Seismic and Dynamic Analysis and Design Considerations for High Level Nuclear Waste Repositories, ASCE* 132-161.

Silva, W.J. (1992). "Factors controlling strong ground motions and their associated uncertainties." *Dynamic Analysis and Design Considerations for High Level Nuclear Waste Repositories, ASCE* 132-161.

Silva, W.J. (1991). "Global characteristics and site geometry." Chapter 6 in *Proceedings: NSF/EPRI Workshop on Dynamic Soil Properties and Site Characterization.* Palo Alto, Calif.: Electric Power Research Institute, NP-7337.

Silva, W. J., R. Darragh, C. Stark, I. Wong, J. C. Stepp, J. Schneider, and S-J. Chiou (1990). "A Methodology to Estimate Design Response Spectra in the Near-Source Region of Large Earthquakes Using the Band-Limited-White-Noise Ground Motion Model". *Procee. of the Fourth U.S. Conf. on Earthquake Engineering,* Palm Springs, California. 1, 487-494.

Silva, W.J., T. Turcotte, and Y. Moriwaki (1988). "Soil Response to Earthquake Ground Motion," Palo Alto, CA: EPRI, RP 2556-07.

Silva, W. J. and R. K. Green (1988). "Magnitude and Distance Scaling of Response Spectral Shapes for Rock Sites with Applications to North American Environments." In *Proceedings: Workshop on Estimation of Ground Motion in the Eastern United States*, EPRI NP-5875, Electric Power Research Institute.

Silva, W.J. and K. Lee (1987). "*WES RASCAL code for synthesizing earthquake ground motions.*" State-of-the-Art for Assessing Earthquake Hazards in the United States, Report 24, U.S. Army Engineers Waterways Experiment Station, Miscellaneous Paper S-73-1.

Toro, G. R. and R. K. McGuire (1987). "An Investigation into Earthquake Ground Motion Characteristics in Eastern North America." *Bull. Seism. Soc. Am.*, 77(2), 468-489.

Toro, G. R. (1985). "Stochastic Model Estimates of Strong Ground Motion." In *Seismic Hazard Methodology for Nuclear Facilities in the Eastern United States*, Appendix B, R. K. McGuire, ed., Electric Power Research Institute, Project P101-29.

Youngs, R.R., N.A. Abrahamson, F. Makdisi, and K. Sadigh (1995). "Magnitude dependent dispersion in peak ground acceleration." *Bull. Seism. Soc. Am.*, 85(1), 1161-1176.

Table D-1

CONTRIBUTIONS TO TOTAL VARIABILITY
IN GROUND MOTION MODELS

	Modeling Variability	Parametric Variability
Uncertainty *(also Epistemic Uncertainty)*	Modeling Uncertainty: Variability in predicted motions resulting from particular model assumptions, simplifications and/or fixed parameter values. *Can be reduced by adjusting or "calibrating" model to better fit observed earthquake response.*	Parametric Uncertainty: Variability in predicted motions resulting from incomplete data needed to characterize parameters. *Can be reduced by collection of additional information which better constrains parameters*
Randomness *(also Aleatory Uncertainty)*	Modeling Randomness: Variability in predicted motions resulting from discrepancies between model and actual complex physical processes. *Cannot be reduced for a given model form.*	Parametric Randomness: Variability in predicted motions resulting from inherent randomness of parameter values. *Cannot be reduced a priori* by collection of additional information.*

* Some parameters (e.g. source characteristics) may be well defined after an earthquake.

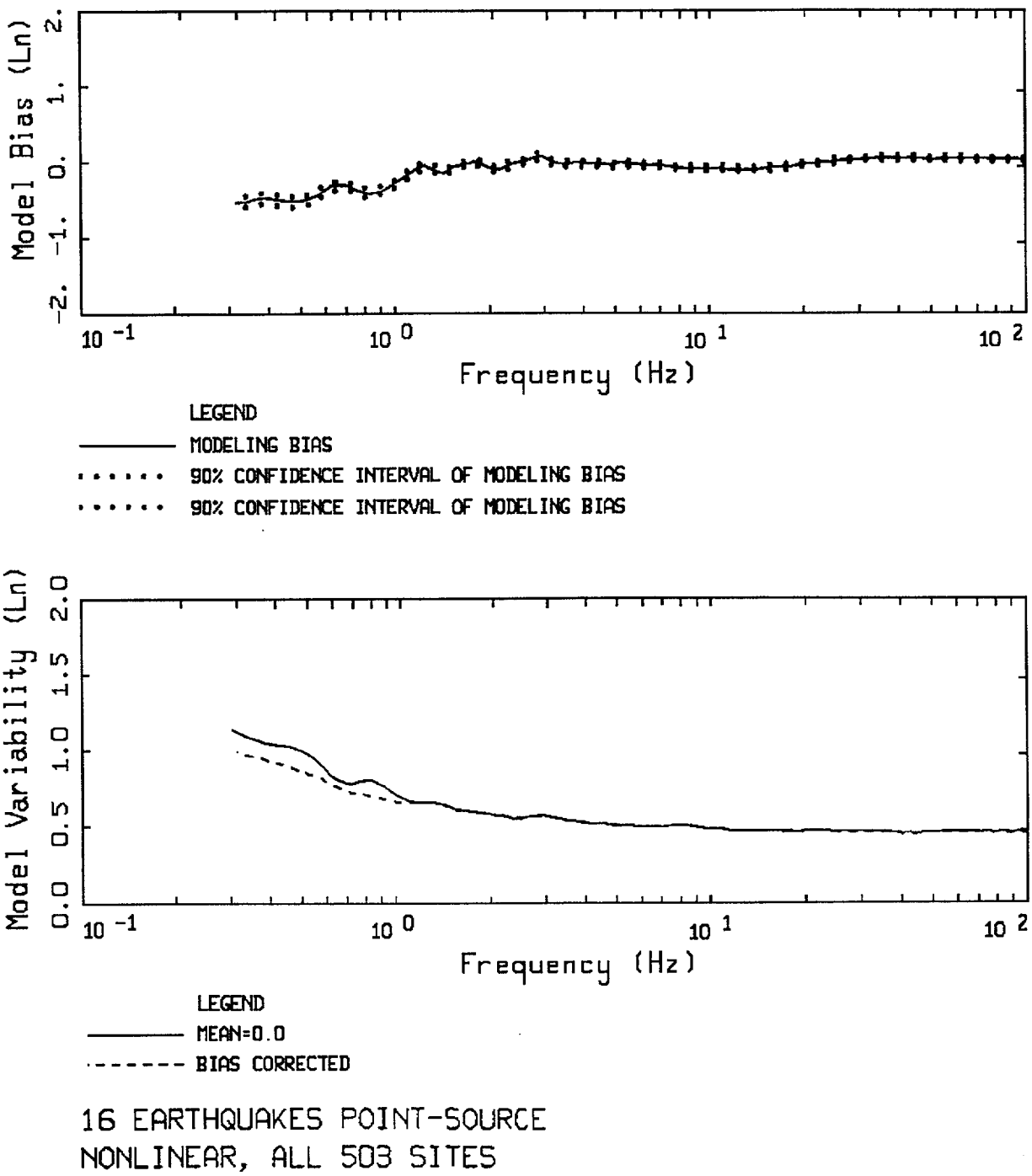

Figure D-1. Model bias and variability estimates for all earthquakes computed over all 503 sites for the point-source model.

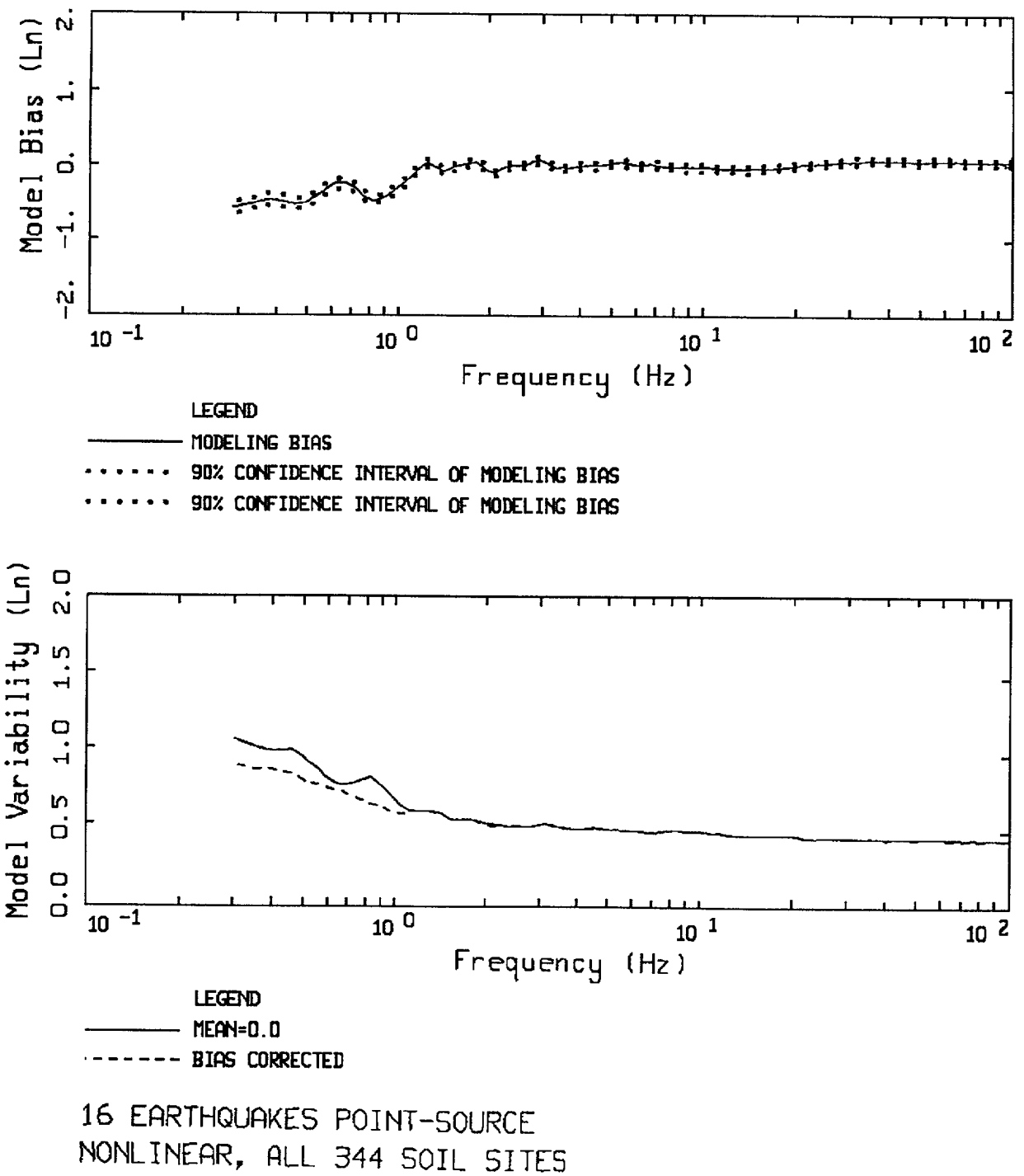

Figure D-2. Model bias and variability estimates for all earthquakes computed over all 344 soil sites for the point-source model.

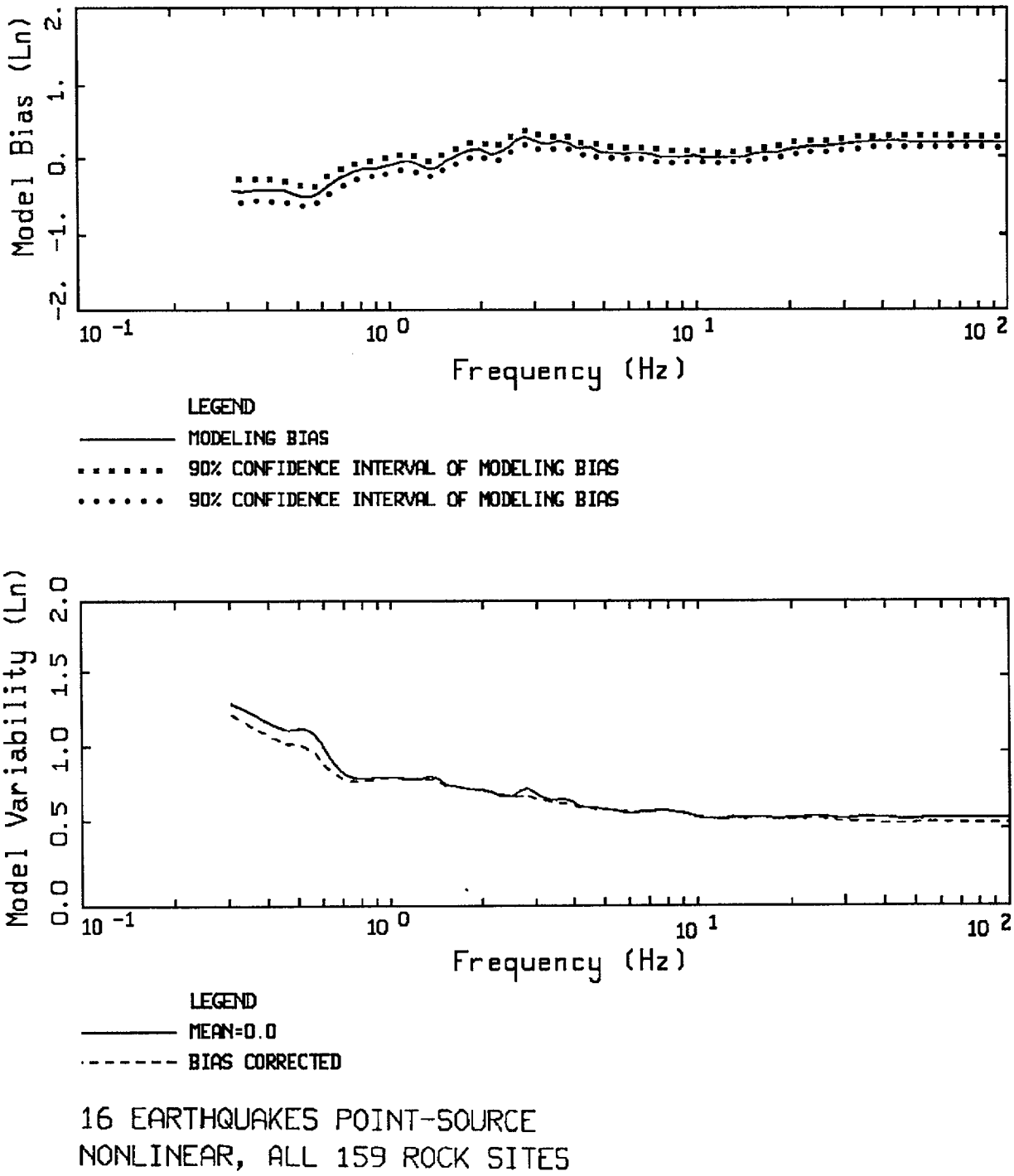

Figure D-3. Model bias and variability estimates for all earthquakes computed over all 159 rock sites for the point-source model.

APPENDIX E FOURIER AMPLITUDE SPECTRA FOR WUS EMPIRICAL MOTIONS

Notation: D1RM55HV

D1	Distance Bin 1 (0 - 10 km)
R	Rock Site
S	Soil Site
M55	Magnitude Bin 5 - 6
H	Horizontal
V	Vertical
AMPAVGH	Average Value Horizontal Records
AMPAVGV	Average Value Vertical Records

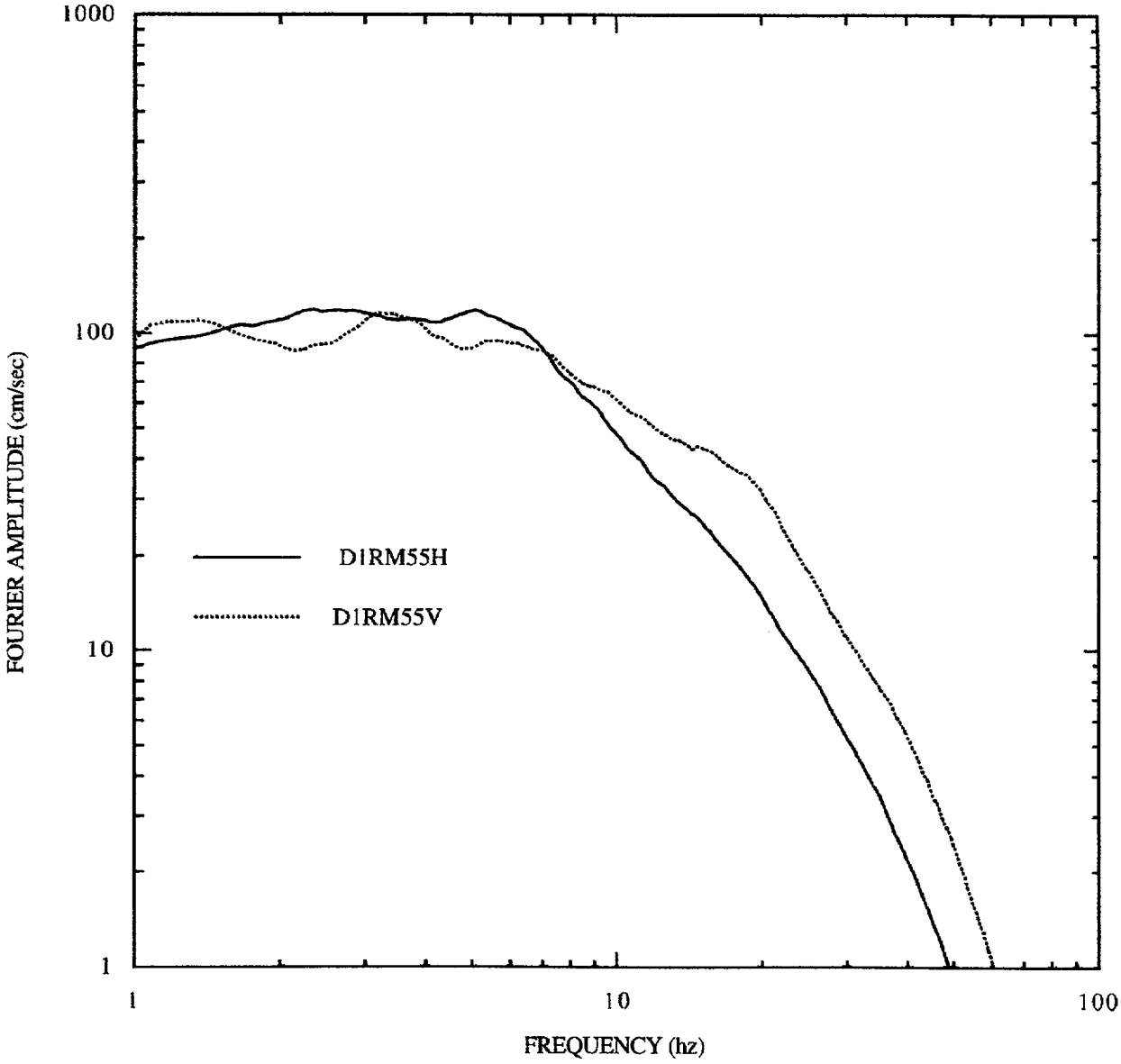

Figure E-1. Mean Fourier spectra for distance 0-10km, rock sites, M5-6

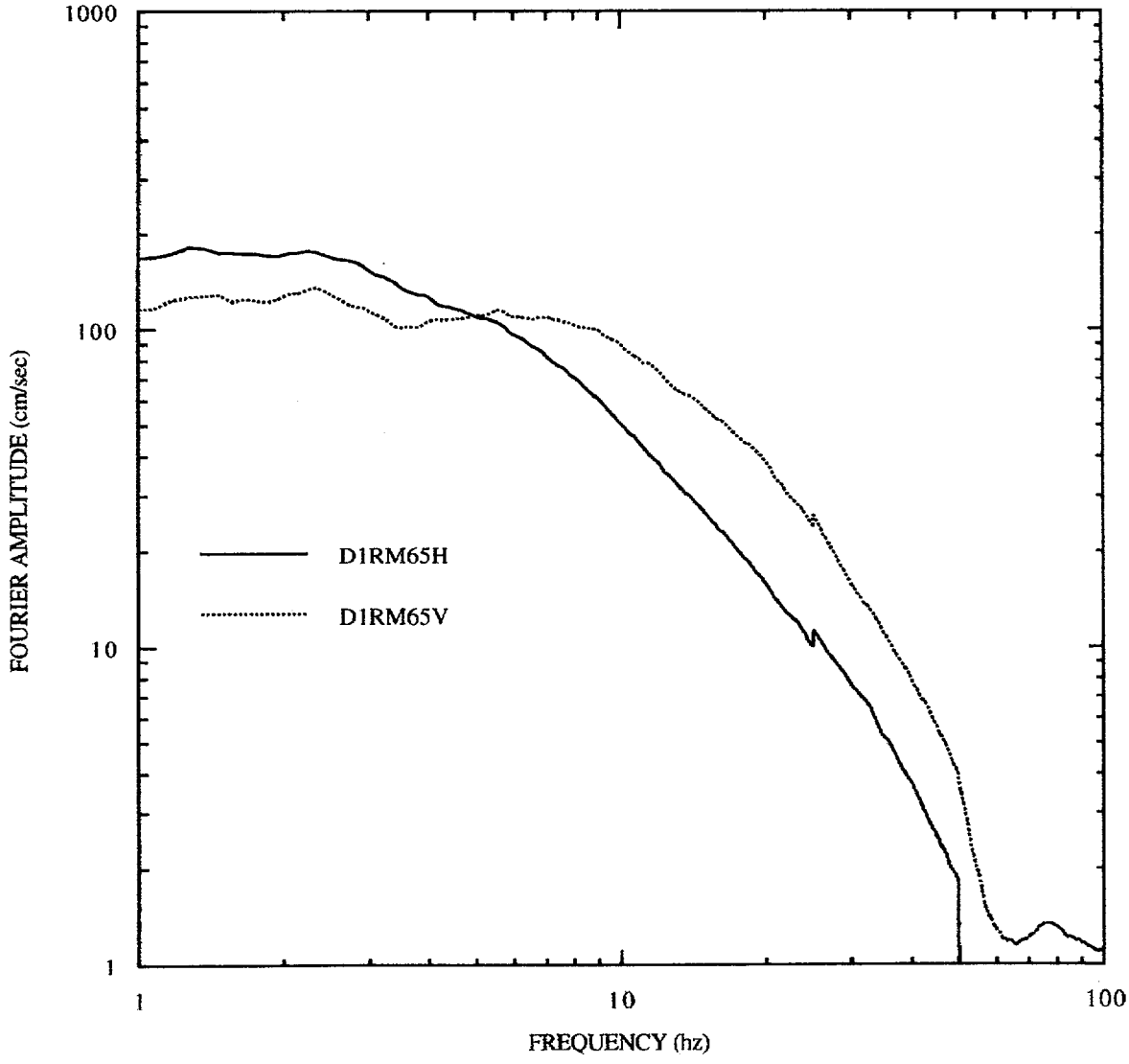

Figure E-2. Mean Fourier spectra for distance 0-10km, rock sites, M6-7

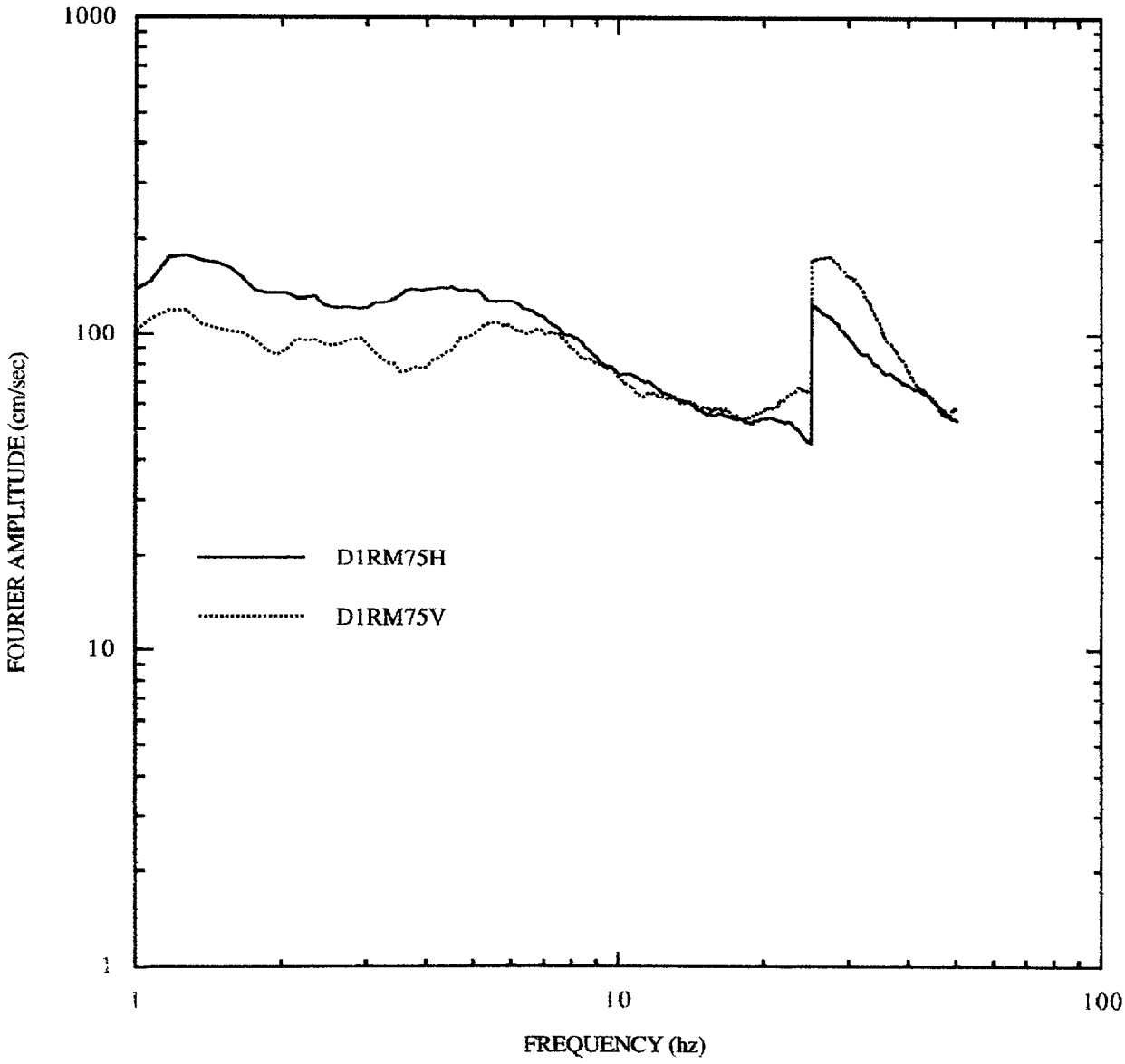

Figure E-3. Mean Fourier spectra for distance 0-10 km, rock sites, M7+. Note: discontinuity at 25 Hz is caused by few records available above that frequency.

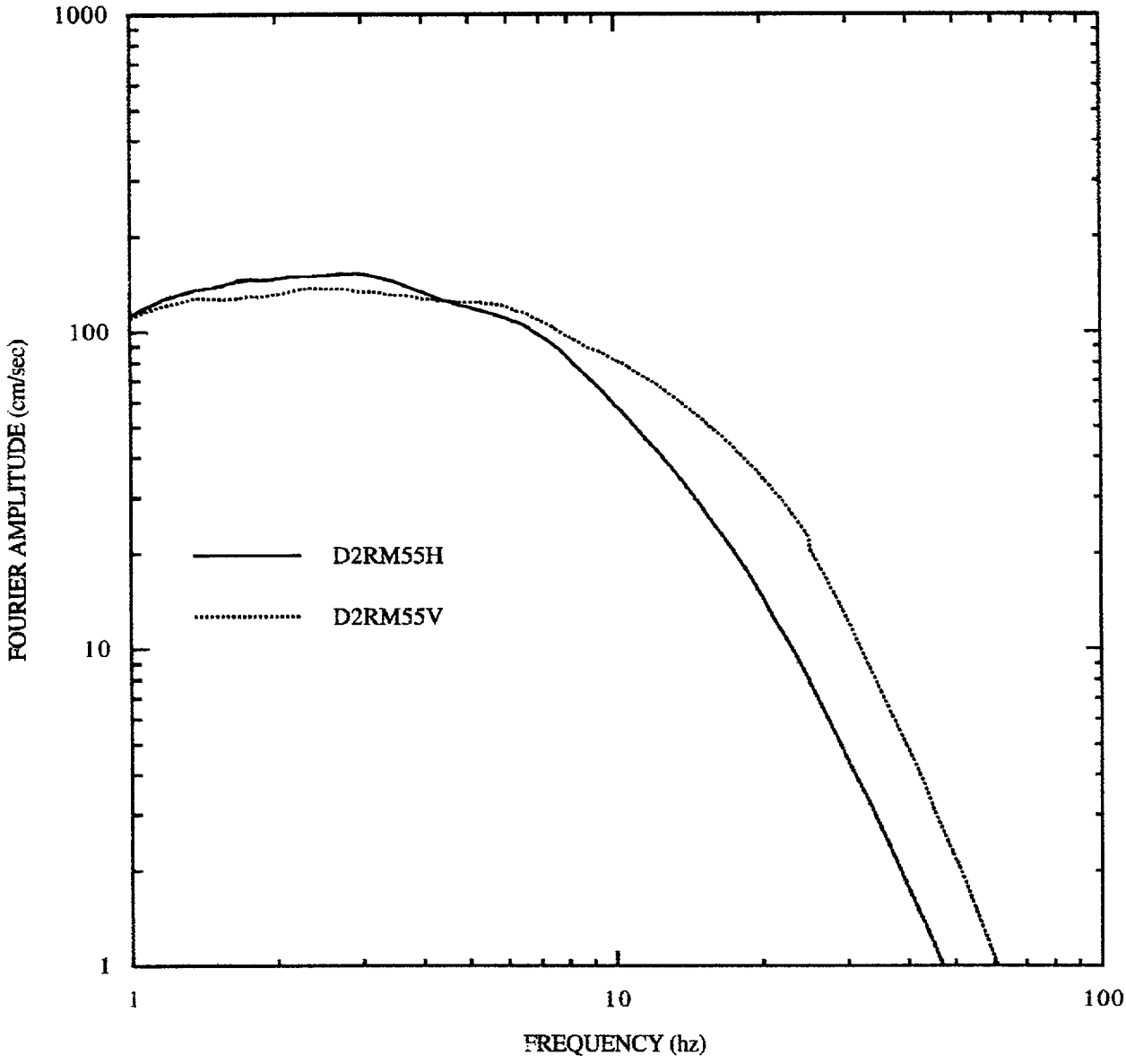

Figure E-4. Mean Fourier spectra for distance 10-50km, rock sites, M5-6

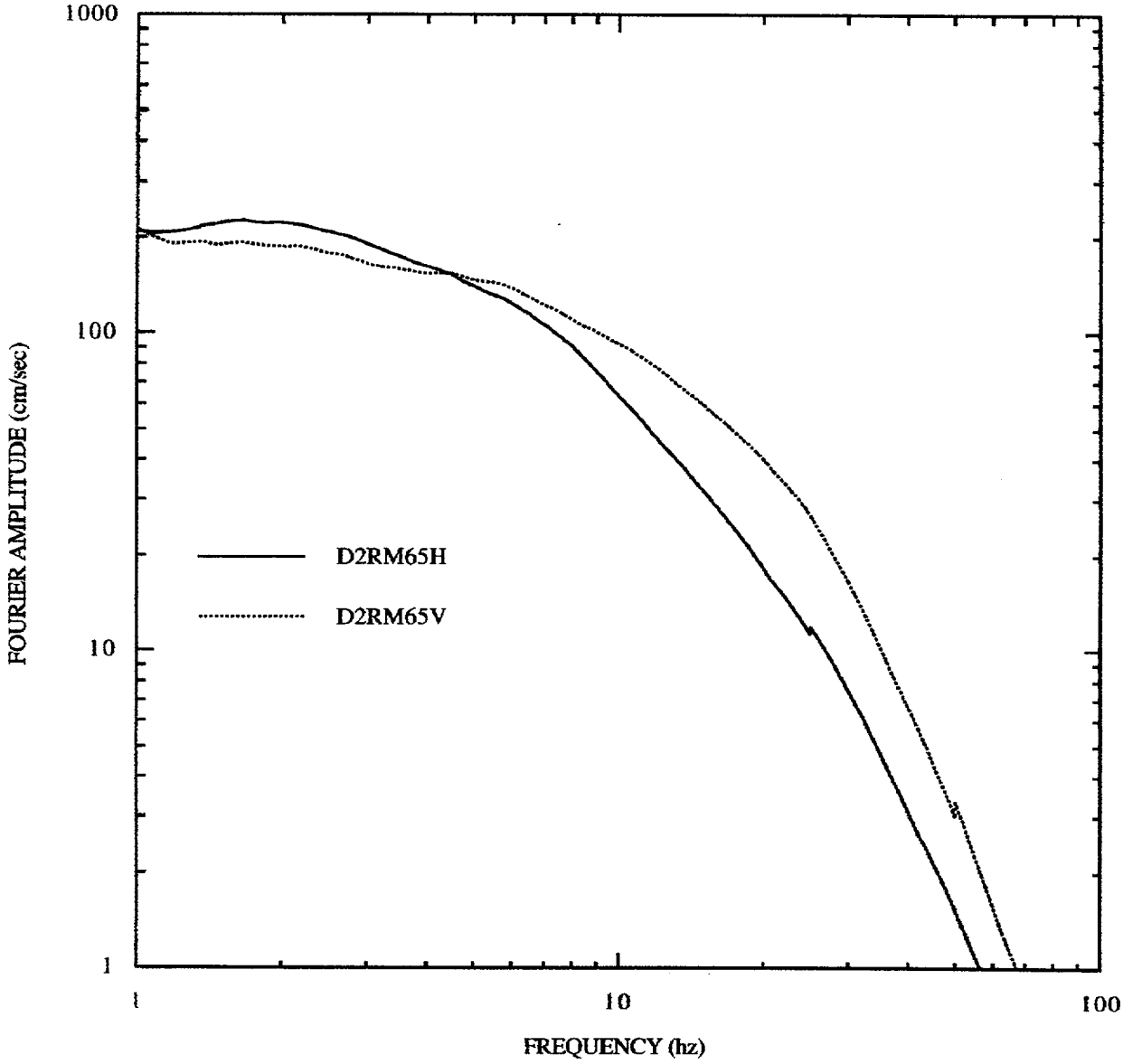

Figure E-5. Mean Fourier spectra for distance 10-50km, rock sites, M6-7.

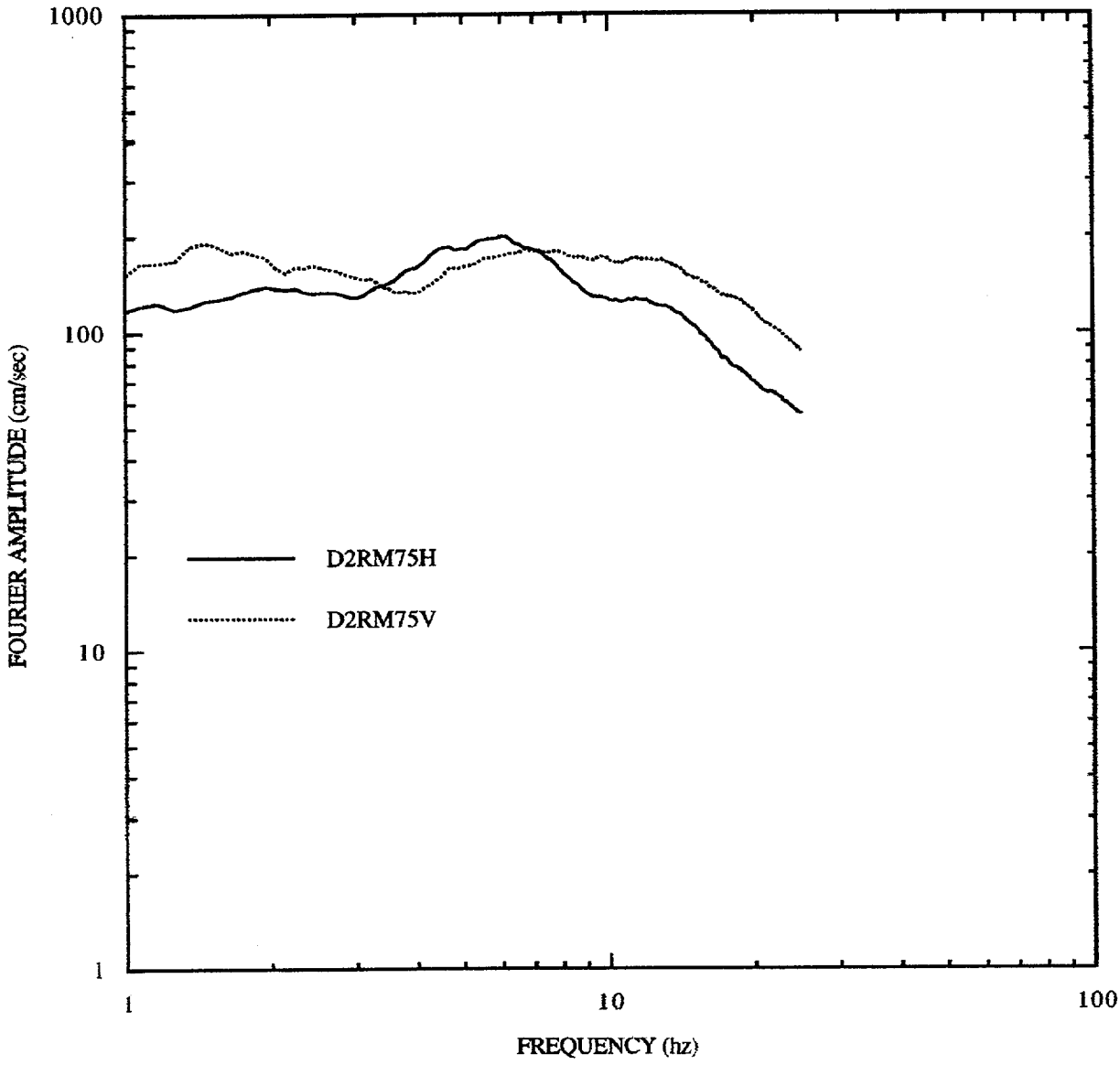

Figure E-6. Mean Fourier spectra for distance 10-50km, rock sites, M7+.

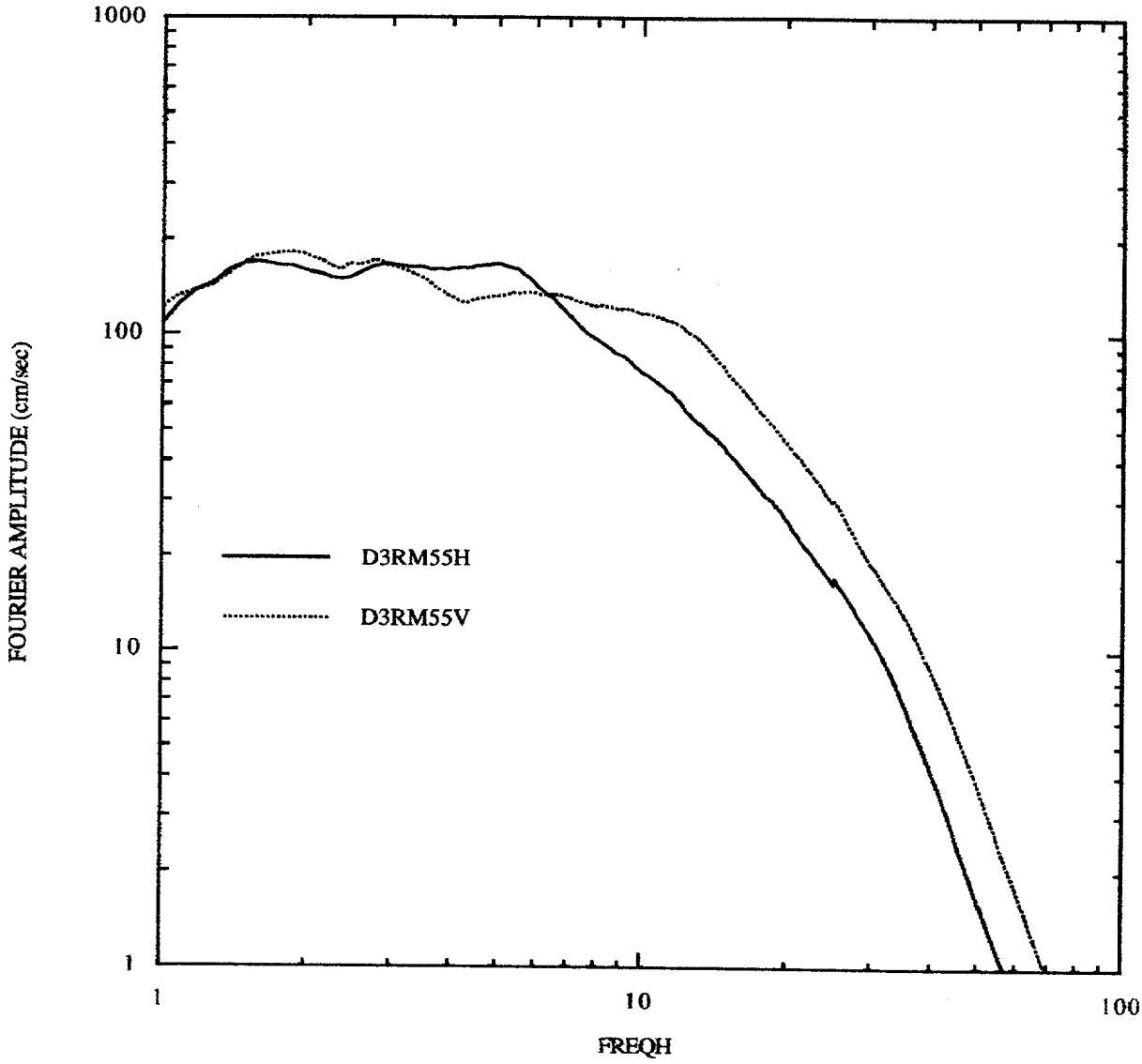

Figure E-7. Mean Fourier spectra for distance 50-100 km, rock sites, M5-6.

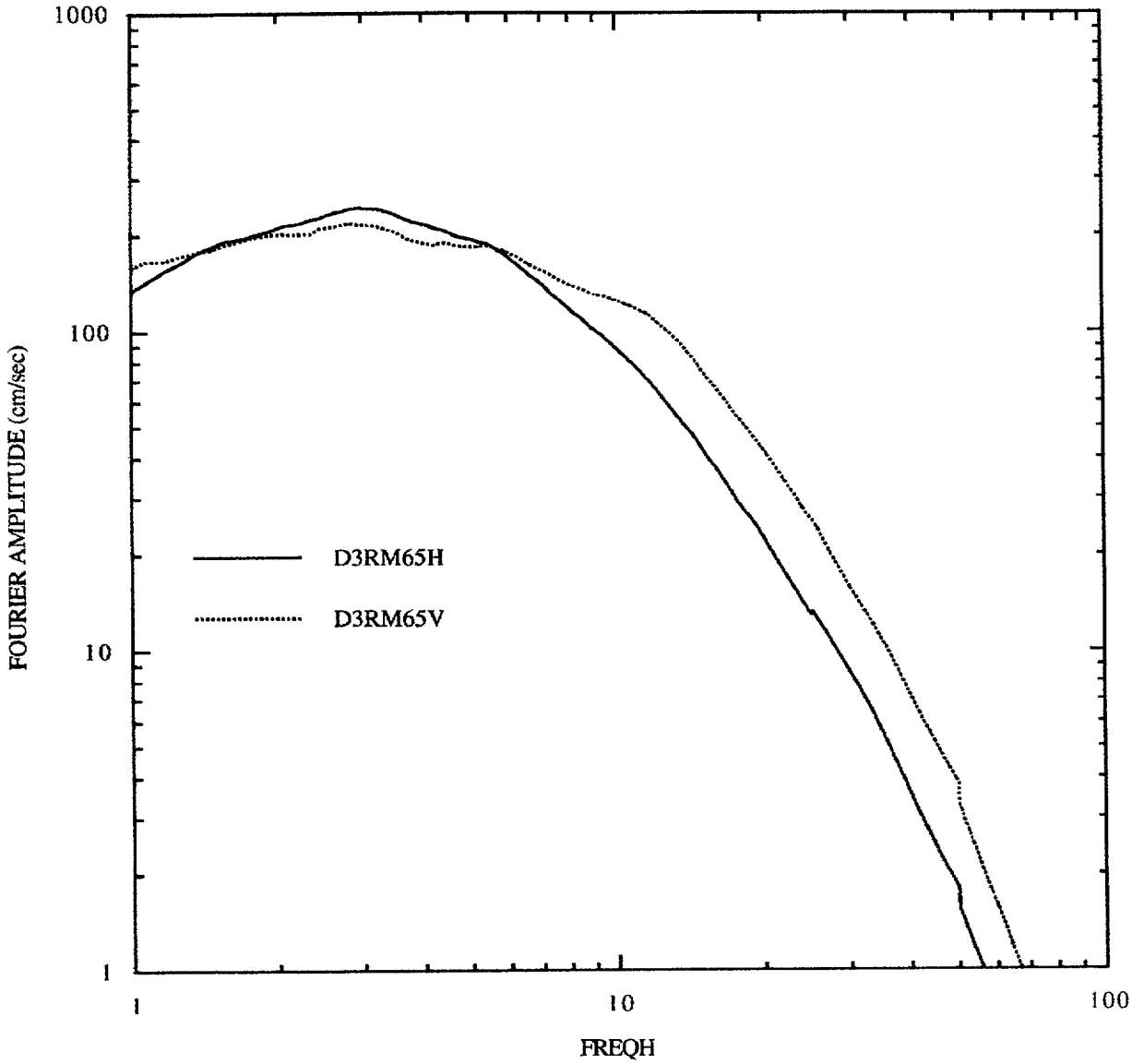

Figure E-8. Mean Fourier spectra for distance 50-100 km, rock sites, M6-7.

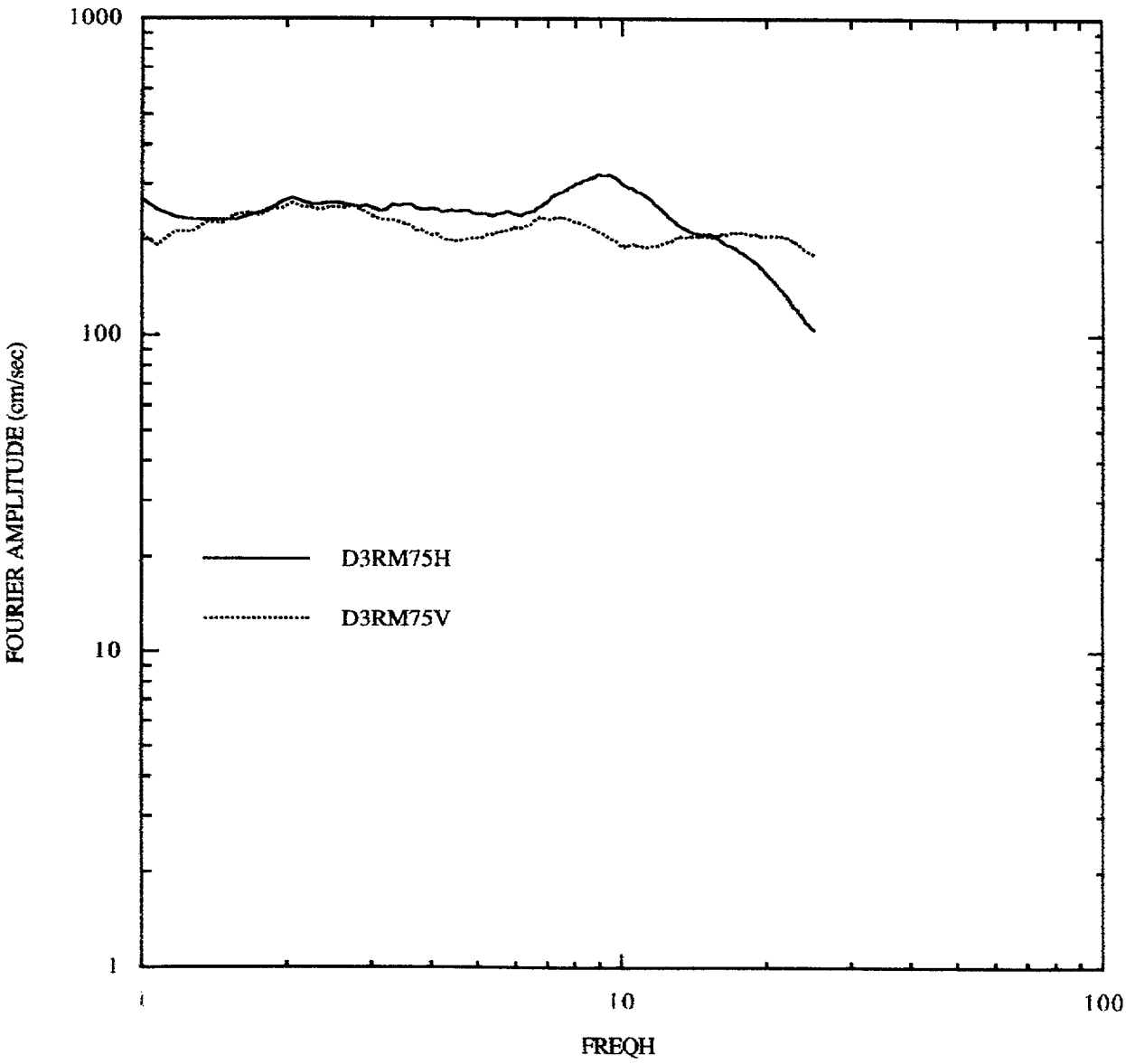

Figure E-9. Mean Fourier spectra for distance 50-100 km, rock sites, M7+.

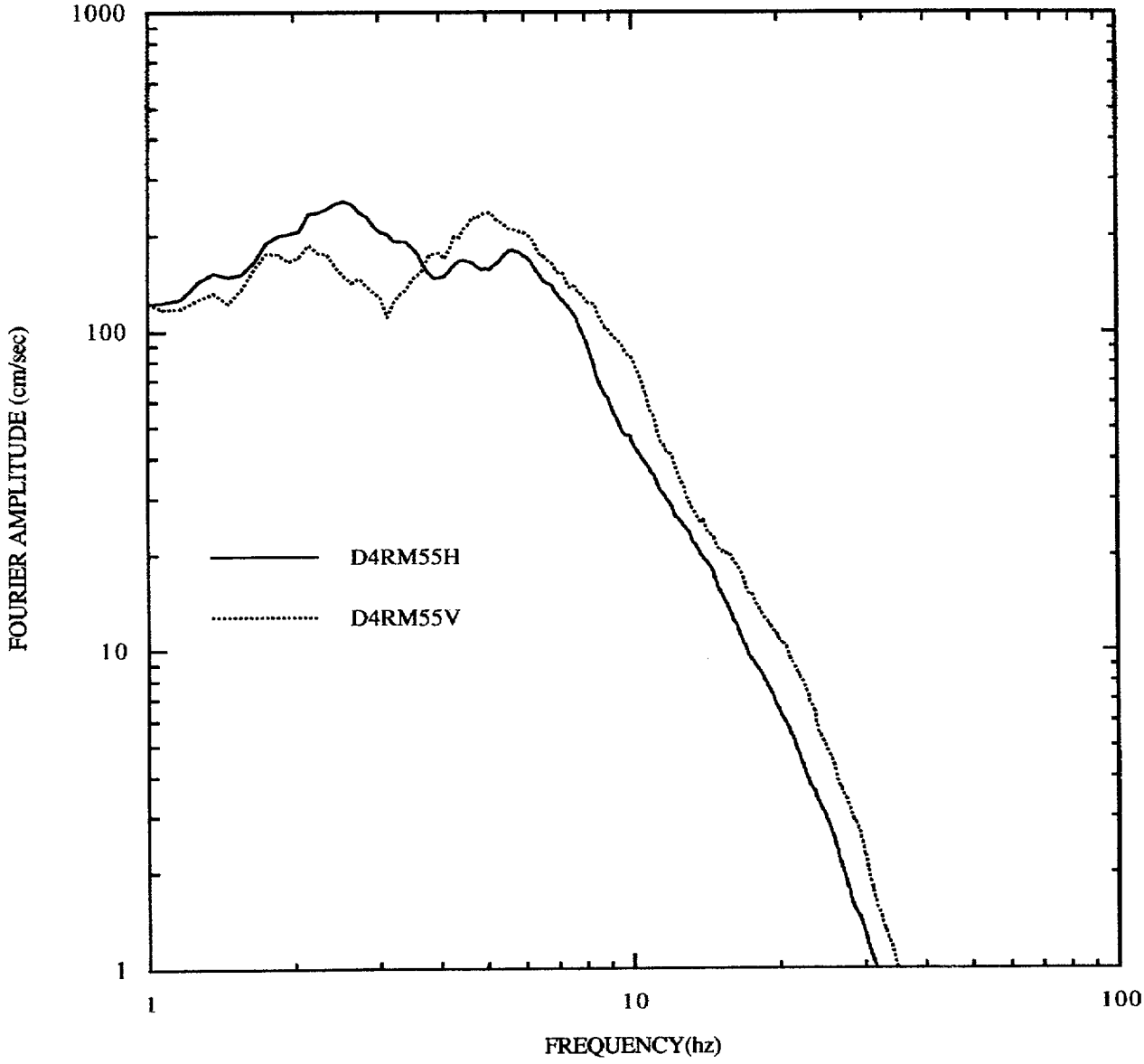

Figure E-10. Mean Fourier spectra for distance 100-200 km, rock sites, M5-6.

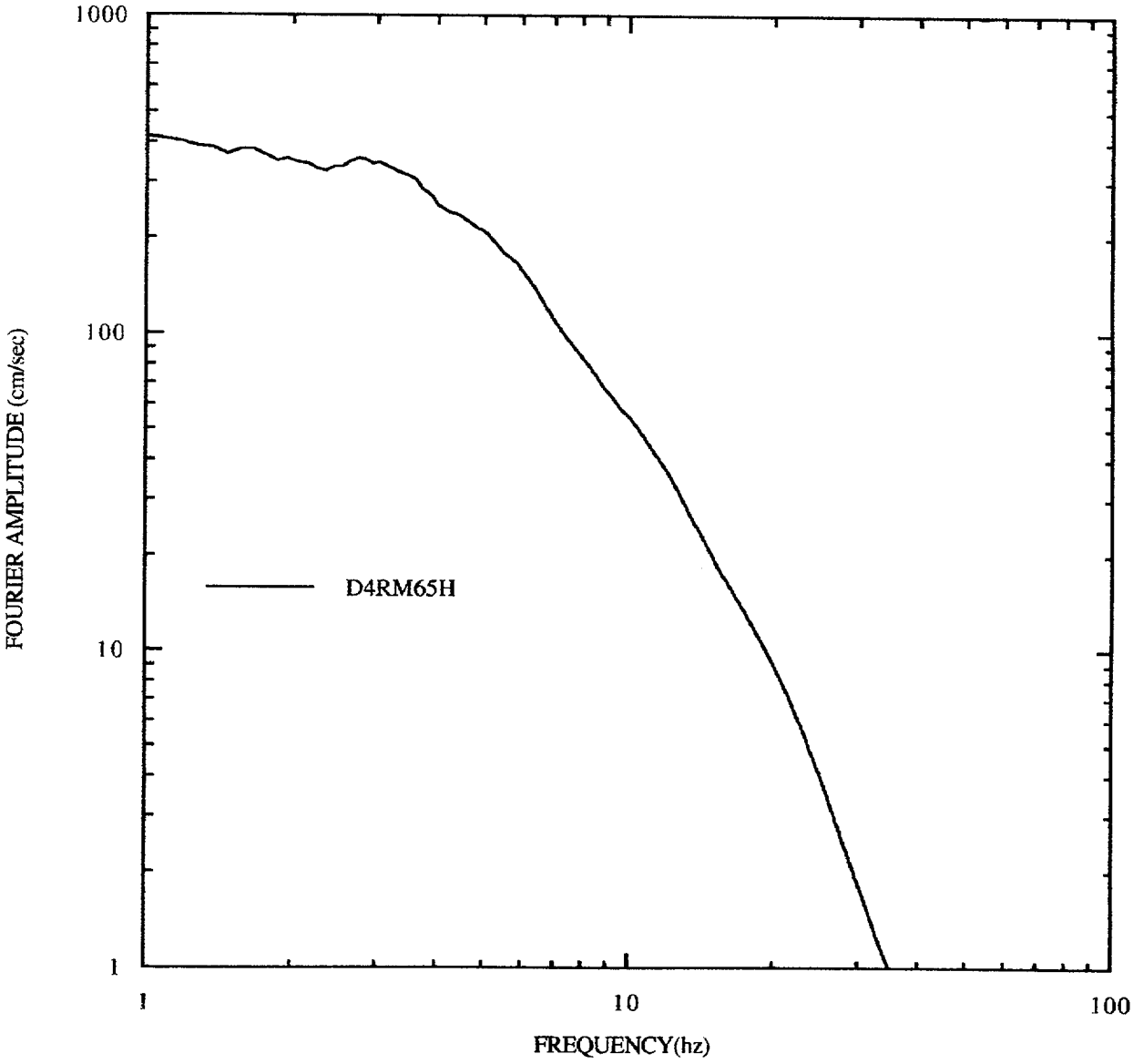

Figure E-11. Mean Fourier spectra for distance 100-200 km, rock sites, M6-7.

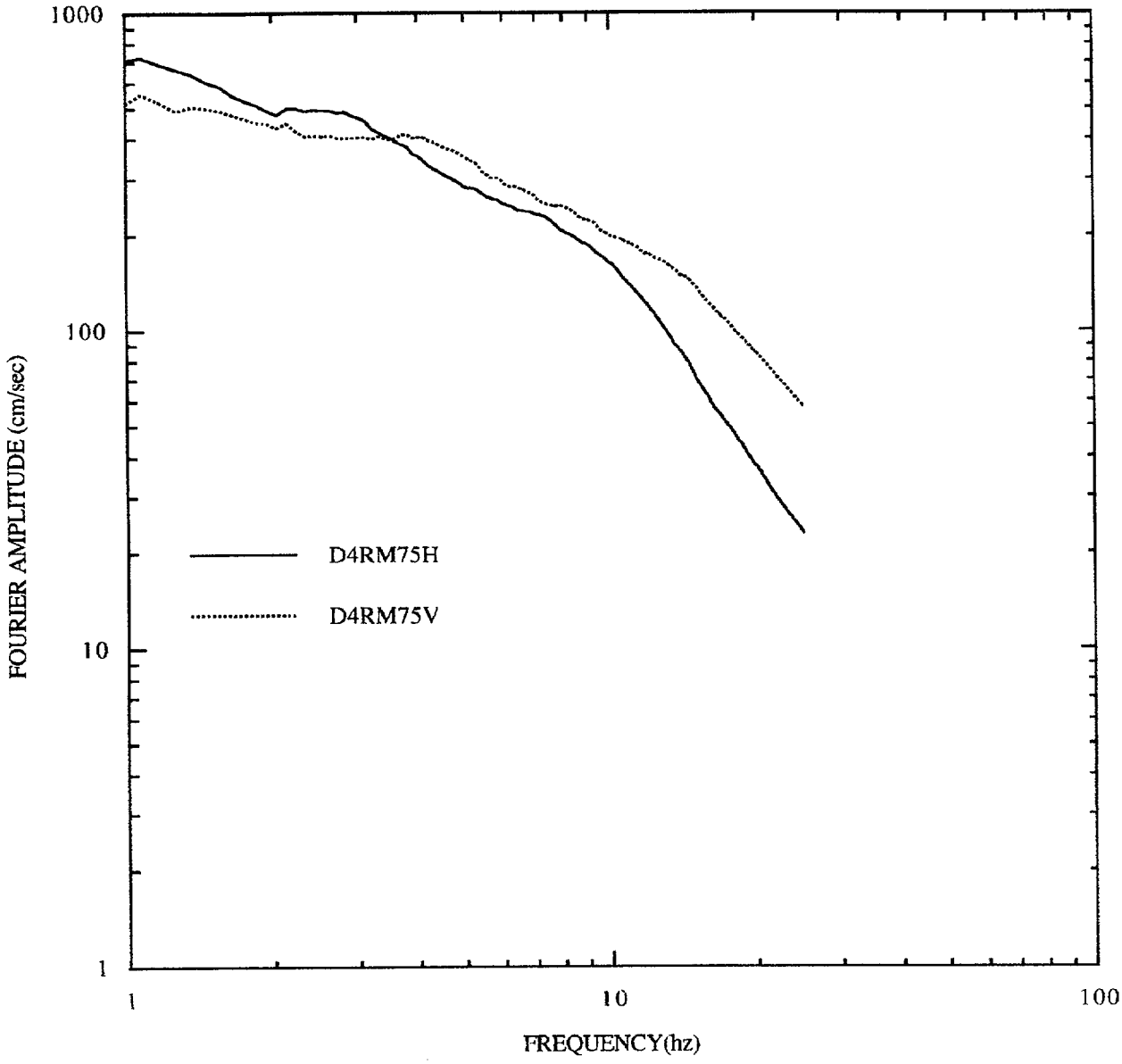

Figure E-12. Mean Fourier spectra for distance 10-200 km, rock sites, M7+.

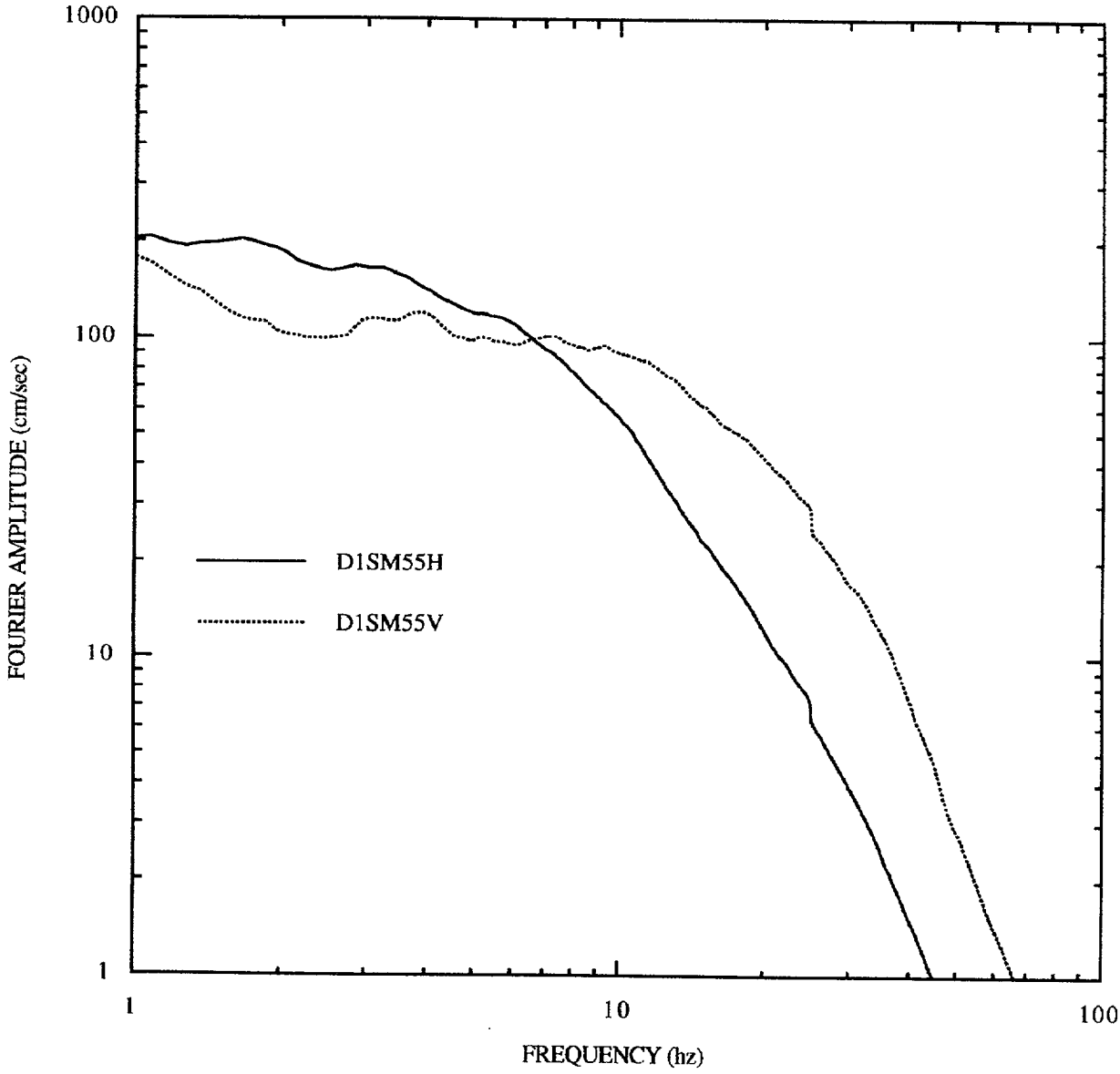

Figure E-13. Mean Fourier spectra for distance 0-10 km, soil sites, M5-6.

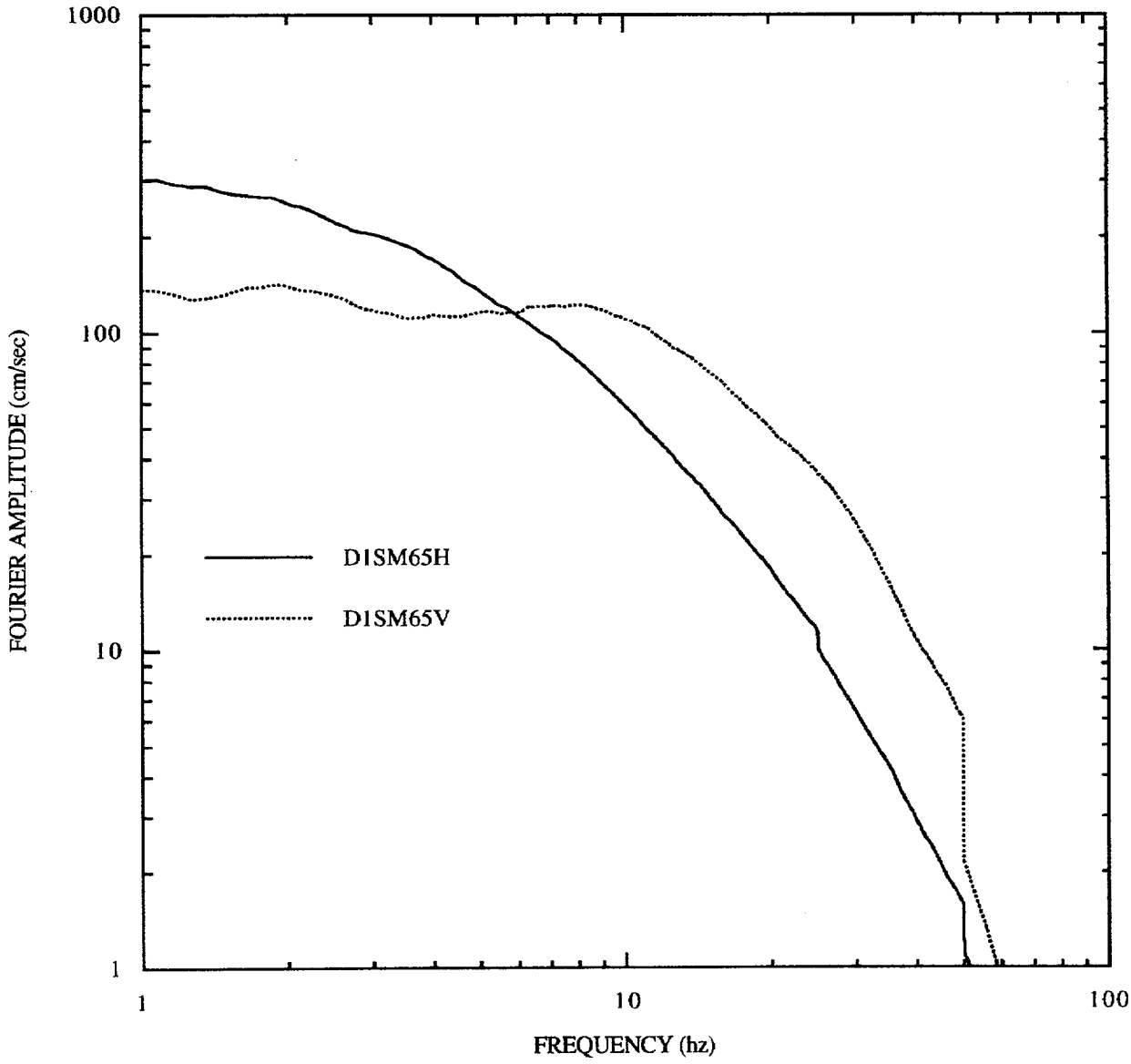

Figure E-14. Mean Fourier spectra for distance 0-10 km, soil sites, M 6-7.

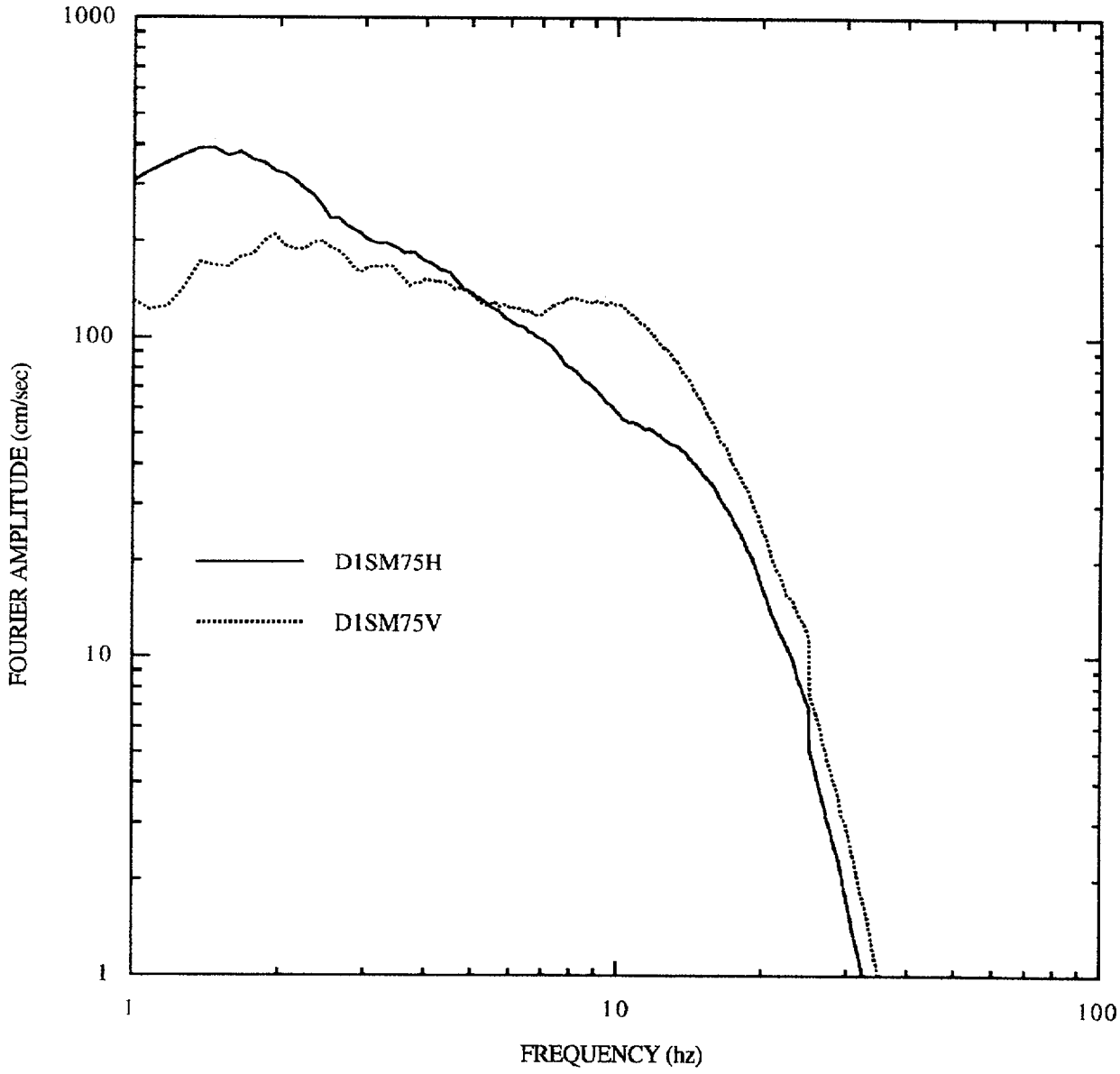

Figure E-15. Mean Fourier spectra for distance 0-10 km, soil sites, **M** 7+.

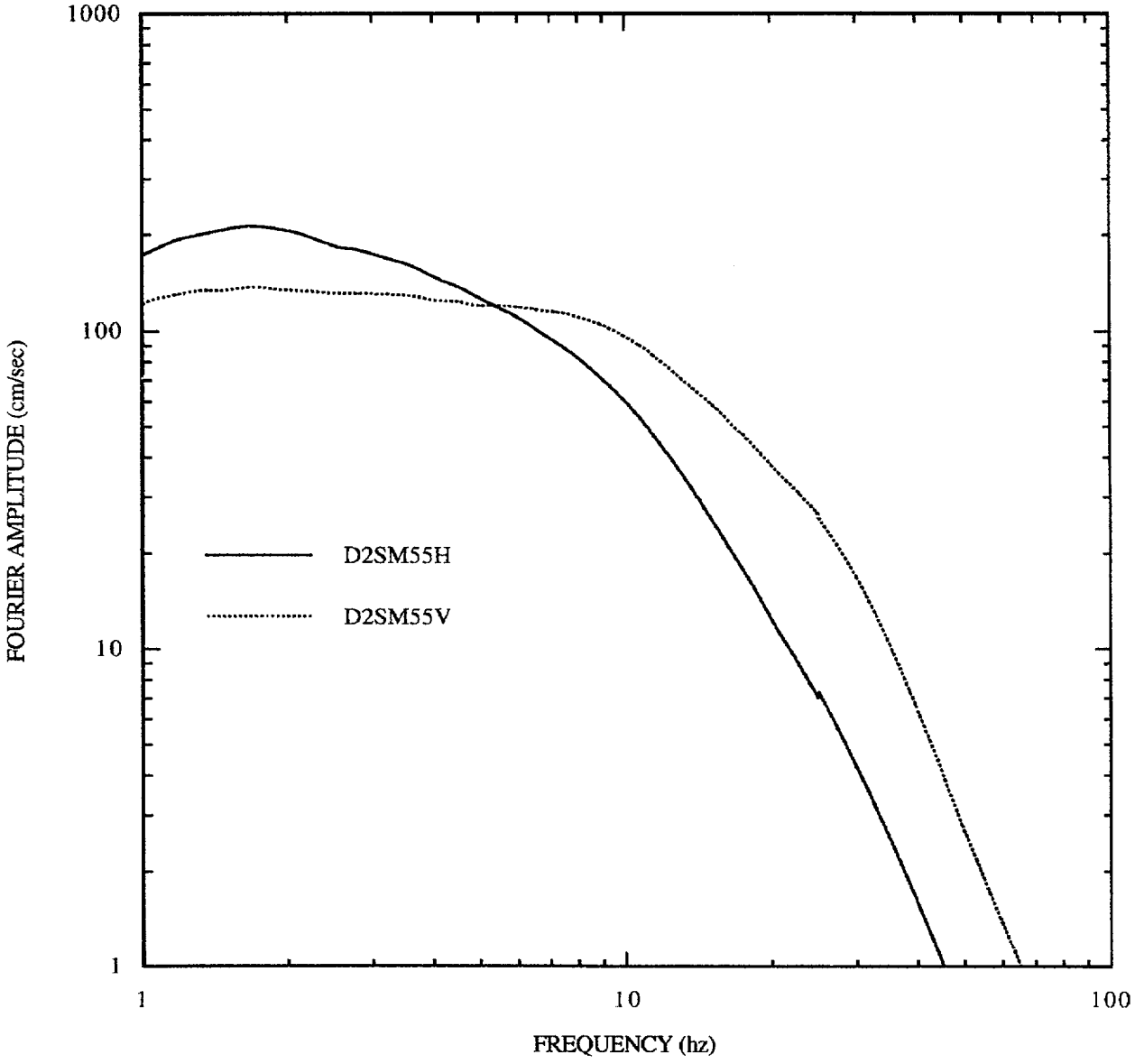

Figure E-16. Mean Fourier spectra for distance 10-50 km, soil sites, **M** 5-6.

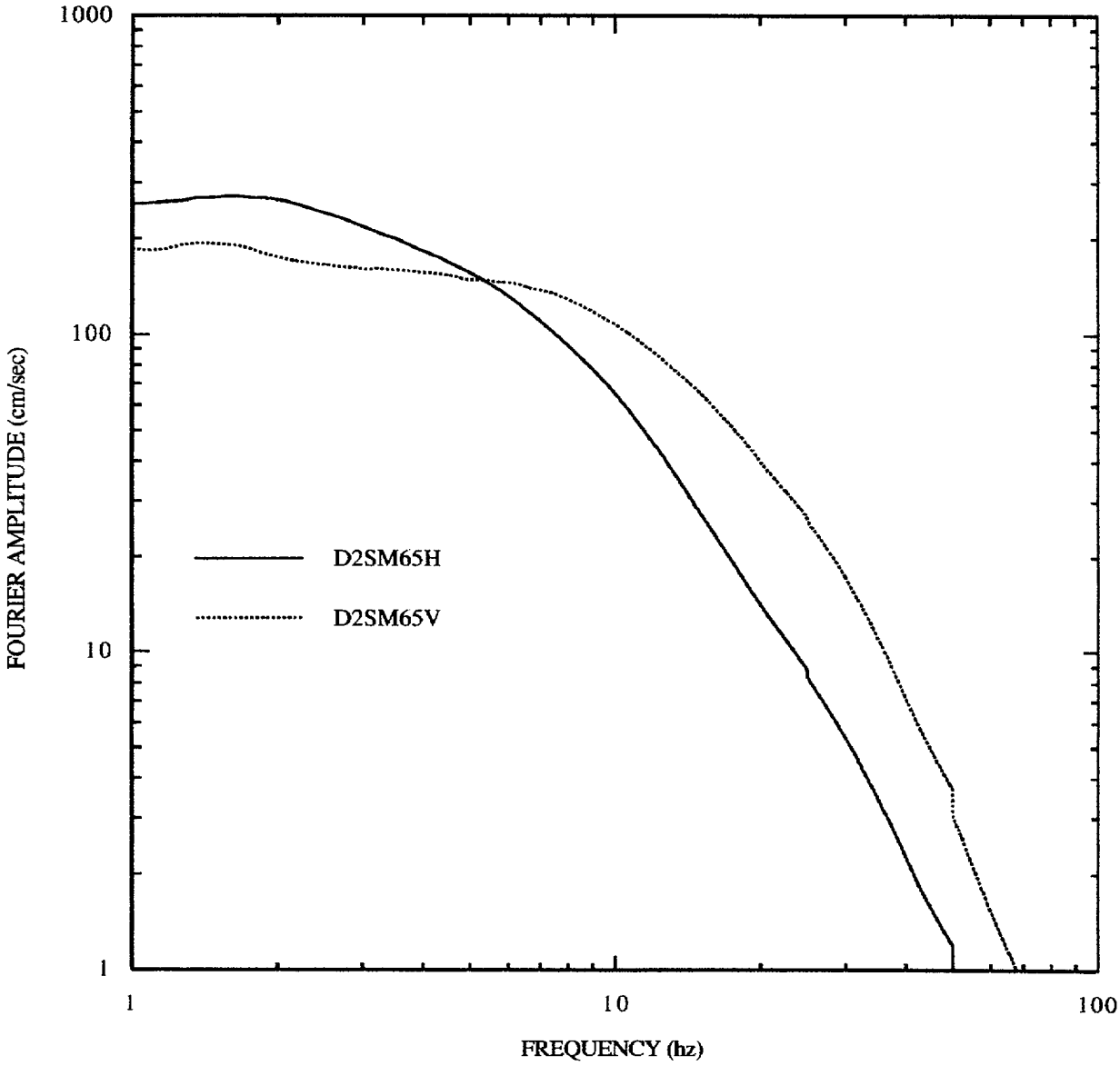

Figure E-17. Mean Fourier spectra for distance 10-50 km, soil sites, **M** 6-7.

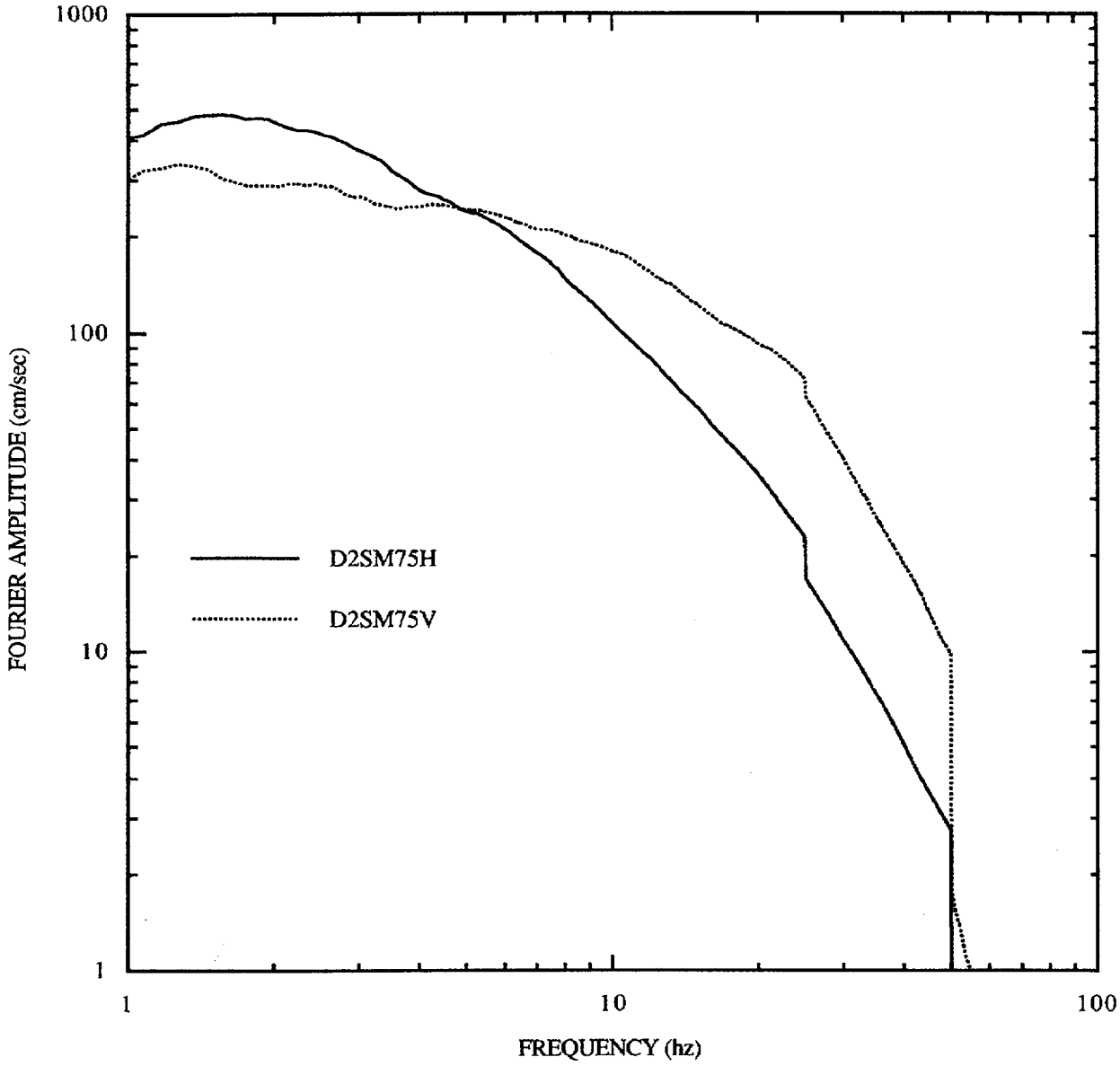

Figure E-18. Mean Fourier spectra for distance 10-50 km, soil sites, **M** 7+. Note: discontinuity at 25 Hz is caused by few records available above that frequency.

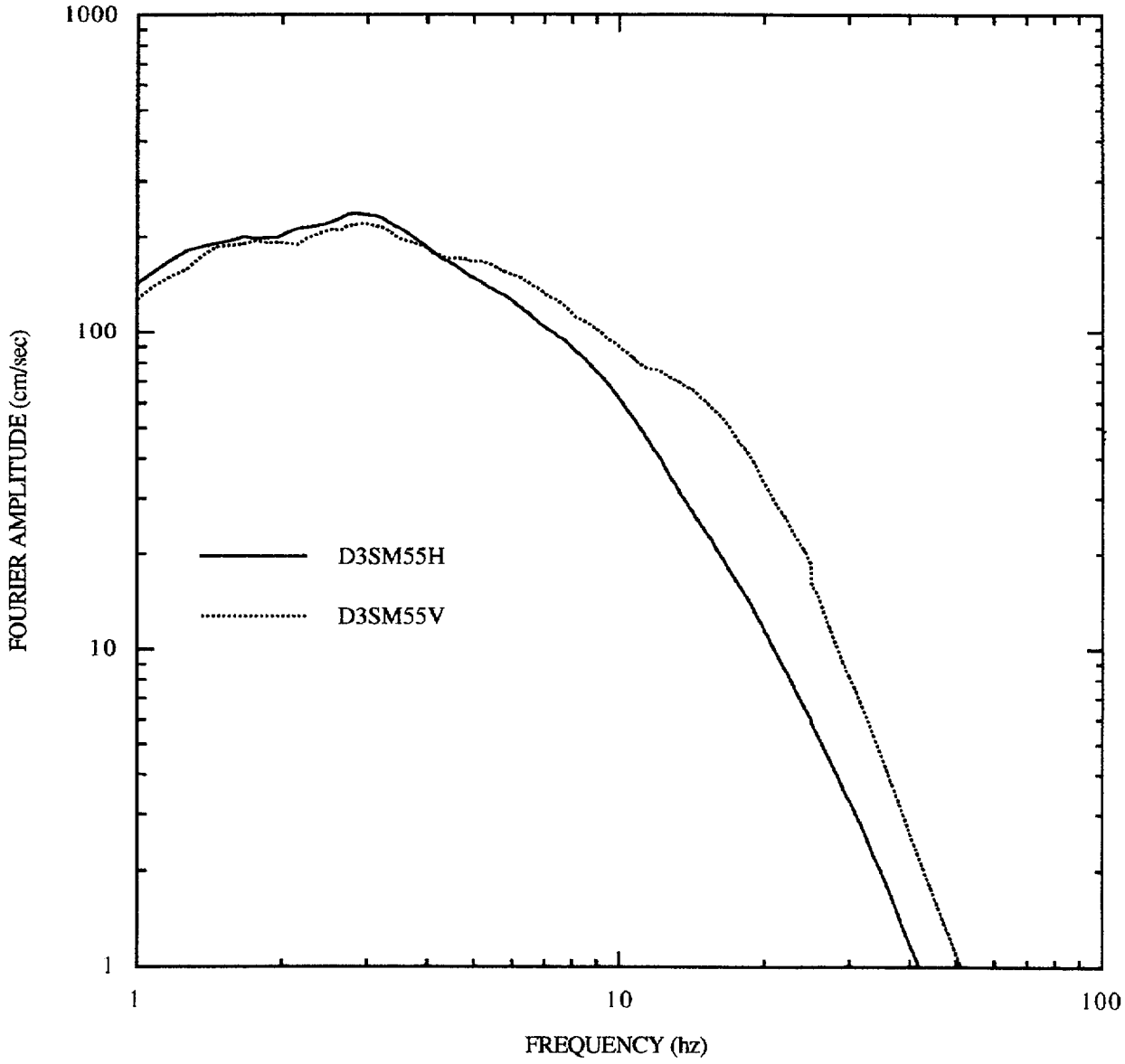

Figure E-19. Mean Fourier spectra for distance 50-100 km, soil sites, **M** 5-6.

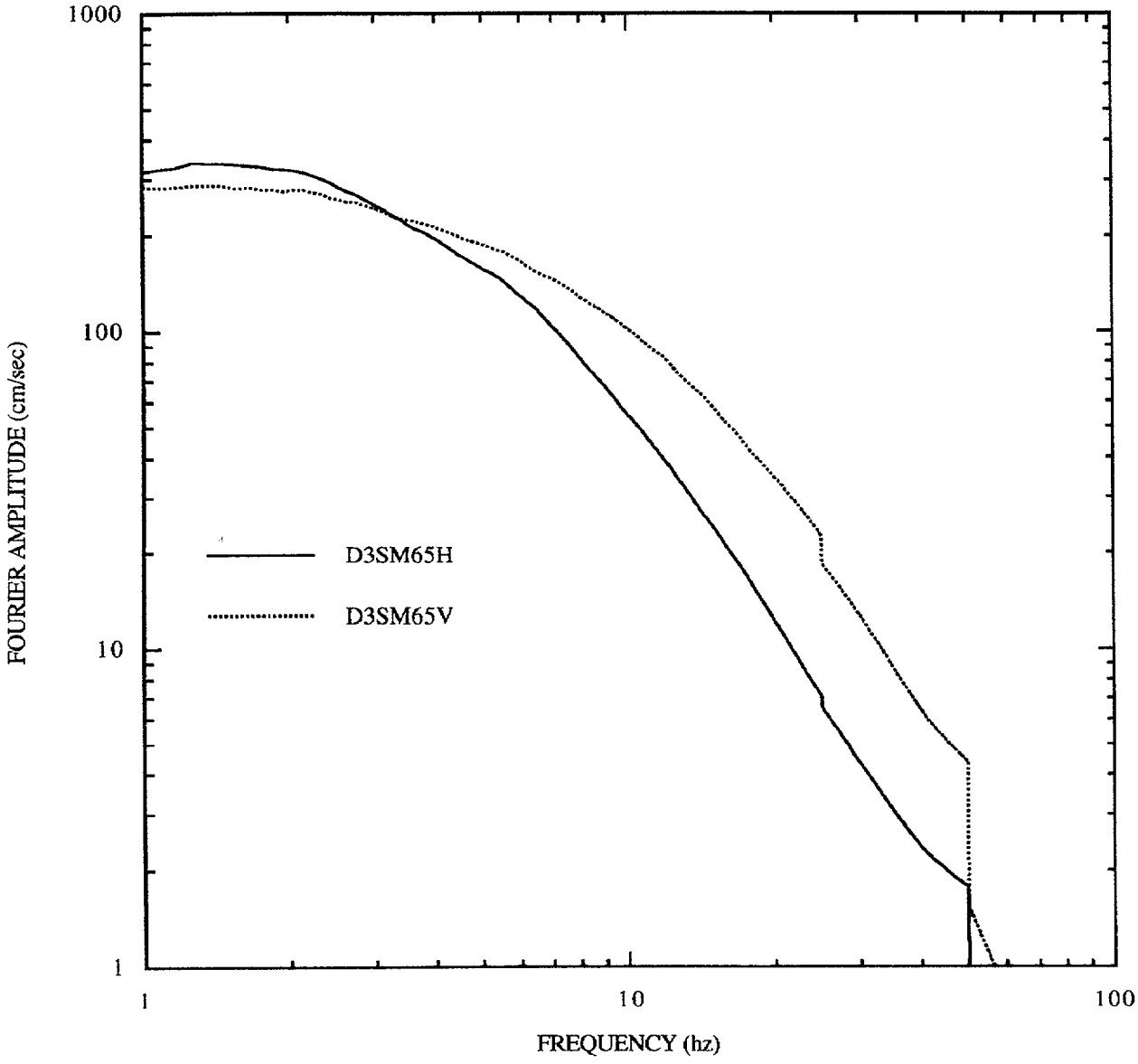

Figure E-20. Mean Fourier spectra for distance 50-100 km, soil sites, **M** 6-7. Note: discontinuity at 50 Hz is caused by few records available above that frequency.

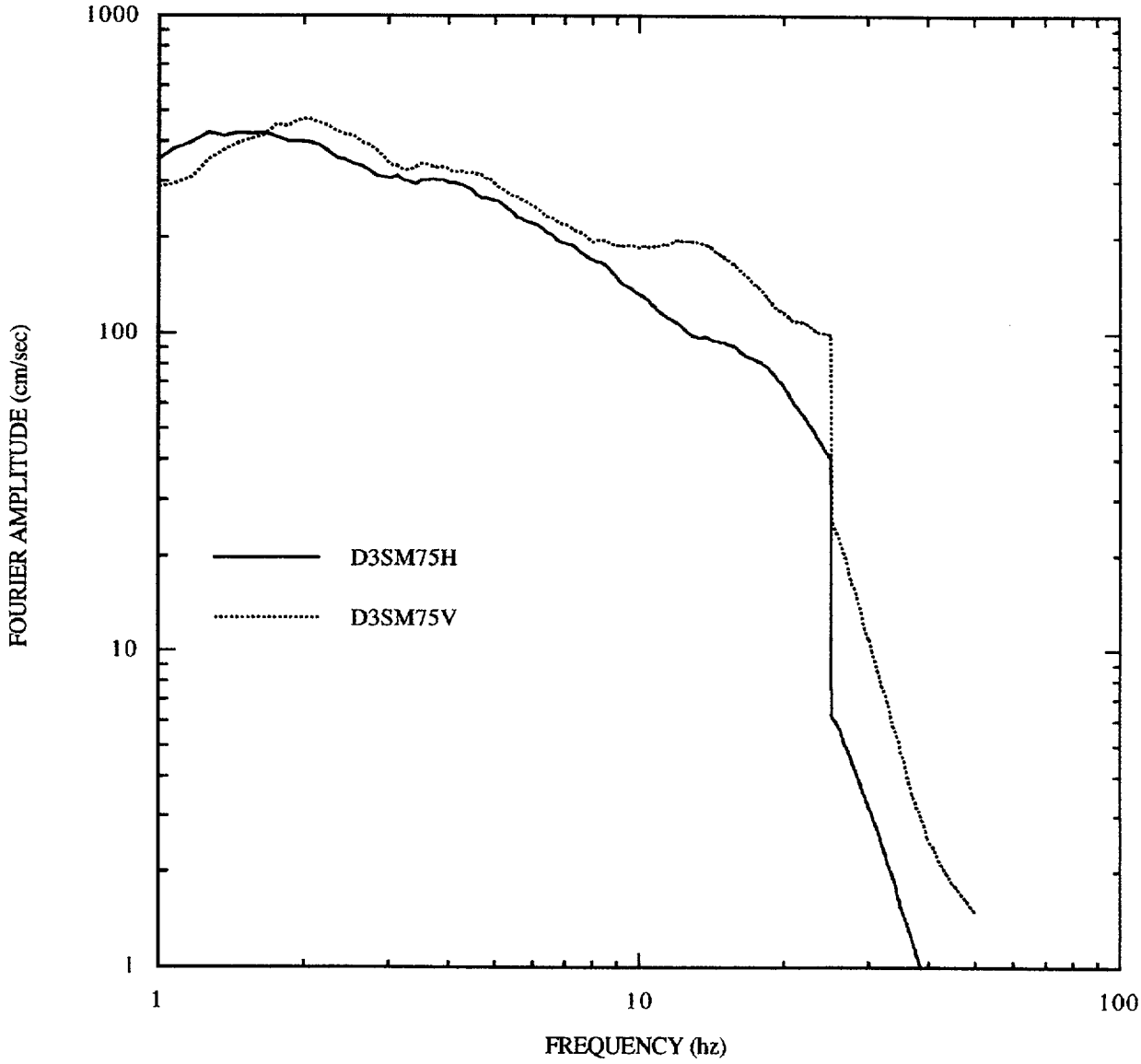

Figure E-21. Mean Fourier spectra for distance 50-100 km, soil sites, **M** 7+. Note: discontinuity at 25 Hz is caused by few records available above that frequency.

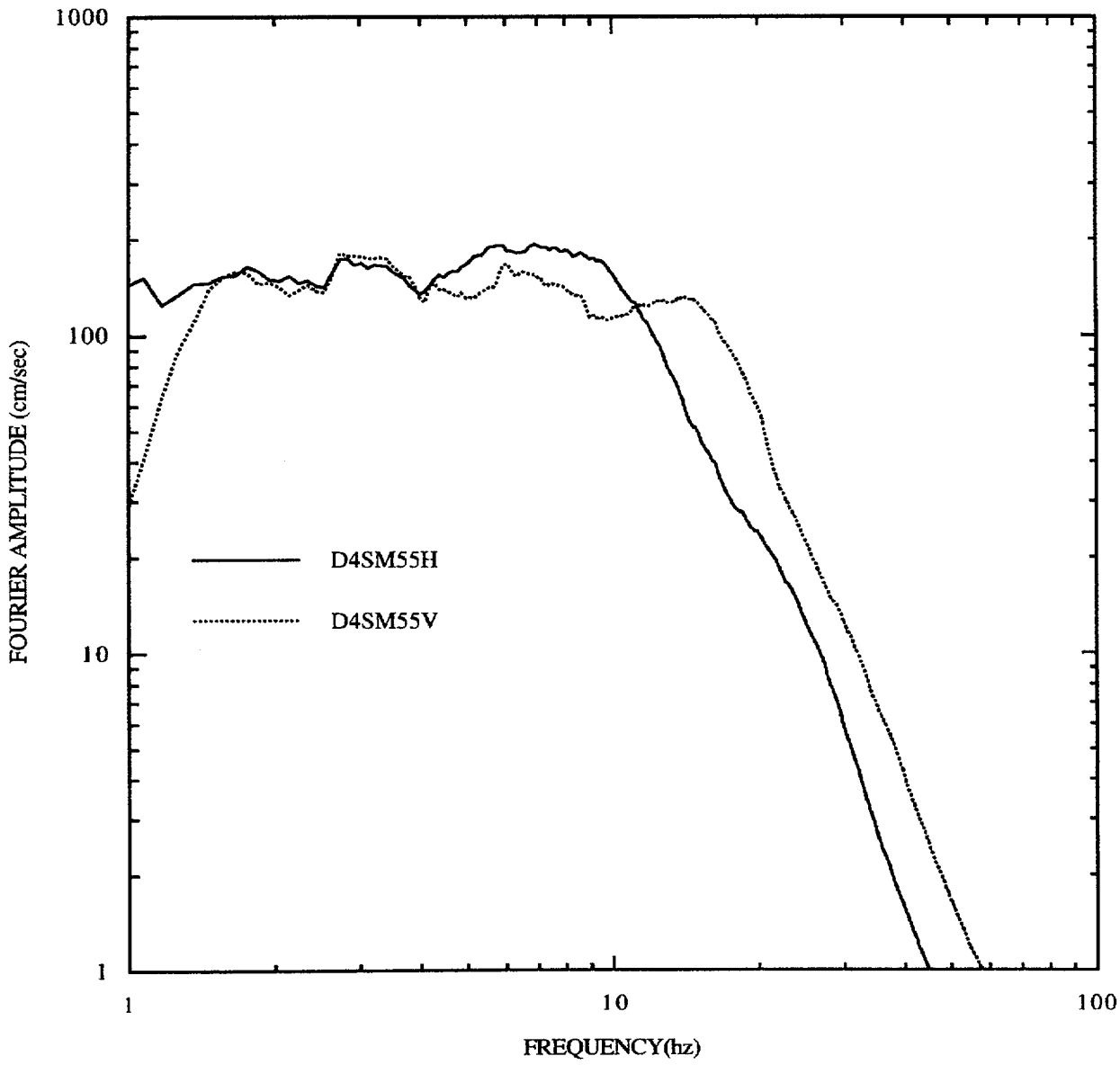

Figure E-22. Mean Fourier spectra for distance 100-200 km, soil sites, **M** 5-6.

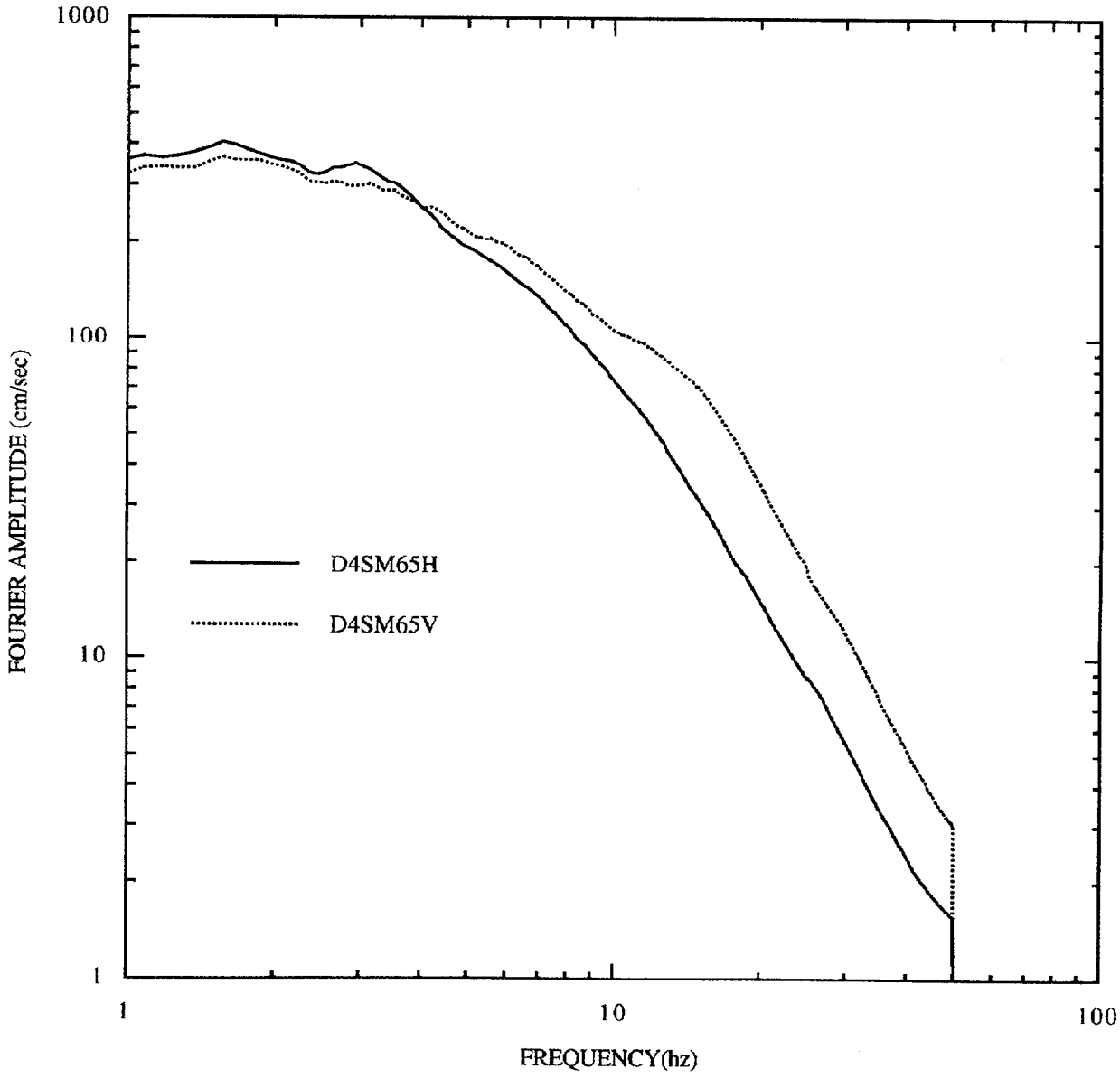

Figure E-23. Mean Fourier spectra for distance 100-200 km, soil sites, M 6-7. Note: discontinuity at 50 Hz is caused by few records available above that frequency.

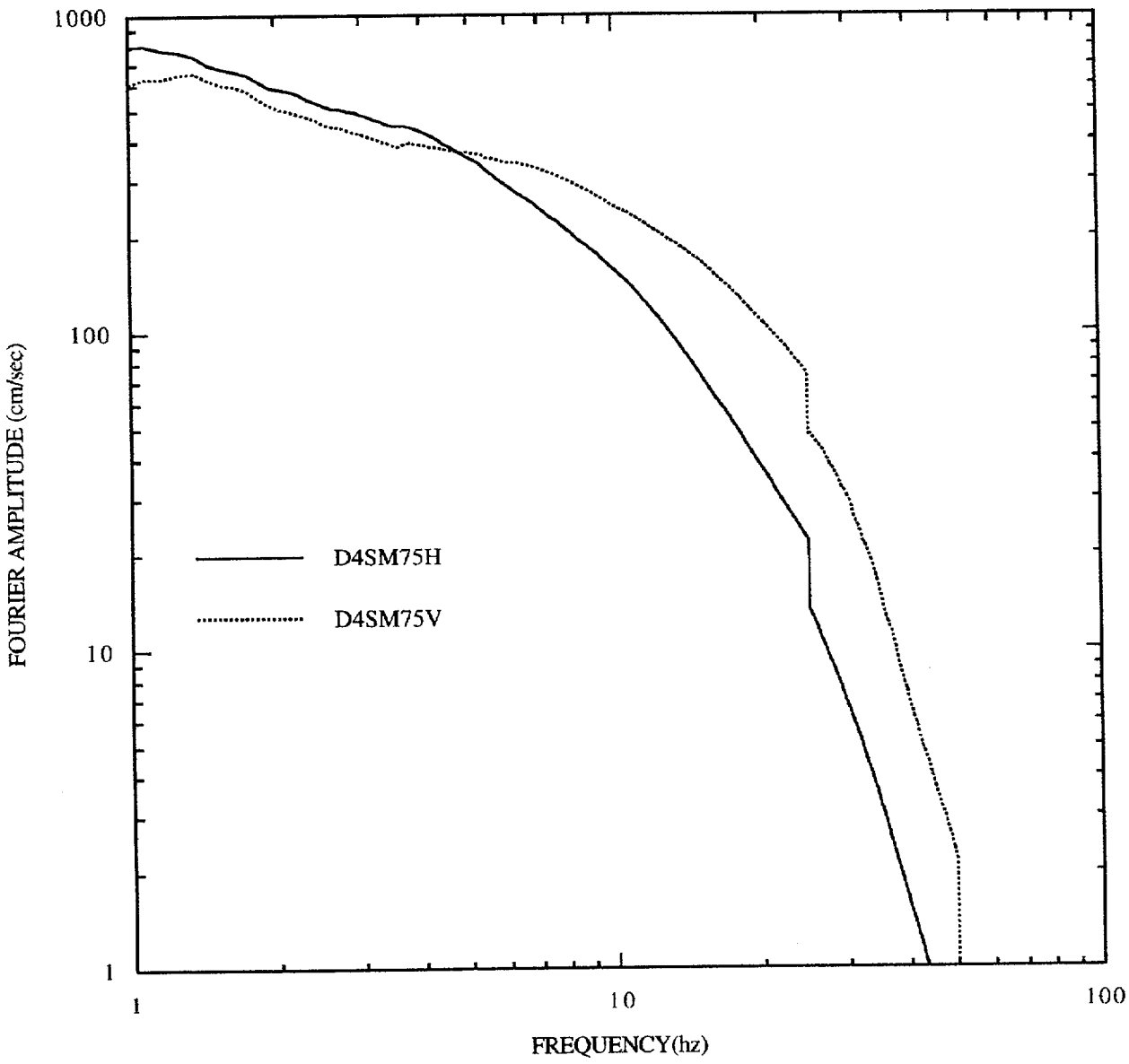

Figure E-24. Mean Fourier spectra for distance 100-200 km, soil sites, **M** 7+.
Note: discontinuity at 25 and 50 Hz is caused by few records available above that frequency.

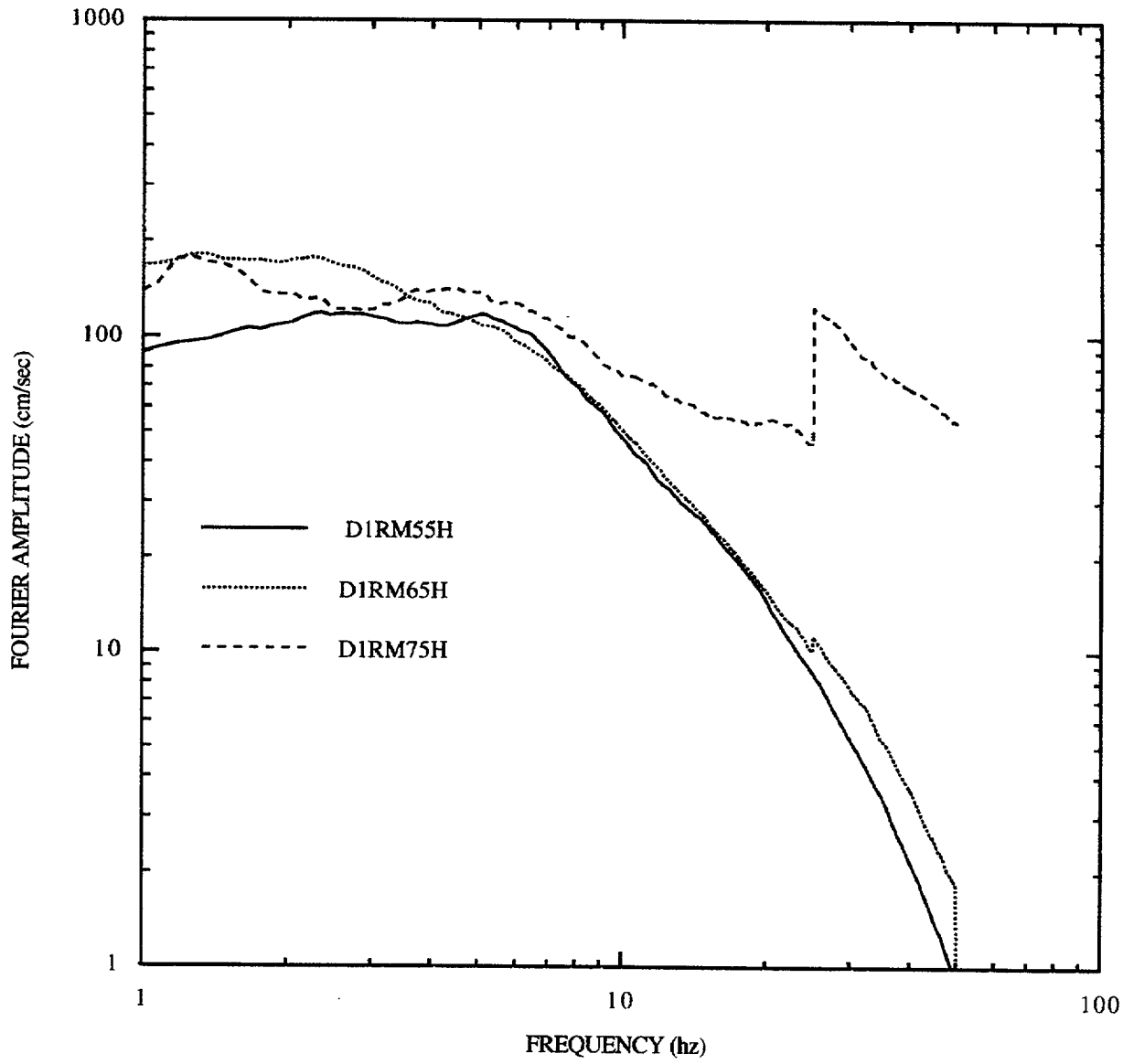

Figure E-25. Mean Fourier spectra for distance 0-10 km, rock sites, horizontal motions. Note: discontinuity at 25 and 50 Hz is caused by few records available above that frequency.

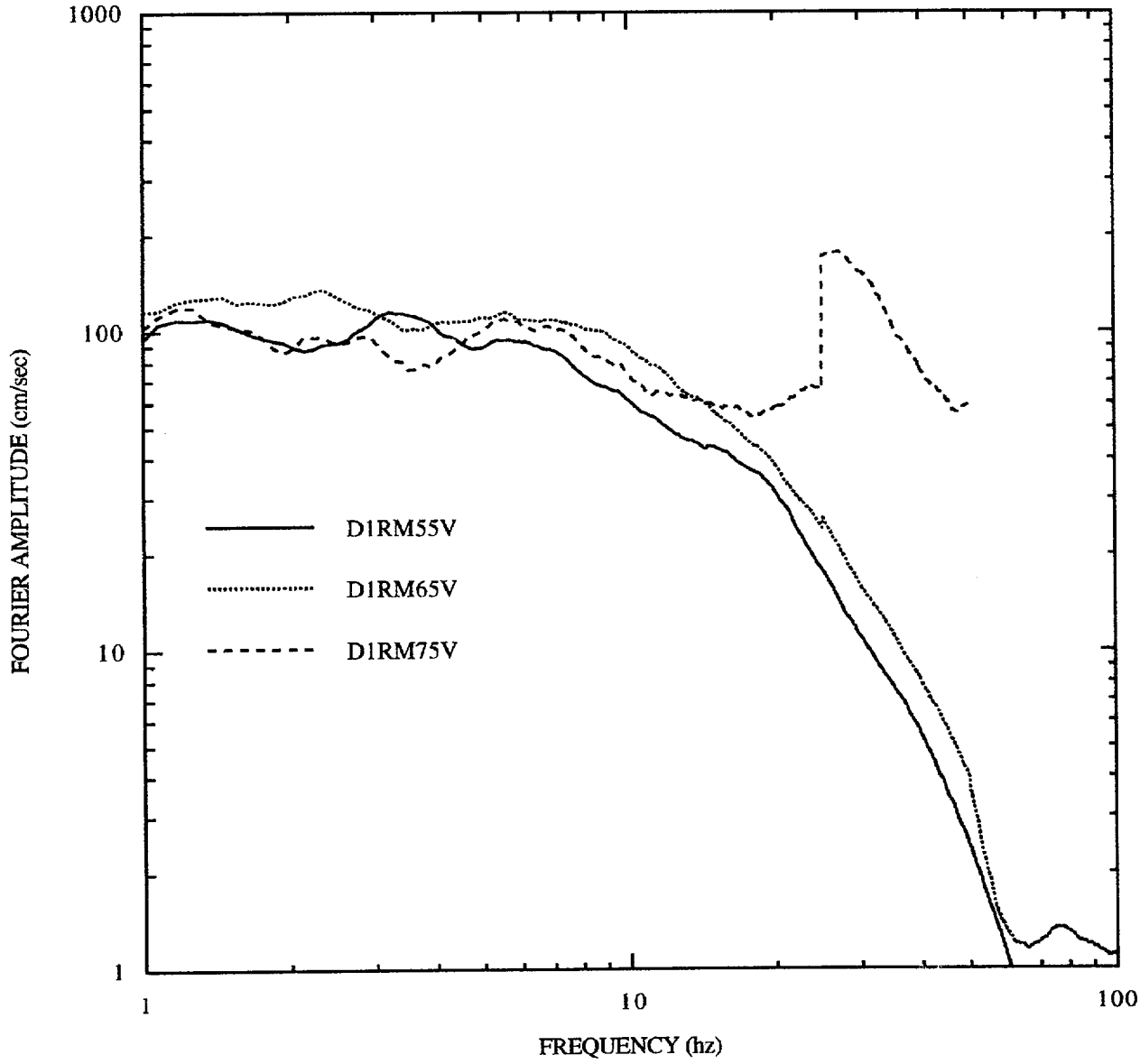

Figure E-26. Mean Fourier spectra for distance 0-10 km, rock sites, vertical motions.
Note: discontinuity at 25 Hz is caused by few records available above that frequency.

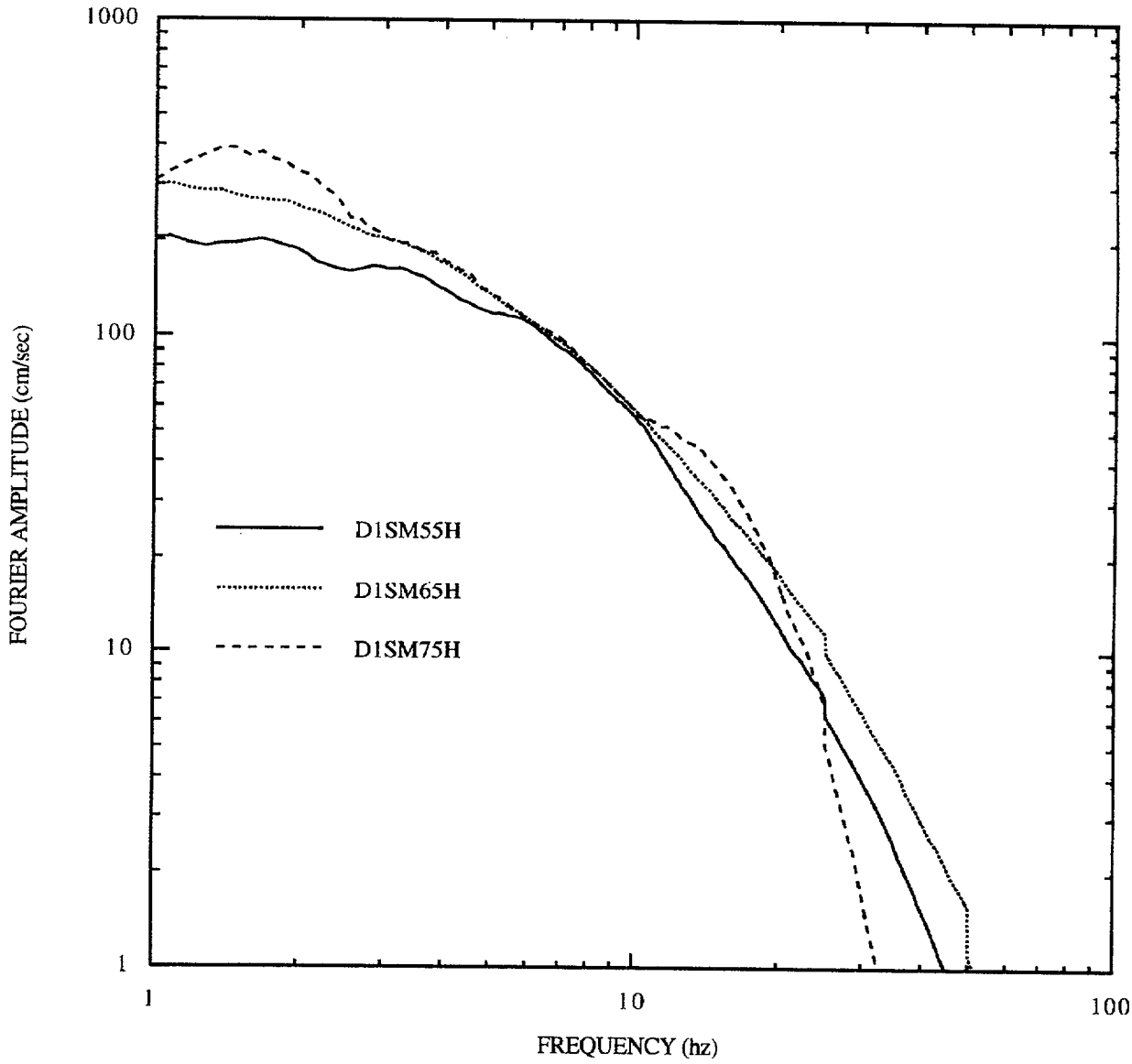

Figure E-27. Mean Fourier spectra for distance 0-10 km, soil sites, horizontal motions.
Note: discontinuity at 25 and 50 Hz is caused by few records available above that frequency.

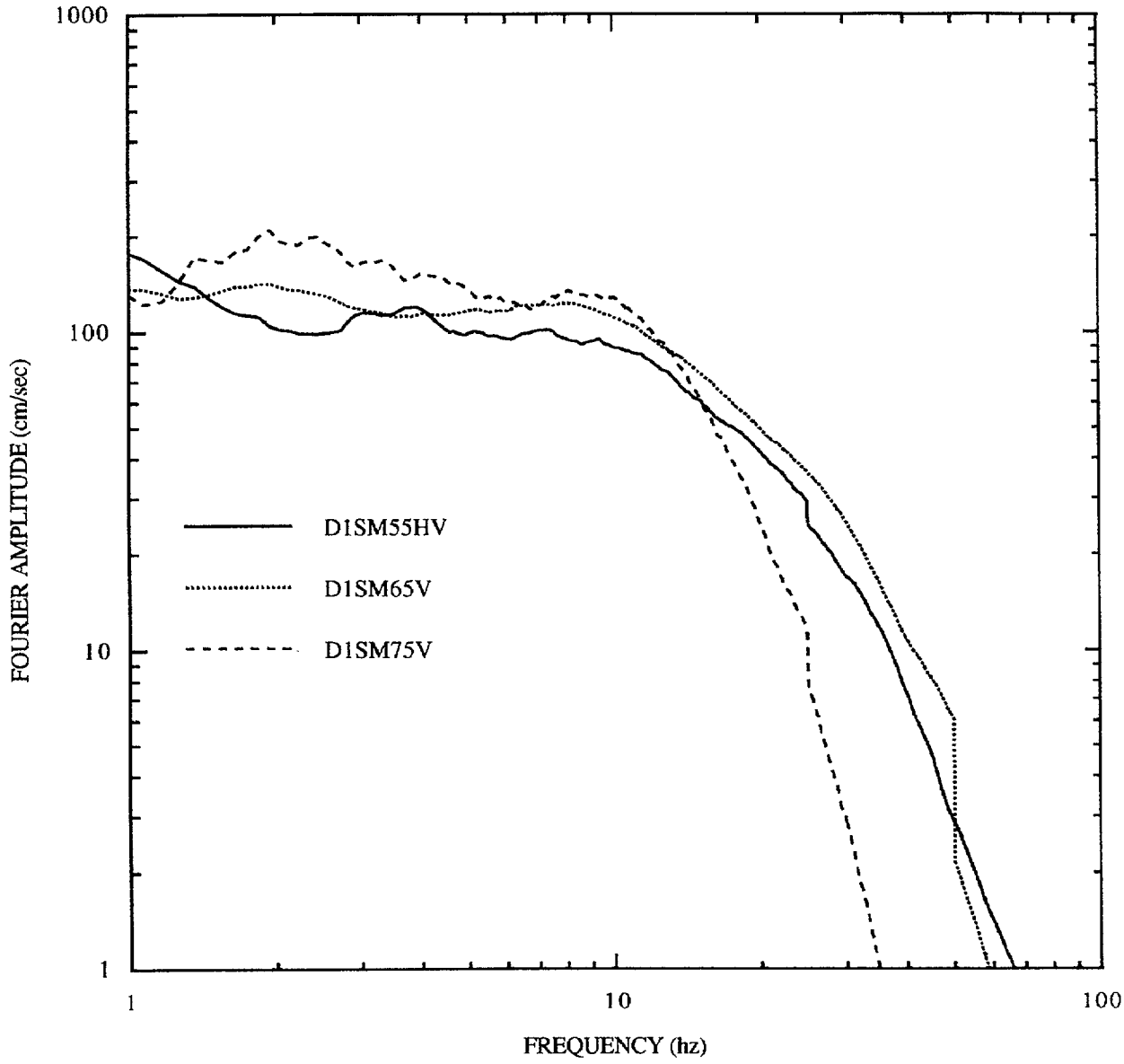

Figure E-28. Mean Fourier spectra for distance 0-10 km, soil sites, vertical motions.
Note: discontinuity at 25 and 50 Hz is caused by few records available above that frequency.

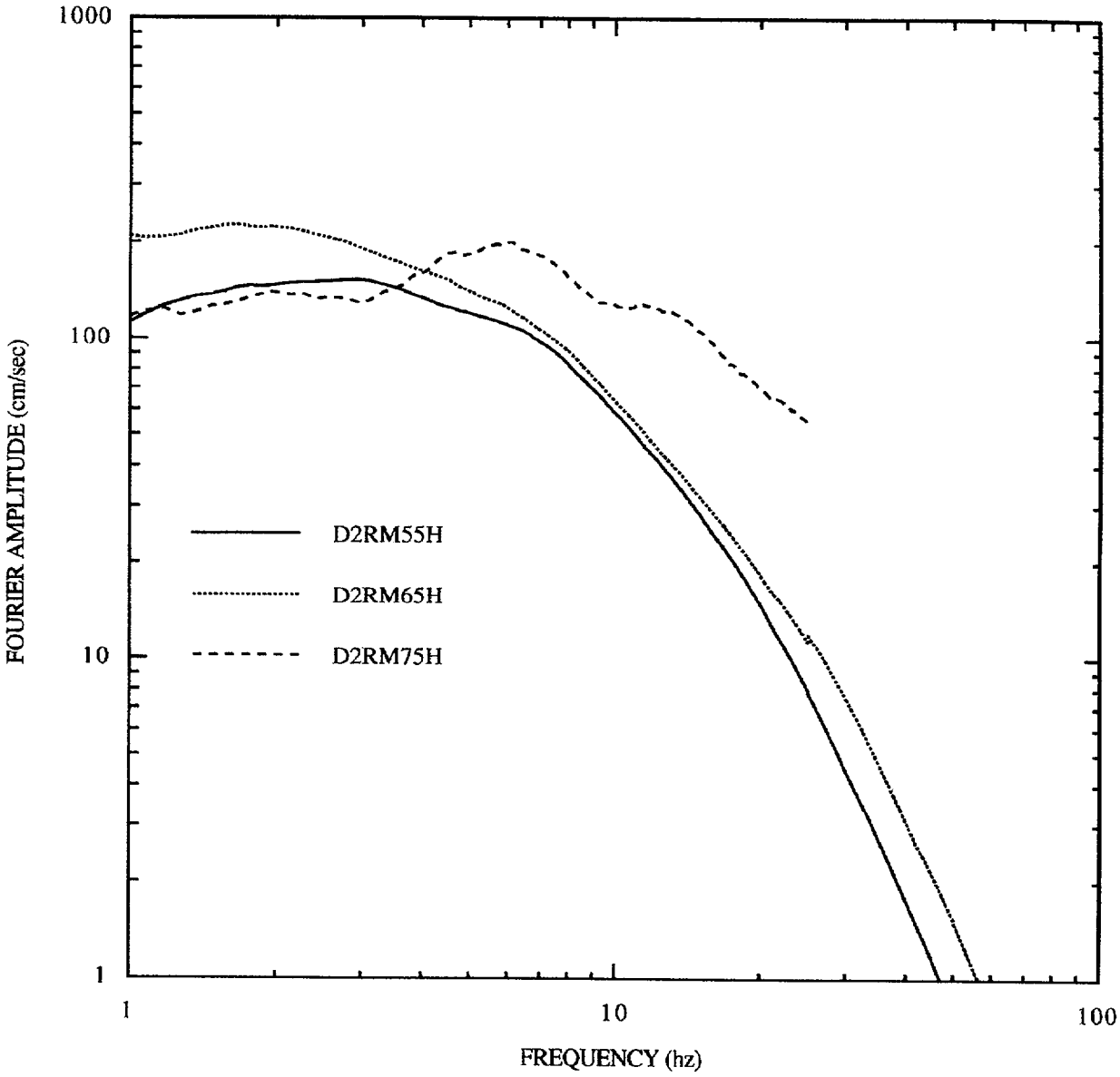

Figure E-29. Mean Fourier spectra for distance 10-50 km, rock sites, horizontal motions.

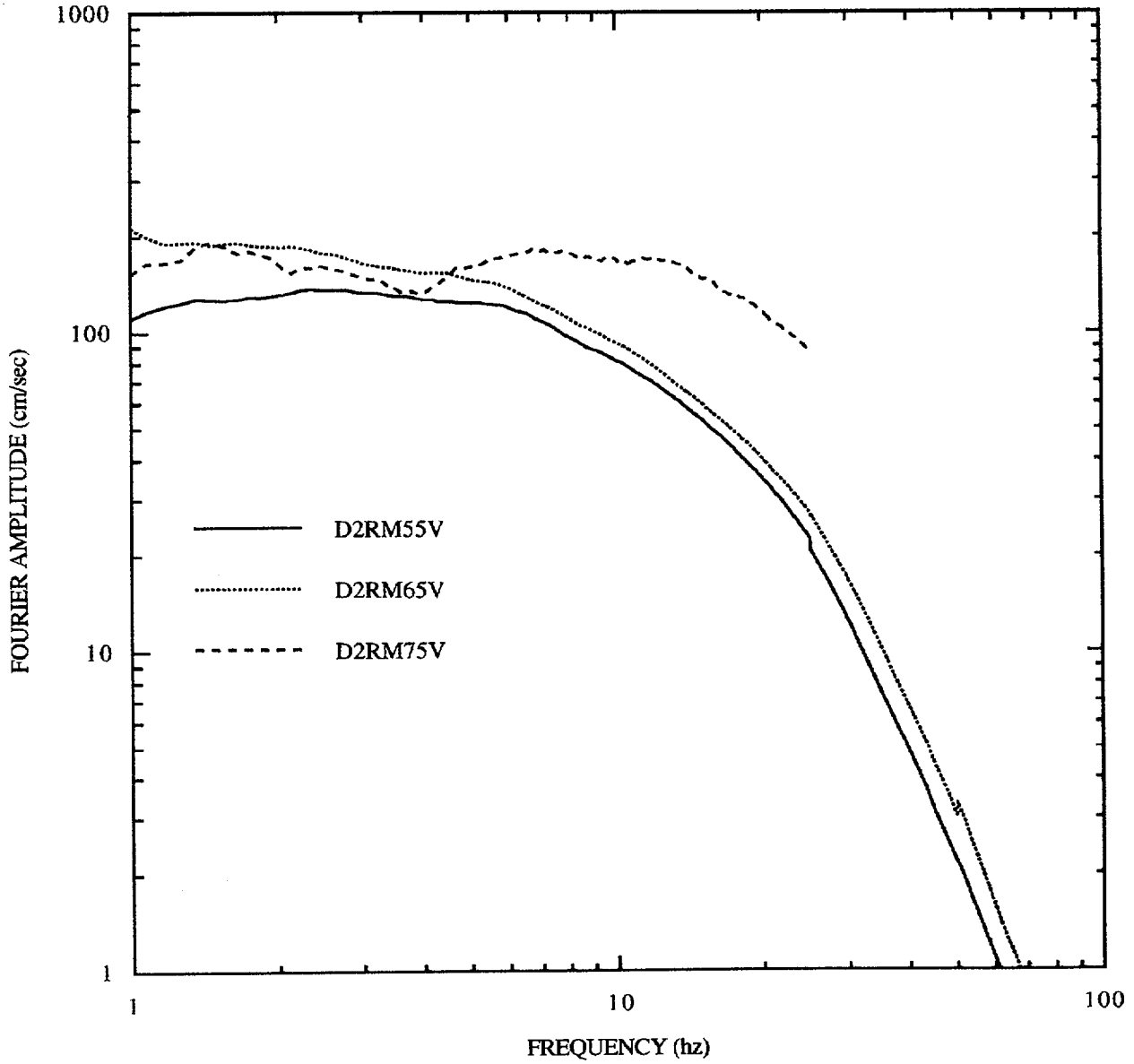

Figure E-30. Mean Fourier spectra for distance 10-50 km, rock sites, vertical motions.

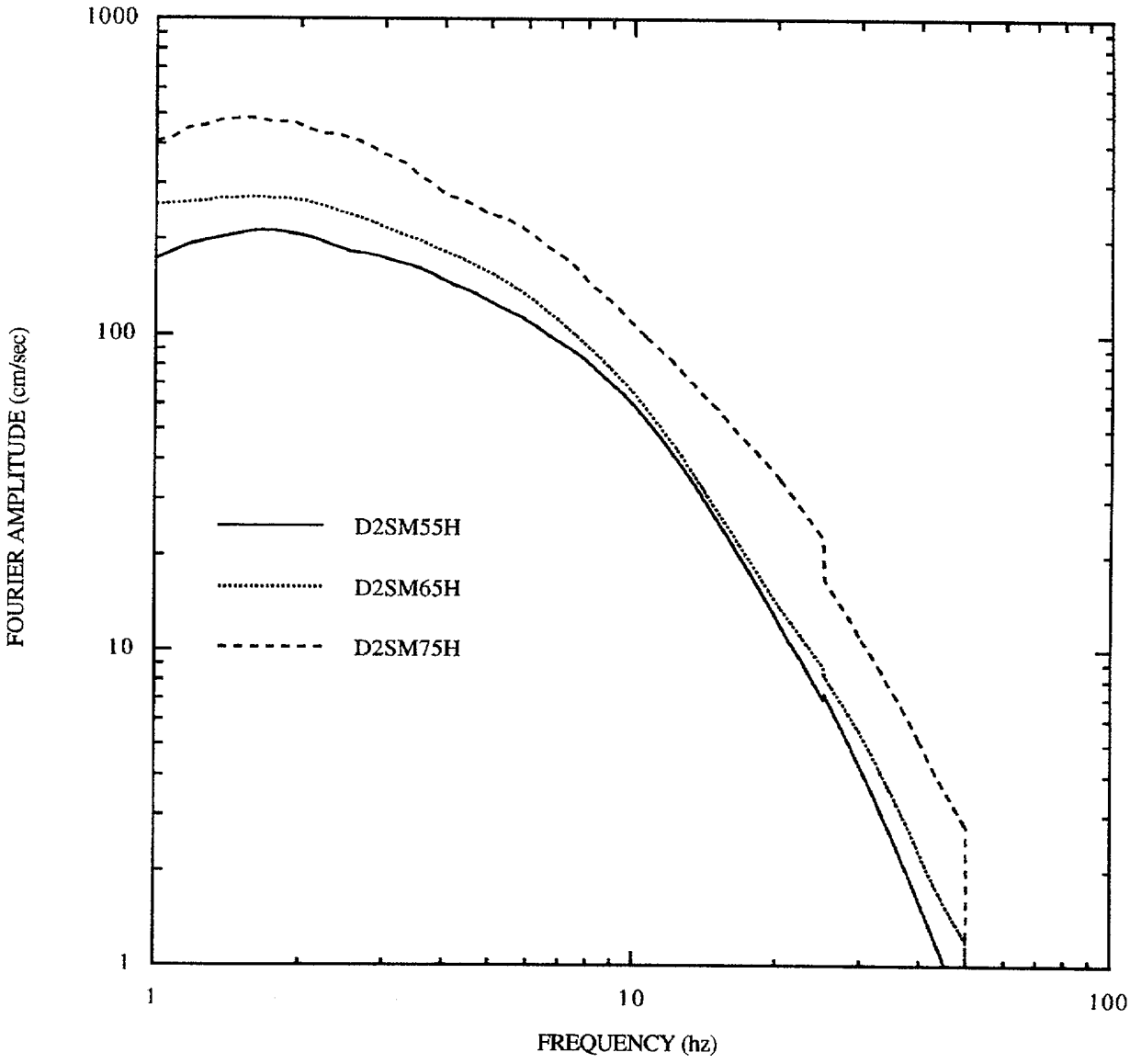

Figure E-31. Mean Fourier spectra for distance 10-50 km, soil sites, horizontal motions. Note: discontinuity at 25 and 50 Hz is caused by few records available above that frequency.

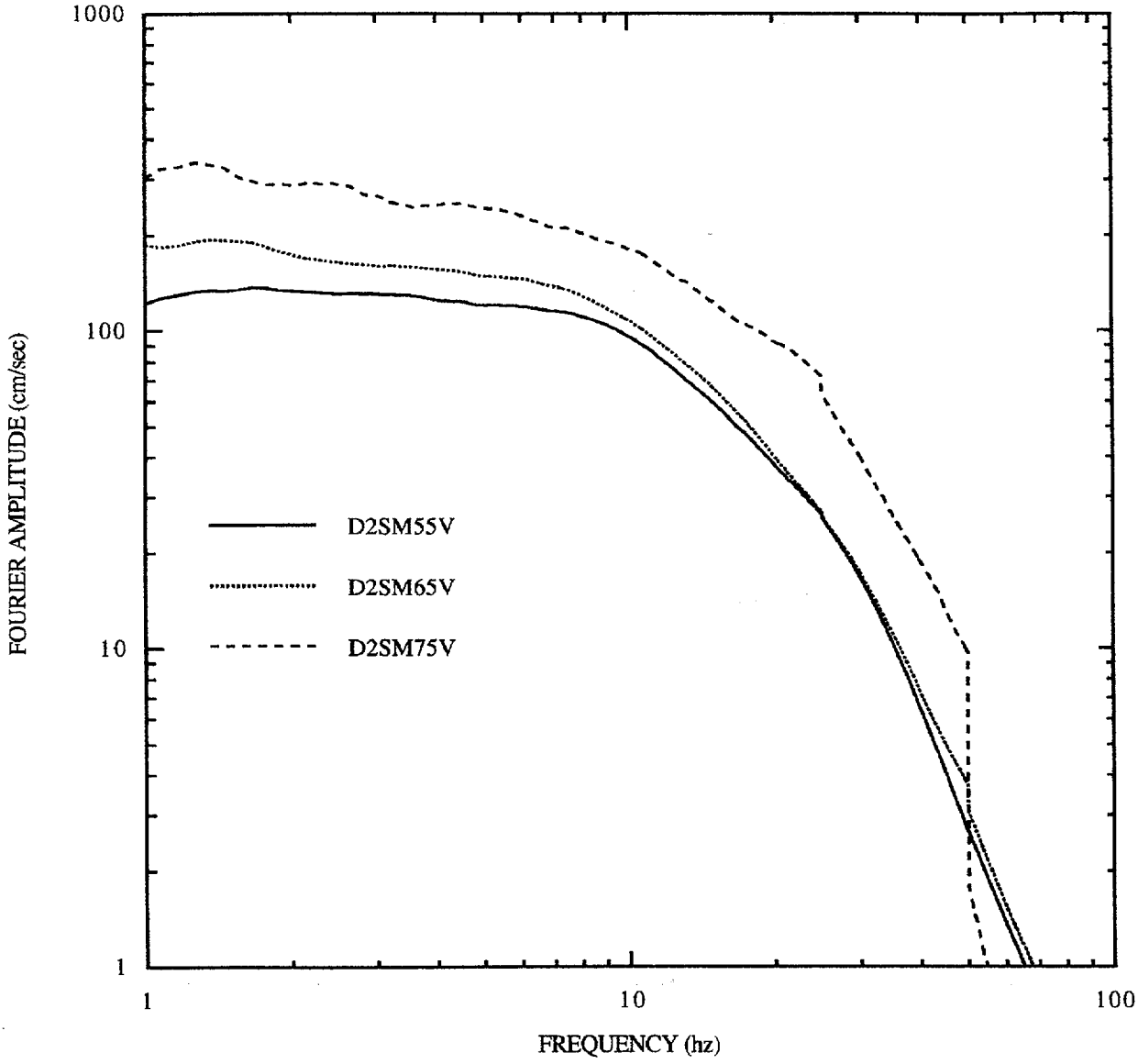

Figure E-32. Mean Fourier spectra for distance 10-50 km, soil sites, vertical motions.
Note: discontinuity at 25 and 50 Hz is caused by few records available above that frequency.

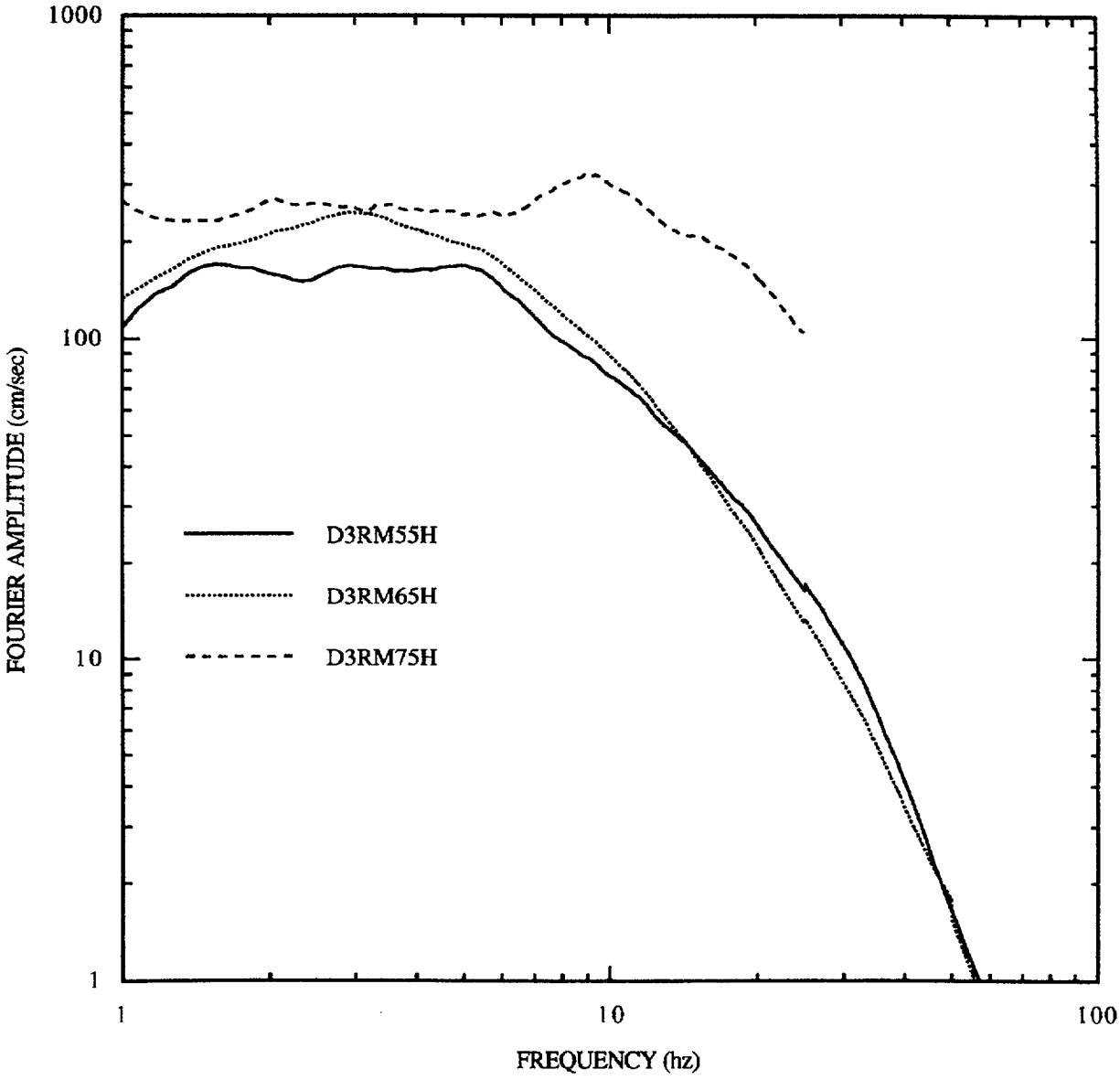

Figure E-33. Mean Fourier spectra for distance 50-100 km, rock sites, horizontal motions.

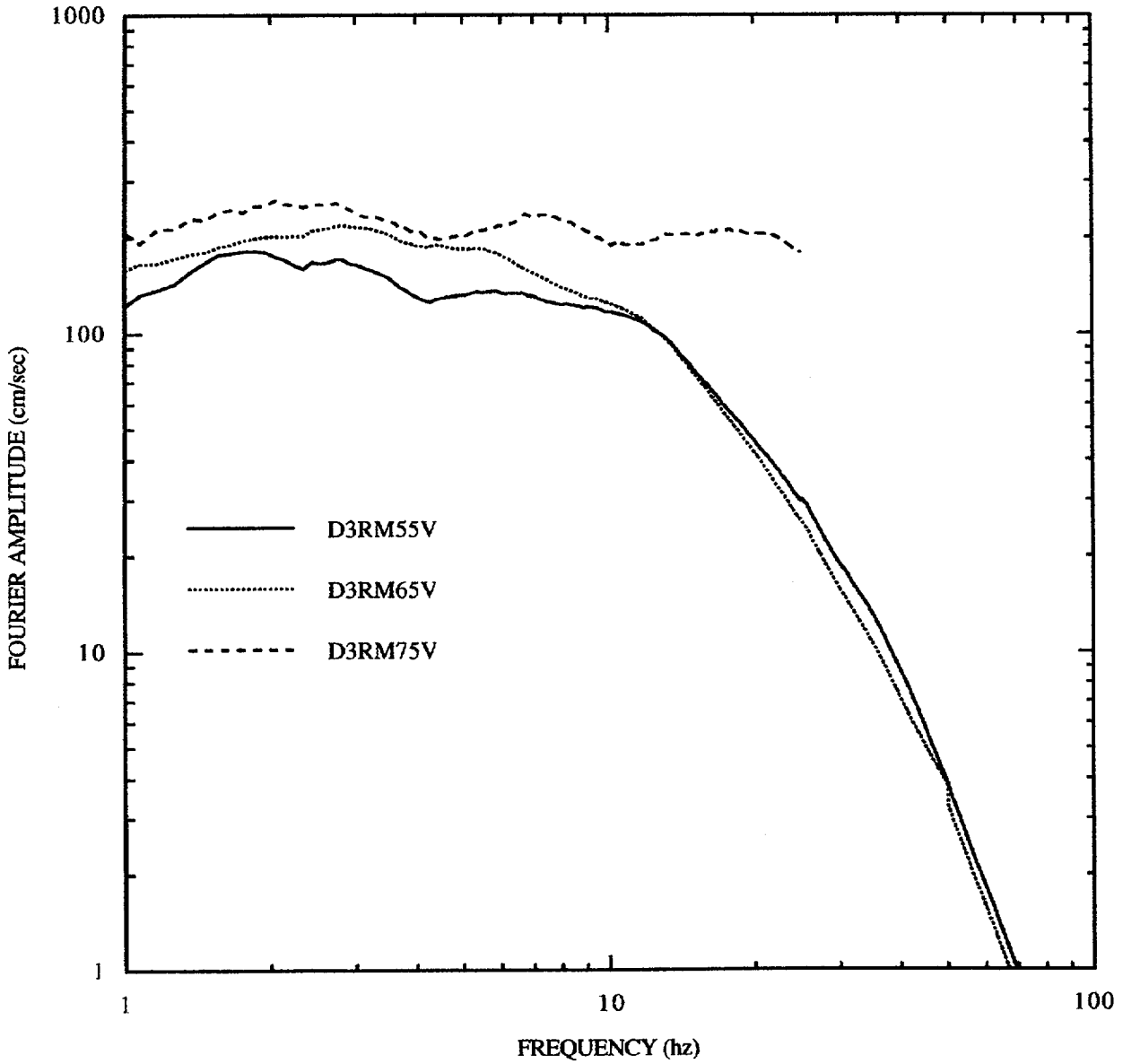

Figure E-34. Mean Fourier spectra for distance 50-100 km, rock sites, vertical motions.

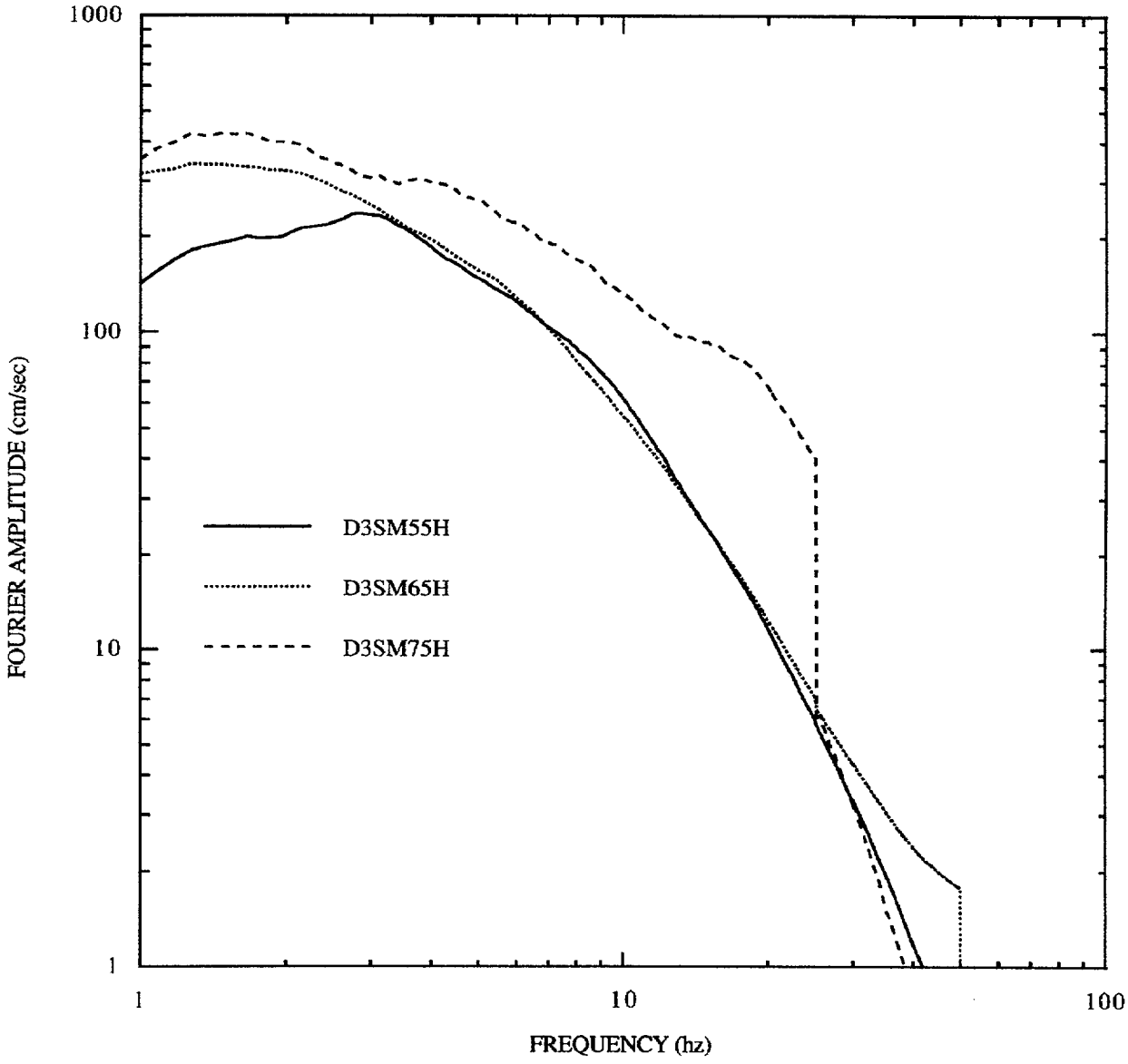

Figure E-35. Mean Fourier spectra for distance 50-100 km, soil sites, horizontal motions. Note: discontinuity at 25 and 50 Hz is caused by few records available above that frequency.

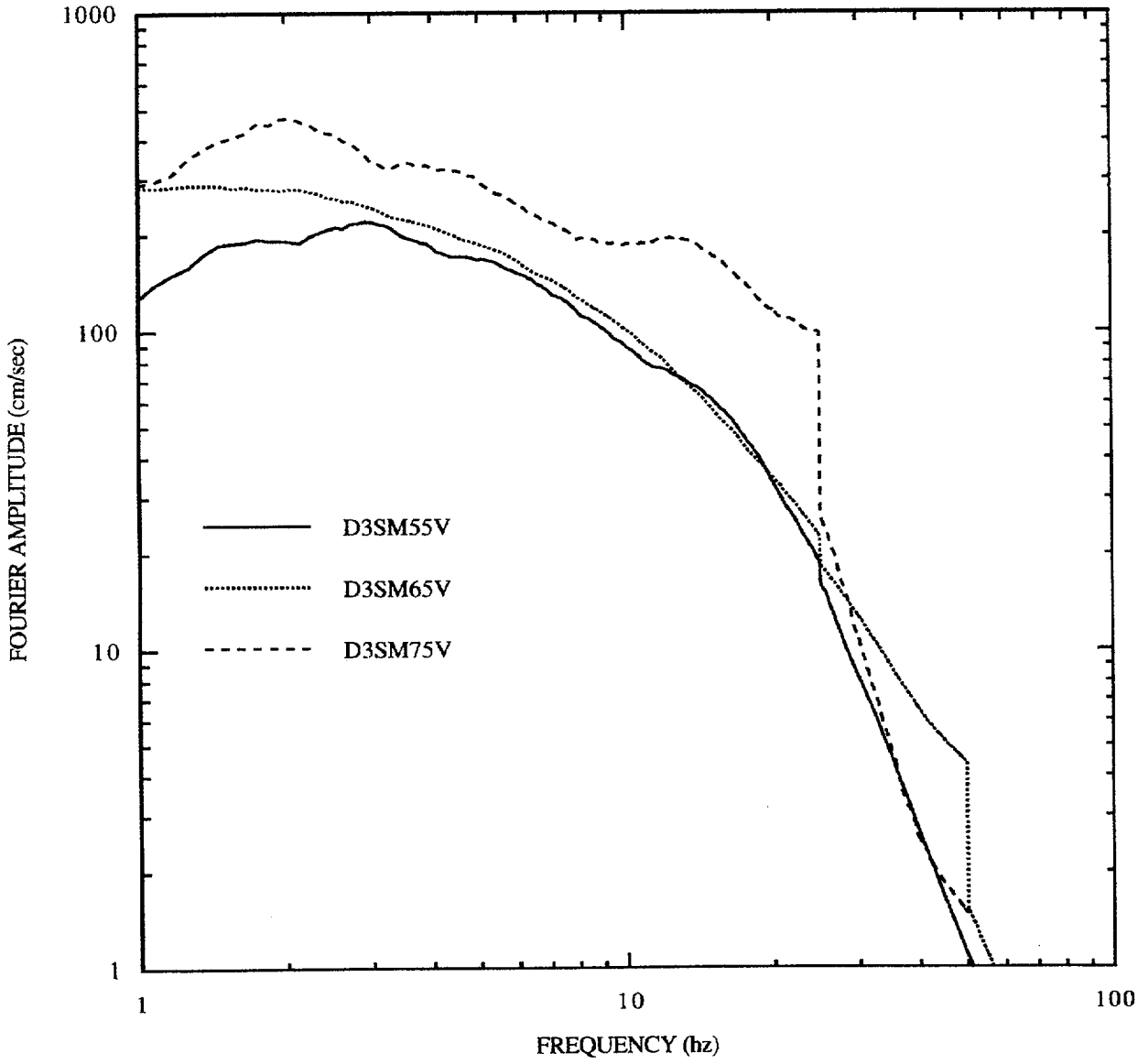

Figure E-36. Mean Fourier spectra for distance 50-100 km, rock sites, vertical motions.
Note: discontinuity at 25 and 50 Hz is caused by few records available above that frequency.

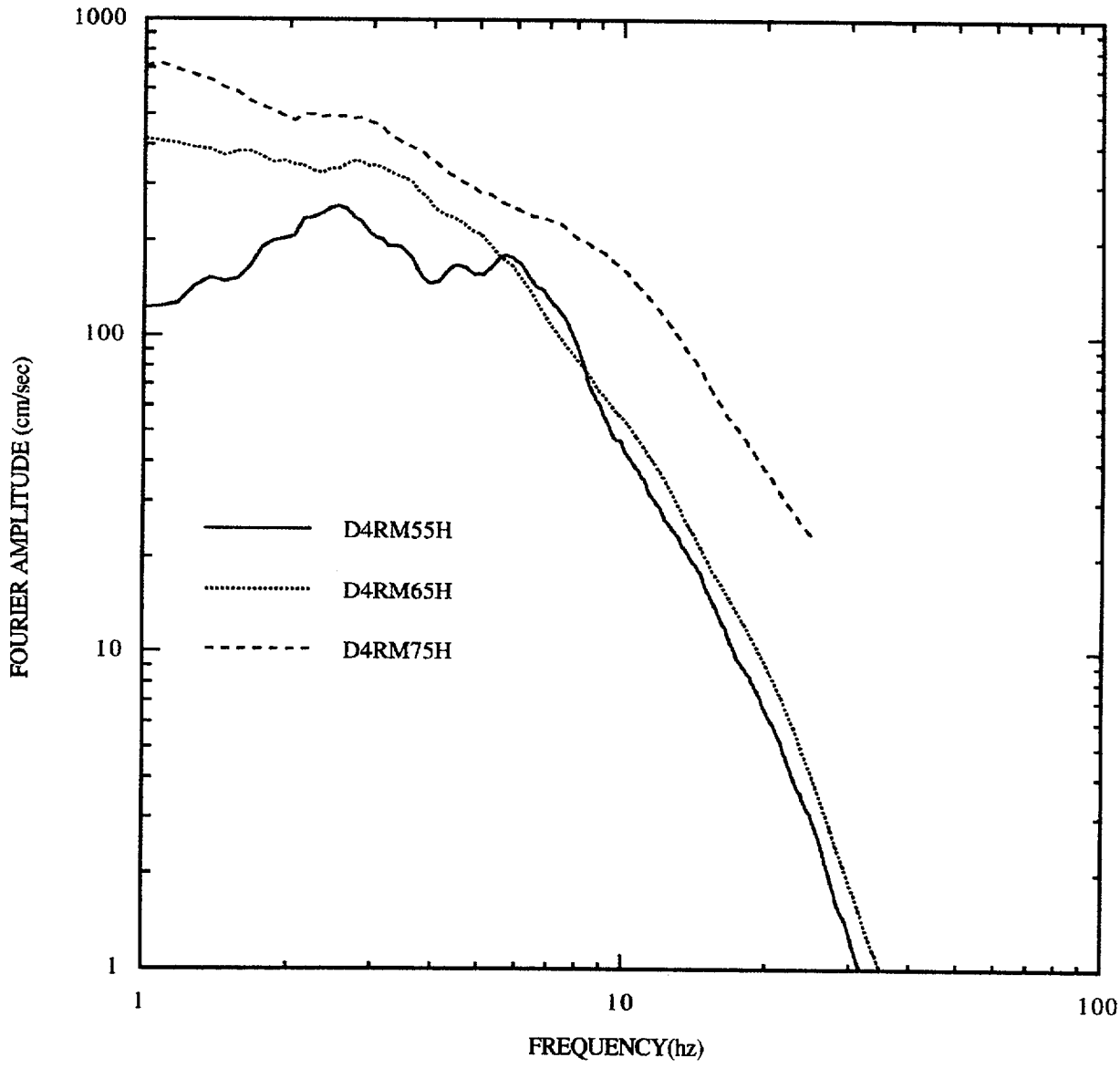

Figure E-37. Mean Fourier spectra for distance 100-200 km, rock sites, horizontal motions.

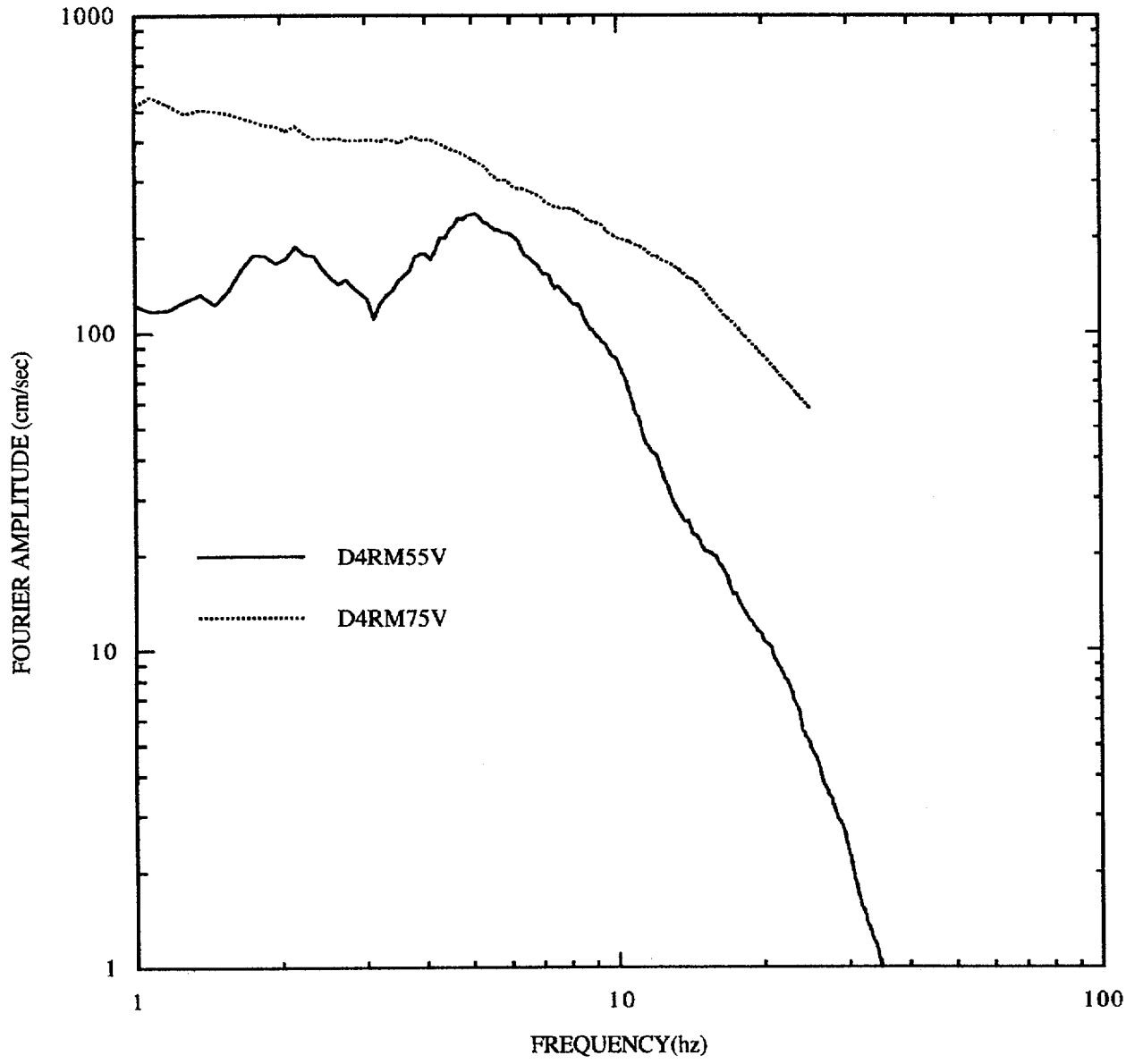

Figure E-38. Mean Fourier spectra for distance 100-200 km, rock sites, vertical motions.

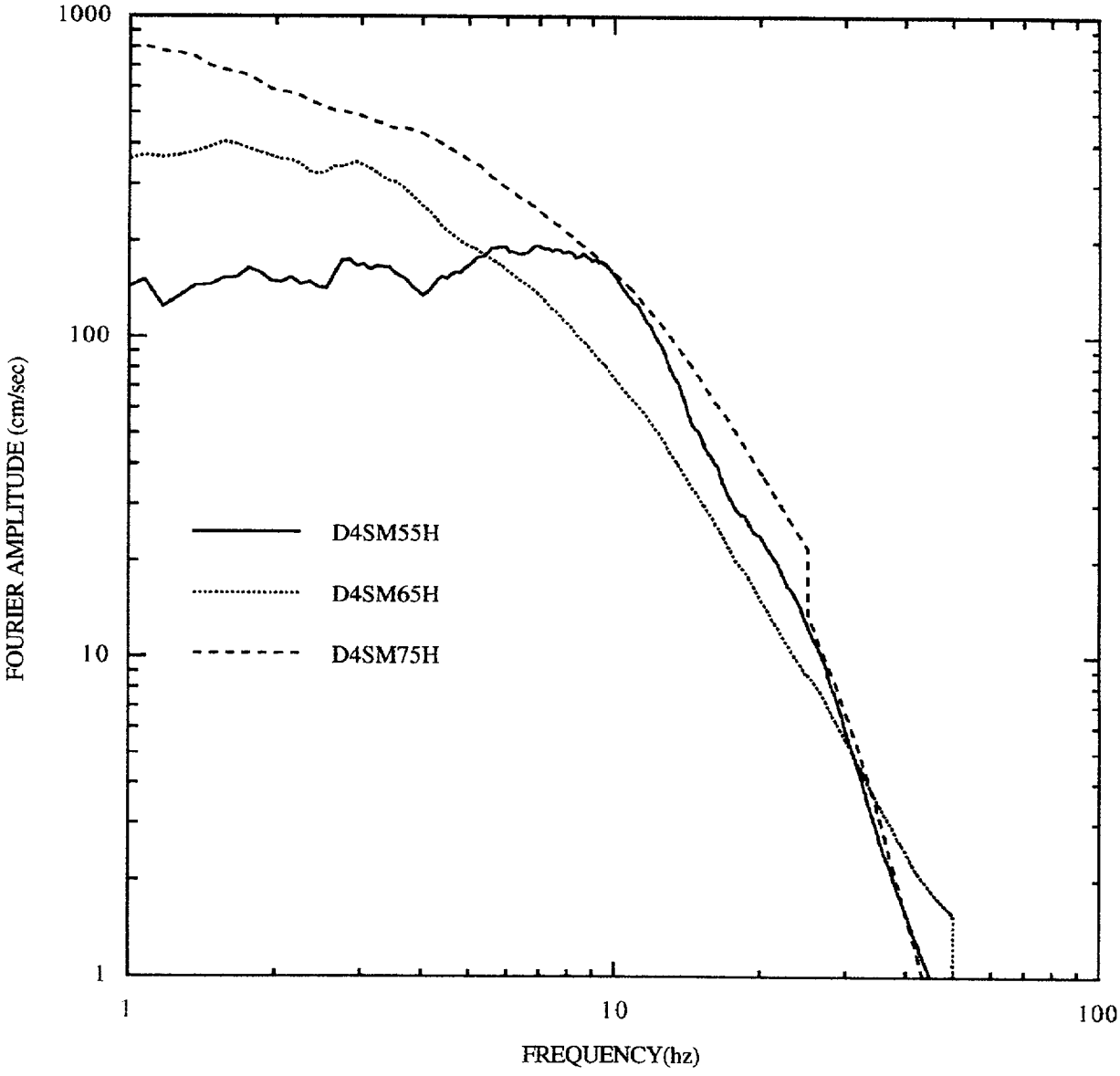

Figure E-39. Mean Fourier spectra for distance 100-200 km, soil sites, horizontal motions. Note: discontinuity at 25 and 50 Hz is caused by few records available above that frequency.

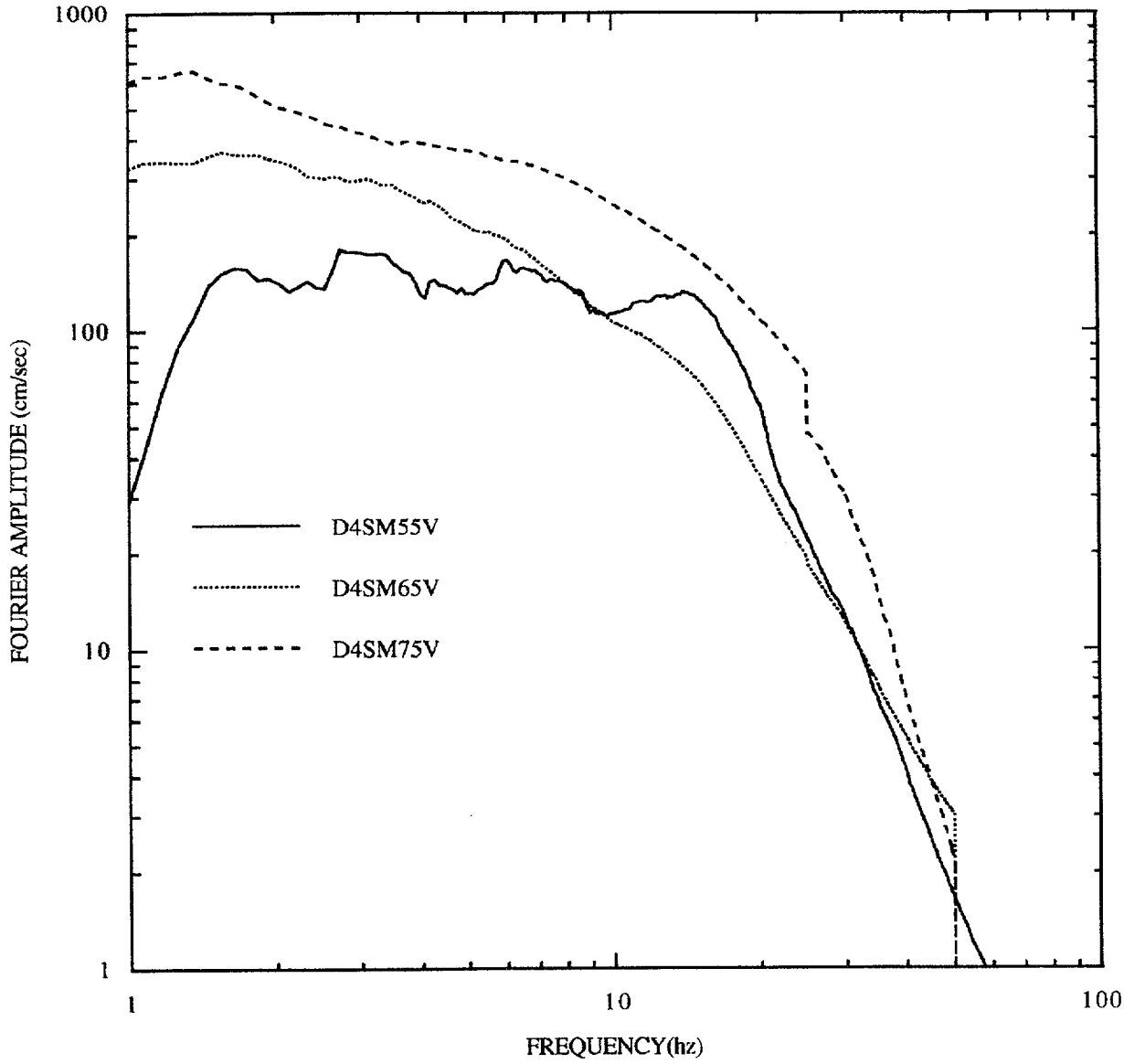

Figure E-40. Mean Fourier spectra for distance 100-200 km, soil sites, vertical motions.
Note: discontinuity at 25 and 50 Hz is caused by few records available above that frequency.

APPENDIX F PLOTS OF EMPIRICAL DATA FROM WUS RECORDS

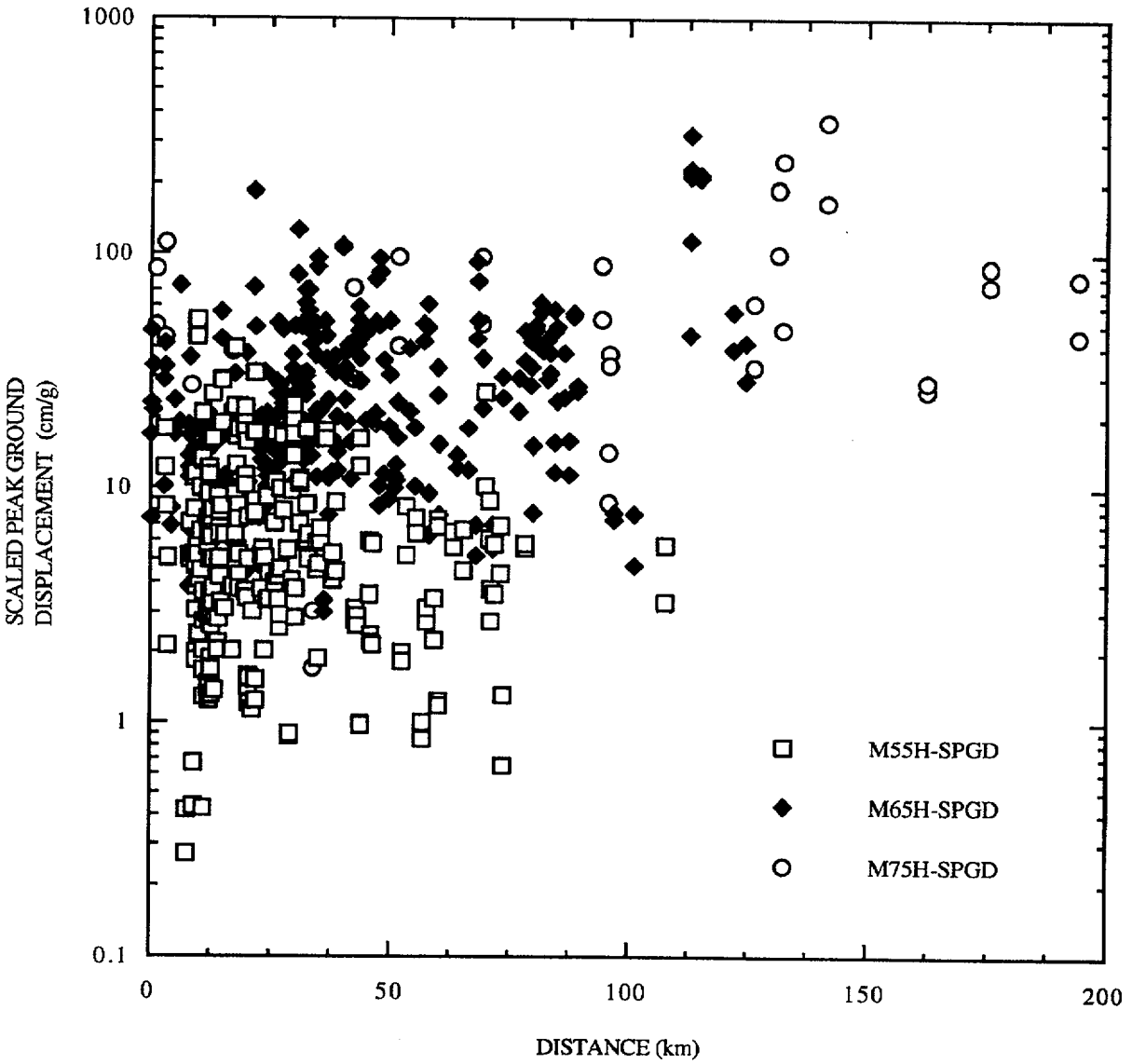

Figure F-1. PGD/PGA (cm/g) for horizontal motion, rock sites

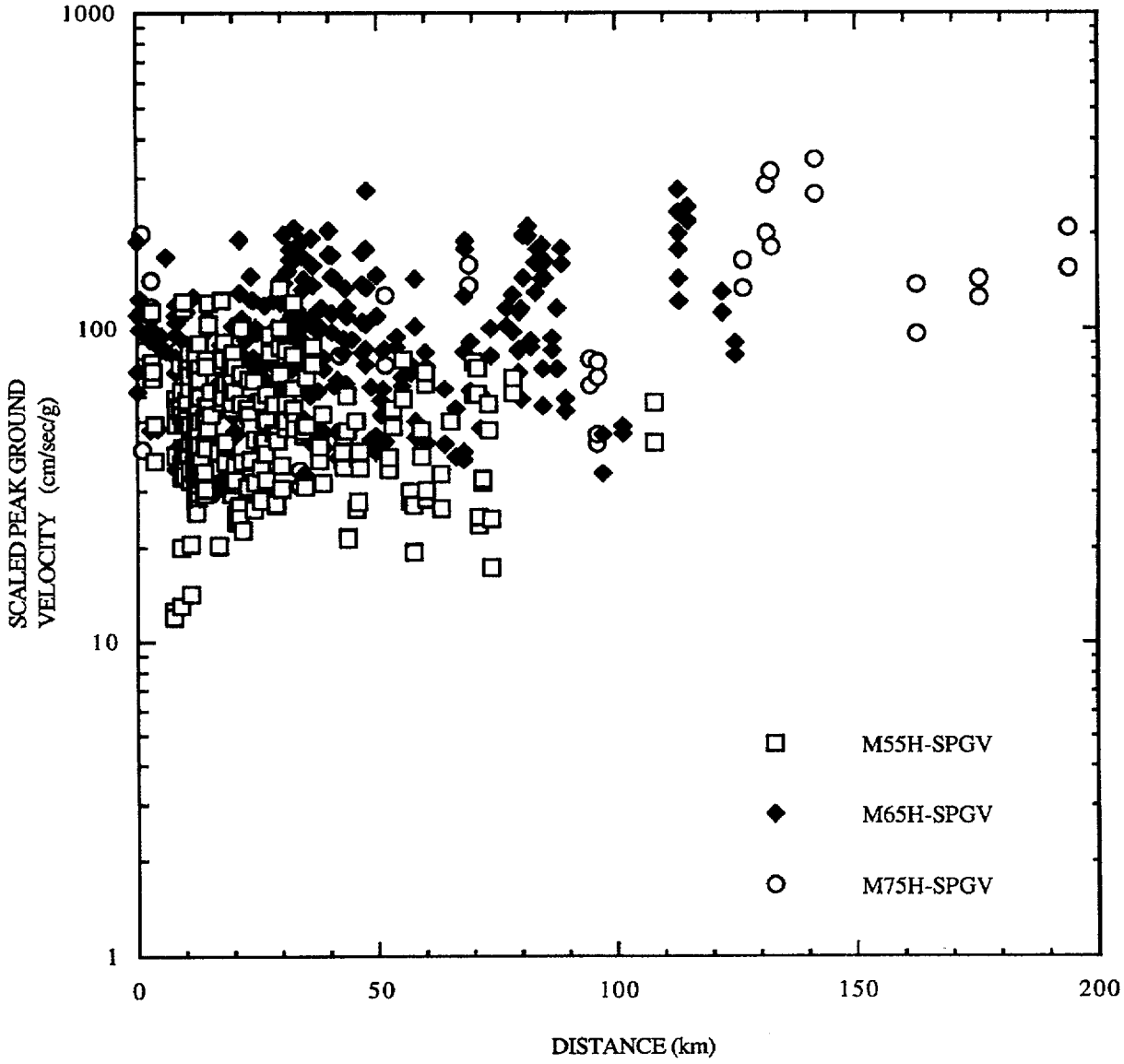

Figure F-2. PGV/PGA (cm/s/g) for horizontal motion, rock sites.

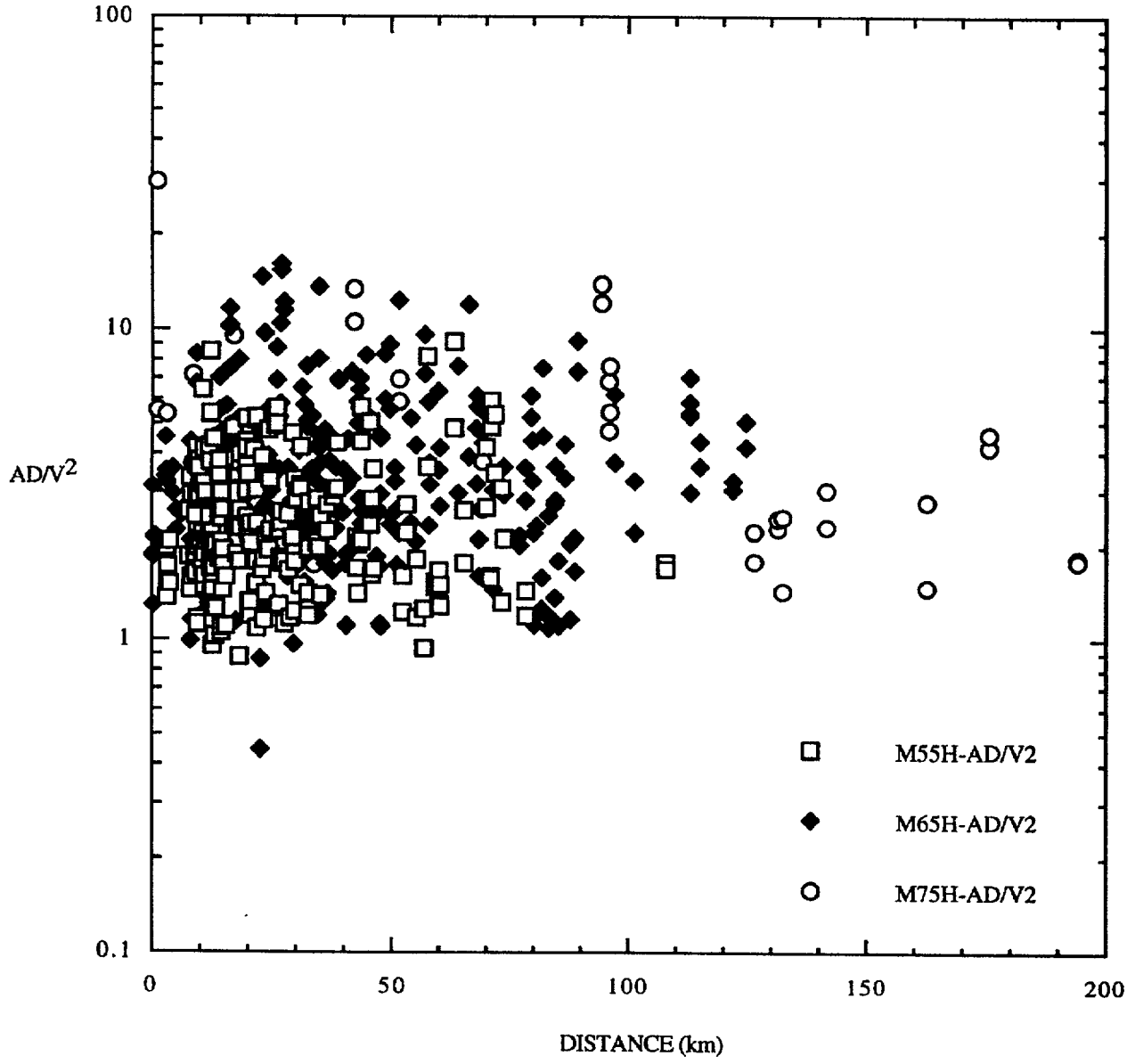

Figure F-3. PGA•PGA/PGV^2 for horizontal motion, rock sites.

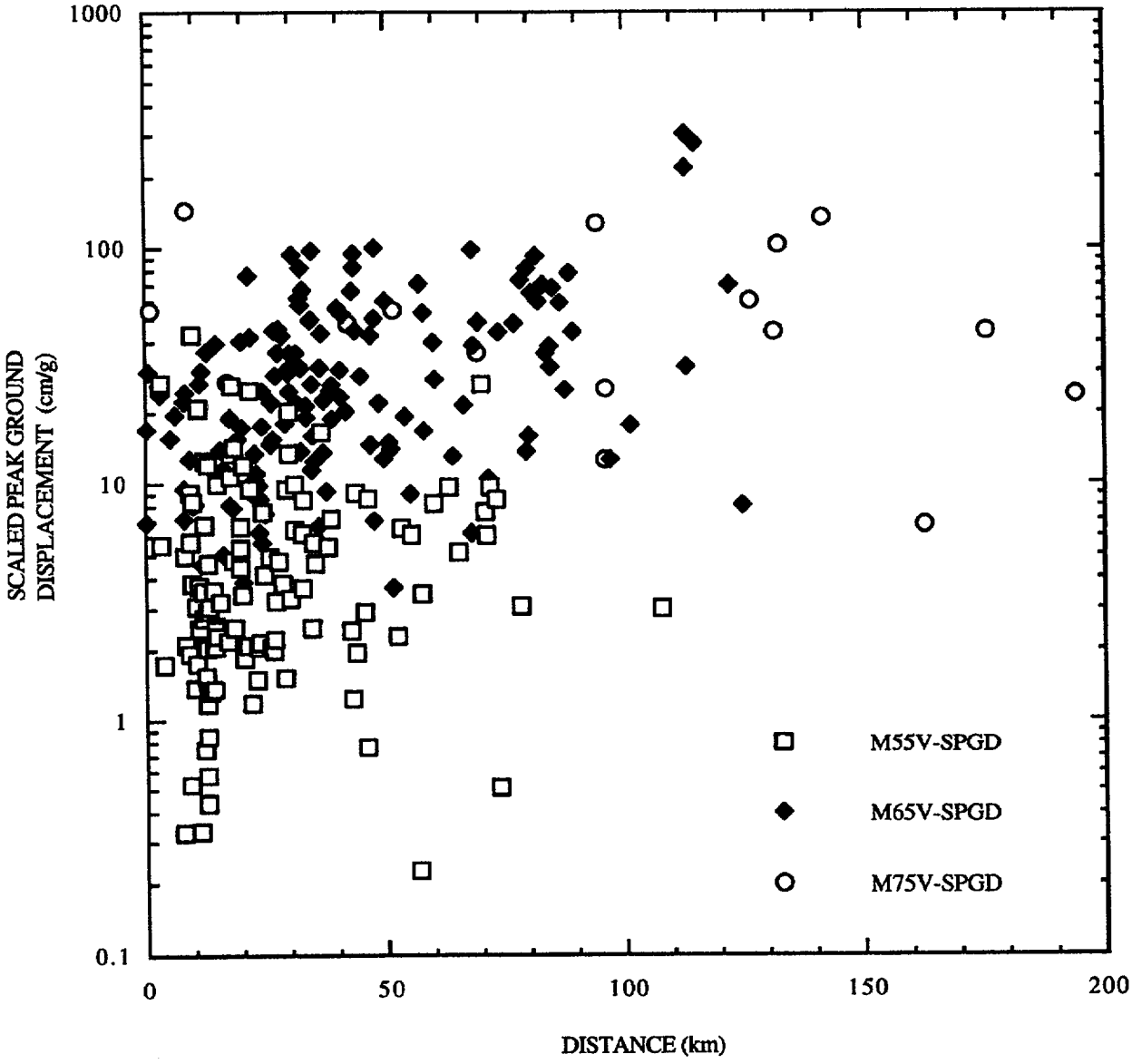

Figure F-4. PGD/PGA (cm/g) for vertical motion, rock sites.

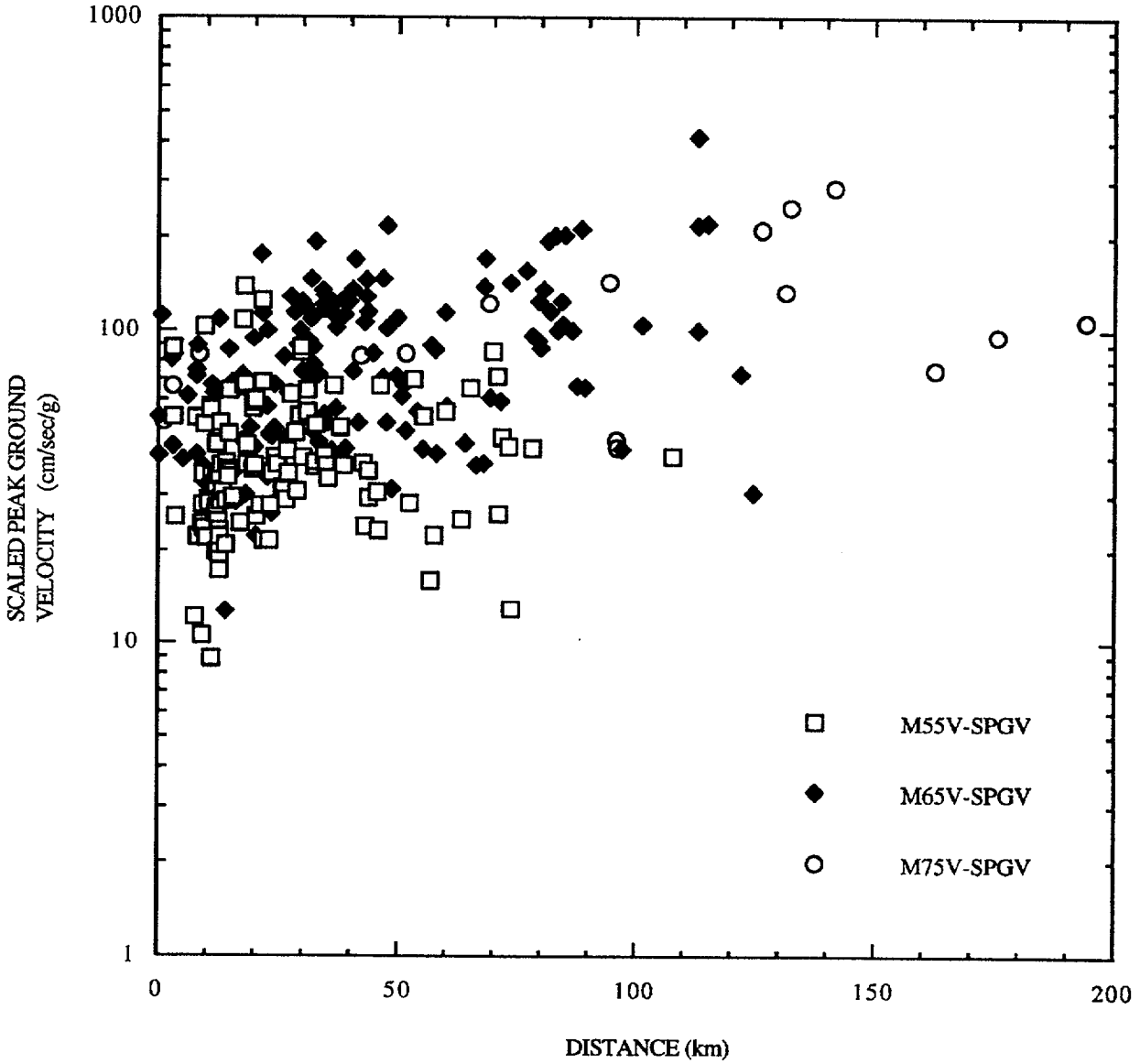

Figure F-5. PGV/PGA (cm/s/g) for vertical motion, rock sites.

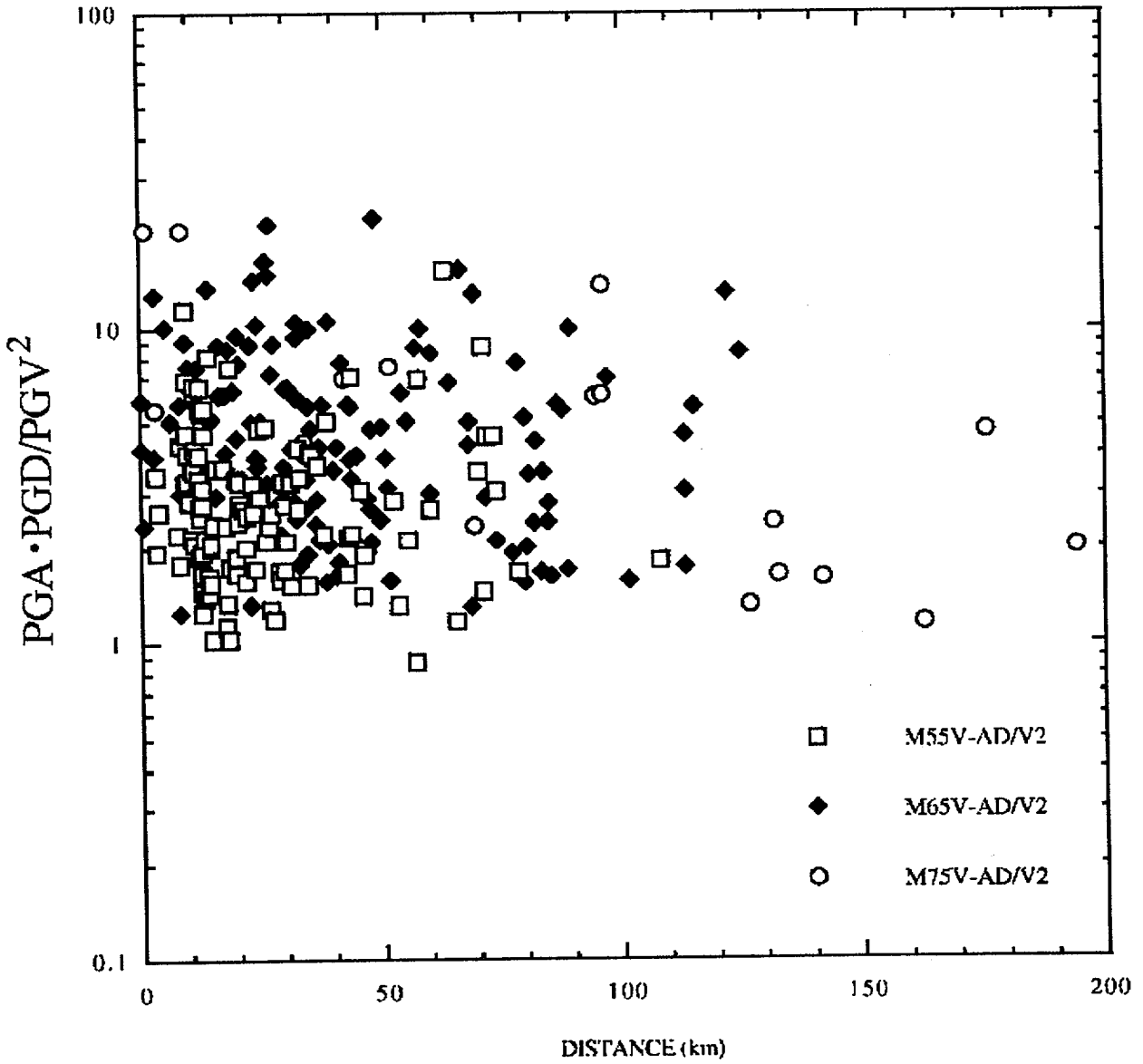

Figure F-6. PGA•PGD/PGV^2 for vertical motion, rock sites.

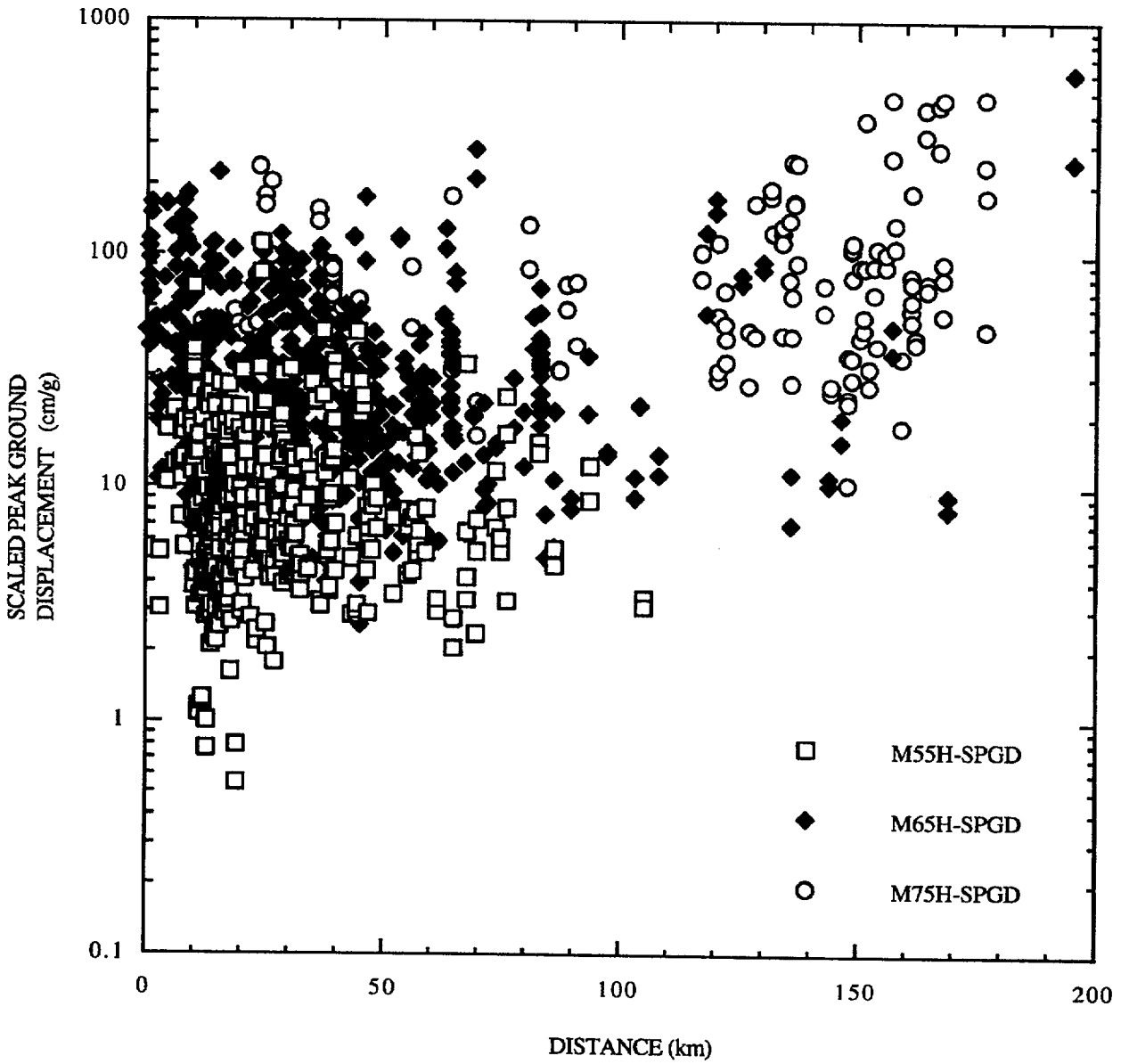

Figure F-7. PGD/PGA (cm/g) for horizontal motion, soil sites.

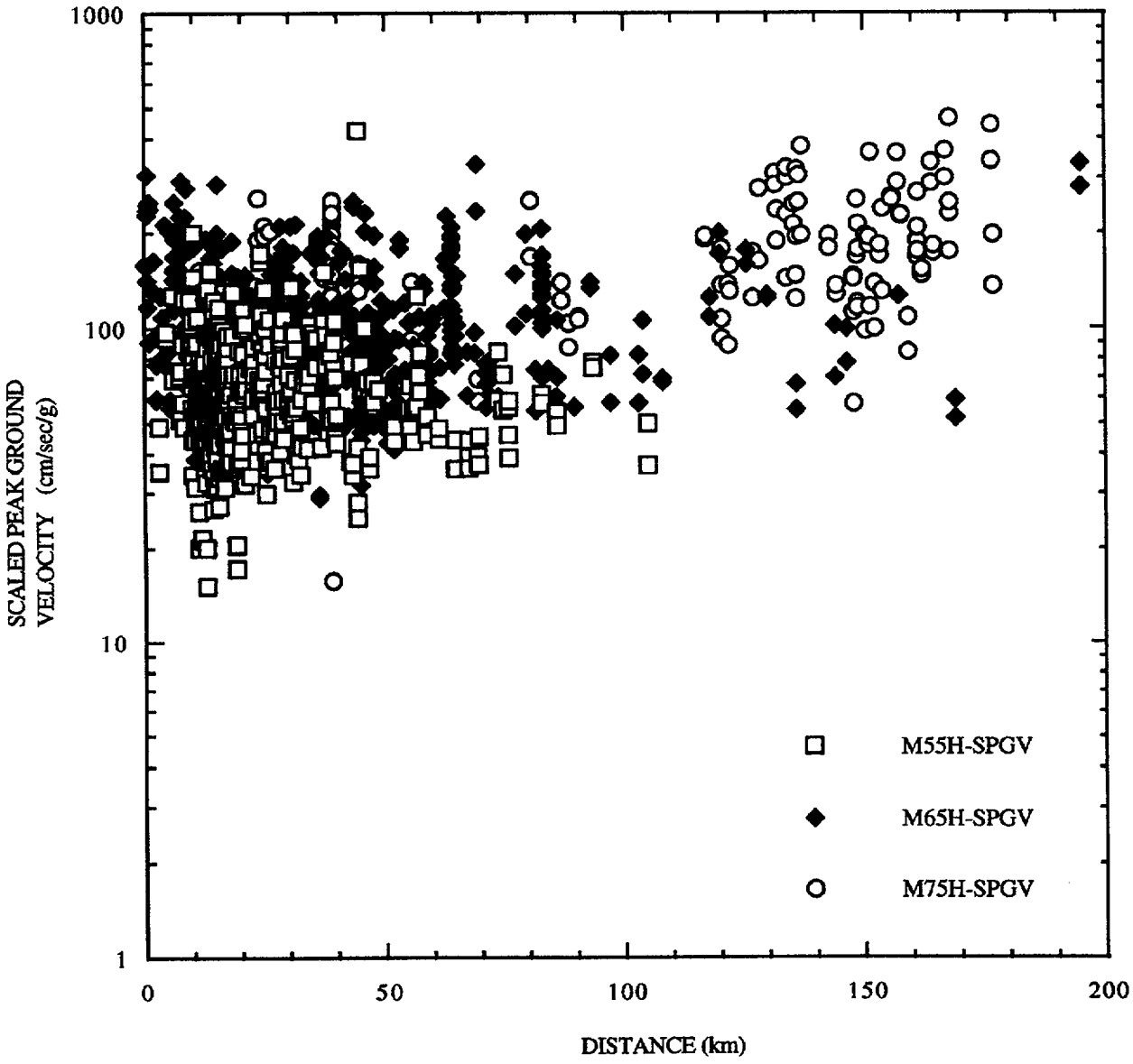

Figure F-8. PGV/PGA (cm/s/g) for horizontal motion, soil sites.

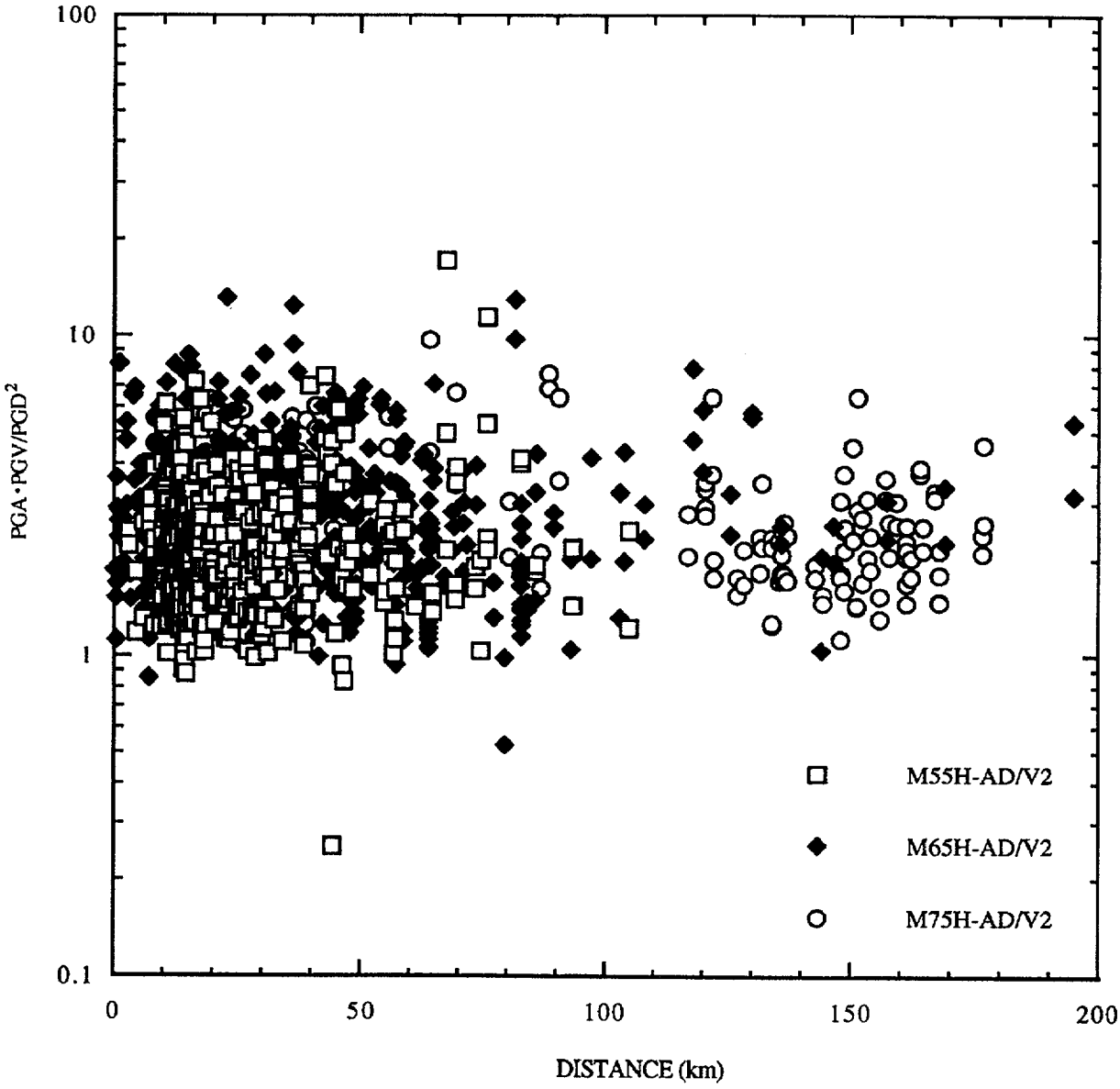

Figure F-9. PGA•PGD/PGV^2 for horizontal motion, soil sites.

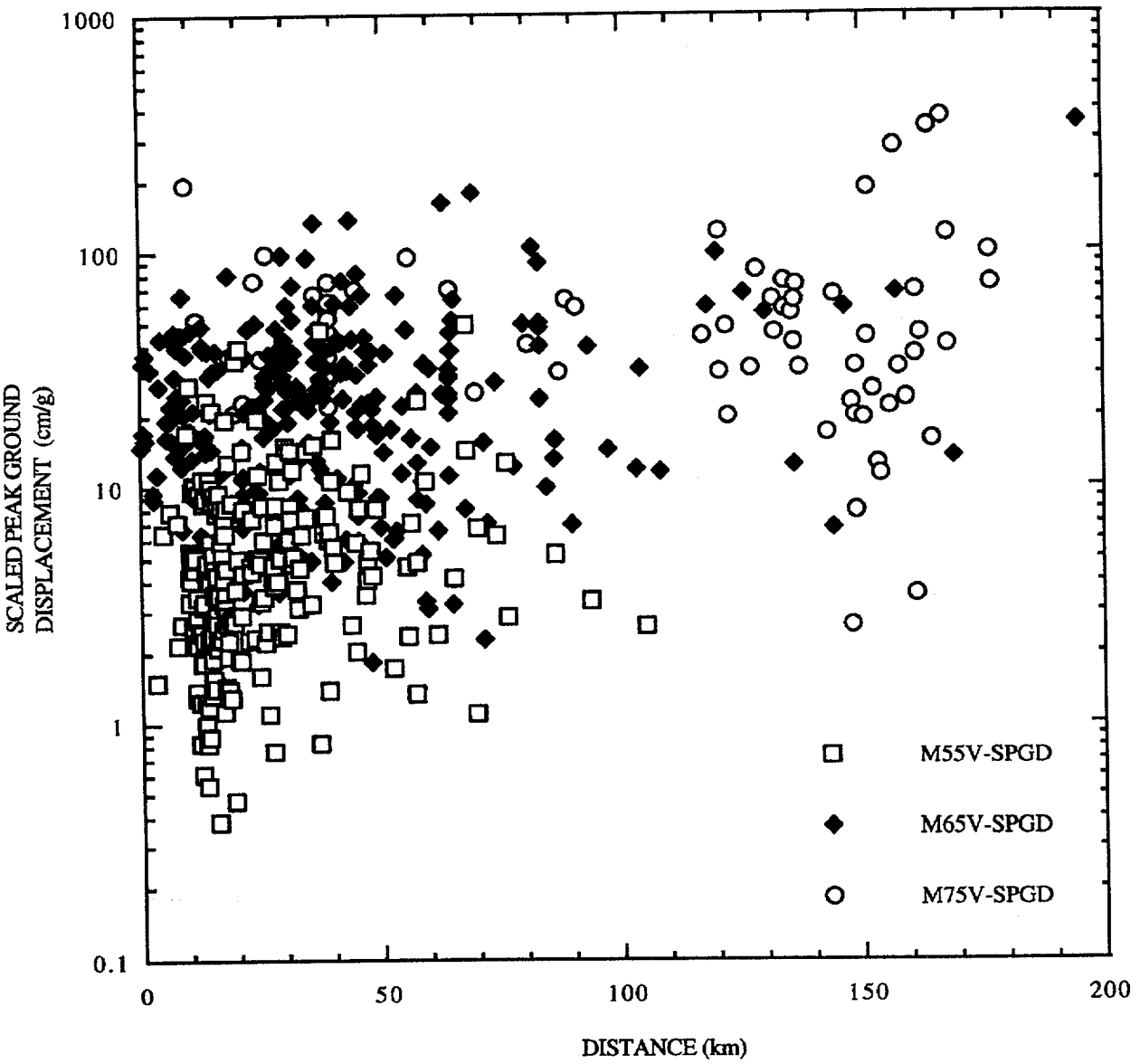

Figure F-10. PGD/PGA (cm/g) for vertical motions, soil sites.

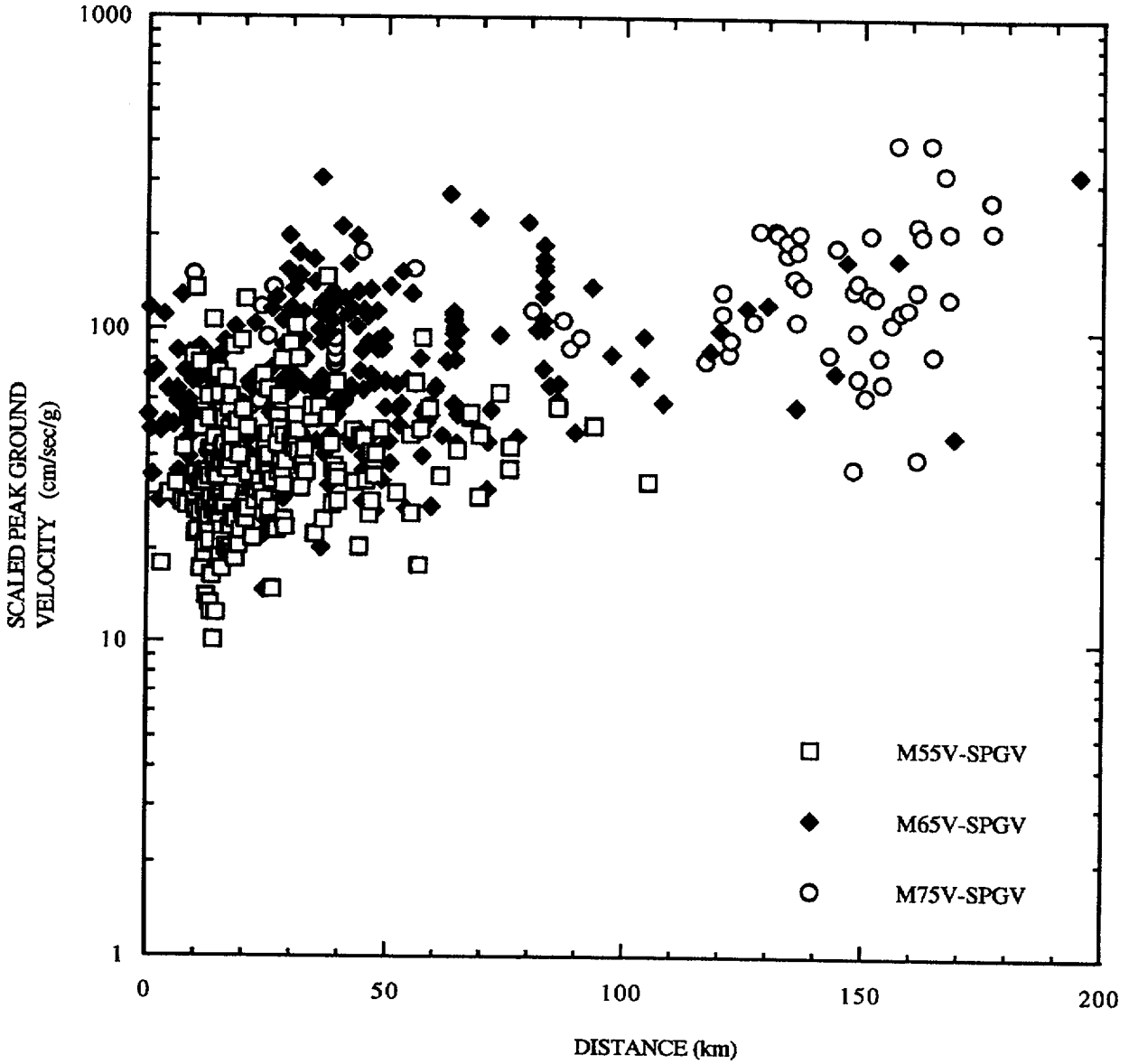

Figure F-11. PGV/PGA (cm/s/g) for vertical motion, soil sites.

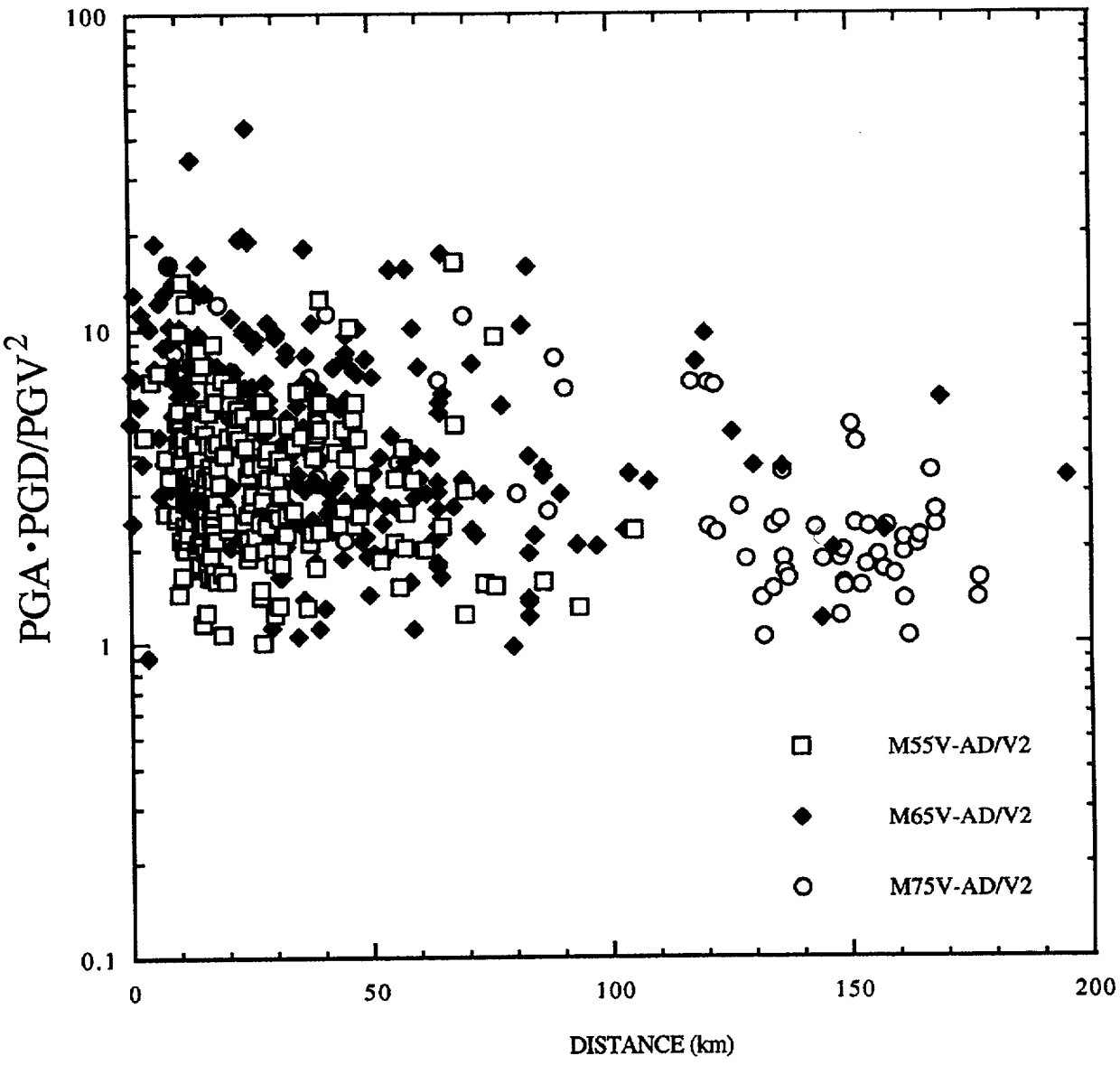

Figure F-12. PGA•PGD/PGV^2 for vertical motion, soil sites.

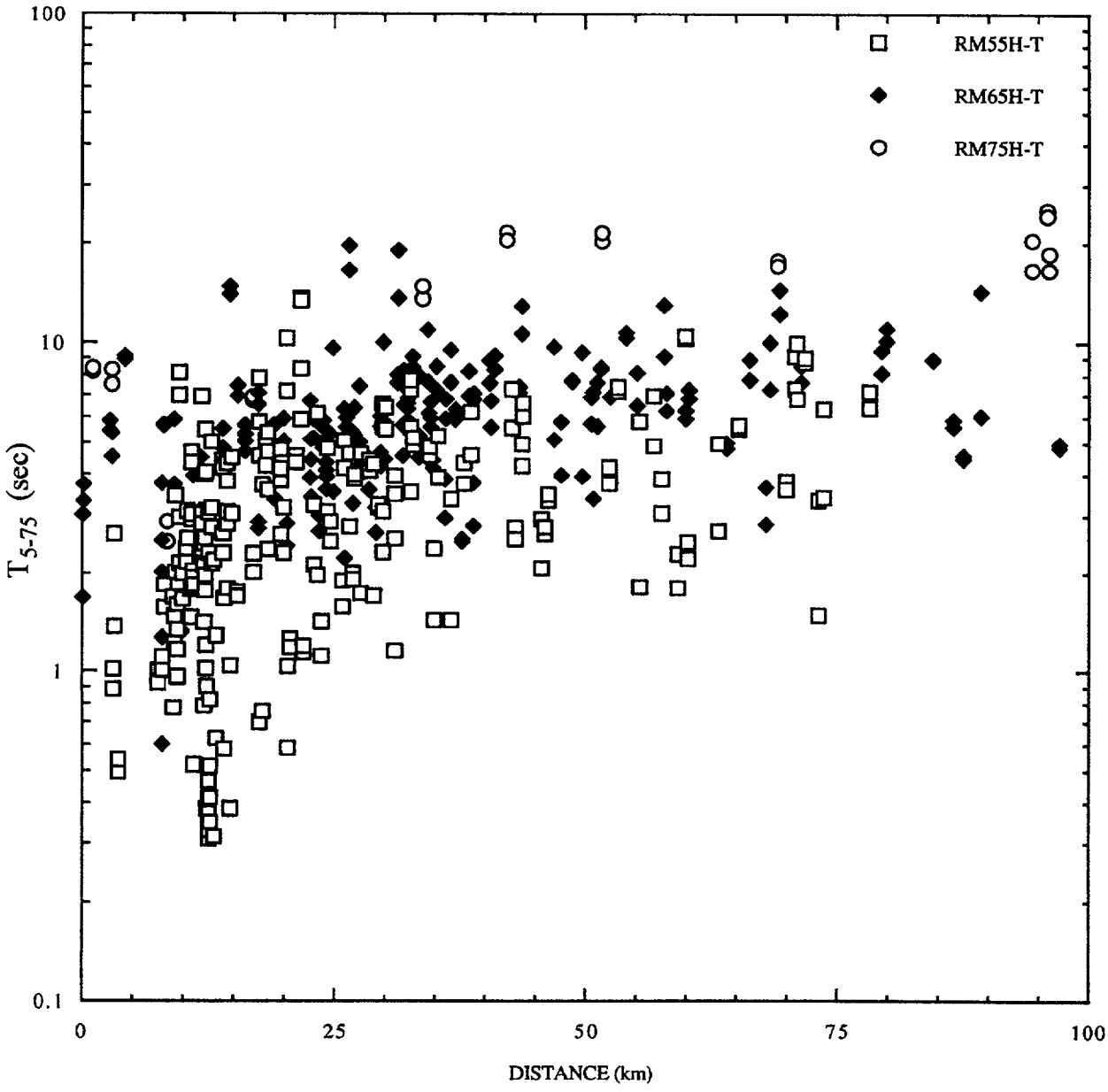

Figure F-13. Duration calculated as 5%-75% of Arias intensity, rock sites, horizontal motion.

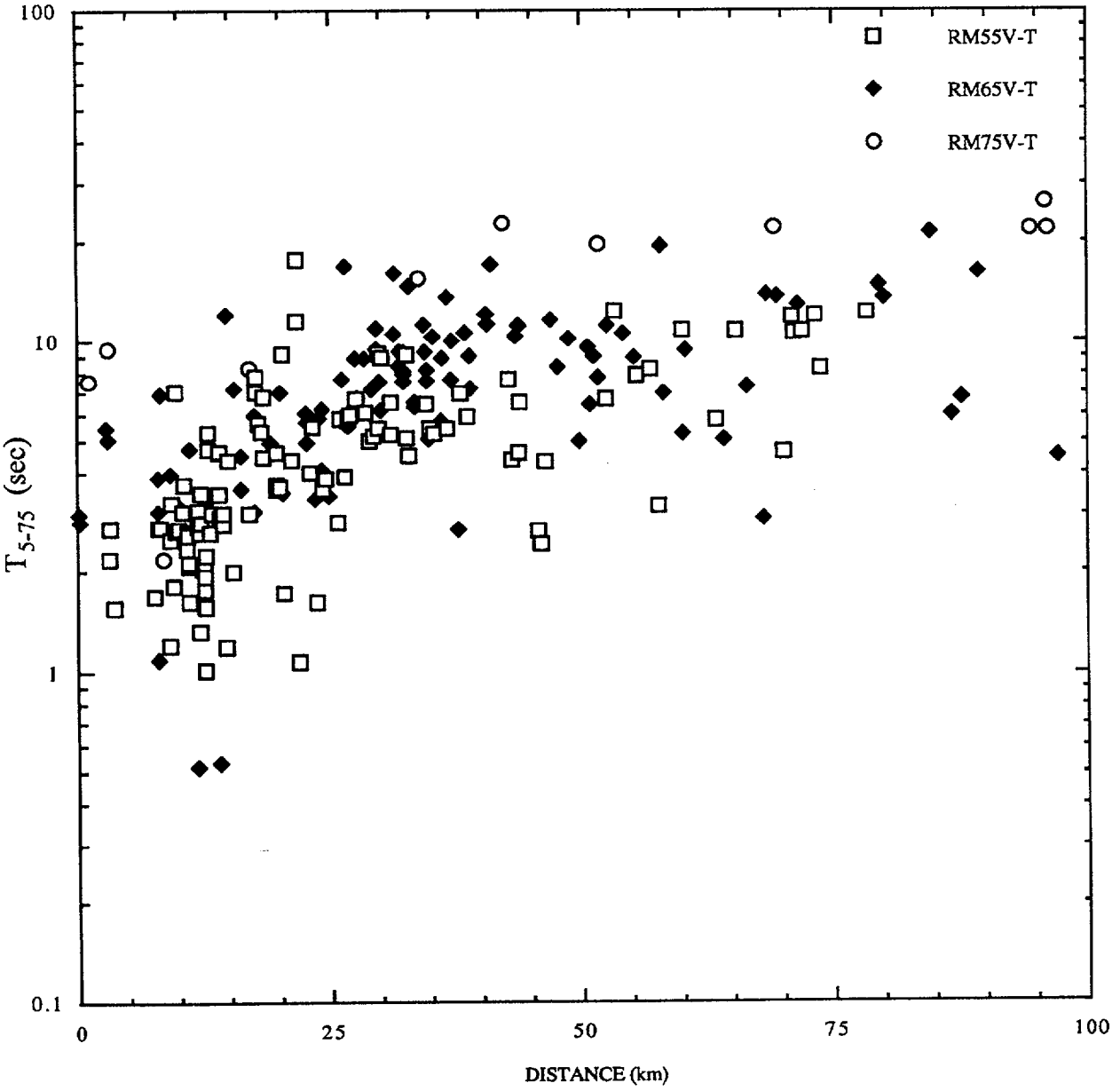

Figure F-14. Duration calculated as 5-75% of Arias intensity, rock sites, vertical motion.

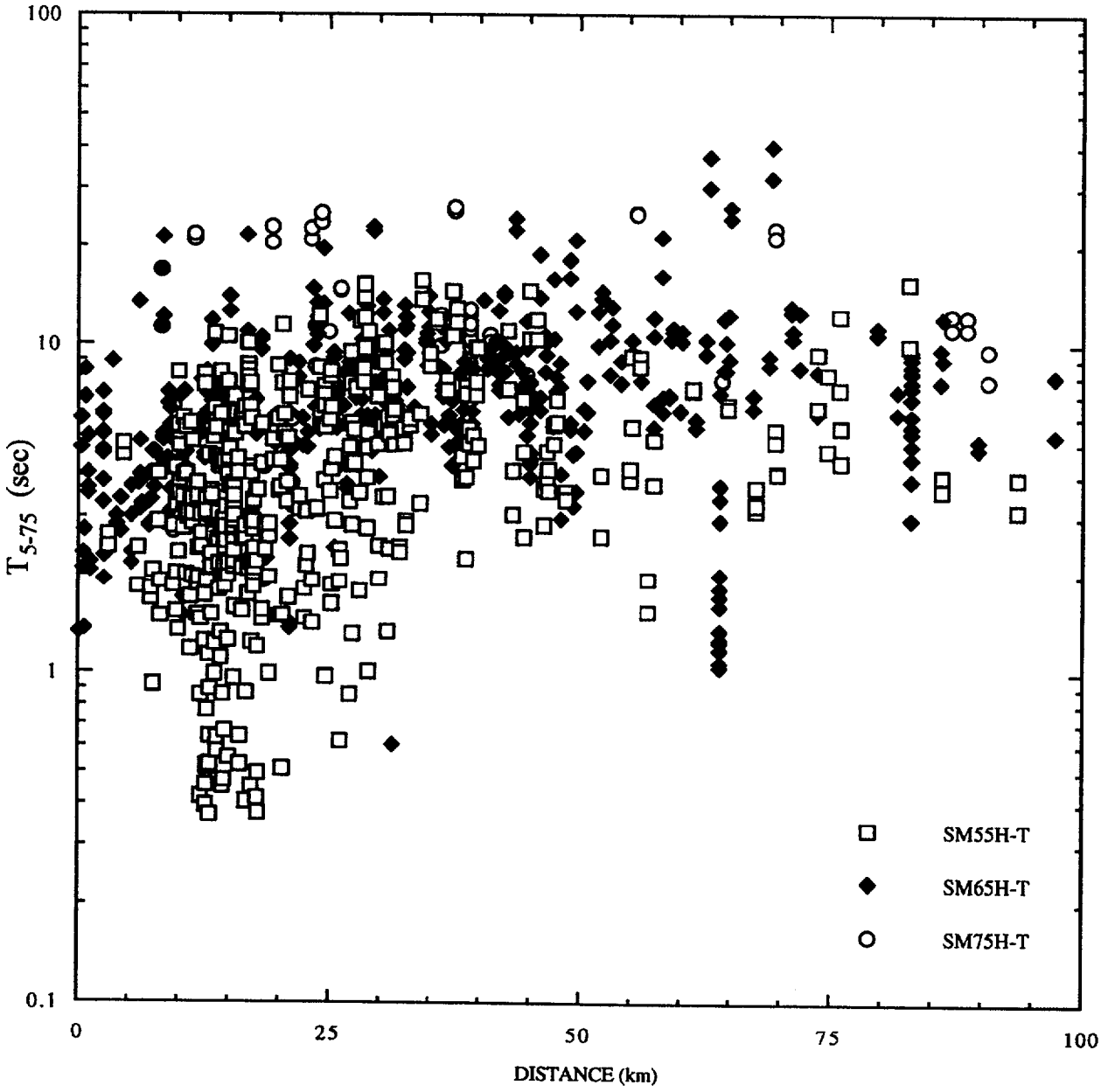

Figure F-15. Duration calculated as 5-75% of Arias intensity, soil sites, horizontal motion.

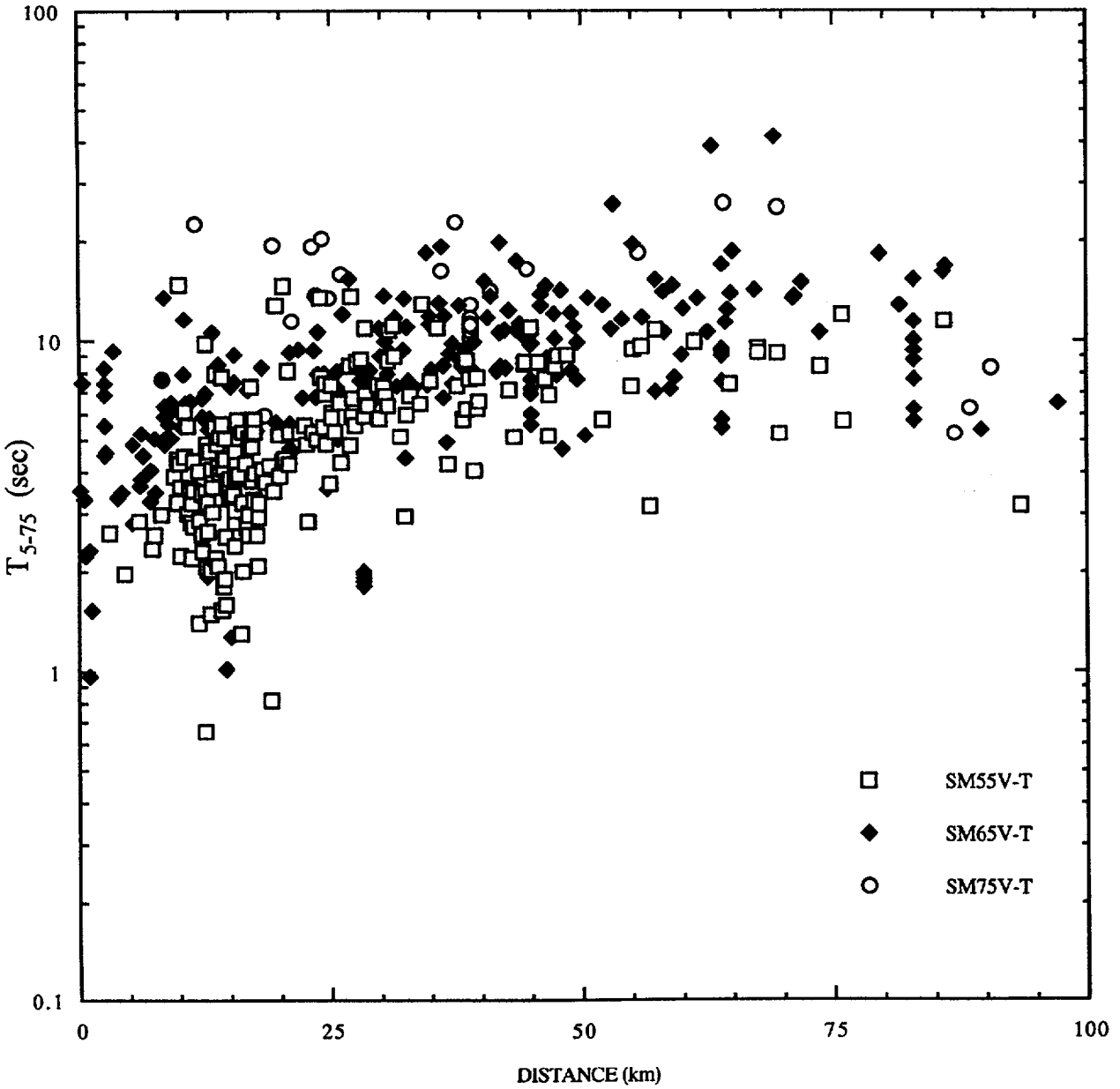

Figure F-16. Duration calculated as 5-75% of Arias intensity, soil sites, vertical motion.

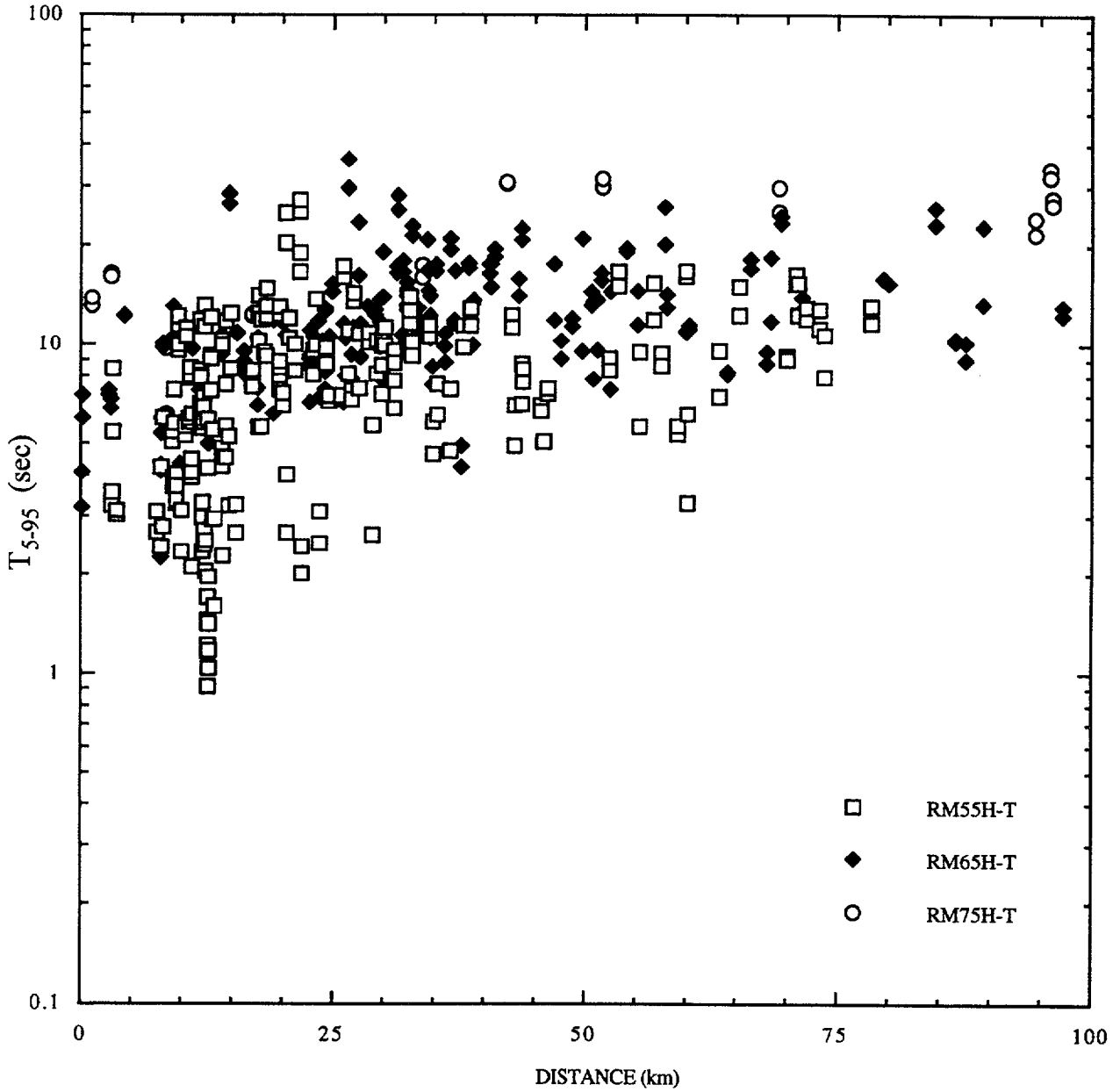

Figure F-17. Duration calculated as 5-95% of Arias intensity, rock sites, horizontal motion.

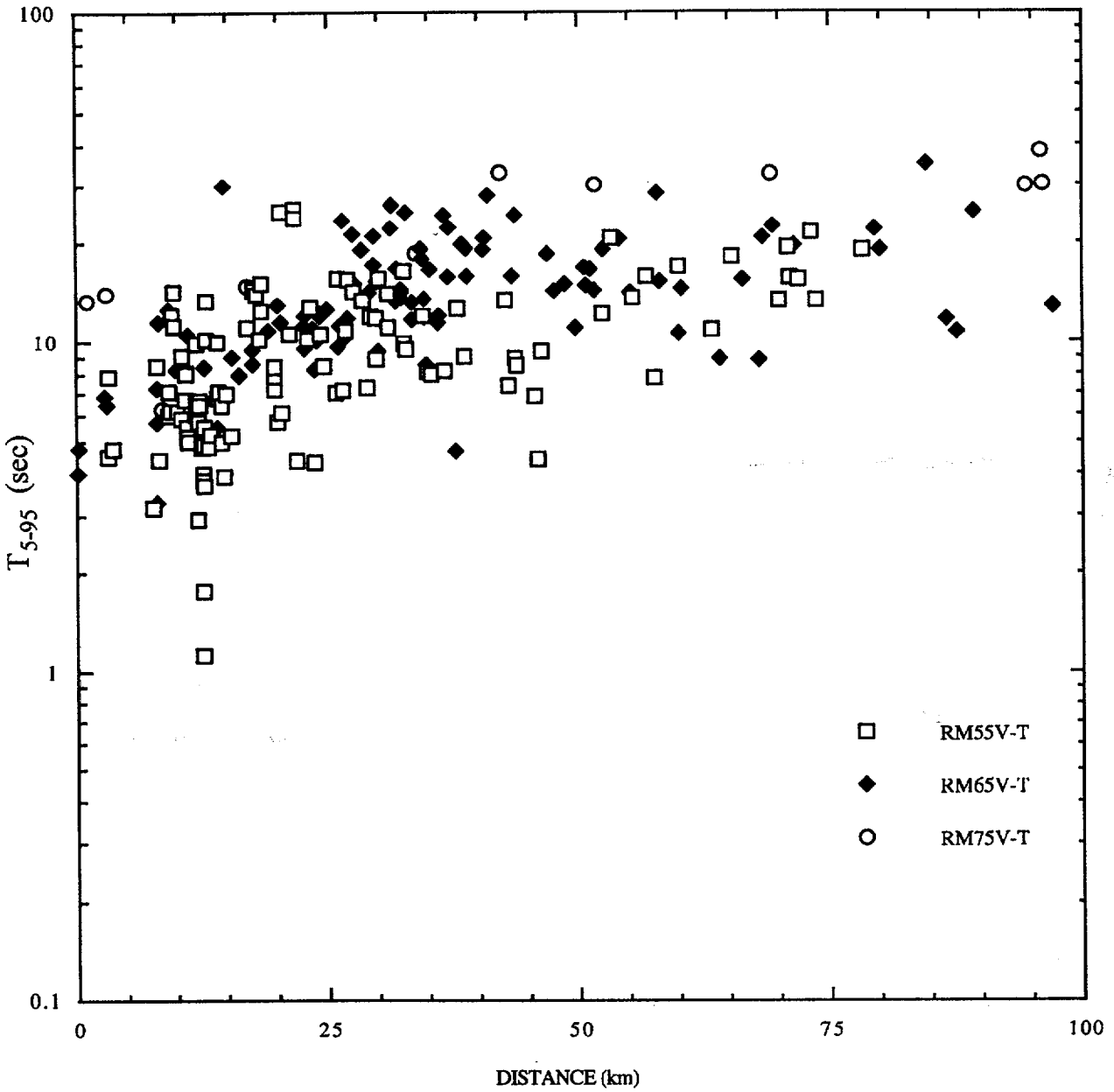

Figure F-18. Duration calculated as 5-95% of Arias intensity, rock sites, vertical motion.

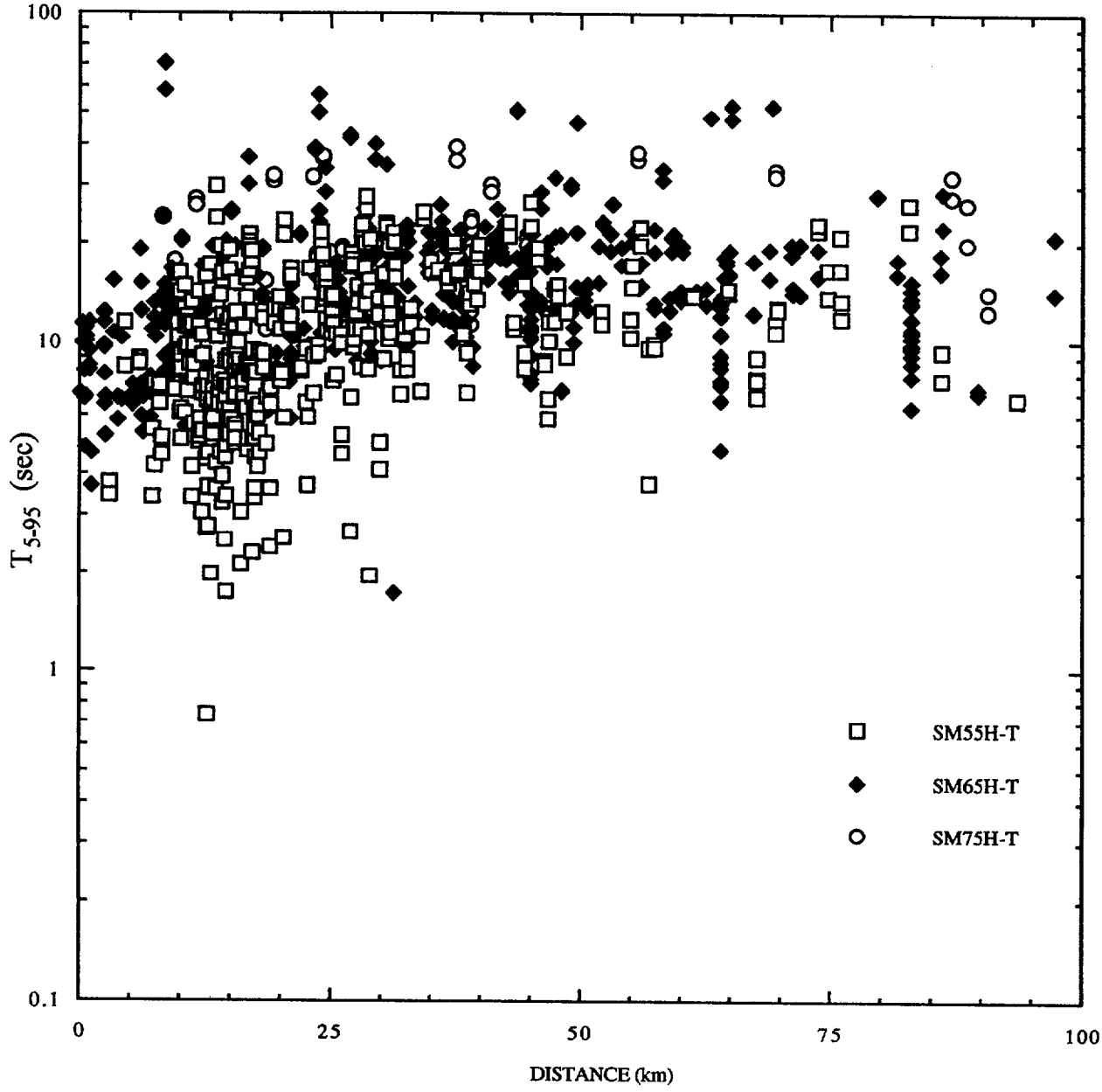

Figure F-19. Duration calculated as 5-95% of Arias intensity, soil sites, horizontal motion.

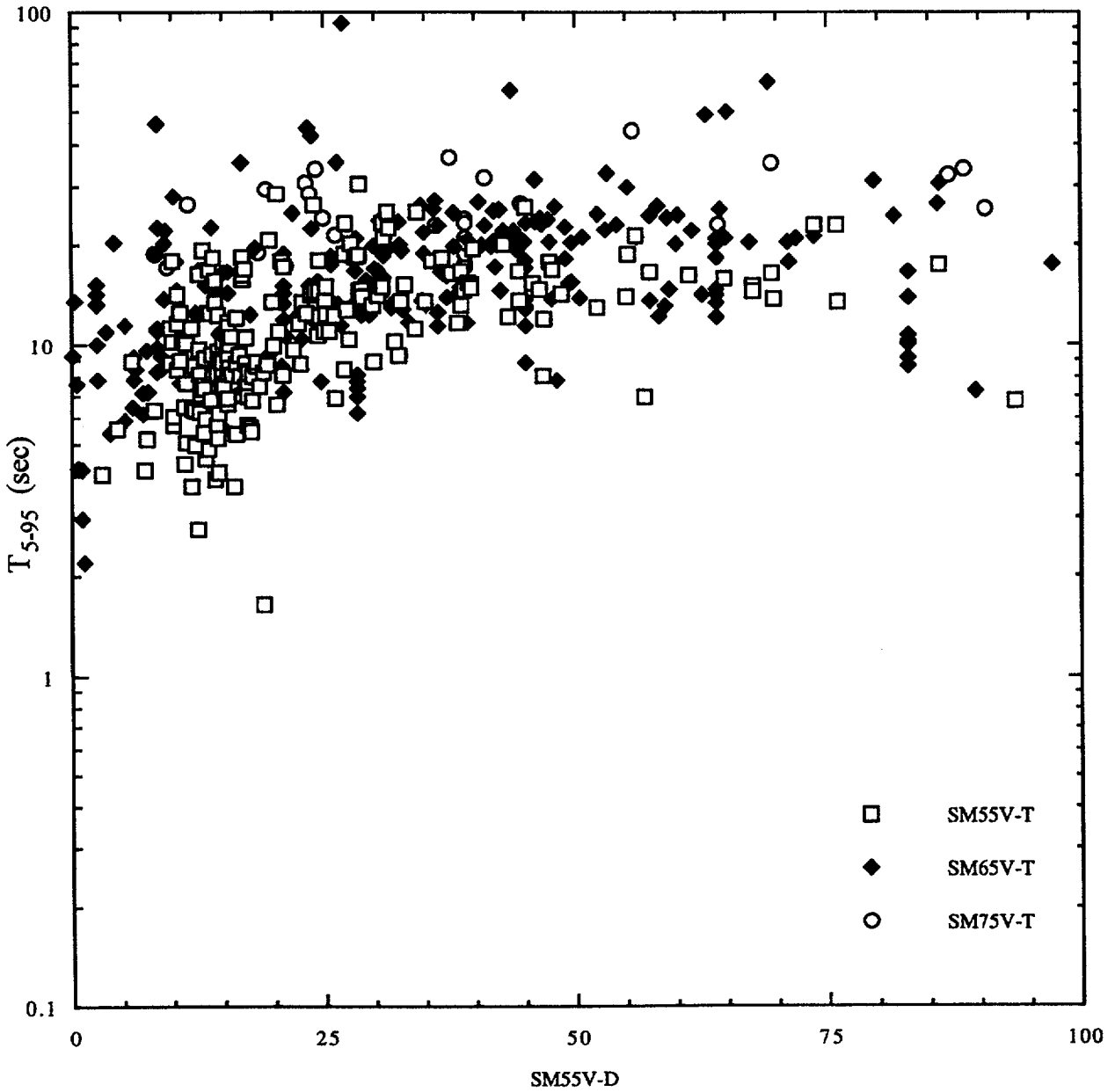

Figure F-20. Duration calculated as 5-95% of Arias intensity, soil sites, vertical motion.

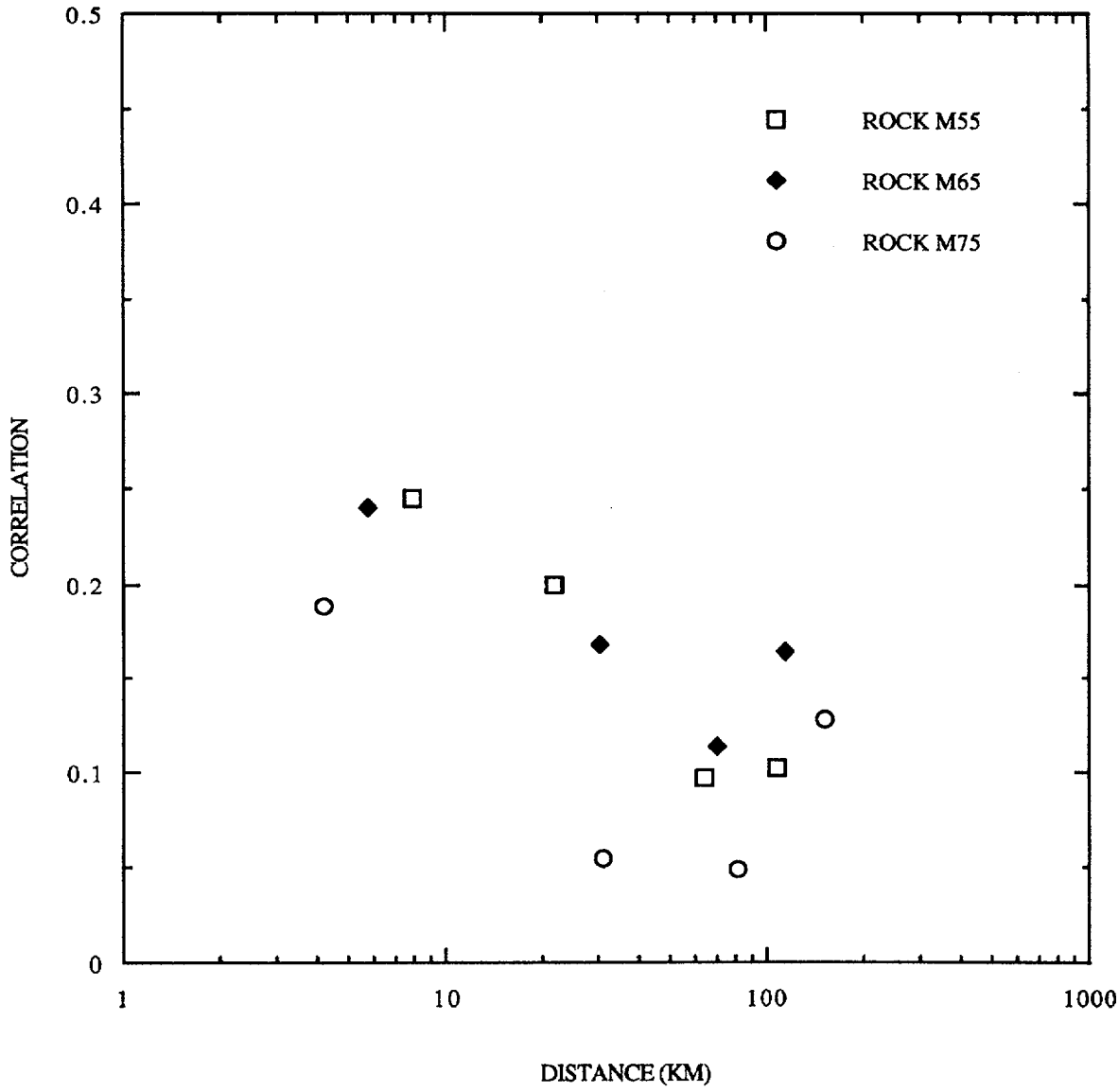

Figure F-21. Correlations of H1/H2 acceleration pairs, WUS rock sites.

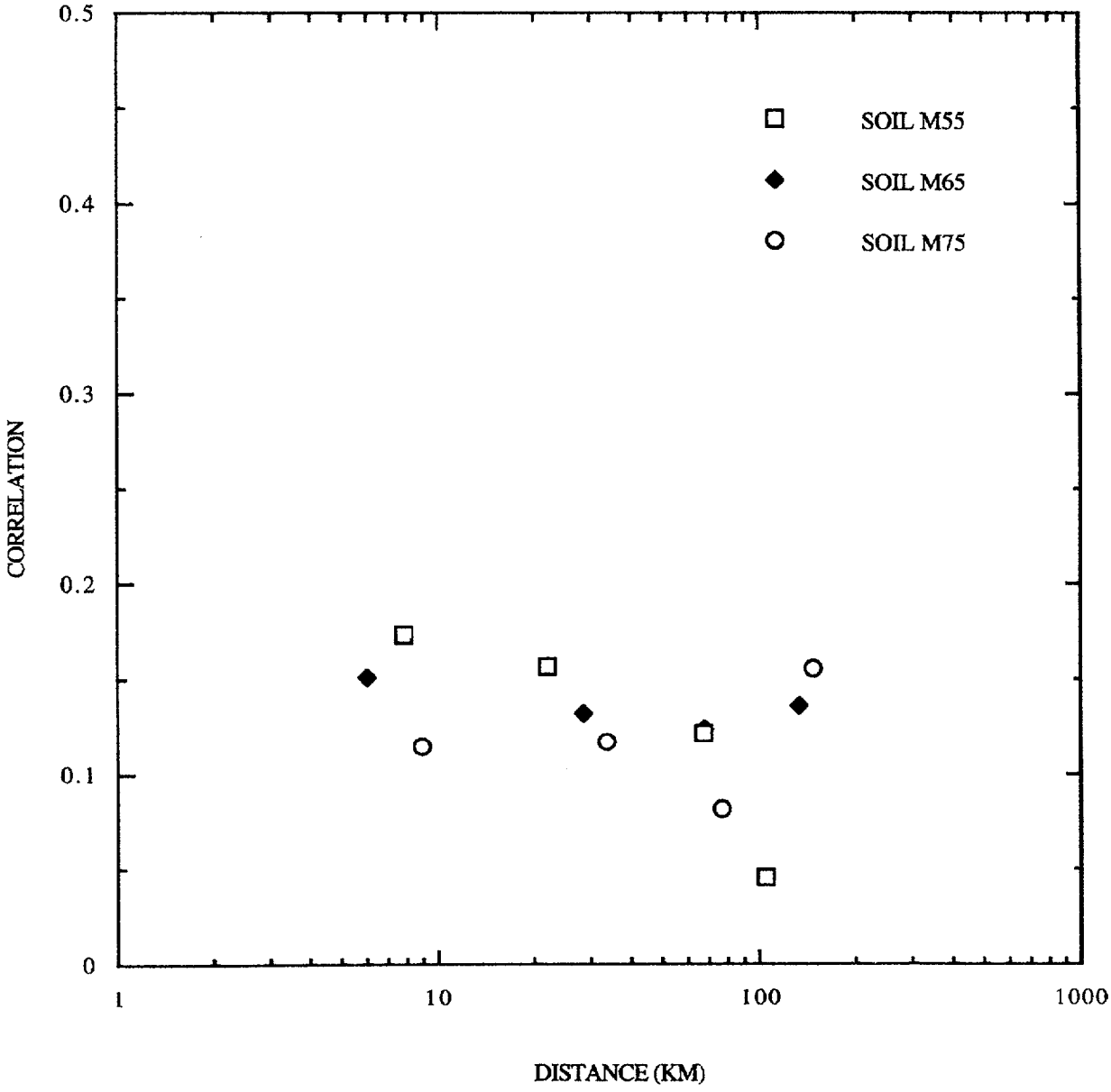

Figure F-22. Correlations of H1/H2 acceleration pairs, WUS soil sites.

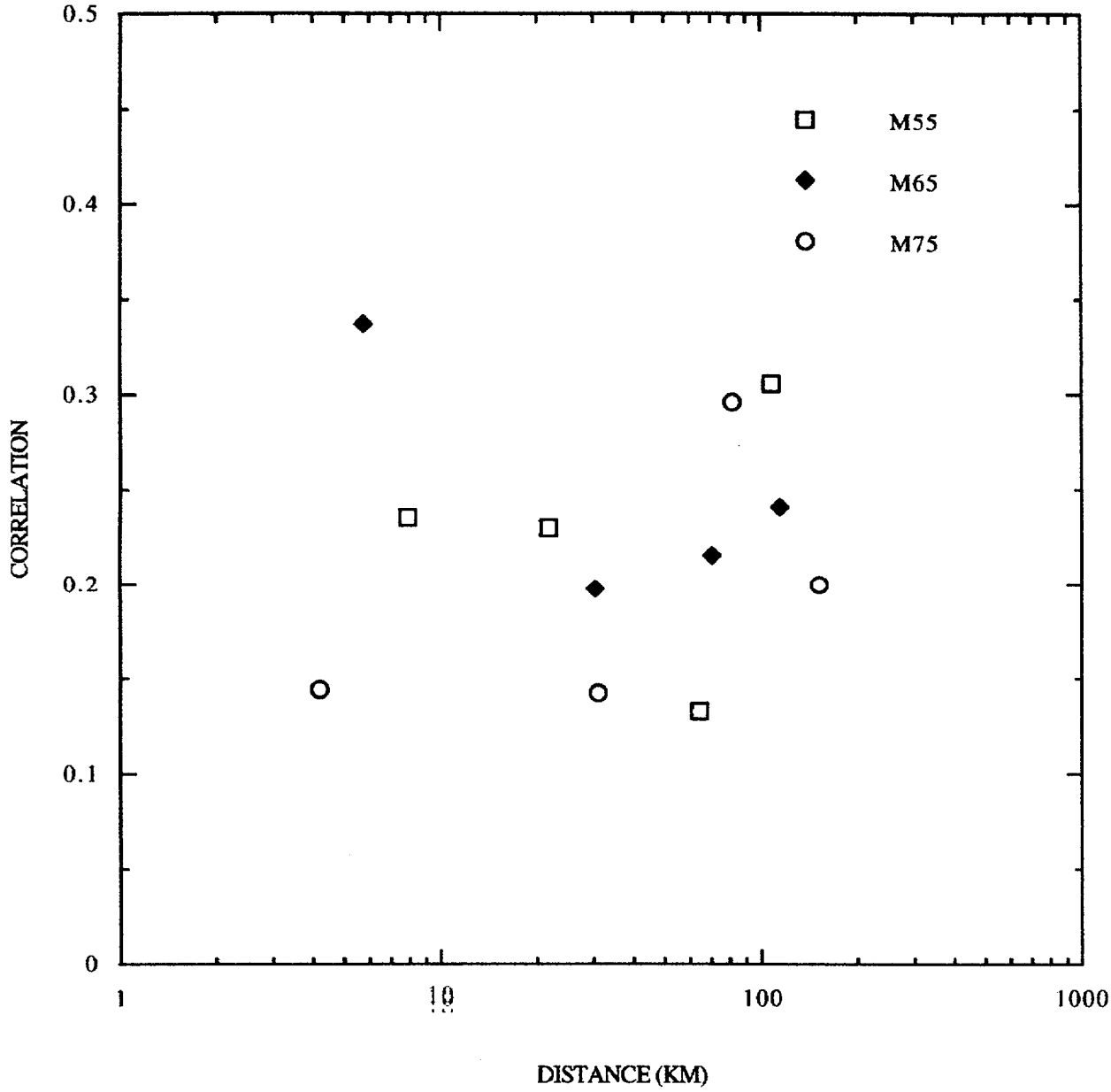

Figure F-23. Correlations of H1/H2 velocity pairs, WUS rock sites.

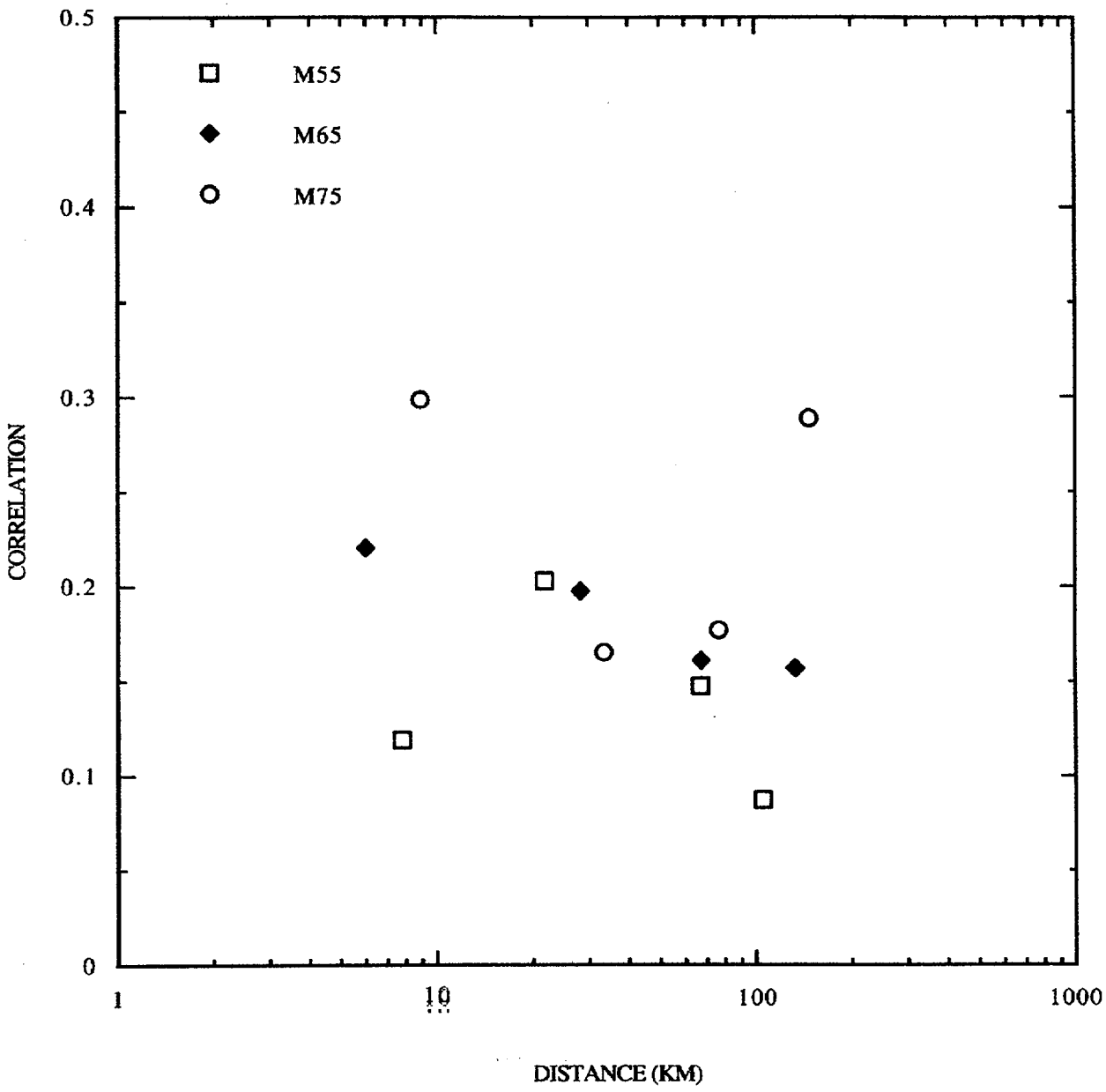

Figure F-24. Correlations of H1/H2 velocity pairs, WUS soil sites.

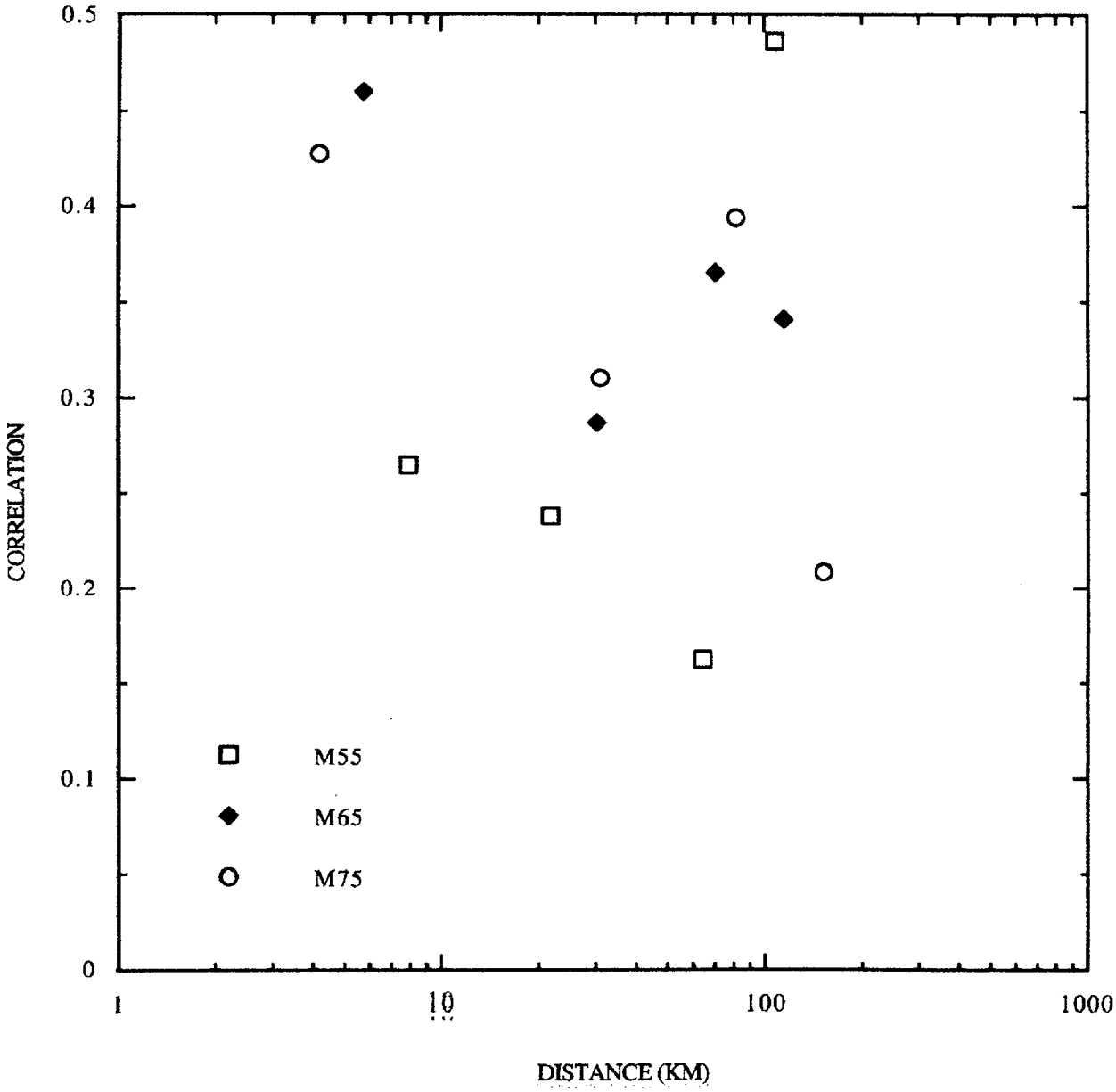

Figure F-25. Correlations of H1/H2 displacement pairs, WUS rock sites.

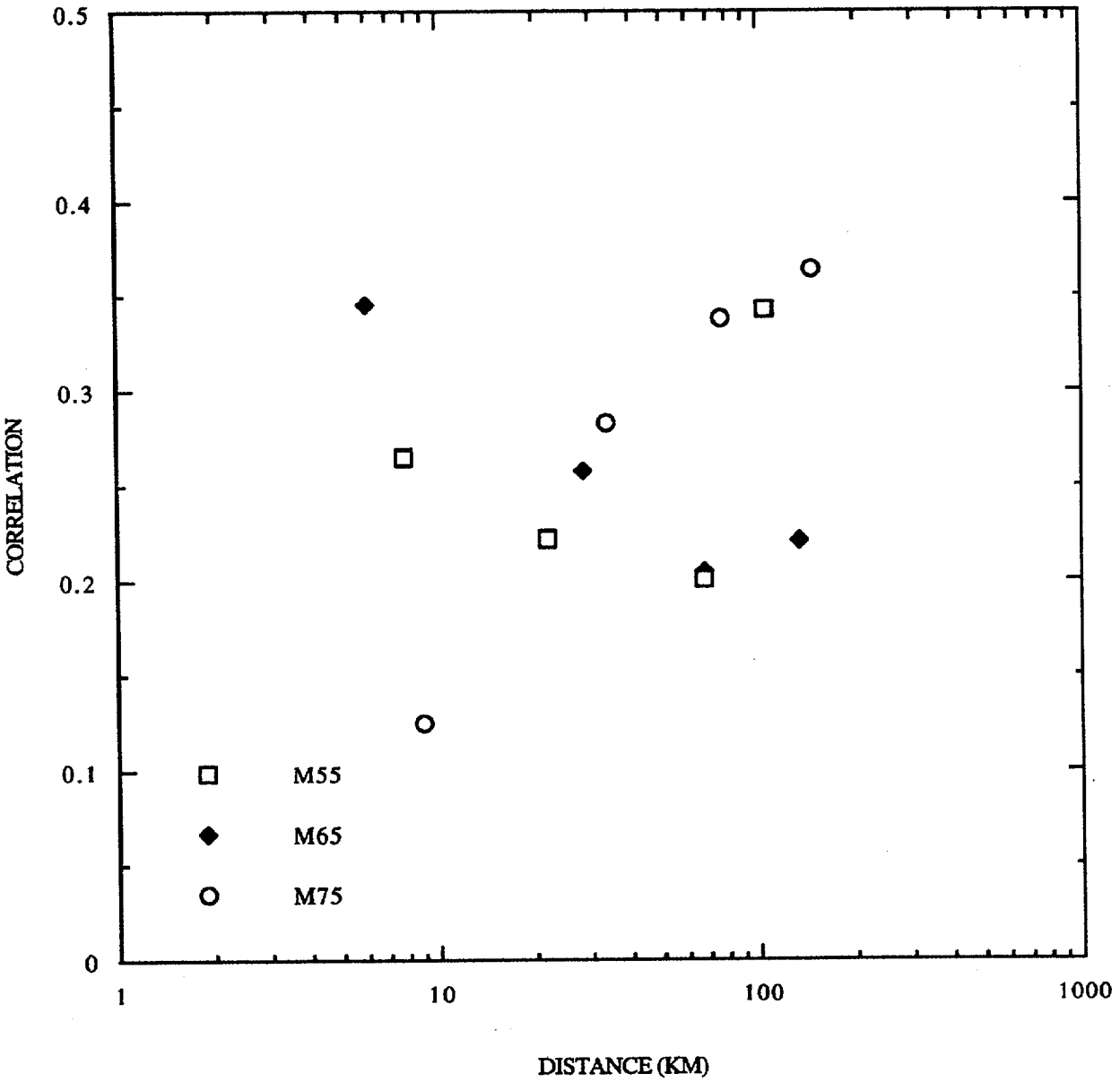

Figure F-26. Correlations of H1/H2 displacement pairs, WUS soil sites.

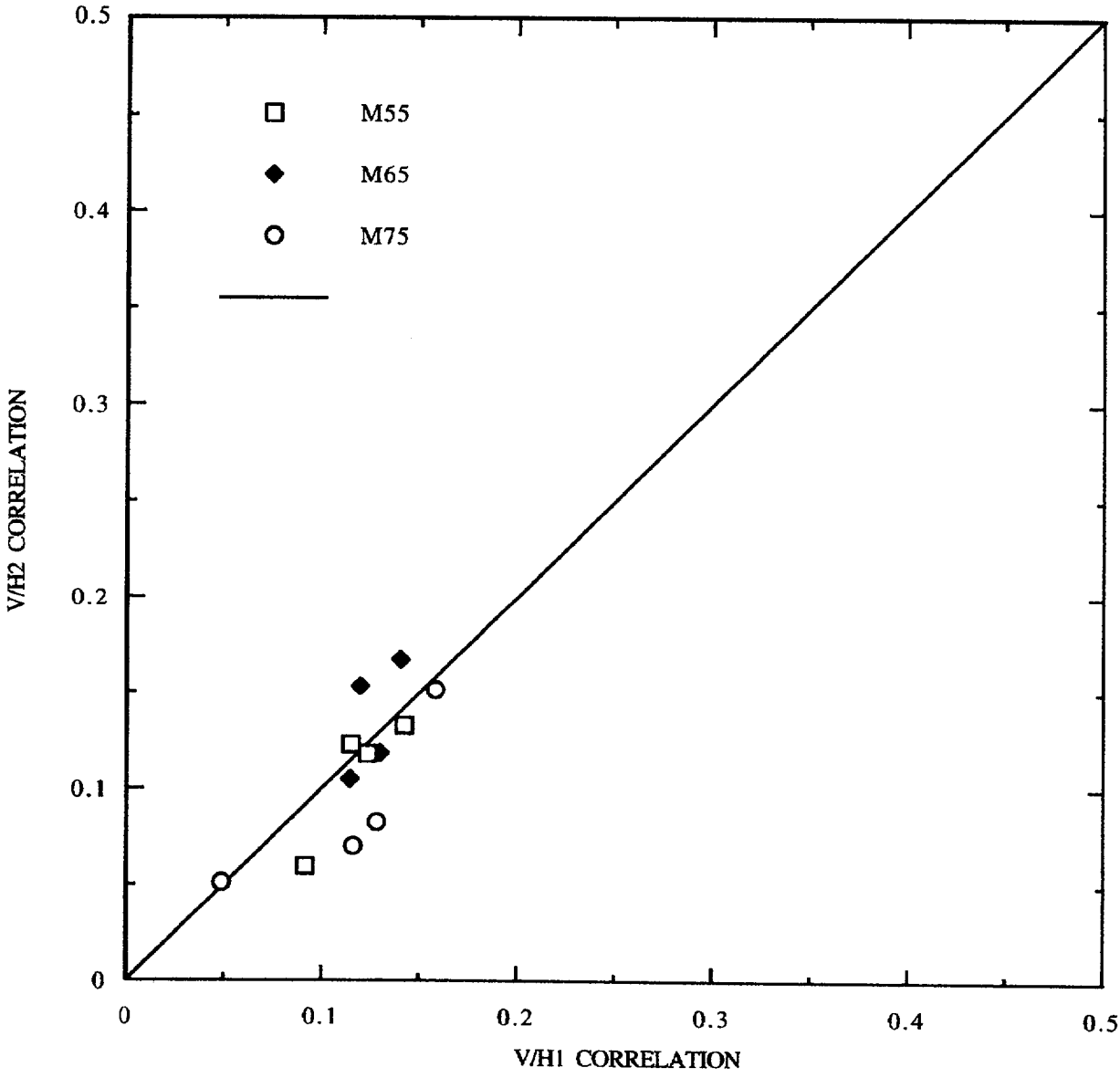

Figure F-27. Comparison of correlations of vertical/horizontal acceleration pairs at WUS rock sites.

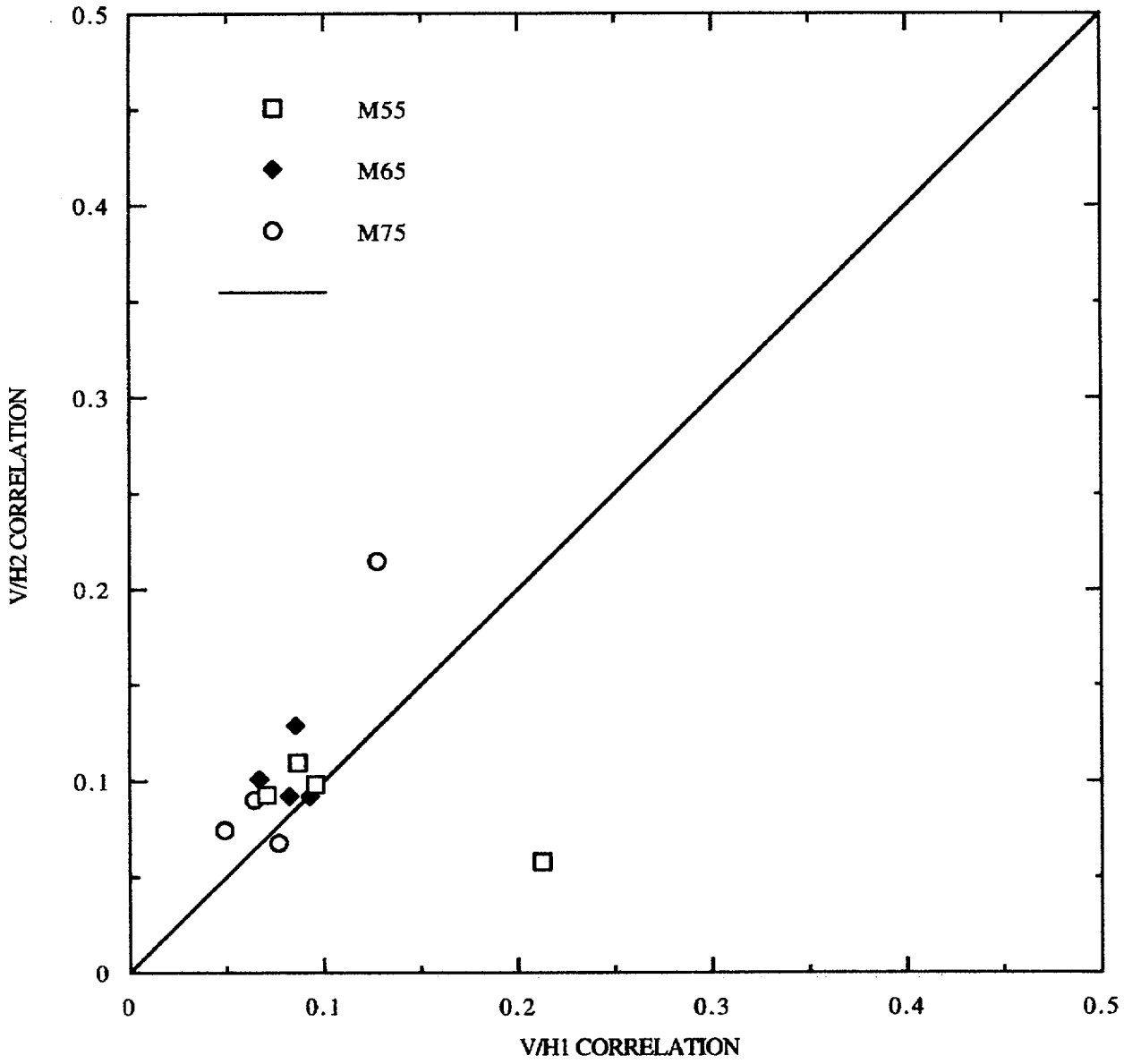

Figure F-28. Comparison of correlations of vertical/horizontal acceleration pairs at WUS soil sites.

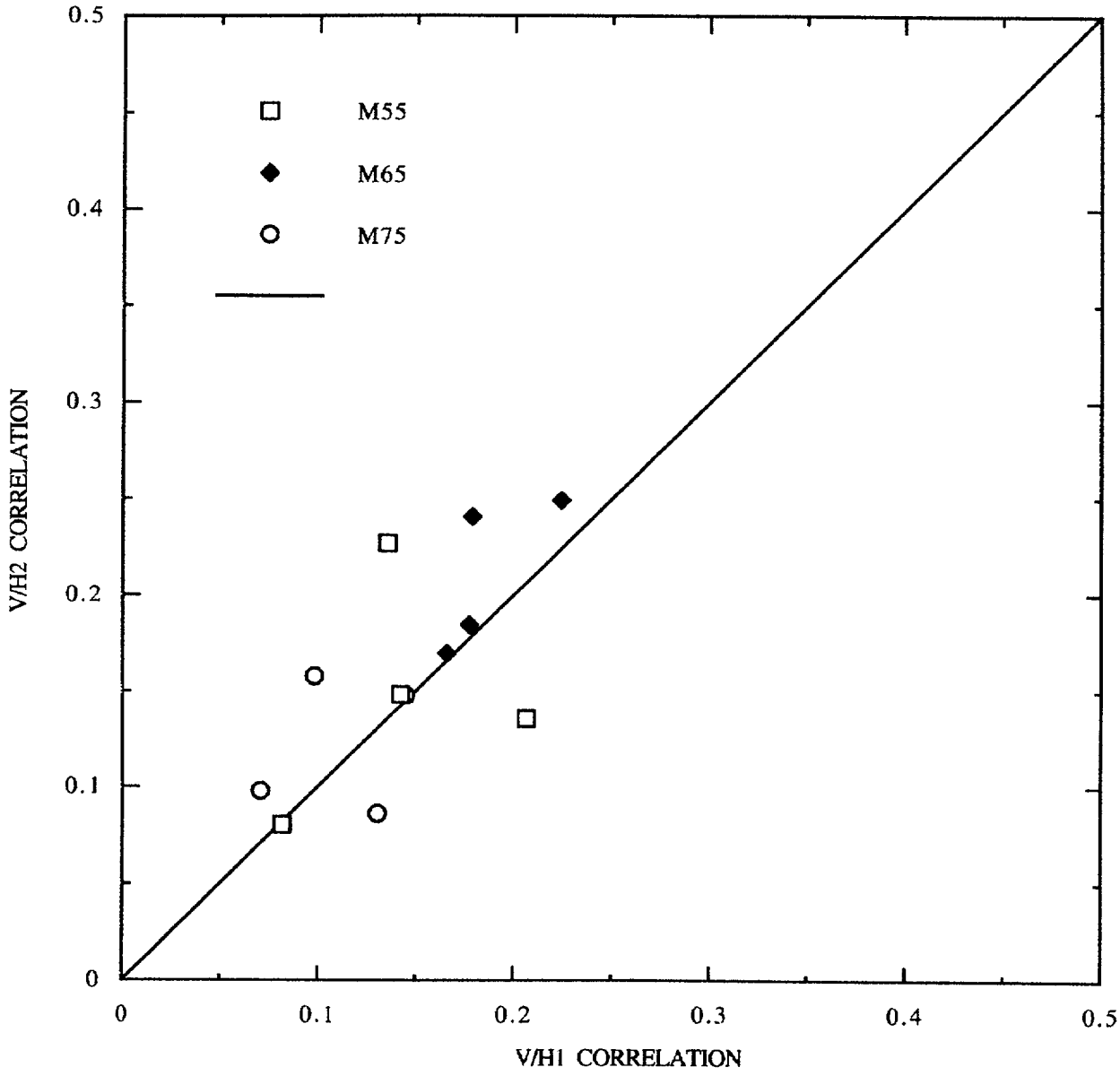

Figure F-29. Comparison of correlations of vertical/horizontal velocity pairs at WUS rock sites.

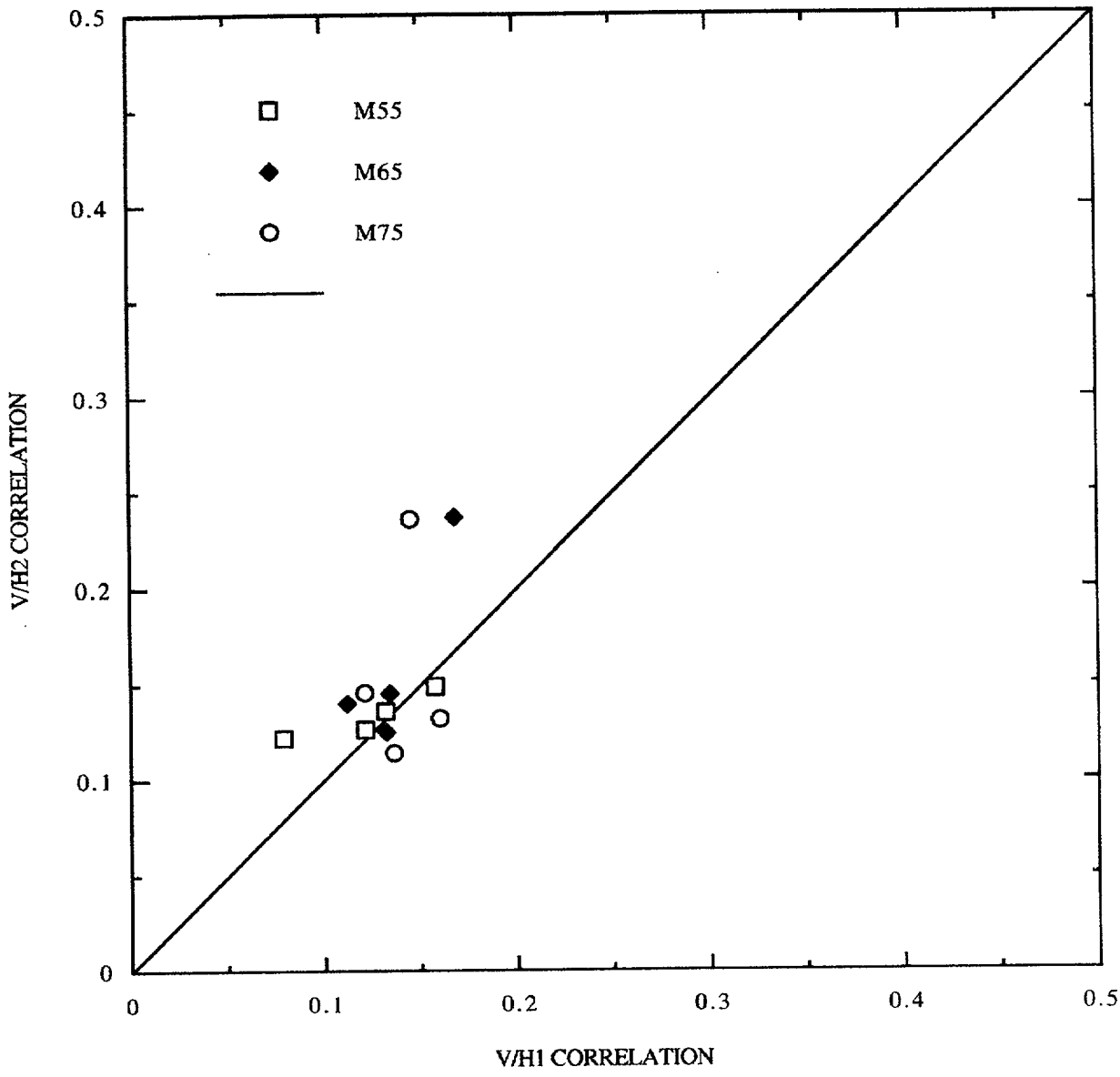

Figure F-30. Comparison of correlations of vertical/horizontal velocity pairs at WUS soil sites.

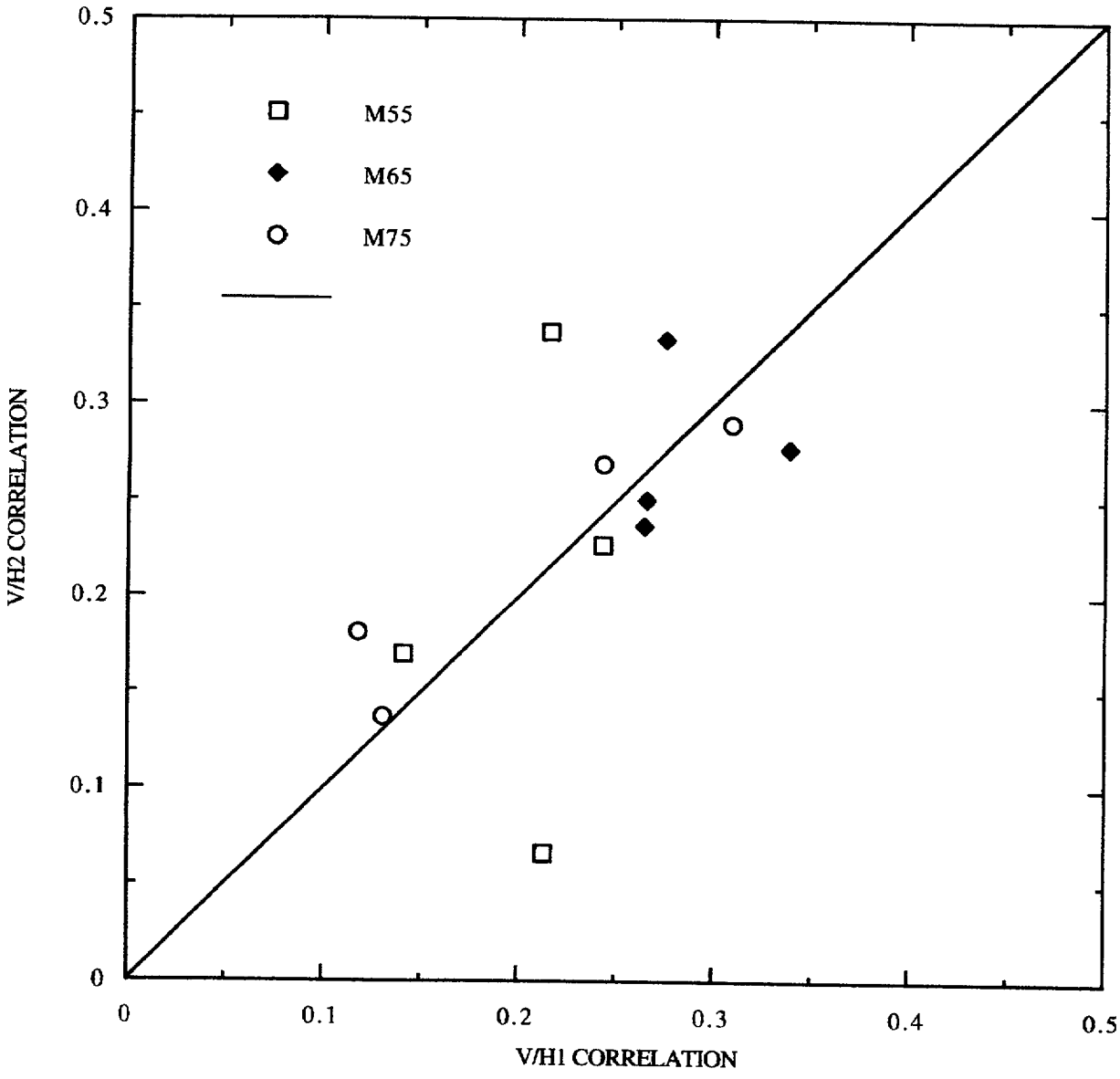

Figure F-31. Comparison of correlations of vertical/horizontal displacement pairs at WUS rock sites.

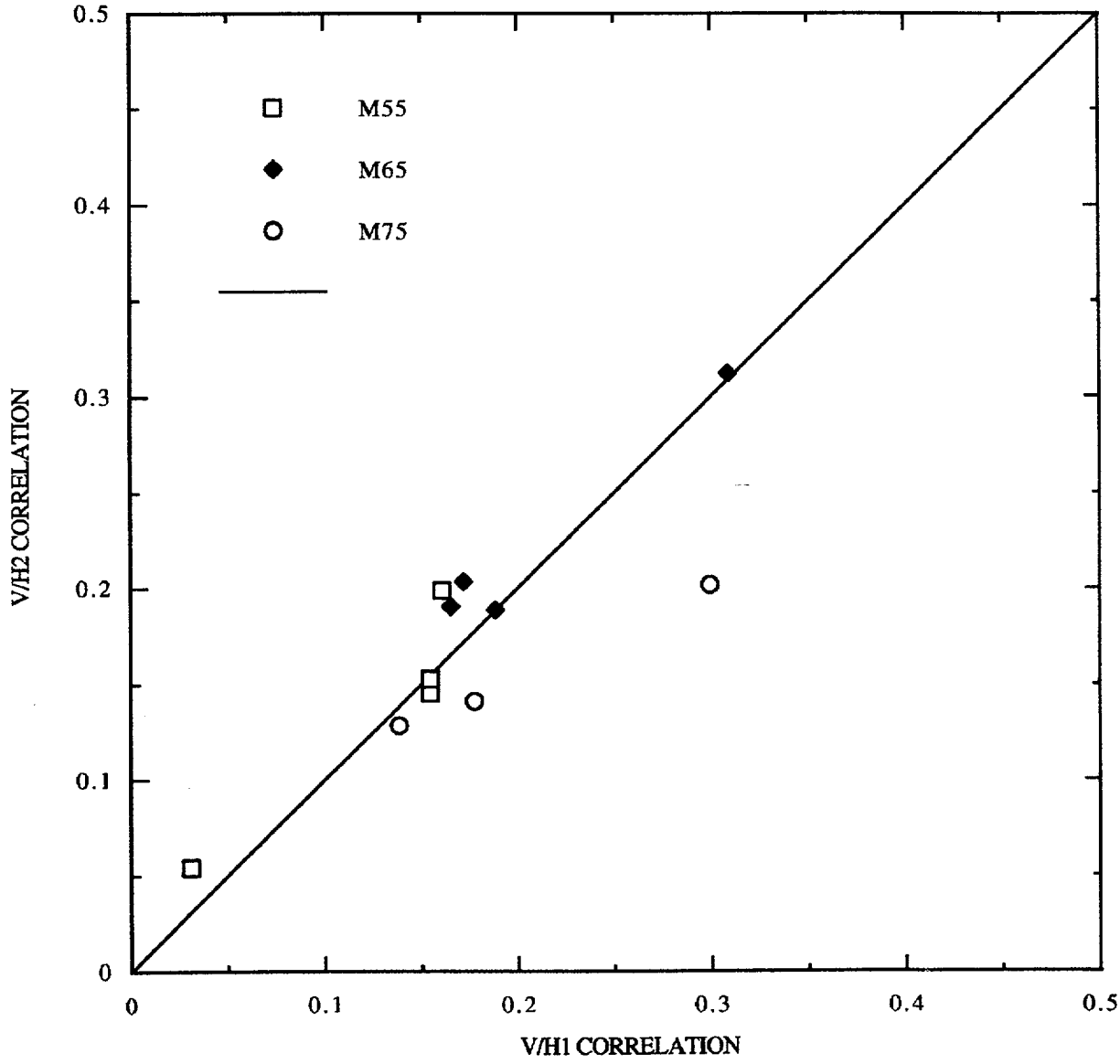

Figure F-32. Comparison of correlations of vertical/horizontal displacement pairs at WUS soil sites.

APPENDIX G PLOTS OF ARIAS INTENSITY AND CUMULATIVE ABSOLUTE VELOCITY FROM WUS RECORDS

Notation: R55H
S55V

R	Rock Site
S	Soil Site
M55	Magnitude Bin 5 - 6
H	Horizontal records
V	Vertical records

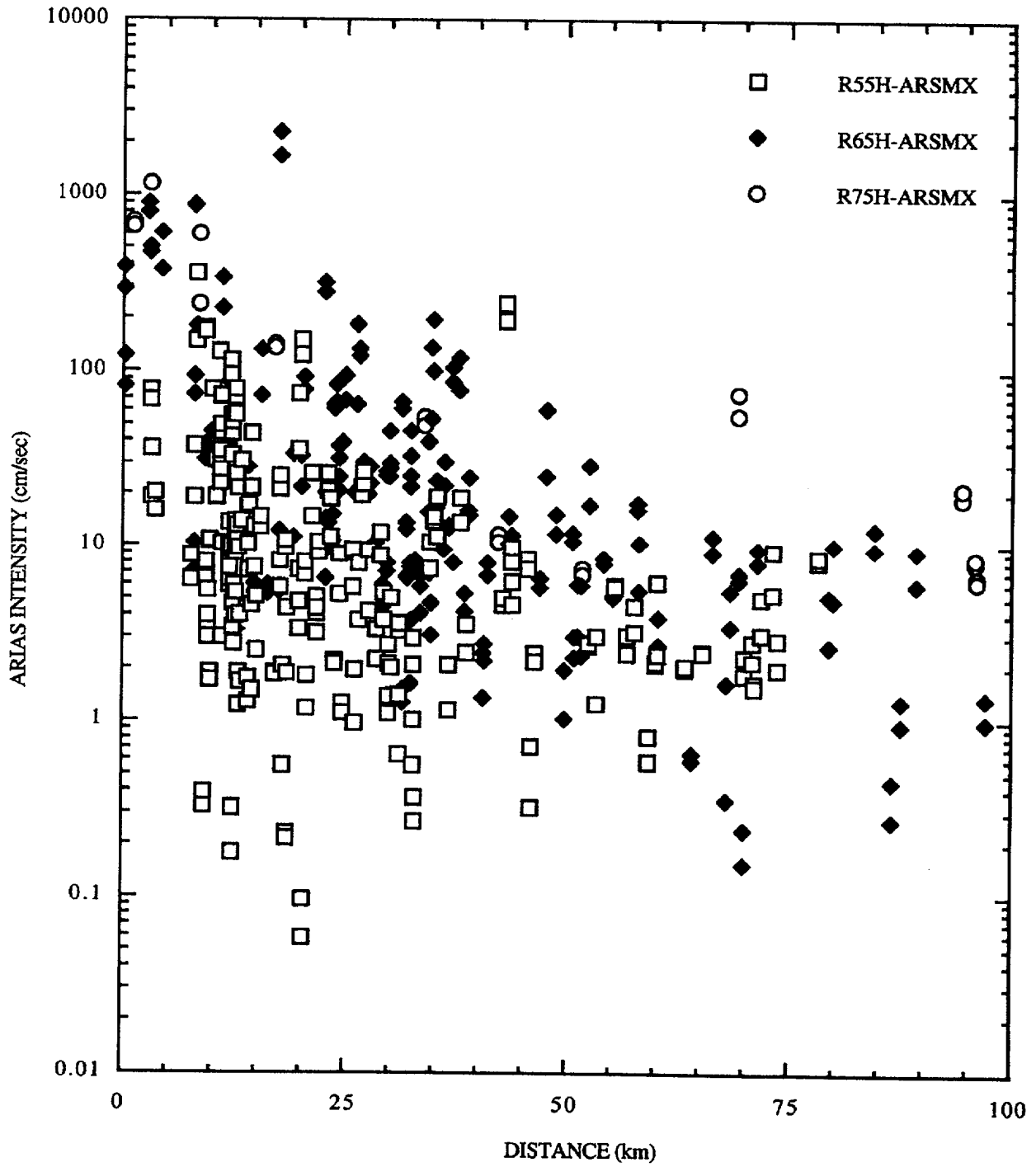

Figure G-1. Arias intensity, WUS horizontal motions, rock sites.

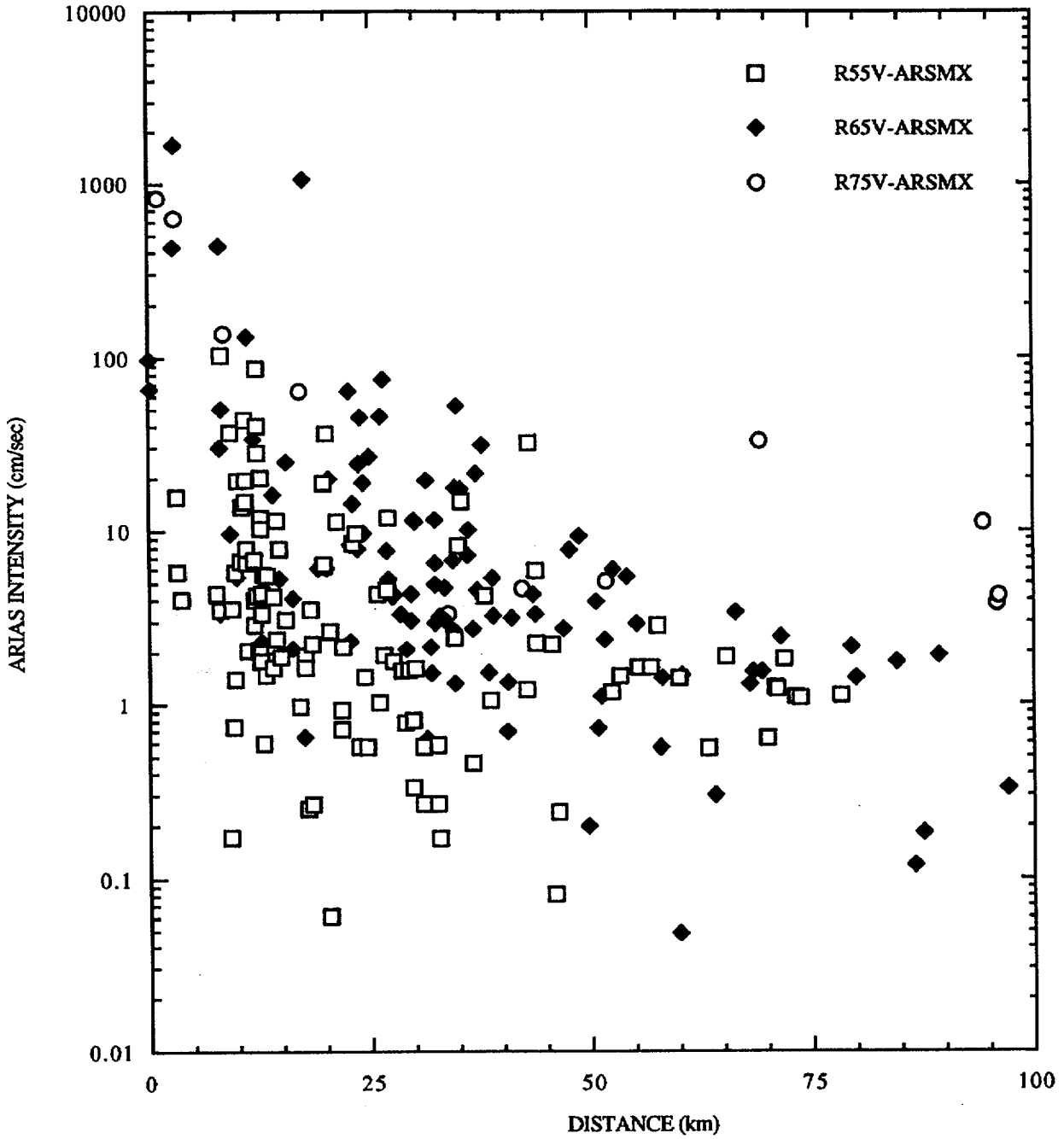

Figure G-2. Arias intensity, WUS vertical motions, rock sites.

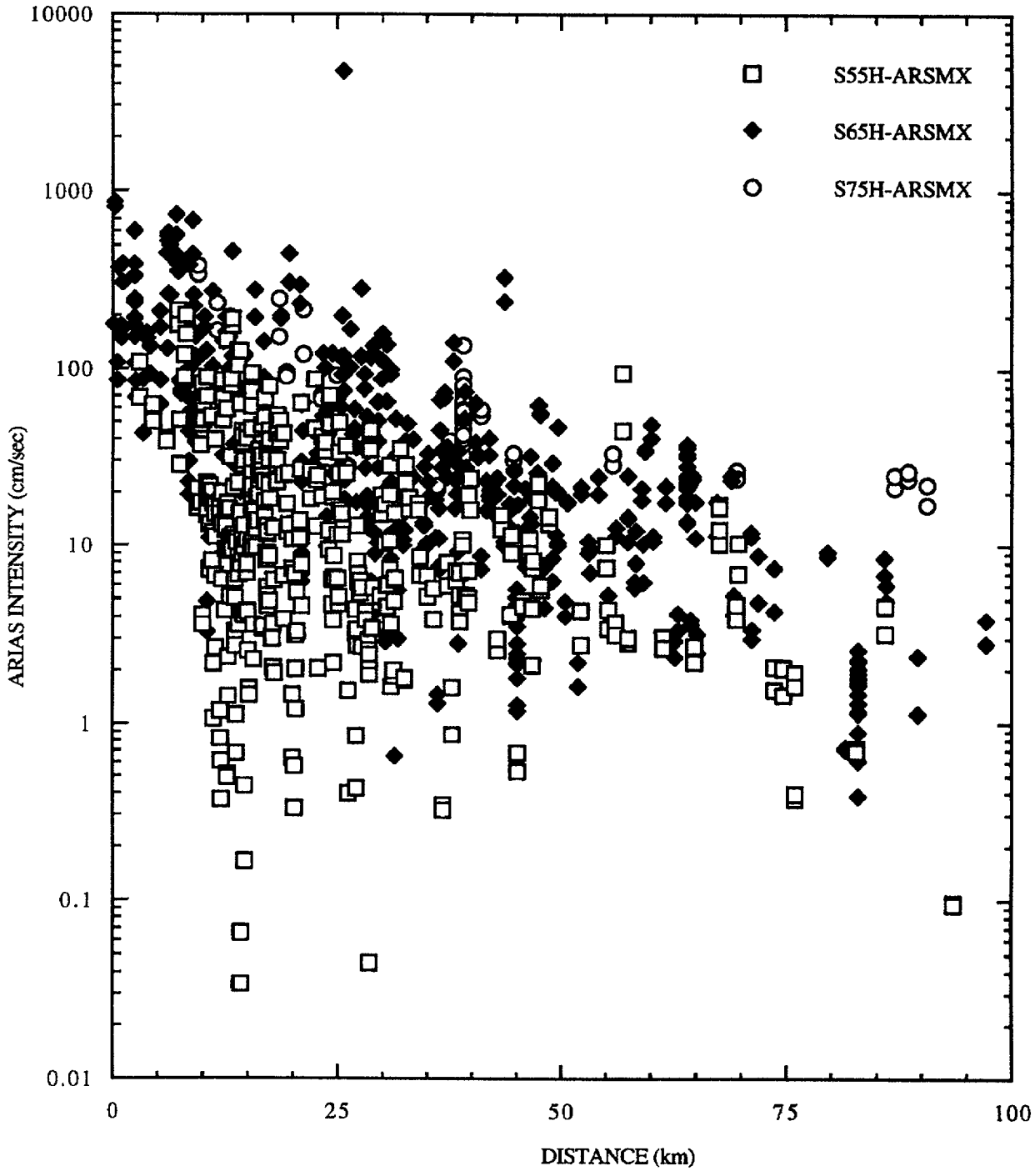

Figure G-3. Arias intensity, WUS horizontal motions, soil sites.

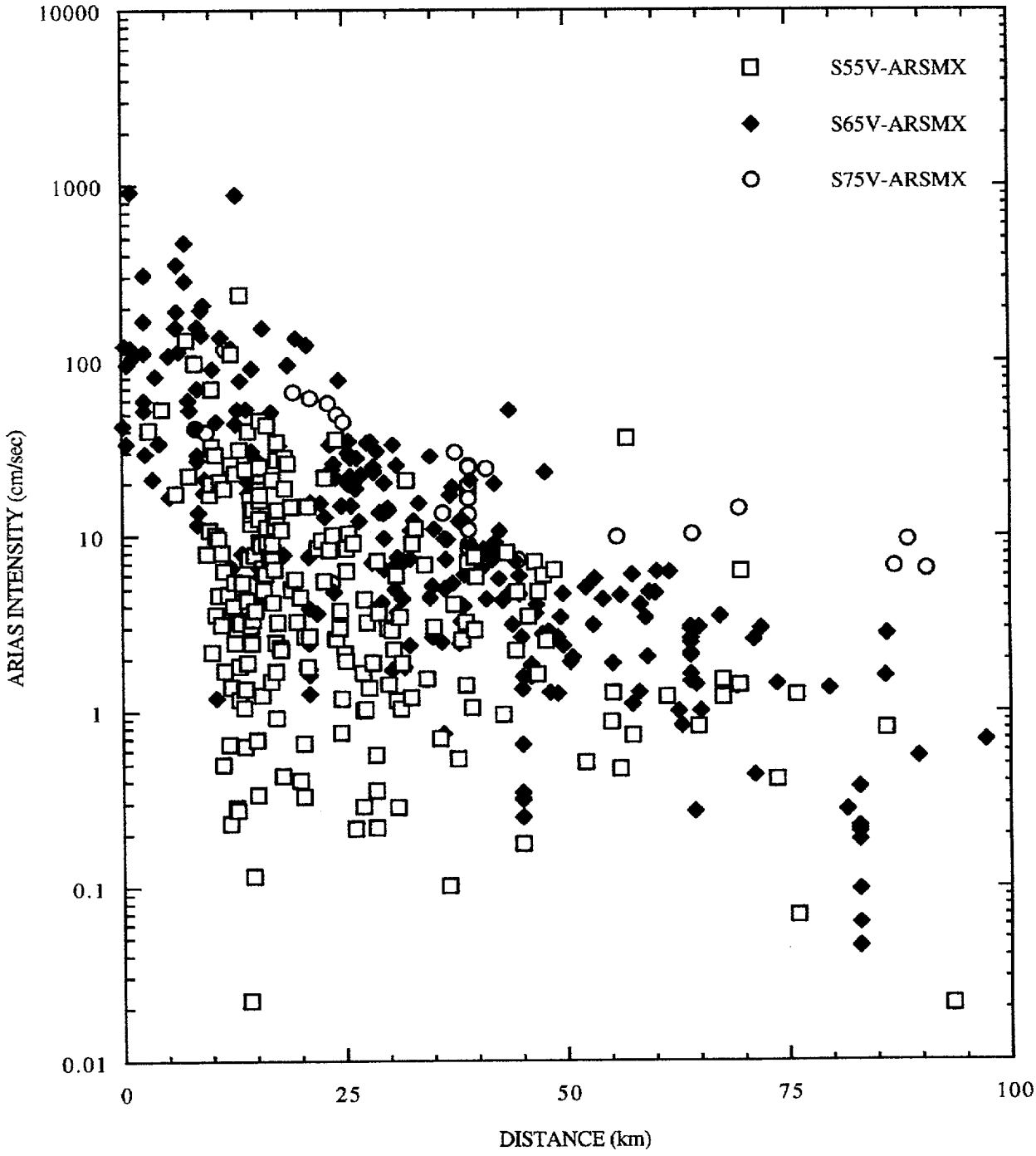

Figure G-4. Arias intensity, WUS vertical motions, soil sites.

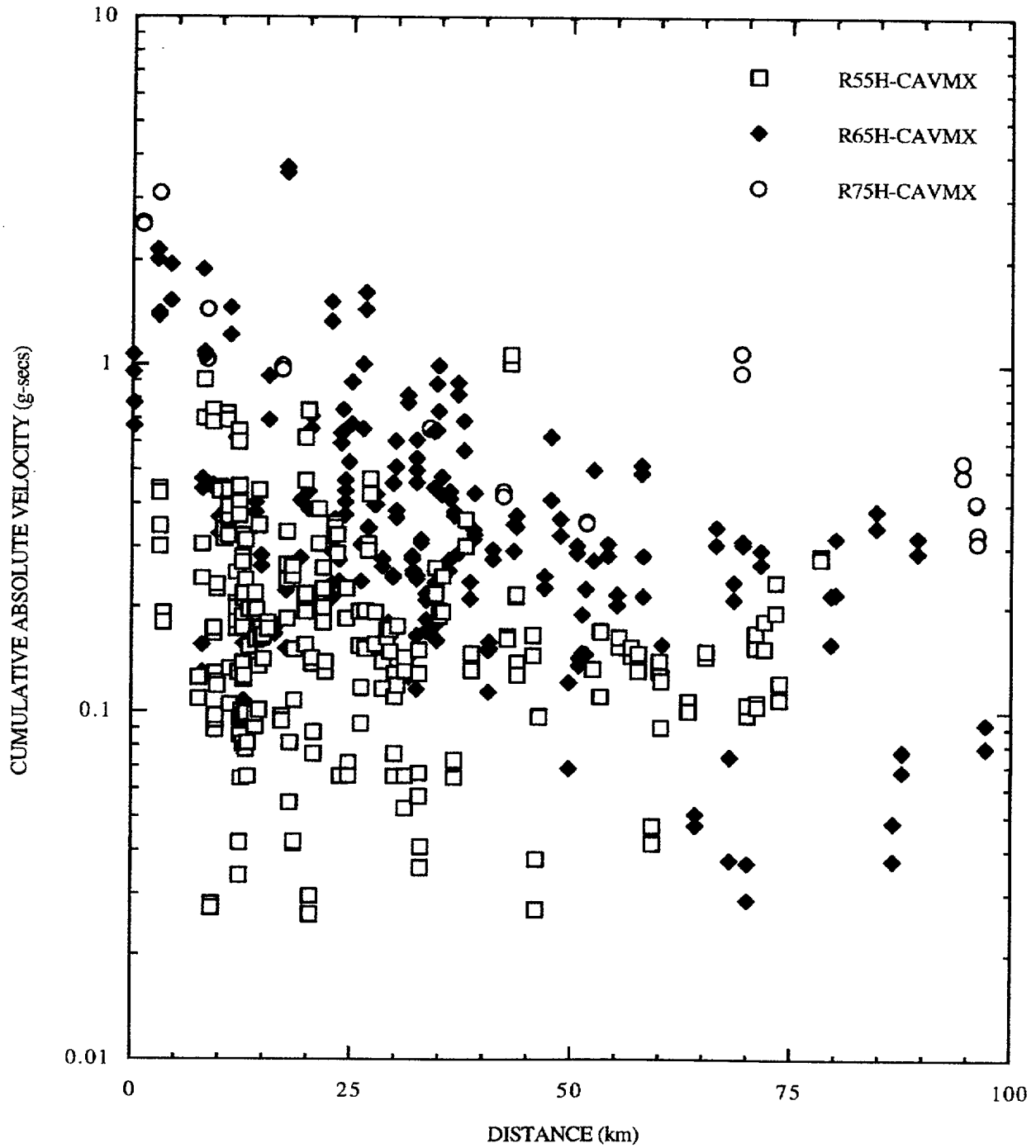

Figure G-5. CAV, WUS horizontal motions, rock sites.

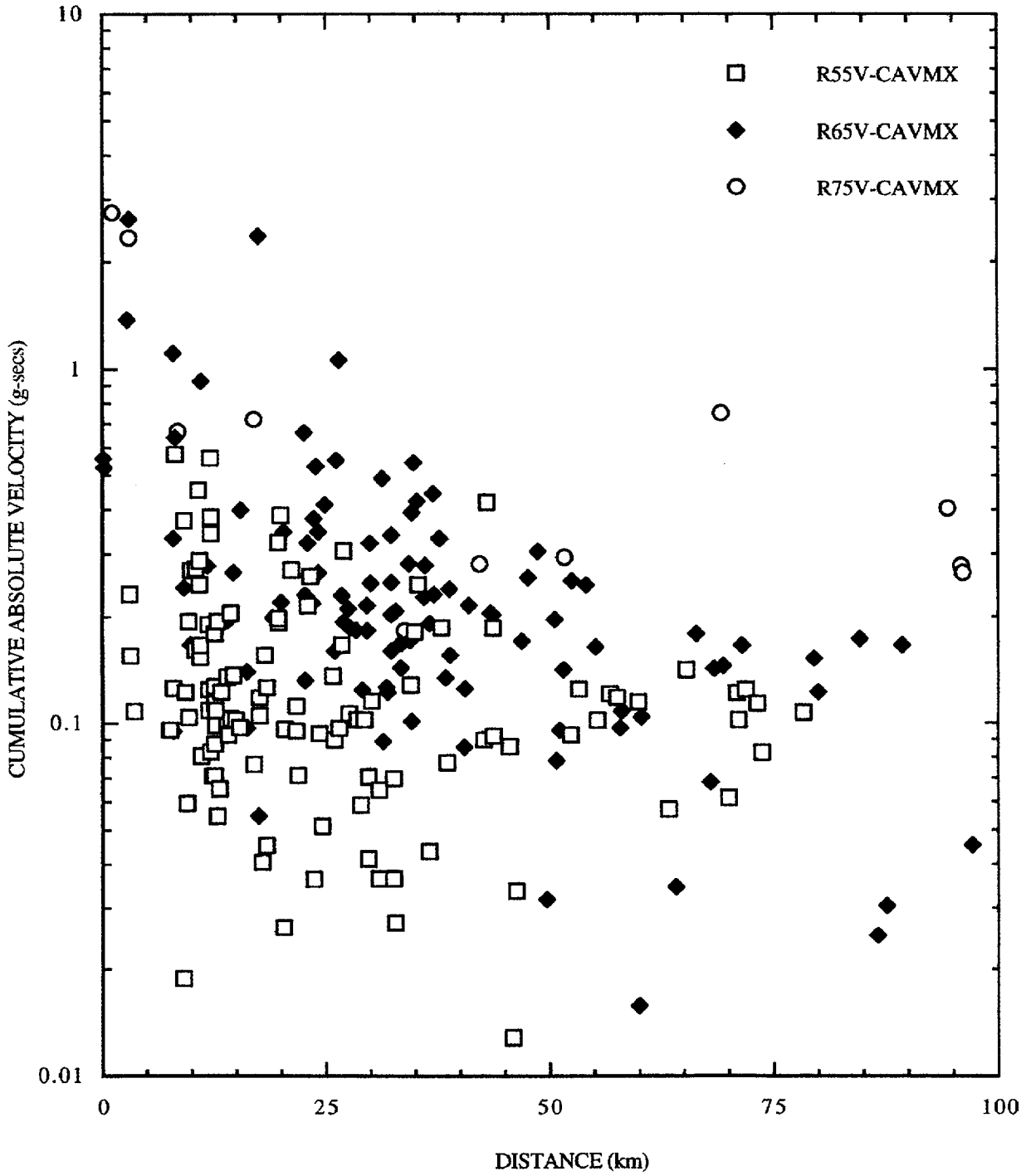

Figure G-6. CAV, WUS vertical motions, rock sites.

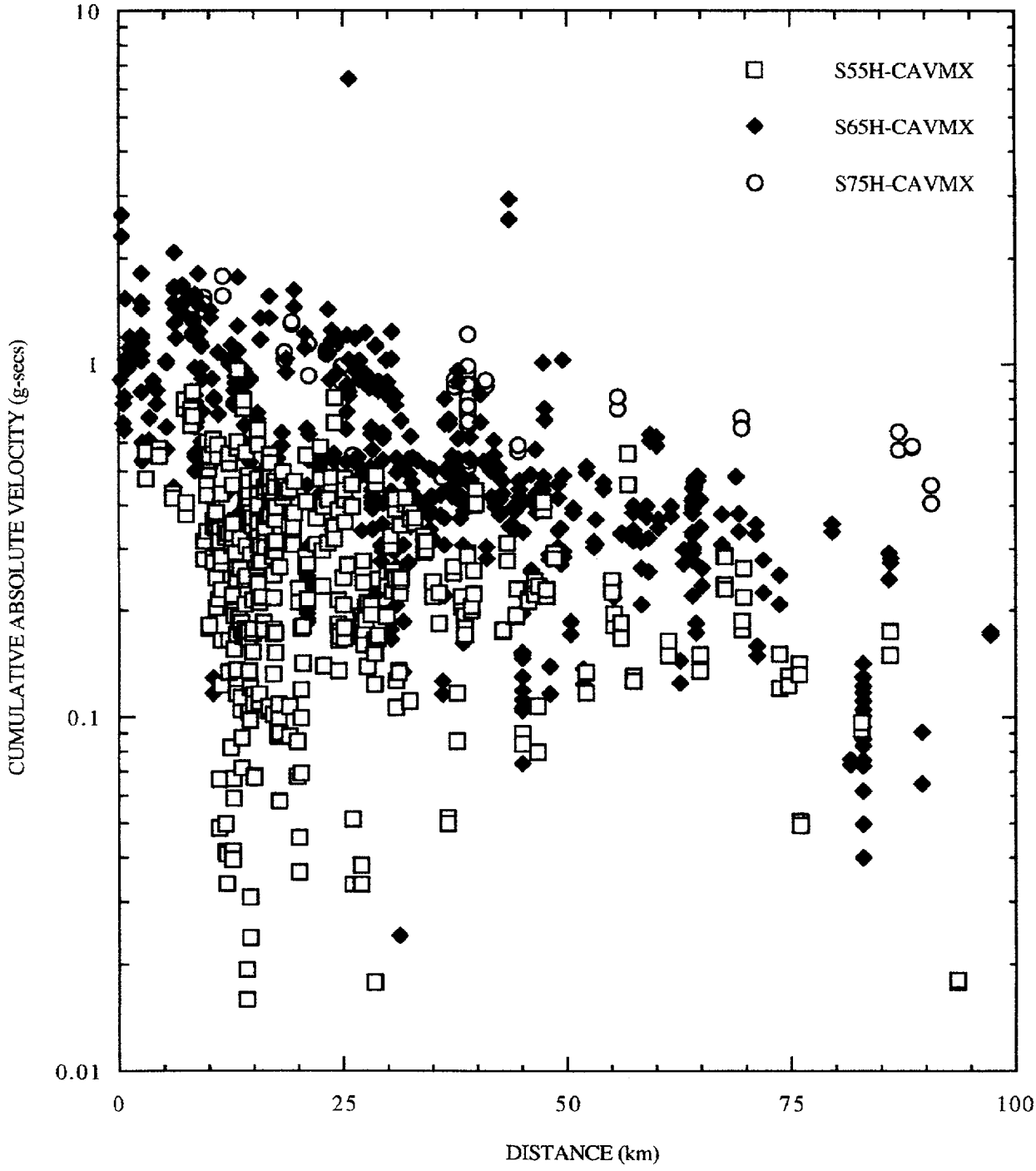

Figure G-7. CAV, WUS horizontal motions, soil sites.

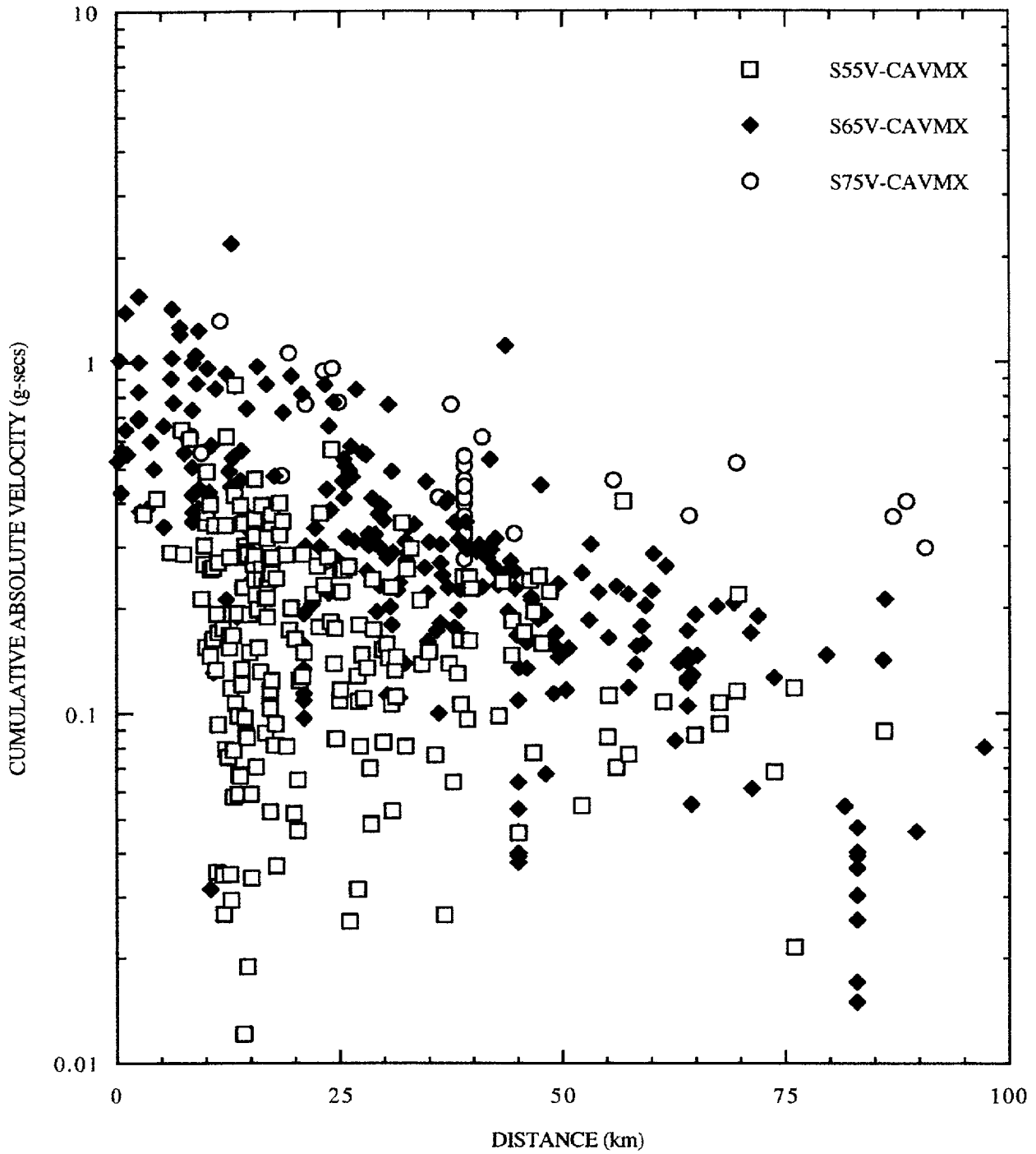

Figure G-8. CAV, WUS vertical motions, soil sites.

APPENDIX H DURATION RELATIONS FOR WUS STRONG GROUND MOTION (MODIFIED FROM ABRAHAMSON AND SILVA, 1997)

H.1 Introduction

Although the duration is an important characteristics of strong ground motion, there has been much less effort for developing empirical models of duration than there has been for developing empirical models of response spectra attenuation relations. Part of the difficulty has been that there are several different definitions of duration that have been used in previous studies. As a result, while duration is well understood in a qualitative sense, there is a wide range of quantitative duration estimates for the same set of recordings.

The definition of duration used here is based on the normalized Arias intensity of acceleration because this is the measure of duration that is most appropriate for the RVT models. The normalized Arias intensity is defined as

$$I(t) = \frac{\int_0^t a^2(\tau)\,d\tau}{\int_0^\infty a^2(\tau)\,d\tau} \qquad \text{(H-1)}$$

where $a(\tau)$ is the acceleration time history and the normalized intensity, I(t), ranges from 0 to 1. The duration is defined as the time history interval between which I(t) reaches two values. That is, given I(t), we then develop the inverse relation for t(I). The duration, $T_{I1\text{-}I2}$, is given by

$$T_{I1\text{-}I2} = t(I_2) - t(I_1) \qquad \text{(H-2)}$$

For example, if I_1=0.05 and I_2=0.75, then $D_{I1\text{-}I2}$ is the duration of the 5-75% normalized Arias intensity.

H.2 Approach

A two-step approach is used to develop the empirical model for duration. In the first step, a model is developed describing the magnitude, distance, and site dependence of duration for the 5-75% normalized Arias intensity ($T_{5\text{-}75}$). In the second step, a model is developed describing the ratio of the duration at other normalized Arias intensity levels (e.g. 5-95%) relative to the 5-75% duration. Together, these two models provide a description of the magnitude, distance, and site dependence of the duration for a range of normalized Arias intensities.

$T_{5\text{-}75}$ Model

In the first step, the model is developed for $T_{5\text{-}75}$. Previous studies have found that at short distances on rock sites, $T_{5\text{-}75}$ is similar to the source duration, which is approximately by $1/f_c$, where f_c is the corner frequency of the earthquake. That is, for short distances at rock sites:

$$T_{5\text{-}75} = \frac{1}{f_c(M_o,\Delta\sigma)} \tag{H-3}$$

where

$$f_c(M_o,\Delta\sigma) = 4.9 \quad 10^6 \beta \left(\frac{\Delta\sigma}{M_o}\right)^{1/3} \tag{H-4}$$

and β is the shear wave velocity at the source (in km / s), $\Delta\sigma$ is the stress drop (in bars), and M_o is the moment (in dyne-cm).

At larger distances, the duration increases due to complexities in wave propagation (scattering and 3-D effects). At soil sites, the duration is typically larger than at rock sites. The distance dependence and site dependence are considered to be additive to the source duration. This leads to a model of the form:

$$T_{5\text{-}75} = \frac{1}{f_c(M_o,\Delta\sigma)} + t_1(r) + t_2(S,r) \tag{H-5}$$

where $t_1(r)$ is the distance dependence on rock and $t_2(S, r)$ is a site dependence that allows for coupling of the site and distance dependence.

The magnitude dependence of the duration is determined by the magnitude dependence of the corner frequency, f_c , which in turn is determined by the magnitude dependence of the moment and stress-drop. The moment is related to magnitude by

$$\log_{10} M_o = 1.5\,M + 16.05 \tag{H-6}$$

The magnitude dependence of the stress drop is estimated as part of the regression analysis.

Previous studies have found that the distance dependence of duration on rock, $f_1(r)$, is approximately proportional to distance. The distance dependence of $T_{5\text{-}75}$ is shown in Figures H-1a and H-1b for the horizontal component and in Figures H-2a and H-2b for the vertical component. These data also indicate that the duration increases approximately linearly with distance at large distances. At short distances the duration is approximately independent of distance. This leads to a piecewise continuous form for $t_1(r)$:

$$t_1(r) = \begin{cases} 0 & for\ r \le r_c \\ d_2(r-r_c) & for\ r > r_c \end{cases} \tag{H-7}$$

where r_c is a cutoff distance determined by the regression analysis.

For the site dependence, t_2 (S, r), a constant is used for short distances. A distance dependence of the site effect is also considered, leading to the following model:

$$t_2(r) = \begin{cases} d_1 S & for\ r \le r_c \\ \{d_1 + d_3(r - r_c)\}S & for\ r > r_c \end{cases} \qquad \text{(H-8)}$$

where S is the site term coefficient and is equal to zero for rock sites and 1 for soil sites. In preliminary evaluations the regression analyses were performed with and without the d_3 term. The d_3 term did not significantly improve the fit so this term was not used further. Also, the distribution of observed residuals was positively skewed (Figure H-3a-b). The hypothesis that the duration residuals are normally distributed can be rejected with greater than 95% confidence. The skewed distribution of residuals is consistent with a lognormal distribution.

The resulting model for mean log duration is

$$Ln\ (T_{5\text{-}75}) = Ln \left[\frac{\left(\dfrac{\Delta\sigma(M)}{10^{1.5M+16.05}} \right)^{-1/3}}{4.9\ 10^6 \beta} + Sd_1 + d_2(r - r_c) \right] for\ r \ge r_c \qquad \text{(H-9a)}$$

and

$$Ln\ (T_{5\text{-}75}) = Ln \left[\frac{\left(\dfrac{\Delta\sigma(M)}{10^{1.5M+16.05}} \right)^{-1/3}}{4.9\ 10^6 \beta} + Sd_1 \right] for\ r < r_c \qquad \text{(H-9b)}$$

In the regression analysis, β was fixed at 3.2 km/s.

In the initial regression, the stress drop term (Eq. H-9a, H-9b) was treated as a constant for all magnitudes. The r_c term was not well resolved by the data and ranged from 5 to 15 km, so it's value was set at 10 km. The remaining coefficients estimated from the initial regression are listed in Table H-1. The distributions of the residuals shown in Figures H-4a and H-4b indicate that a lognormal distribution is appropriate; the hypothesis that the duration residuals are lognormally distributed cannot be rejected with 40% confidence.

It is important to note that the "duration" stress drop given in Table H-1 is a ground motion parameter with units of bars that lead to the appropriate duration under the assumption that the 5-75% normalized Arias intensity is given by a source duration equal to $1/f_c$. It is by definition different from the static stress drop or RMS stress drop.

When fixing other coefficients fixed to their values from Table I-1; the value of $\Delta\sigma$ varies with magnitude. The estimated stress drop for the individual magnitude bins are shown in Figures H-5a and H-5b, for horizontal and vertical components respectively. The standard errors of the mean estimates are also shown. An exponential form of the magnitude dependence of $\Delta\sigma$ was selected because it is consistent with the trend in the estimates shown in Figures H-5a and H-5b and because it is consistent with the exponential magnitude dependence of seismic moment. (For short distances on rock, the magnitude dependence of the log duration reduces to a linear function in magnitude if an exponential magnitude dependence of $\Delta\sigma$ is used.) The magnitude dependence of $\Delta\sigma$ is modeled by

$$\Delta\sigma(M) = \exp\{b_1 + b_2(M-6)\} \qquad \text{(H-10)}$$

Substituting this form for $\Delta\sigma$(M) in Eq (H-9), the regression analysis was repeated holding the remaining coefficients fixed to their values from the initial regression (from Table H-1). The estimates of the coefficients are listed in Table H-2. The solid curves in Figures H-5a and H-5b show the resulting model for duration stress drop. The magnitude dependence of $\Delta\sigma$ found here (increasing duration stress drop with increasing magnitude) indicates that the magnitude dependence of the duration is weaker than implied by constant stress drop scaling.

The residuals were computed for separate, unit magnitude bins to evaluate the fit. The residuals for the horizontal and vertical duration ($T_{5\text{-}75}$) are shown as a function of distance in Figures H-6a and H-7a, for M6.5-7.0. (Data for other magnitude ranges are similar.)

The resulting magnitude and distance dependence of the model for the 5-75% duration is shown in Figures H-8a through H-8d.

Duration for Other Ranges

The second part of the duration regression evaluates the shape of the normalized Arias intensity so that the duration at the other ranges can be estimated. For each record, the duration values were normalized by the $T_{5\text{-}75}$ value for that record. The mean normalized durations for the average horizontal component are shown in Figures H-9 and H-10 for different distance ranges (given $6.5 < M < 7.0$) and magnitude ranges (given $30 < R < 60$), respectively. Curves for other magnitudes, distances, and vertical components are similar. The normalized duration does not show a significant systematic dependence on either magnitude or distance, so a magnitude- and distance- independent functional form is used. Several alternative forms were evaluated and the following power relations was found to provide a good fit to the mean:

$$\ln\left(\frac{T_{5\text{-}I}}{T_{5\text{-}75}}\right) = e_1 + e_2 \ln\left(\frac{I-5}{1-.01I}\right) + e_3\left(\ln\left(\frac{I-5}{1-0.01I}\right)\right)^2 \qquad \text{(H-11)}$$

where I is the percentage of the normalized Arias intensity defining the duration. The coefficients were estimated using ordinary least-squares and are listed in Table H-3. The mean predicted relation is compared to the mean of the data in Figures H-12a and H-12b for the horizontal and vertical components, respectively.

H.3 Duration Model

Combining the two models, the resulting duration model is given by

$$Ln\ (T_{5\text{-}I}) = Ln\left[\frac{\left(\frac{\Delta\sigma(M)}{10^{1.5M+16.05}}\right)^{-1/3}}{4.9\ 10^{6}\beta} + Sd_1 + d_2(r - r_c)\right] + \ln\left(\frac{T_{5\text{-}I}}{T_{5\text{-}75}}\right) \qquad \text{(H-12a)}$$

for $r \geq r_c$ and by

$$Ln\ (T_{5\text{-}I}) = Ln\left[\frac{\left(\frac{\Delta\sigma(M)}{10^{1.5M+16.05}}\right)^{-1/3}}{4.9\ 10^{6}\beta} + Sd_1\right] + \ln\left(\frac{T_{5\text{-}I}}{T_{5\text{-}75}}\right) \qquad \text{(H-12b)}$$

for $r < r_c$.

The standard error is computed from this combined model to estimate the total standard error directly (not a combination of the standard error of the two parts of the model). The standard errors are plotted in Figure H-12 and are listed in Table H-4.

H.4 Model Predictions

The model predictions for the horizontal duration for a distance of 30 km are shown in Figure H-13 for rock and Figure H-14 for soil. Similar plots of the model predictions for the vertical component are shown in Figures H-15 and H-16.

References

Abrahamson, N.A. and W. J. Silva (1997), "Empirical ground motion models," Appendix in Silva et al. (1997).

Silva, W.J., N. Abrahamson, G. Toro, C. Costantino (1997). "Description and validation of the stochastic ground motion model." Report to Brookhaven National Laboratory, Associated Universities, Inc. Upton, New York, Contract 77053.

Table H-1
INITIAL REGRESSION ESTIMATES OF COEFFICIENTS
FOR $T_{5\text{-}75}$ USING $\Delta\sigma$ INDEPENDENT OF MAGNITUDE

Coefficient	Horizontal	Vertical
d_1	0.805 0.130	1.076 0.155
d_2	0.063 0.006	0.107 0.008
$\Delta\sigma$	230 34	152 23
r_c	10*	10*
β	3.2*	3.2*

* fixed values

Table H-2
REGRESSION ESTIMATES OF COEFFICIENTS
FOR $T_{5\text{-}75}$ USING MAGNITUDE DEPENDENT $\Delta\sigma$

Coefficient	Horizontal	Vertical
d_1	0.805*	1.076*
d_2	0.063*	0.107*
b_1	5.204 0.105	4.61**
b_2	0.851 0.146	1.536**
r_c	10*	10*
β	3.2*	3.2*
Standard Error	0.55	0.46

* fixed values
**standard deviations not reported

Table H-3
REGRESSION ESTIMATES FOR THE NORMALIZED DURATION

Coefficient	Horizontal	Vertical
e_1	-0.532 0.005	-0.466 0.009
e_2	0.552 0.002	0.540 0.005
e_3	-0.0262 0.0013	-0.0537 0.0026

Table H-4
STANDARD ERROR FOR DURATION (EQ. H-12a,b)

I	Horizontal	Vertical
10%	0.843	0.915
15%	0.759	0.841
20%	0.713	0.788
25%	0.691	0.742
30%	0.674	0.703
35%	0.660	0.666
40%	0.646	0.630
45%	0.636	0.609
50%	0.628	0.583
55%	0.616	0.555
60%	0.605	0.535
65%	0.594	0.519
70%	0.582	0.500
75%	0.565	0.478
80%	0.545	0.462
90%	0.510	0.443
95%	0.493	0.449

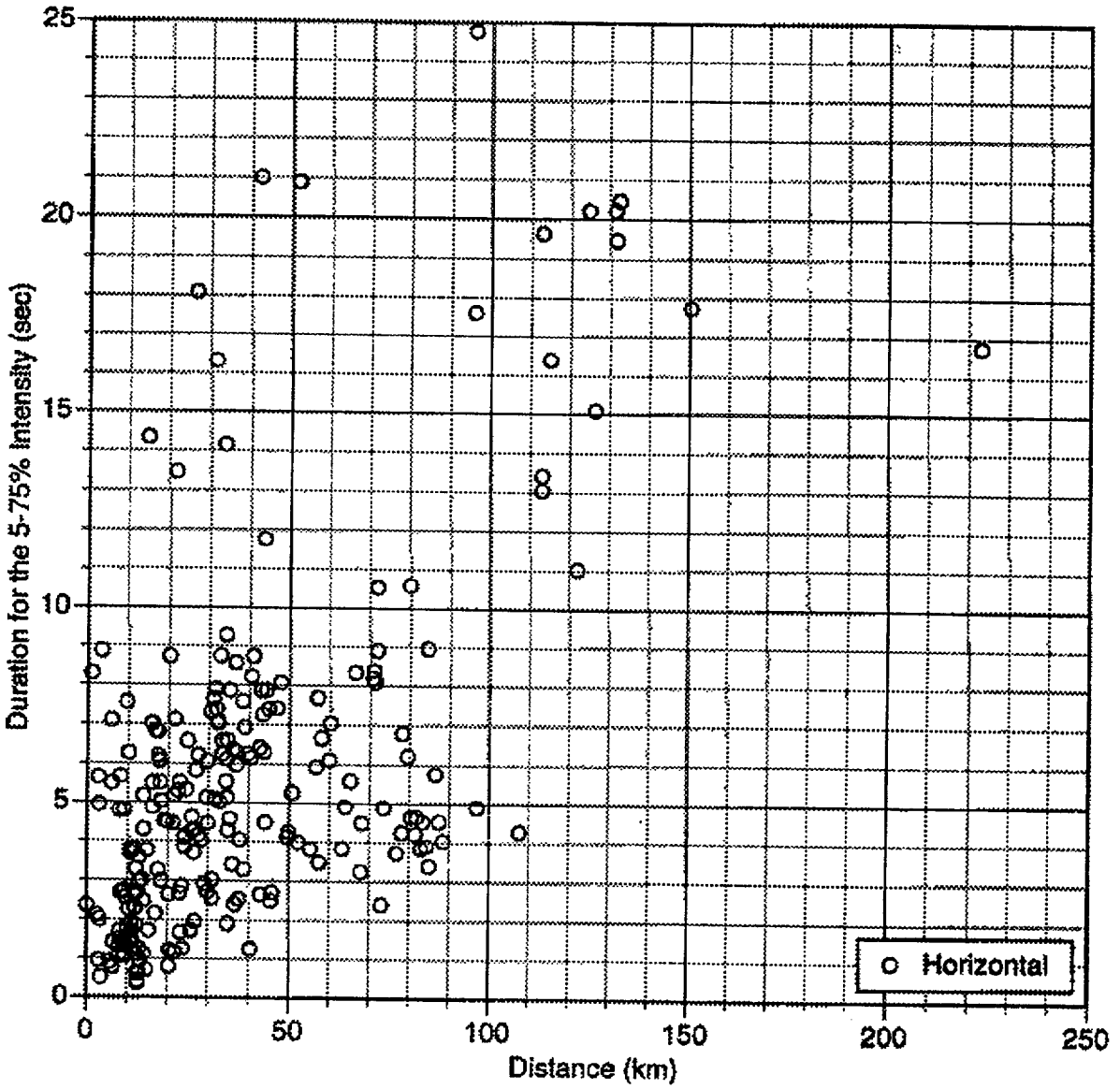

Figure H-1a. Distance dependence of the horizontal duration for the 5-75% intensity for rock site conditions.

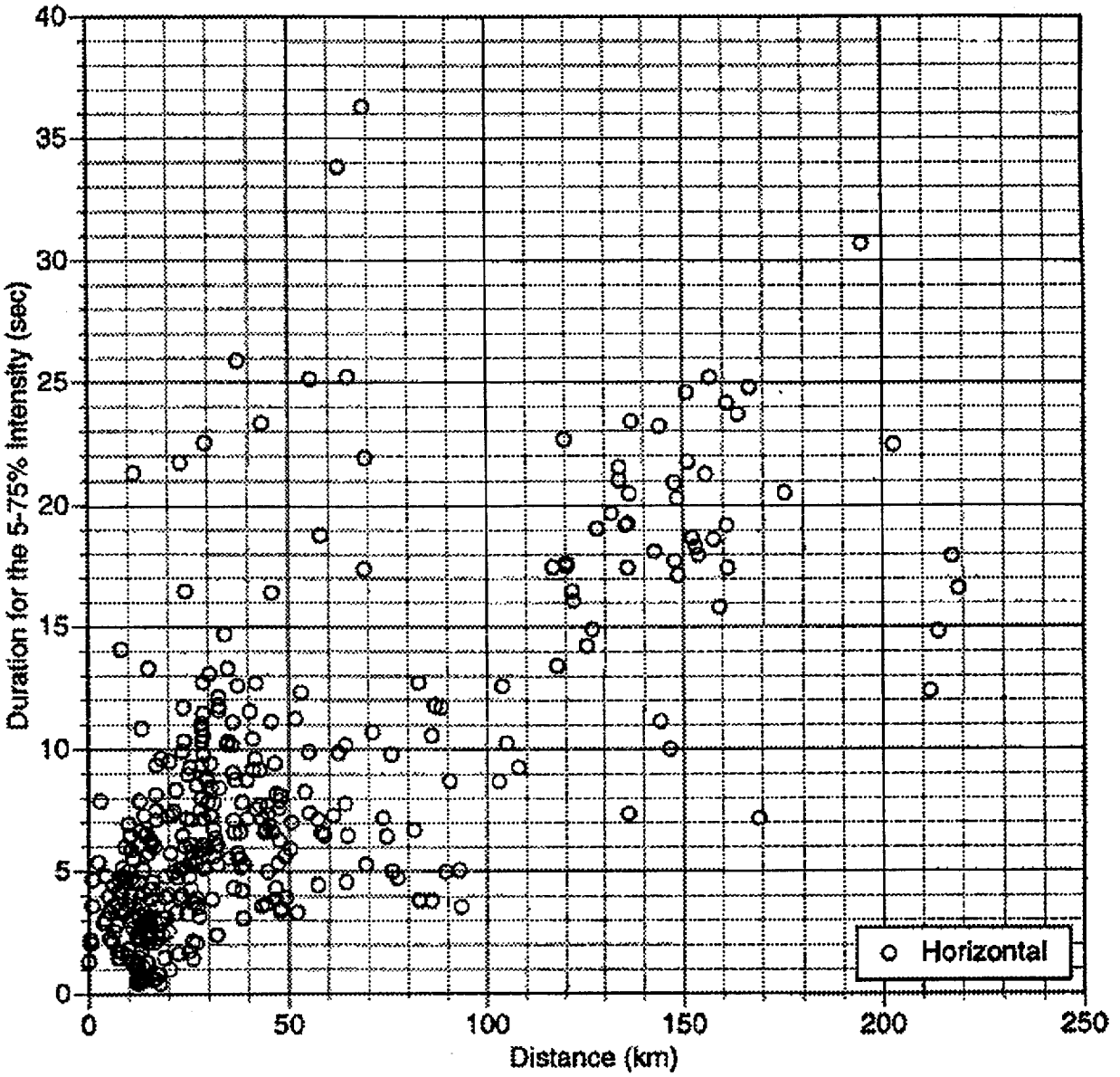

Figure H-1b. Distance dependence of the horizontal duration for the 5-75% intensity for soil site conditions.

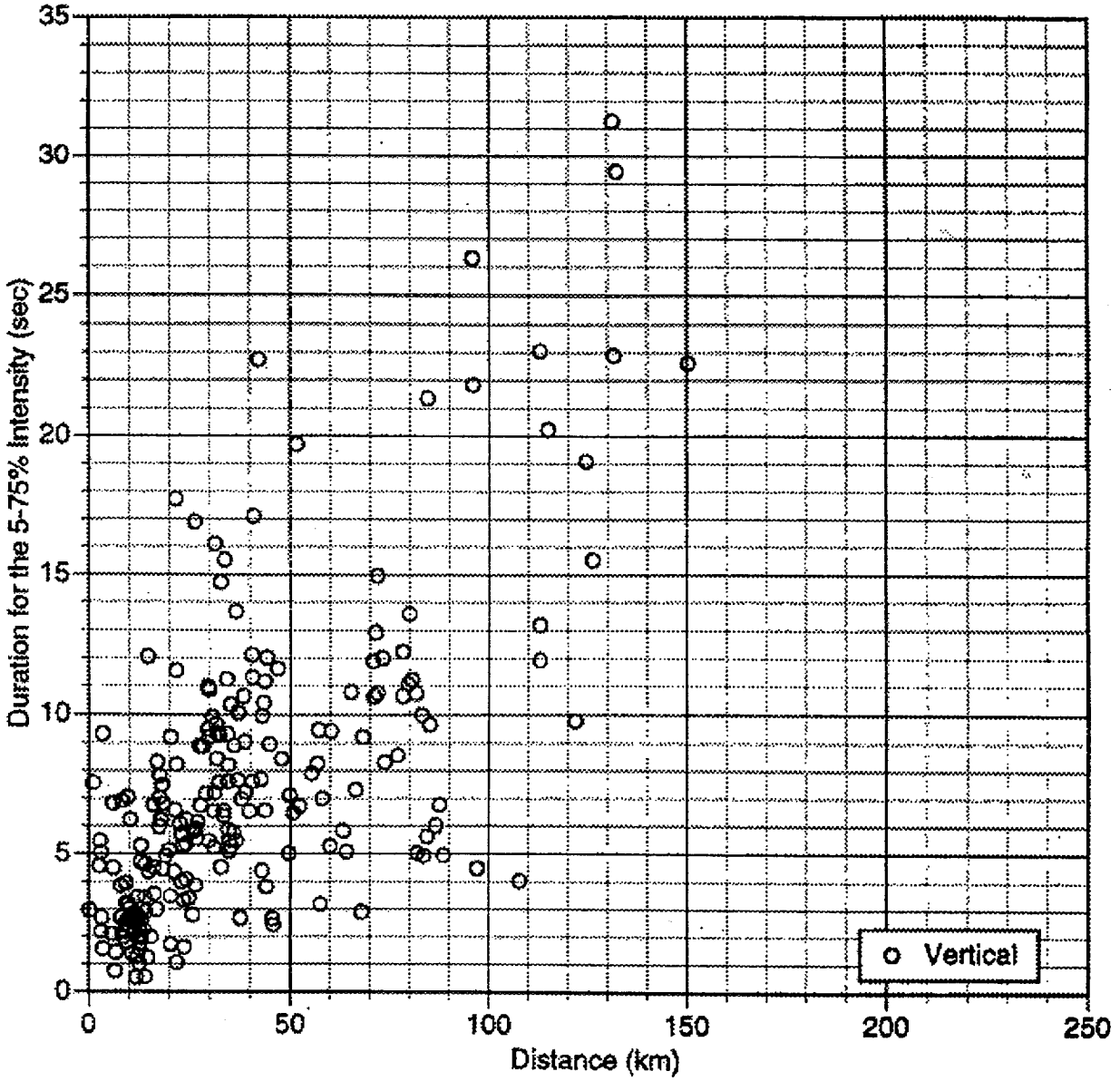

Figure H-2a. Distance dependence of the vertical duration for the 5-75% intensity for rock site conditions.

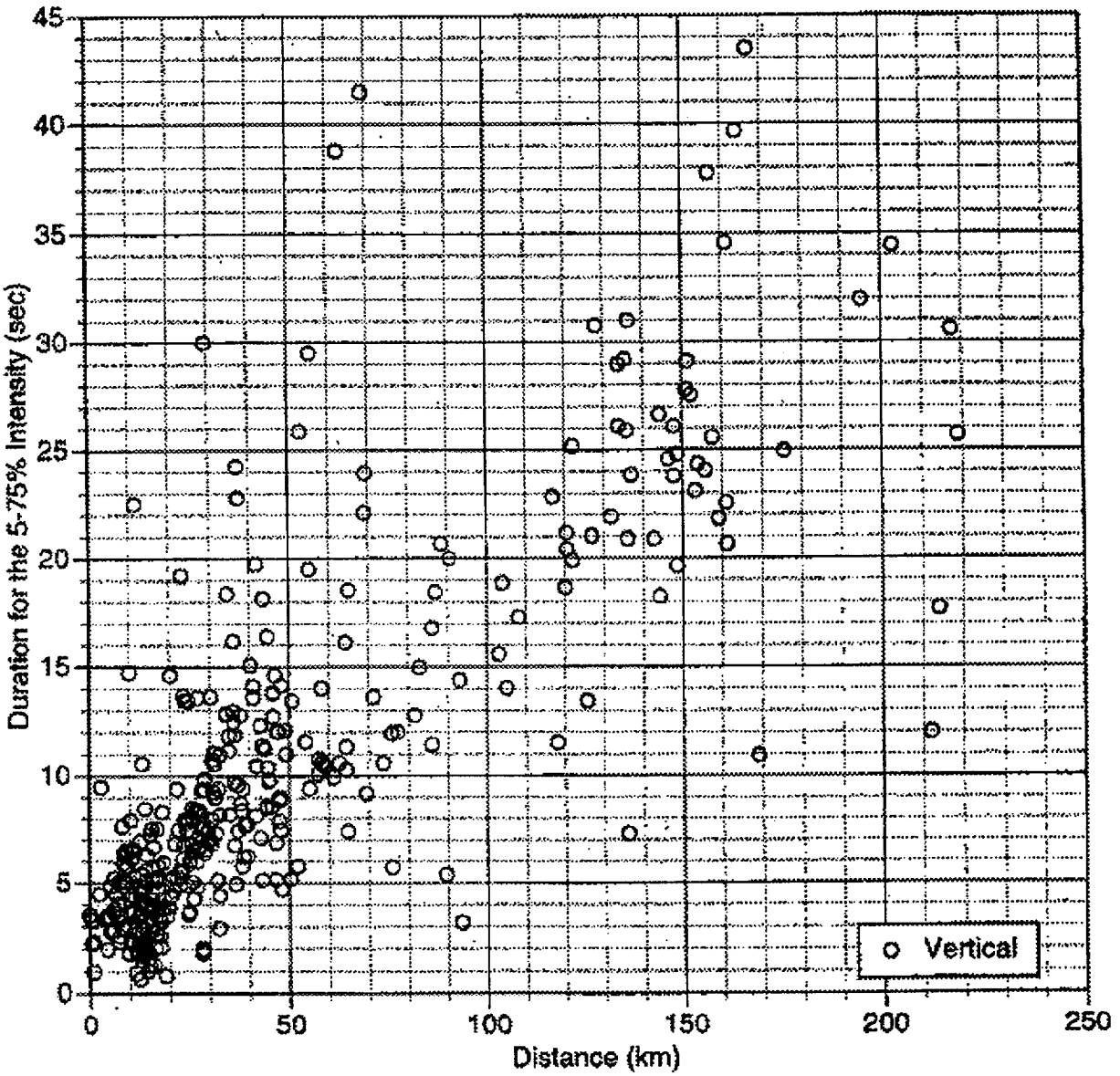

Figure H-2b. Distance dependence of the vertical duration for the 5-75% intensity for soil site conditions.

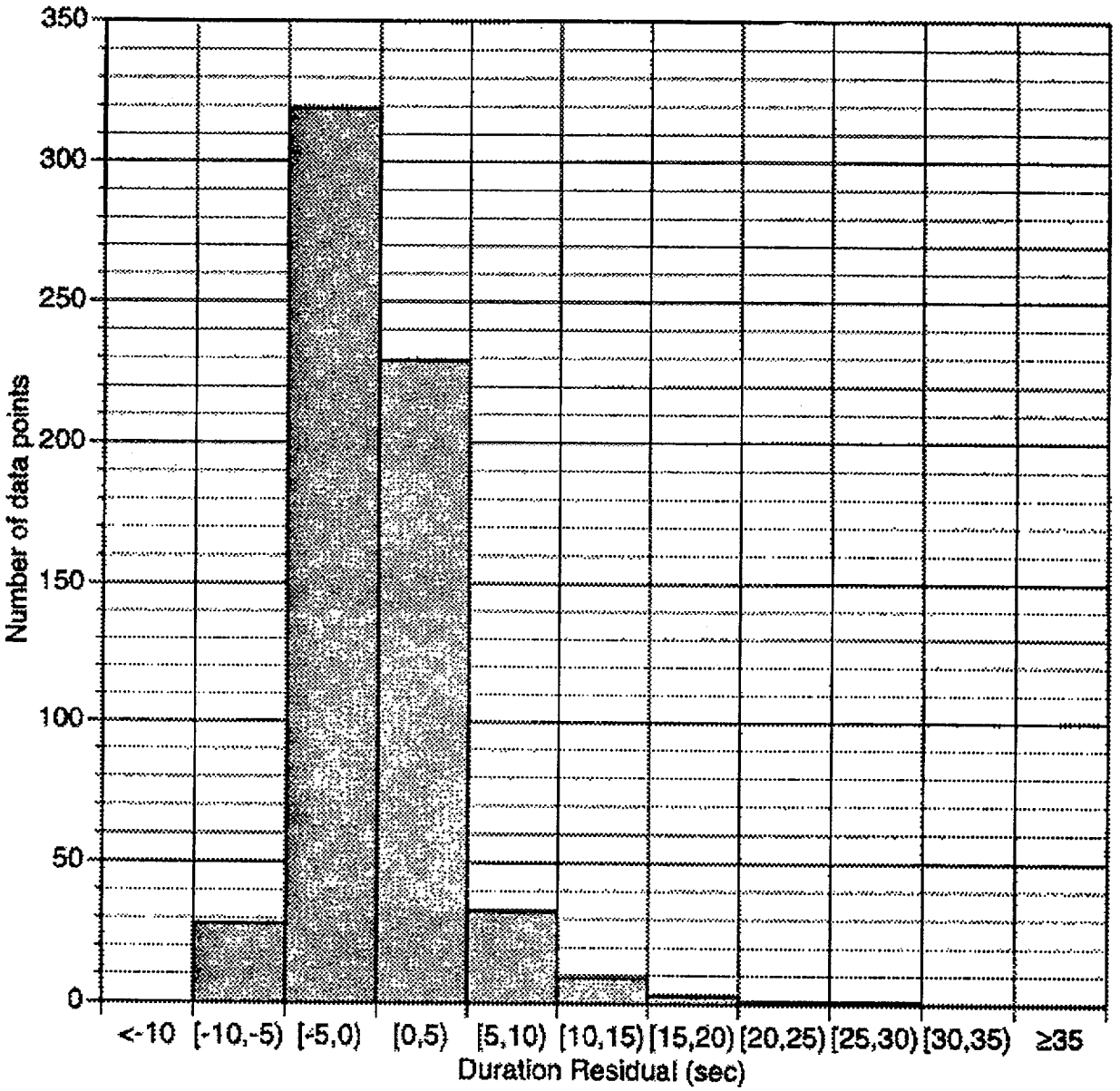

Figure H-3a. Distribution of the horizontal 5-75% intensity model (Equation H-9).

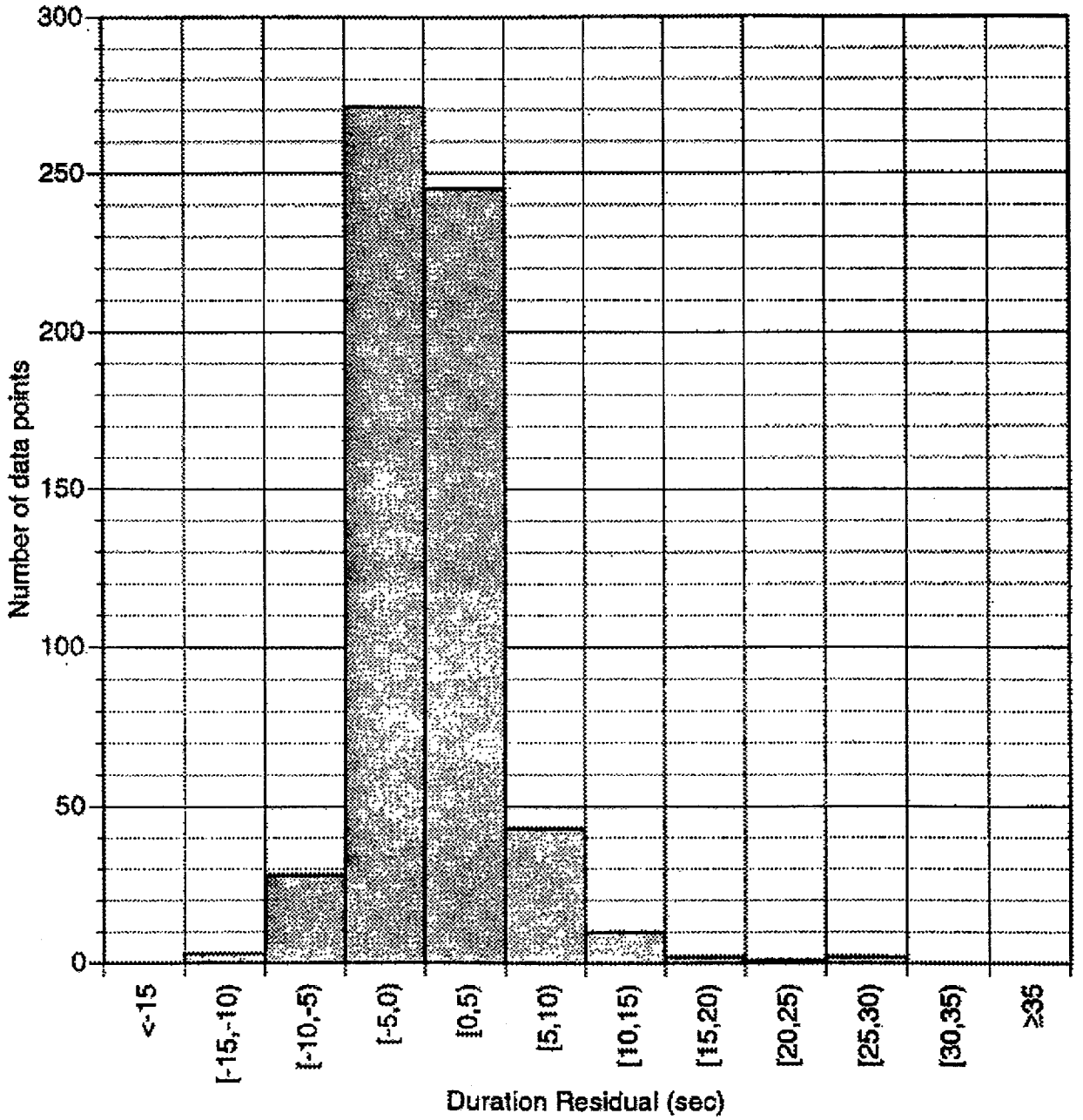

Figure H-3b. Distribution of the vertical 5-75% intensity model (Equation H-9).

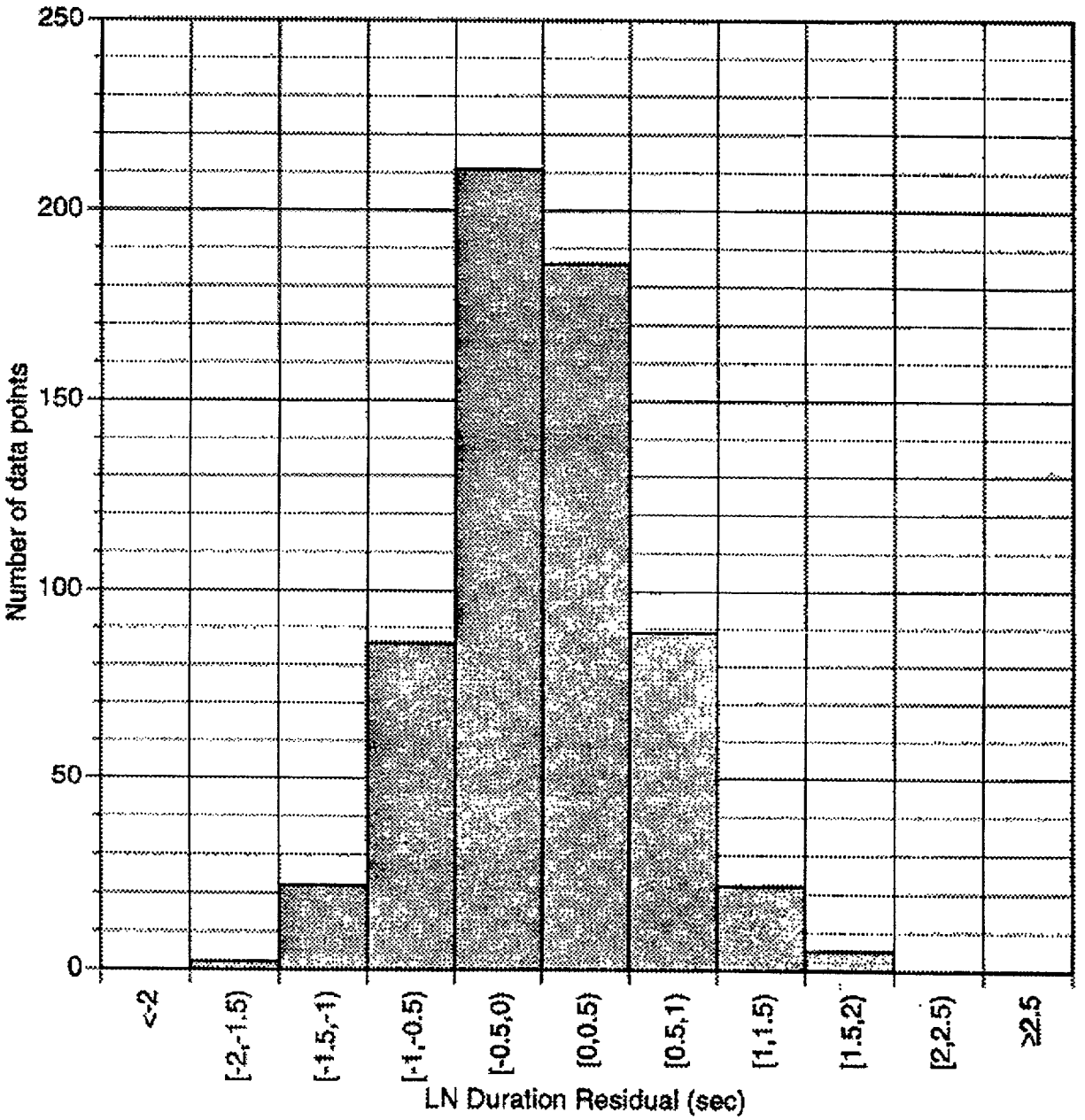

Figure H-4a. Distribution of the horizontal 5-75% intensity model (Equation H-9).

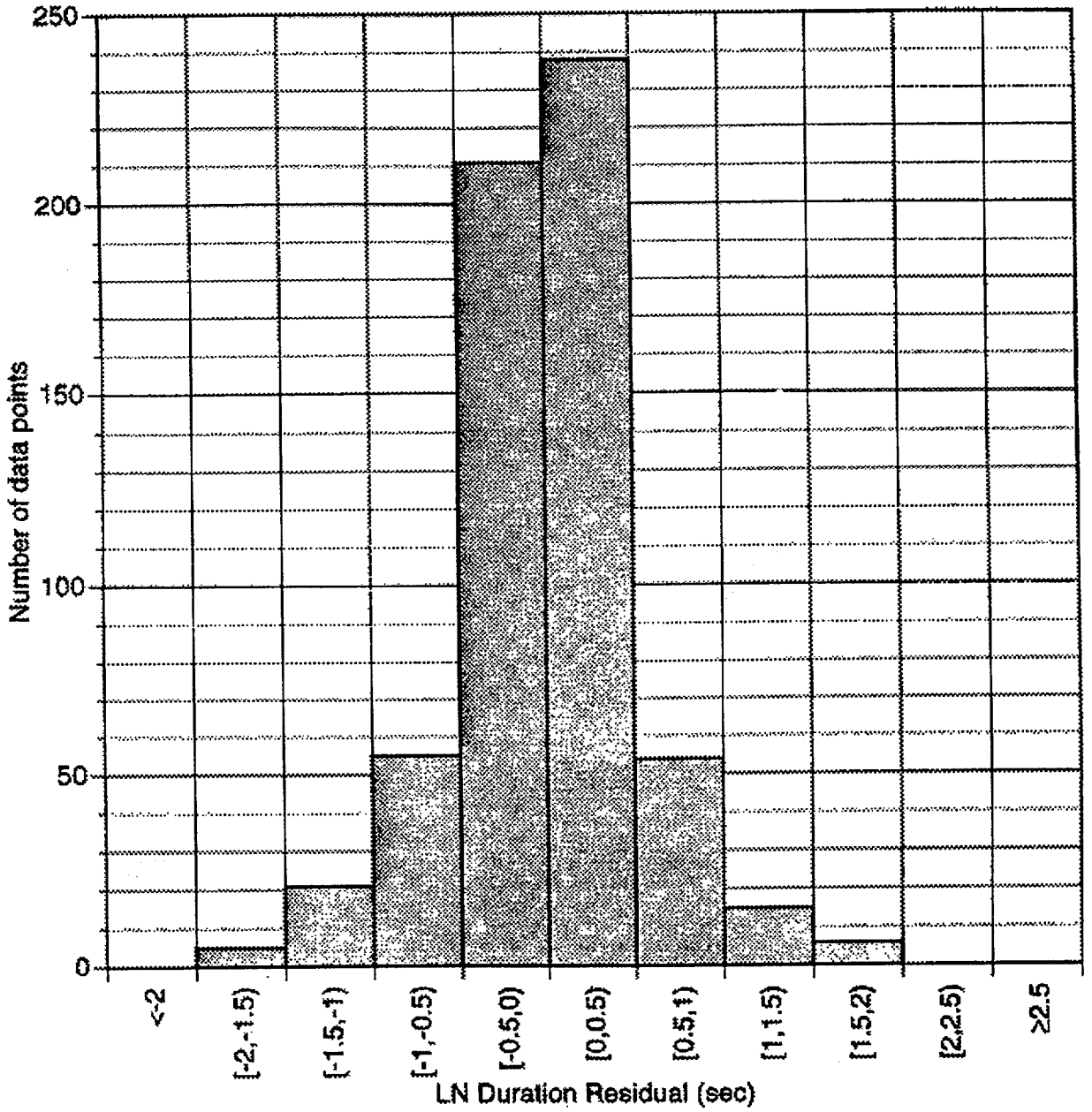

Figure H-4b. Distribution of the vertical 5-75% intensity model (Equation H-9).

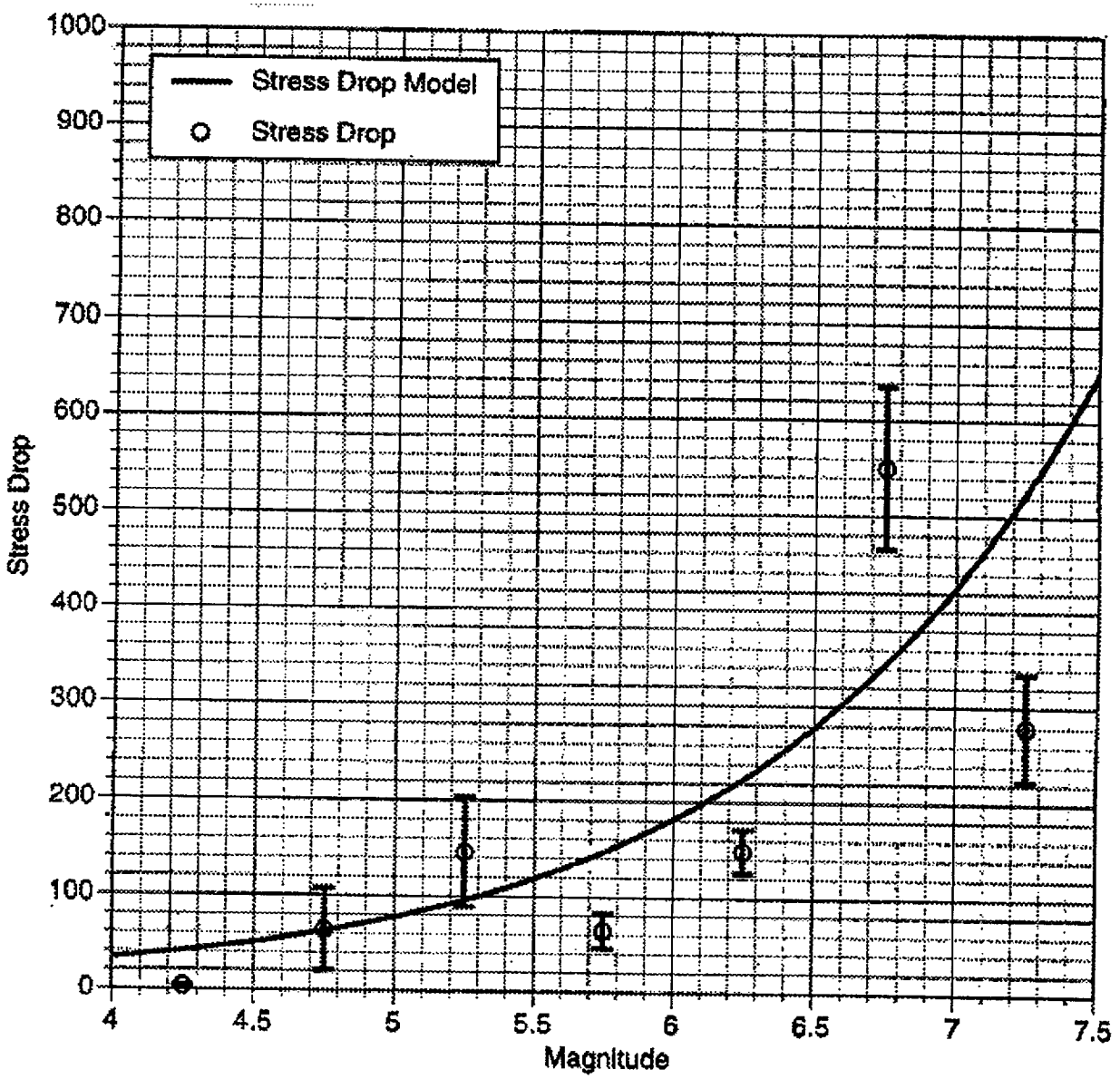

Figure H-5a. Stress drop estimates and model for the horizontal component.

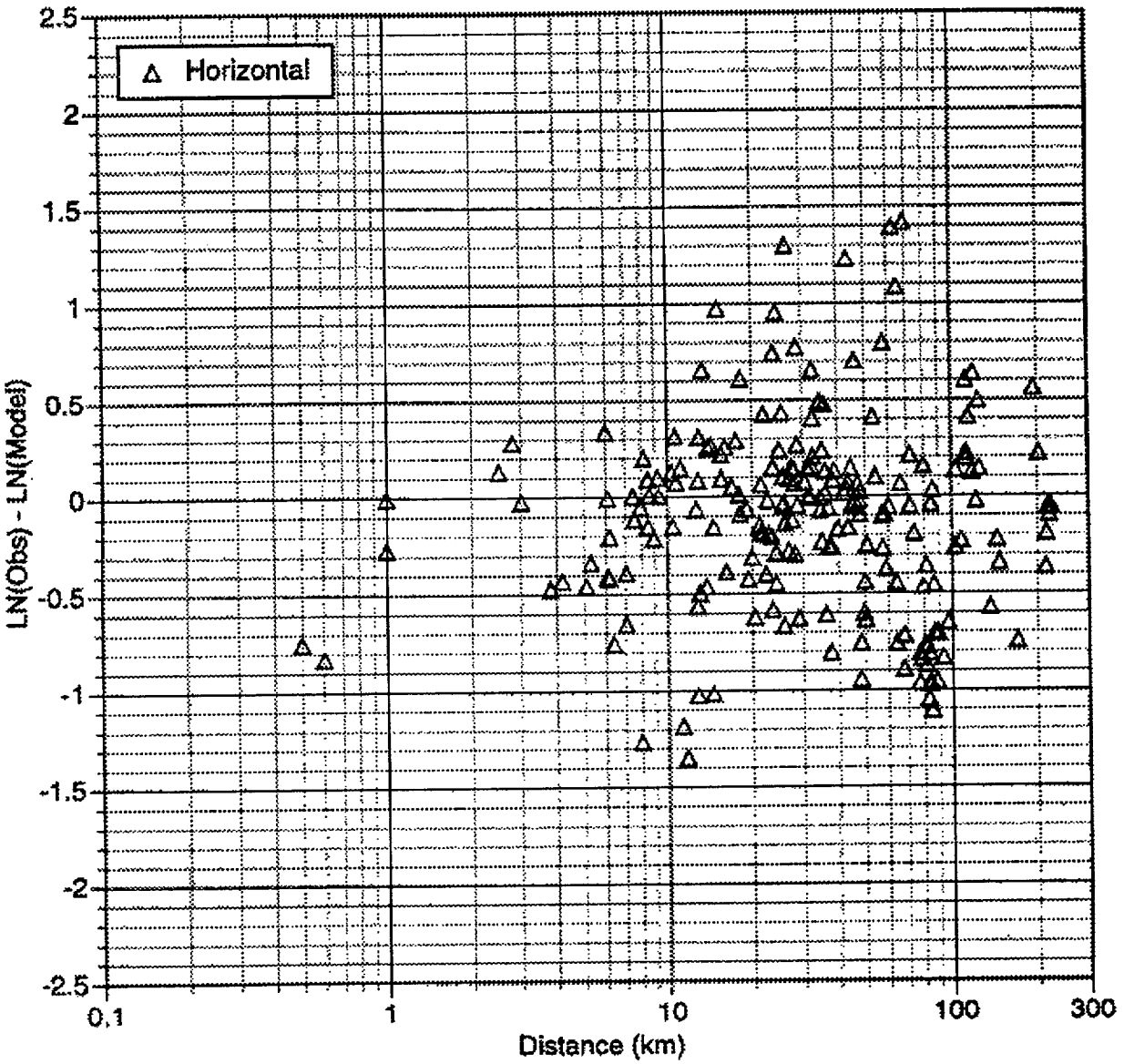

Figure H-6. Horizontal residuals for magnitudes between $6.5 < M < 7.0$.

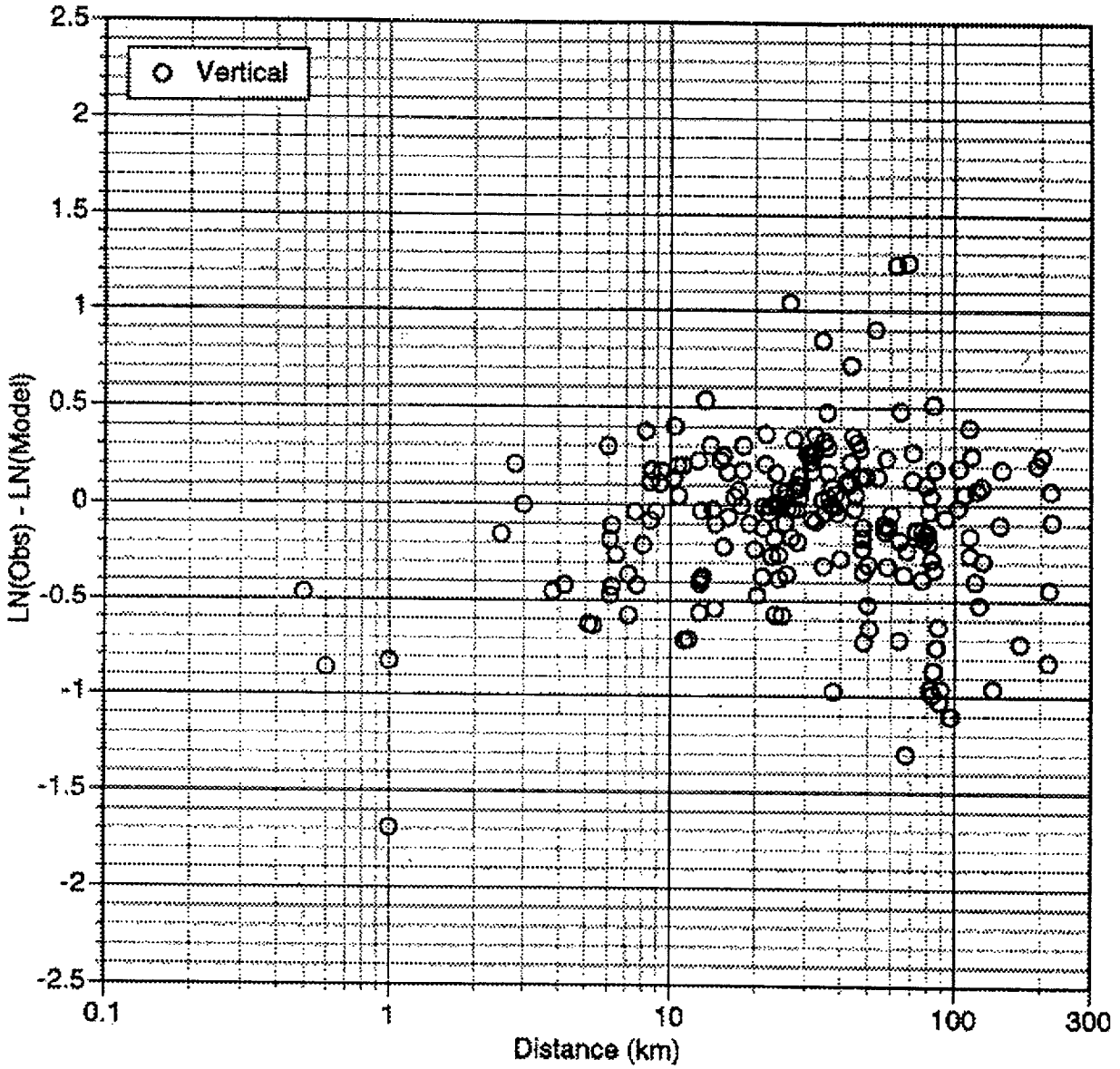

Figure H-7. Vertical residuals for magnitudes between $6.5 < M < 7.0$.

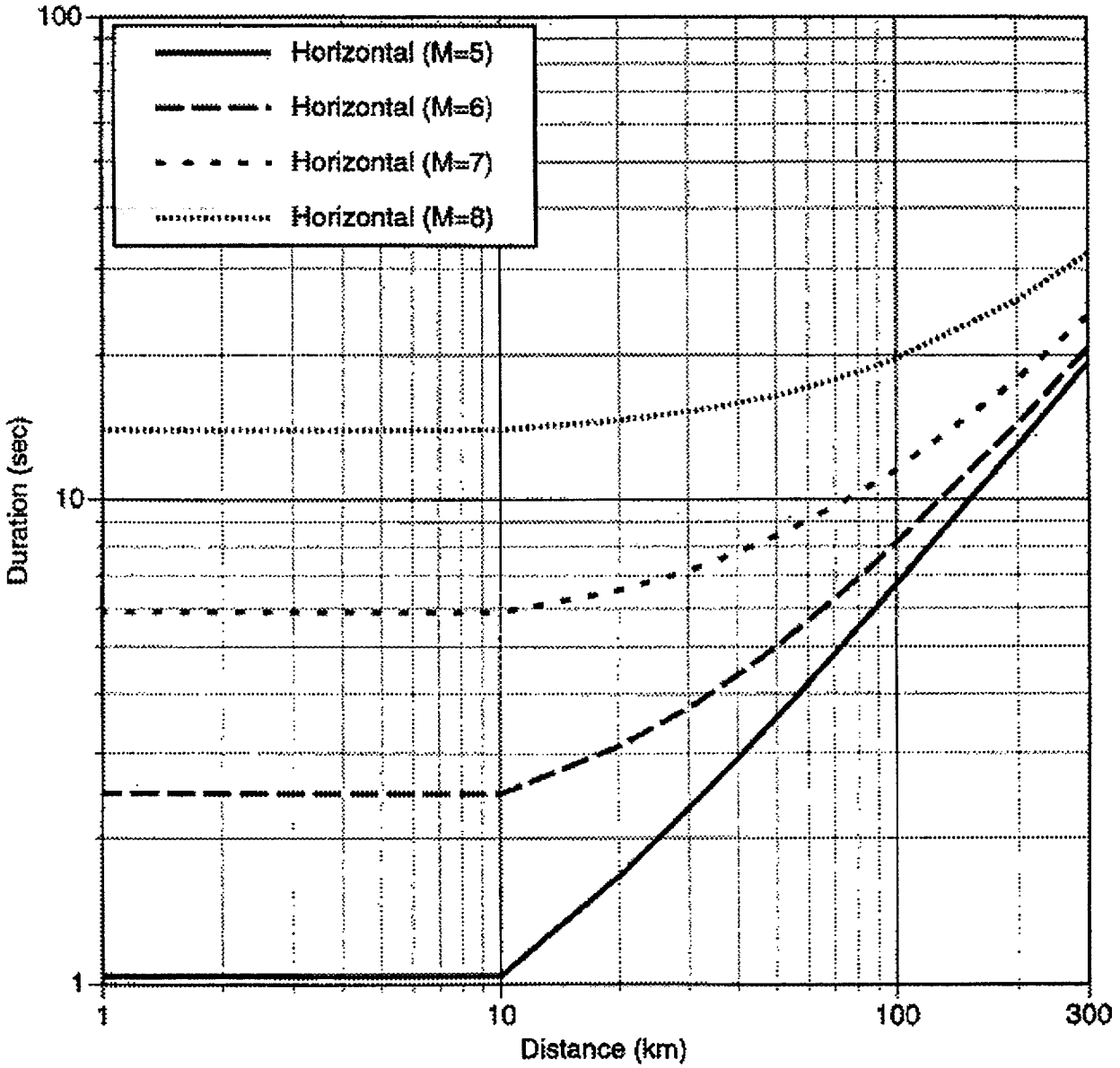

Figure H-8a. Horizontal 5-75% intensity duration model for rock site conditions.

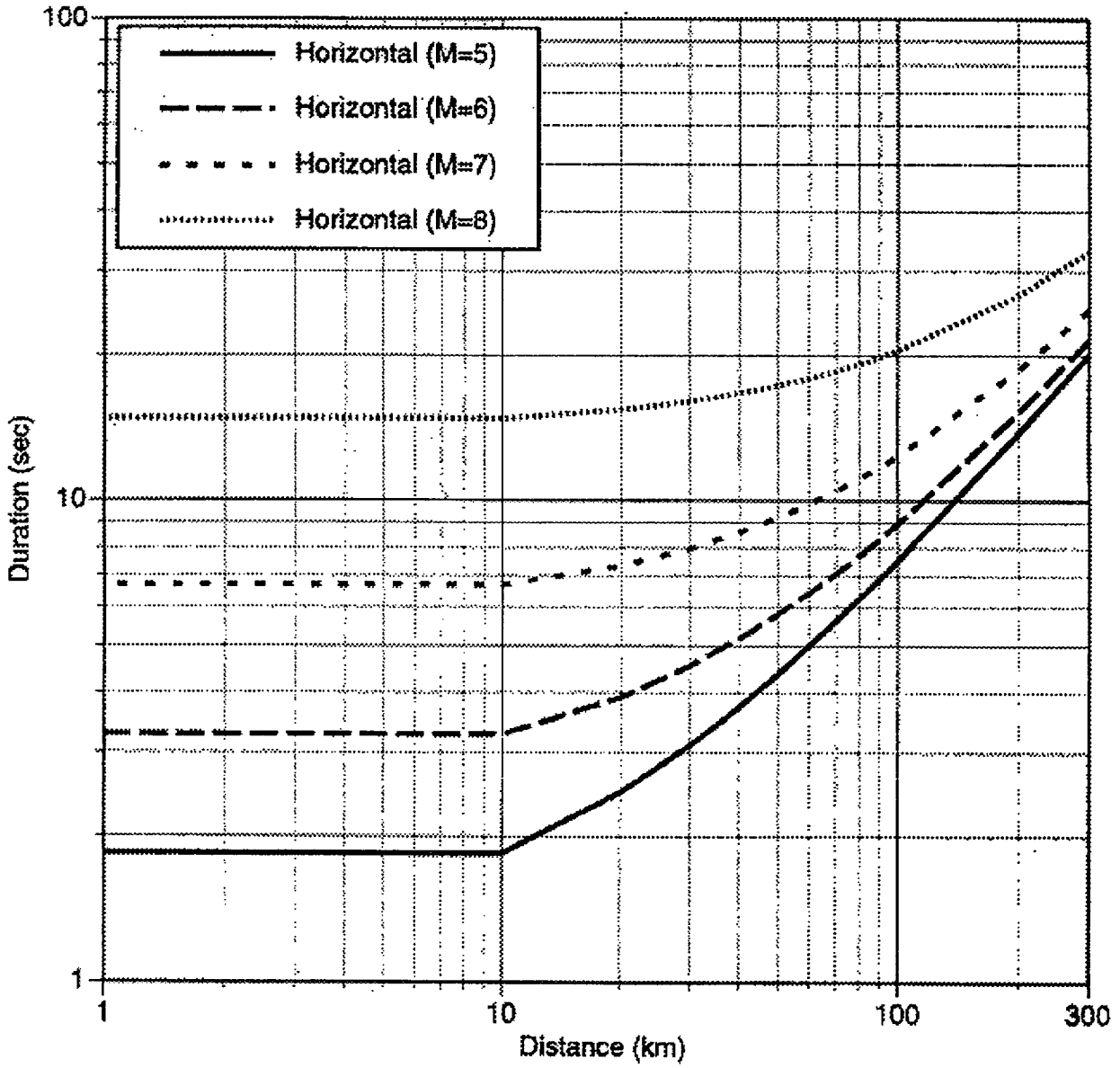

Figure H-8b. Horizontal 5-75% intensity duration model for soil site conditions.

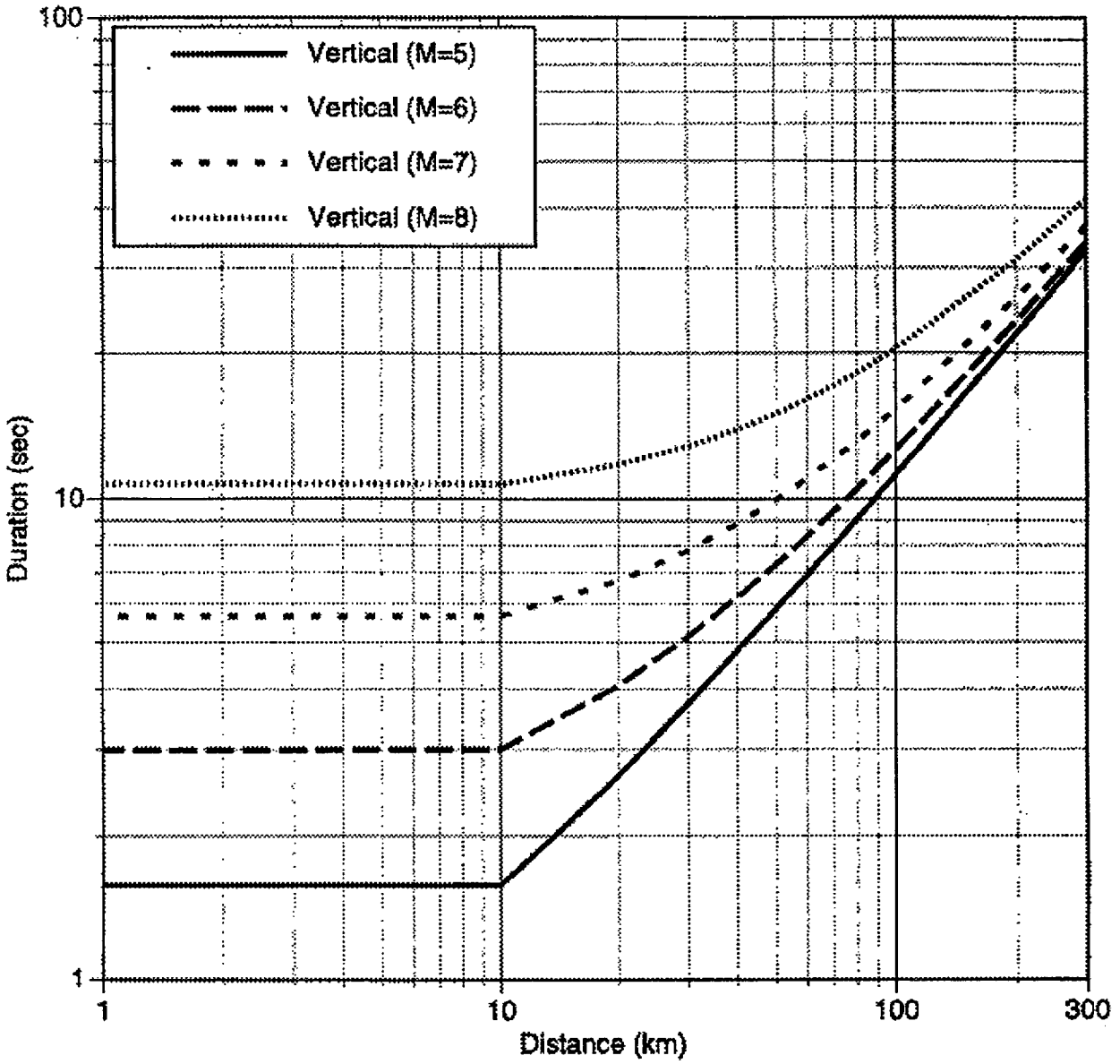

Figure H-8c. Vertical 5-75% intensity duration model for rock site conditions.

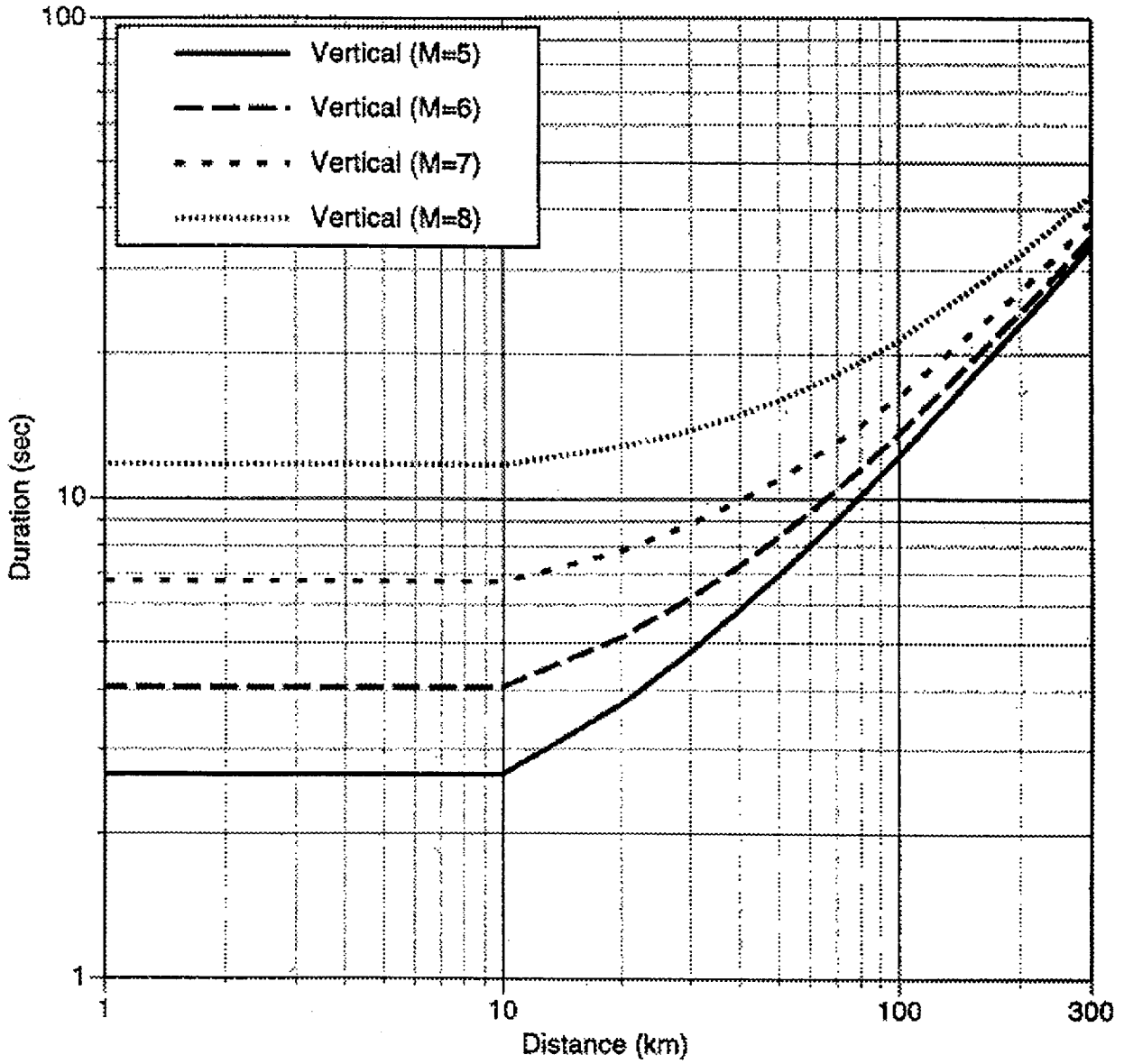

Figure H-8d. Vertical 5-75% intensity duration model for soil site conditions.

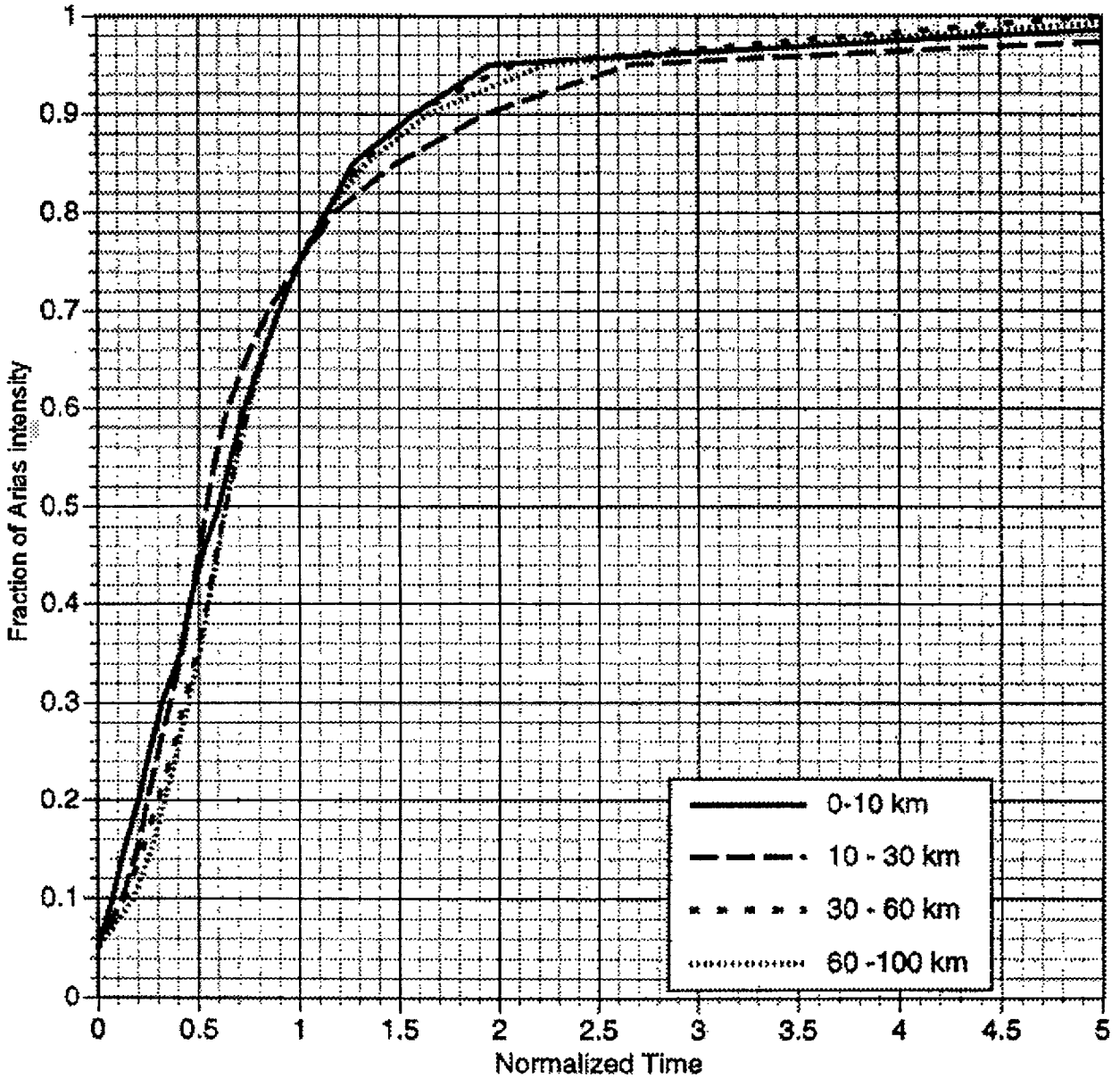

Figure H-9. Mean normalized durations averaged over distance bins for the horizontal component for rock site conditions and $6.5 < \mathbf{M} < 7.0$.

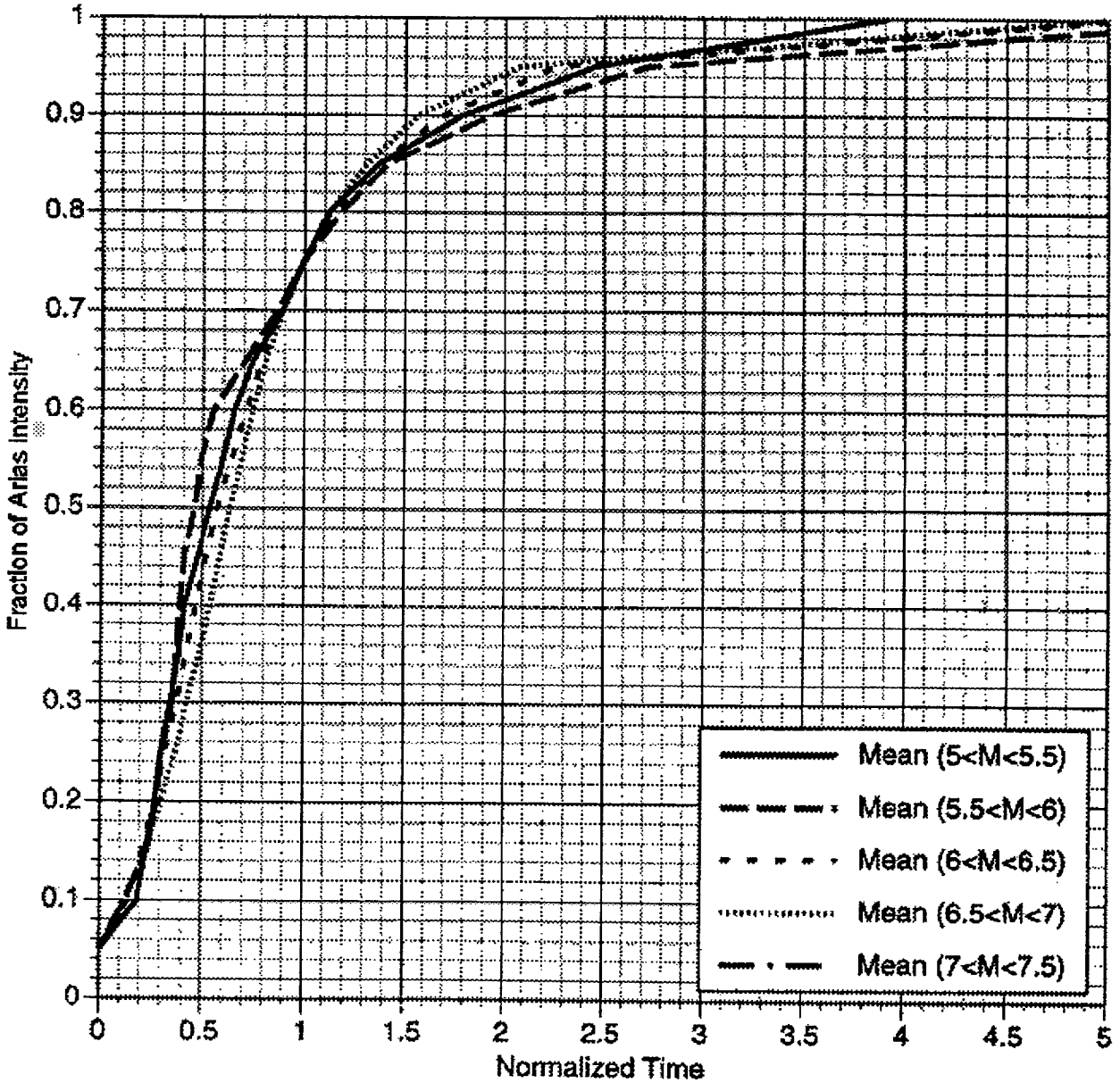

Figure H-10. Mean normalized durations averaged over magnitude bins for the horizontal component for rock site conditions and distance = 30-60 km.

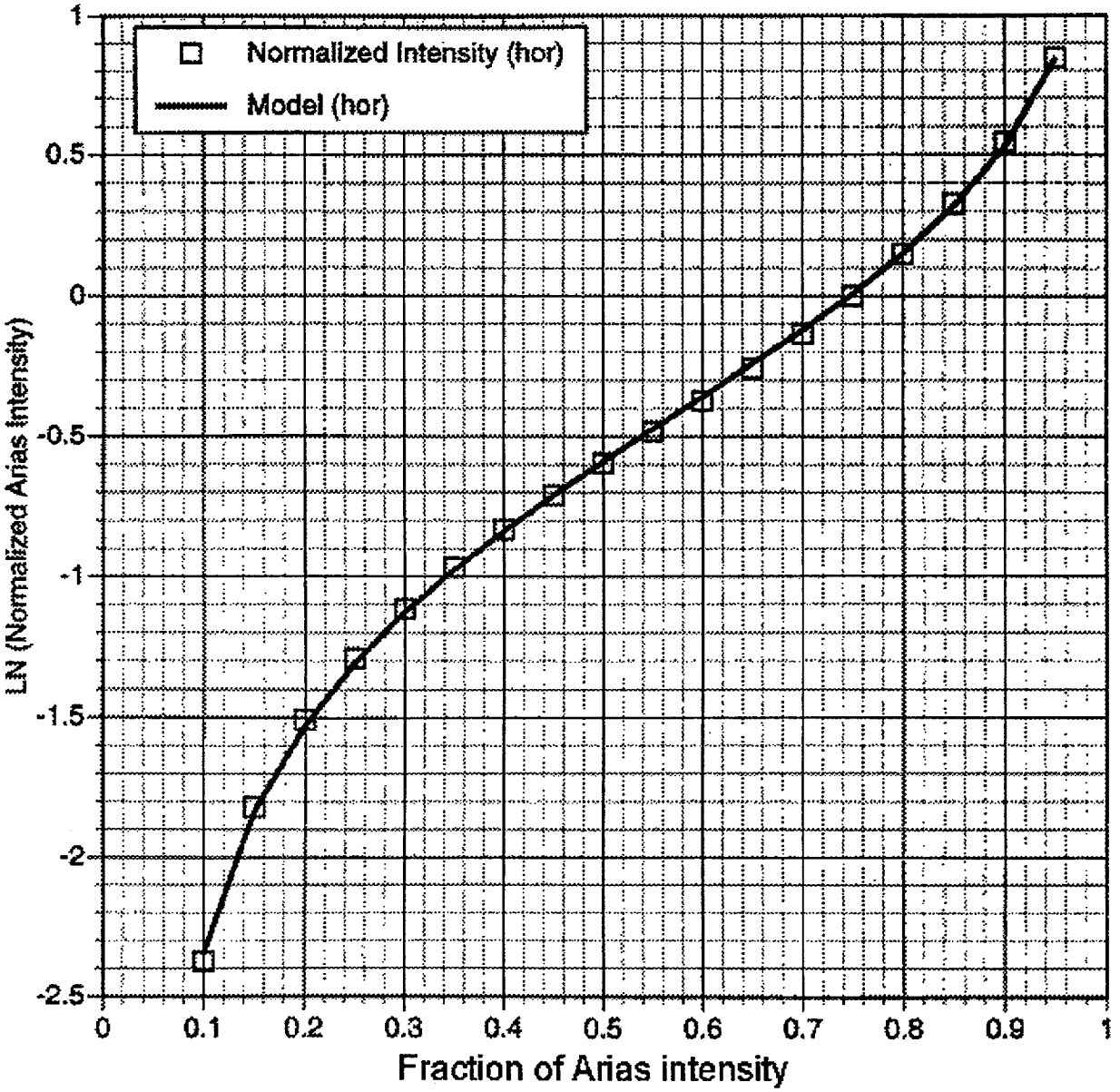

Figure H-11a. Mean predicted model (Equation H-11) compared to the mean of the data for the horizontal component.

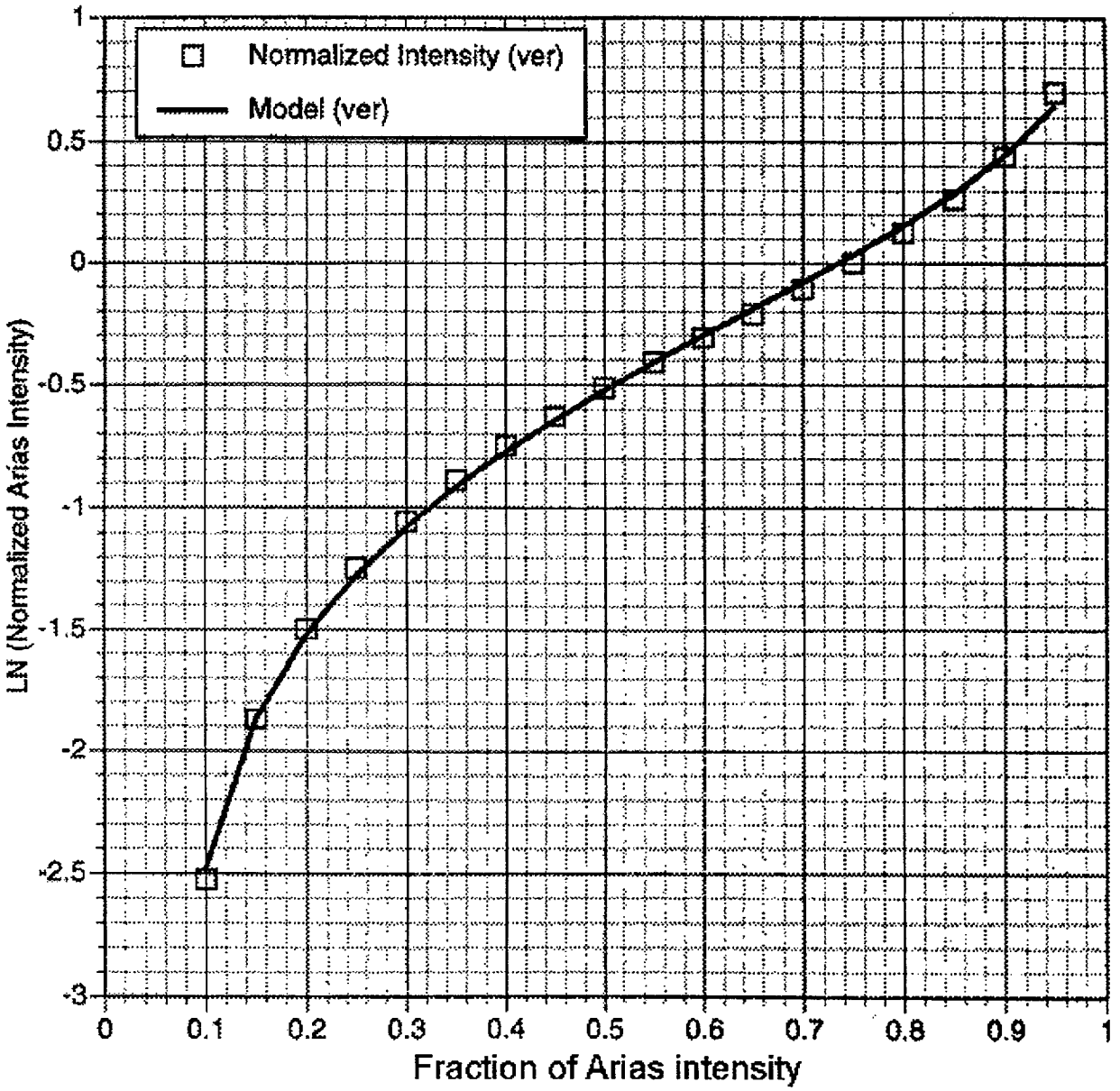

Figure H-11b. Mean predicted model (Equation H-11) compared to the mean of the data for the vertical component.

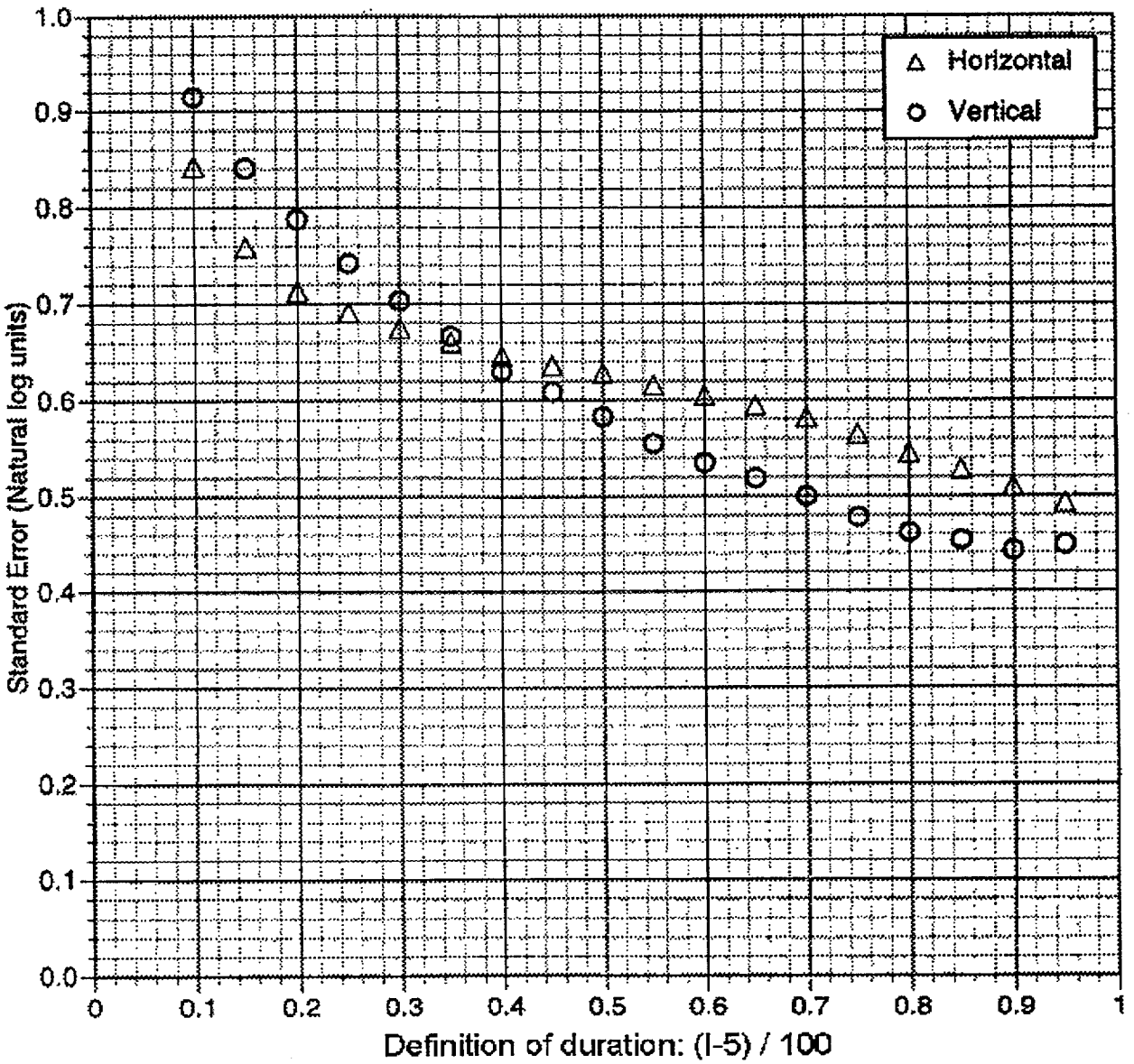

Figure H-12. Standard errors for the horizontal and vertical duration models.

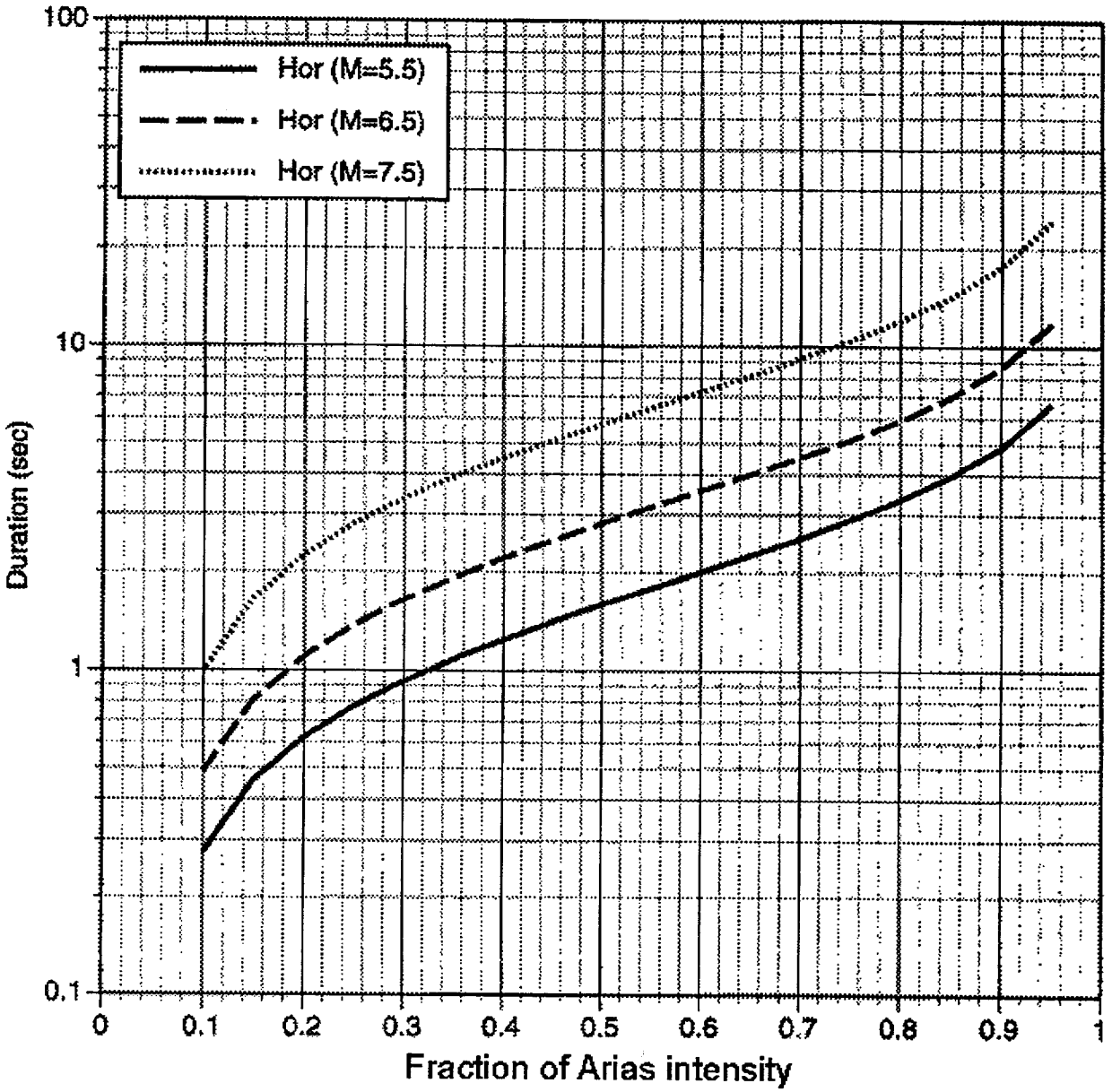

Figure H-13. Duration model for horizontal component for rock site conditions and distance of 30 km.

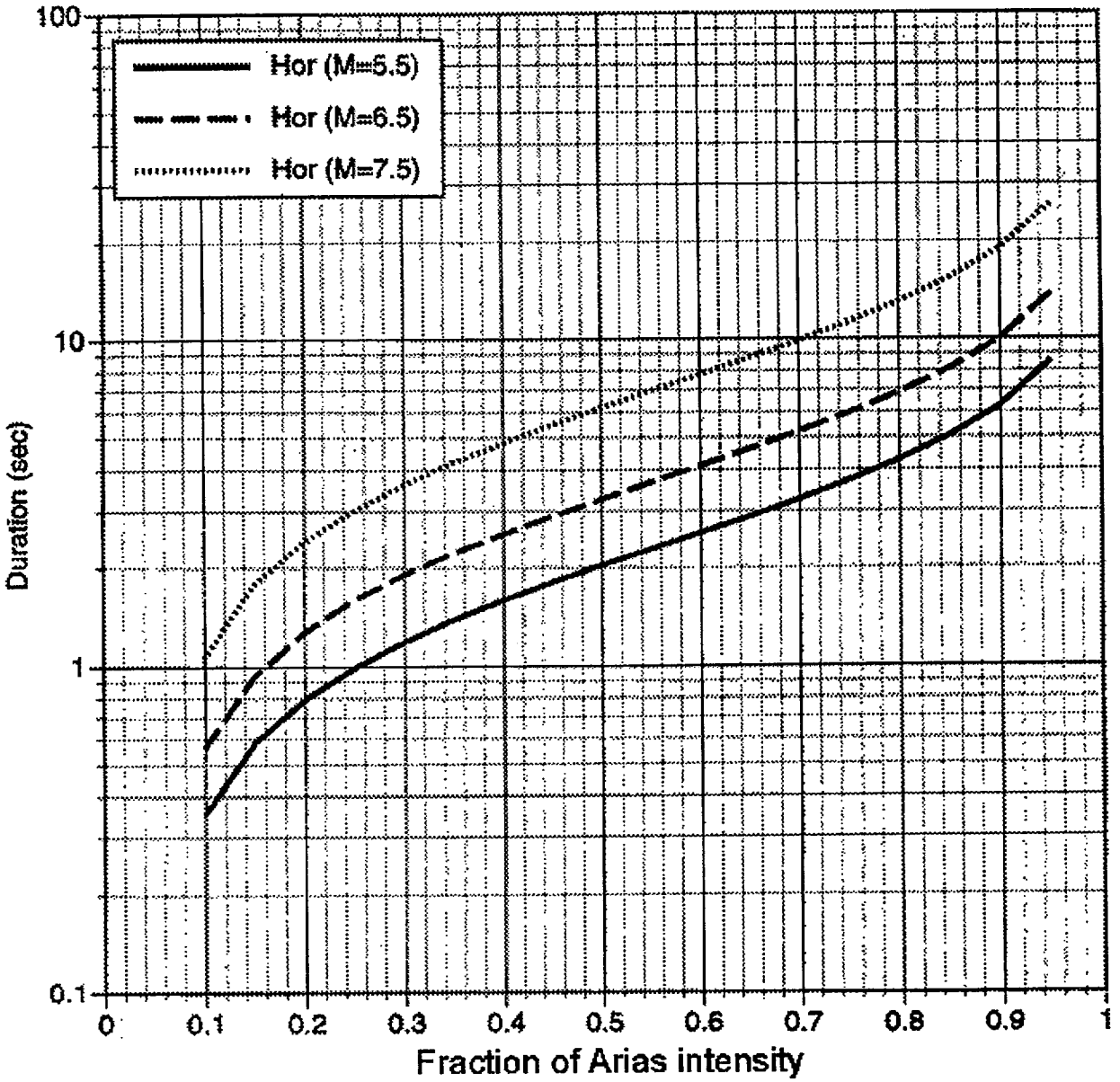

Figure H-14. Duration model for horizontal component for soil site conditions and distance of 30 km.

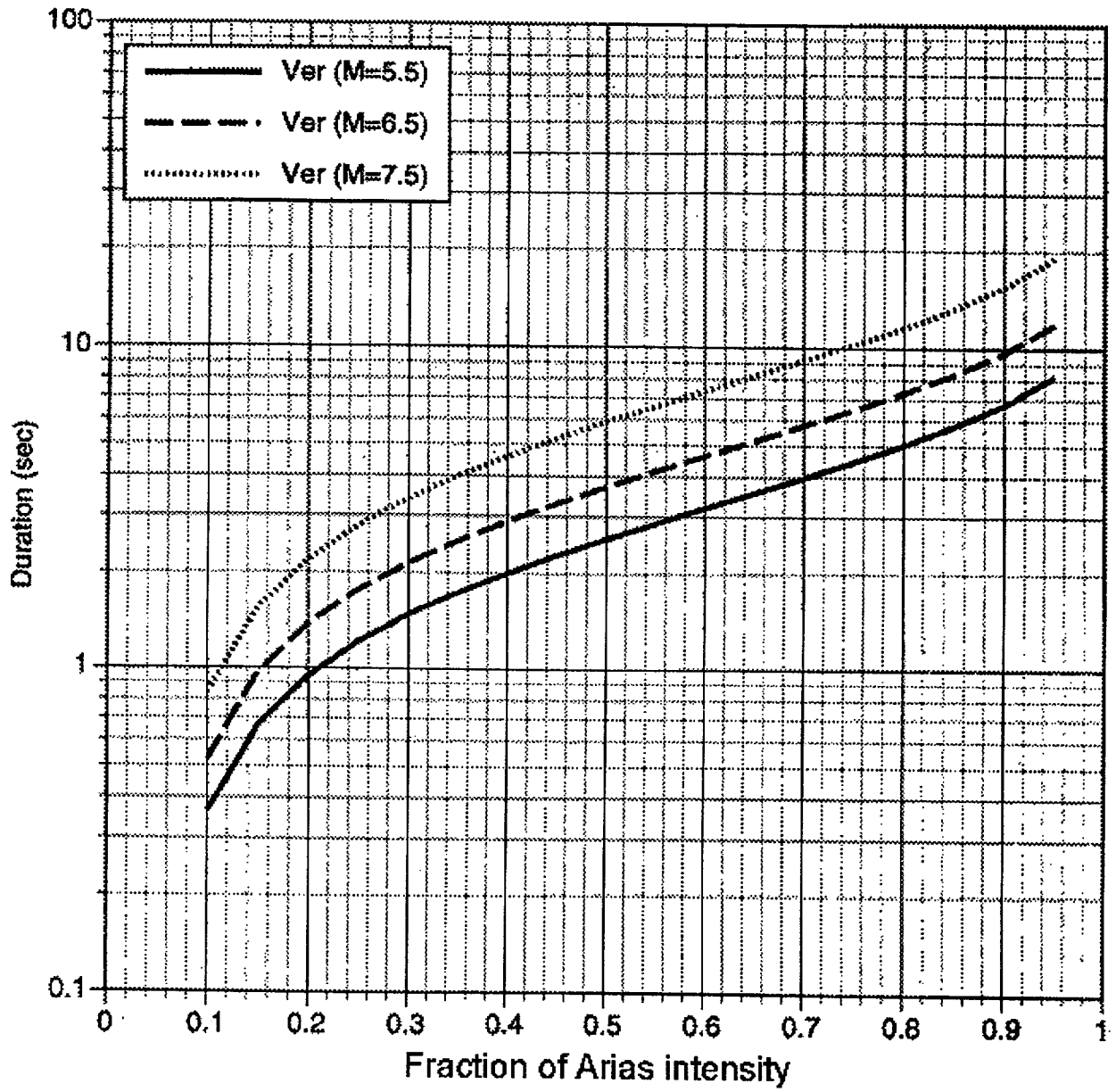

Figure H-15. Duration model for vertical component for rock site conditions and distance of 30 km.

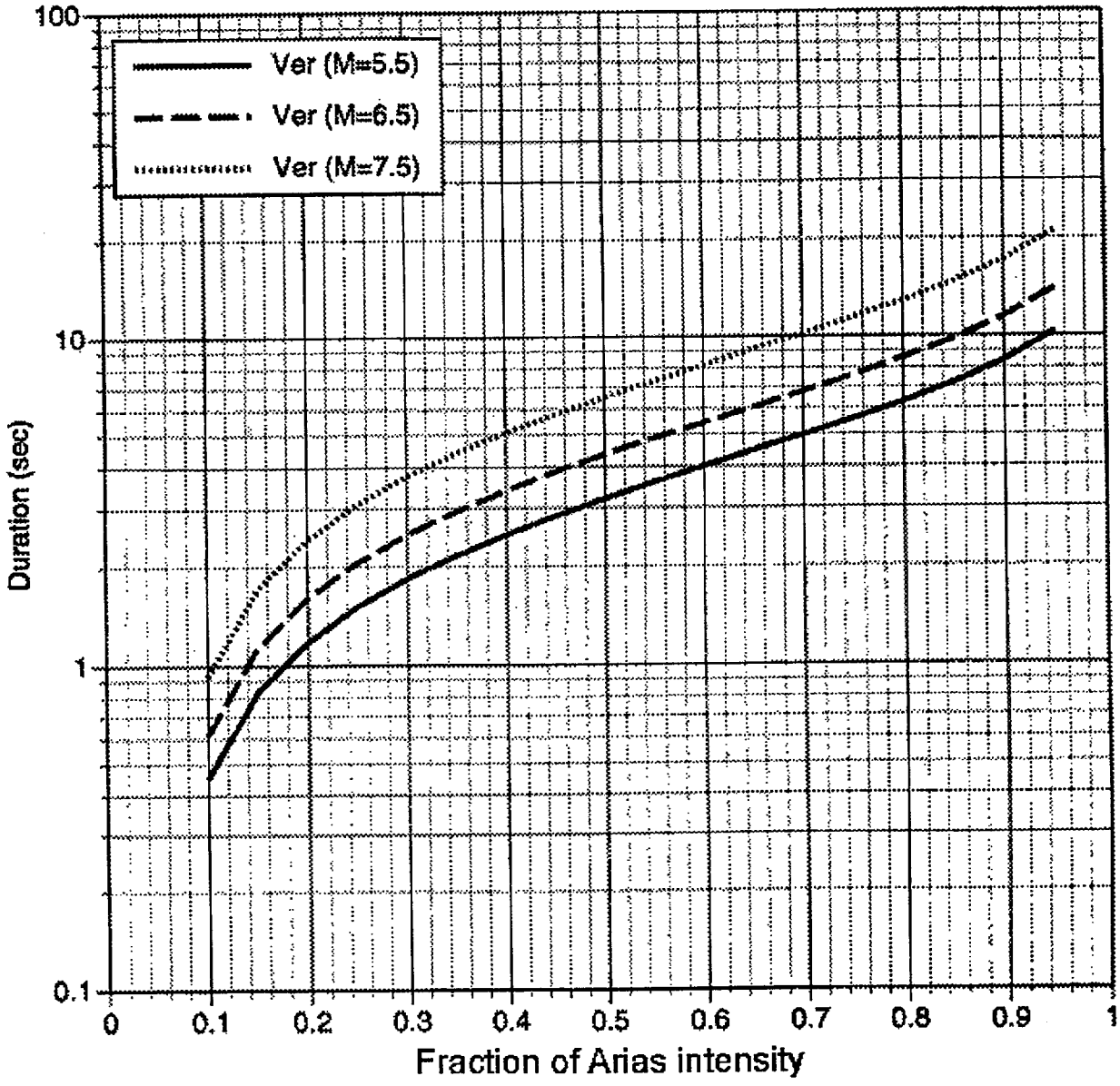

Figure H-16. Duration model for vertical component for soil site conditions and distance of 30 km.

APPENDIX I SITE- AND SOIL-SPECIFIC PSHA FOR NONLINEAR SOIL SITES[a]

[a] Bazzurro, P., Cornell, C.A., and F. Pelli (1999). "Site- and Soil-specific PSHA for Nonlinear Soil Sites", Proceedings of 2nd International Symposium on Earthquake Resistant Engineering Structures – ERES99, Published by WIT Press, Southhampton, UK, Paper No. 27214, 15-17 June, Catania, Italy

I.1 Introduction

The probabilistic site amplification of ground motions has been extensively studied by others.[5,10,4] The procedure proposed here, however, is fully probabilistic since it includes the variability both in the ground motion and in the soil parameters at the site. Moreover, the soil nonlinear response is evaluated by driving real rock ground motions through a finite element model of the column using a program capable of predicting the pore water pressure build-up and dissipation. In practical applications this method can use a small number of records/runs, as few as ten or less, which is a big advantage if resources and/or "appropriate" records for a site are a major constraint. Results suggest, in fact, that sufficient accuracy is achieved without running many records at many magnitude and distance pairs. This implies that real accelerograms rather than simulated ones can often be used. Two case studies involving both a sandy and clayey soil deposit are discussed here.

I.2 Methodology

For brevity, this section describes only the main features of the methodology. More details can be found in Bazzurro and Cornell.[2] The effect of the soil on the intensity of the ground motion at the surface is studied in terms of a site-specific, frequency-dependent amplification function, AF(f), where f is a generic oscillator frequency:

$$AF(f) = \frac{S_a^s(f)}{S_a^r(f)} \tag{1}$$

where $S_a^s(f)$ and $S_a^r(f)$ are the 5%-damped spectral acceleration values at the soil surface and at the bedrock, respectively.

The behavior of AF (f) for multiple ground motion records has shown that $S_a^r(f)$ is the most effective predictor variable for estimating AF (f) (at the same frequency f) among different bedrock ground motion parameters, such as magnitude, M, source-to-site distance, R, Peak Ground Acceleration, PGA_r, and spectral acceleration values, $S_a^r(f_{sc})$, at the initial resonant frequency, f_{sc}, of the soil column. Furthermore, results showed that once the $S_a^r(f)$ value of a record at the bedrock is known, the additional knowledge of M and R, which implicitly define its average response spectrum shape, do not appreciably improve the estimation of AF (f) at the same frequency f. In other words, AF (f) conditioned on $S_a^r(f)$ is virtually independent on M and R (see Fig. 4 to come).

The proposed method for computing surface hazard curves for $Z = S_a^s(f)$ *convolves* the site-specific rock hazard curves for $X = S_a^r(f)$, which may be exogenously provided, with the $Y = AF(f)$ estimates obtained through nonlinear dynamic analyses of the soil. Bazzurro and Cornell[2] describe also a different but equally effective approach which requires performing a PSHA for the site with

$$P[Z > z] = G_z(z) = \sum_{all\,x_j} G_{Y|X}\left(\frac{z}{x}|X = x_j\right) P[X = x_j]$$

where $G_W(w)$ is the complementary cumulative distribution function (CCDF) of any random variable, W (e.g., $G_Z(z)$ is the sought hazard curve for $S_a^s(f)$, i.e., the annual probability of exceeding level z), and $P[X = x_j] = p_X(x_j)$ is the probability that the rock input level is x_j. The latter can be approximately derived by differentiating the rock hazard curve in "discrete" or numerical form. $G_{Y|X}$ is the CCDF of $AF(f)$, conditional on a rock level amplitude x_j.

Assuming lognormality of Y given X, the $G_{Y|X}$ is given by:

$$G_{Y|X}\left(\frac{z}{x}|x_j\right) = \hat{\Phi}\left(\frac{\ln[\frac{z}{x}] - \ln[\hat{m}_{Y|X}(x)]}{\sigma_{\ln Y|X}}\right)$$

in which $\hat{\Phi}(\cdot)$ is the widely tabulated complementary standard Gaussian CDF. Estimates of the distribution parameters of Y, (i.e., the conditional median of Y, $\hat{m}_{Y|X}$, and the conditional standard deviation of natural logarithm of Y, $\sigma_{\ln Y|X}$) can be found by driving a suite of n rock ground motion records through a sample of soil column representations (recall that the soil properties are uncertain) and then regressing, for each frequency f, the values of ln Y on ln X.

For the two case studies presented later the values of $\sigma_{\ln Y|X}$ were found to be between 0.2 and 0.35 for *all* oscillator frequencies, f, of interest, and to be virtually independent of the level x_j. When the dependence of $AF(f)$ on $S_a^r(f)$ was *not* considered the $\sigma_{\ln Y}$ values increased from 0.2 to 0.3 (at f around 0.25Hz to 0.5Hz) to 0.6 to 0.7 (at f around 10Hz) and then decreased to approximately 0.5 at infinite f (i.e., PGA).

This reduction in dispersion translates into requiring a smaller number of runs to attain the same accuracy, ζ, in the estimate of the median $AF(f)$. The number of records, n, needed to keep the standard error, $\sigma_{Y|X}$, of the regression line within a specified ζ is given by $n = [\sigma_{Y|X}/\zeta]^2$. To achieve $\zeta =$ 10% only ten analyses are sufficient.

I.3 Applications

I.3.1 Ground Motion Database

For validating the procedure, we used a large database of 78 free-field surface rock strong ground motions from 28 different earthquakes that occurred worldwide between 1966 and 1995. It is emphasized again, however, that in real applications only about 10 records would be needed. The magnitude range is between $M5$ and $M7.4$, while the shortest distances to the rupture are between 0km and 142km. Approximately 40% of such accelerograms were recorded during three earthquakes: the Loma Prieta (1989), Landers (1992), and Northridge (1994) events in California. This concentration, however, does not statistically affect the results of the amplification analyses. In the amplification study we chose at random one horizontal component of each recording (Fig. 1). The PGA_r values range from 0.01g to 1.5g. These seismograms, which contain "true" signal up to a

period of at least 5 seconds, were applied directly at the base of the soil column without any prior deconvolution. This assumption, which implies same rock outcrop and bedrock motions, is known to underestimate the motion at the column base above a site-dependent f value usually around 2Hz.[8] Deconvolution was not performed because a possible underestimation of the amplification at high f is not crucial for the majority of longer period structures (e.g, taller buildings, bridges, offshore platforms, etc.) which may warrant a detailed soil amplification study like the one proposed here.

I.3.2 Soil Amplification Software and Soil Modeling

The computer program adopted for computing the soil site effects is a modified version of the finite element program SUMDES, [6] which is based on the effective stress principle, vectored motion, transient pore fluid movement, and generalized material stiffness formulation. Unlike SHAKE, [7] SUMDES is capable of predicting the pore pressure build-up and dissipation and can adequately describe liquefaction and cyclic mobility phenomena. We used a inelastic constitutive reduced-order bounding surface model which is a special version of the hypoplasticity model with fewer material parameters. The boundary conditions (i.e., elastic base) were chosen to accommodate the rock-outcrop nature of the input.

Both soil deposits are located in the Mediterranean Sea. The sandy deposit consists of sands and gravels with occasional presence of cobbles. The relative density is between 60 and 80% and the total unit weight is 20kN/m^3. The behavior of this sand under undrained shear is dilative and the effect of pore pressure build-up and cyclic mobility can be relevant. This effect tends to soften the soil by increasing the shear strain level at which dilation occurs. The clayey deposit is cohesive (silts and clays) and soft with both normally and overconsolidated layers. The shear modulus at small strain levels, G_{max}, was established based on both shear wave velocity, V_s, measurements and on correlations between the cone (CPT) tip resistance and V_s. The G/G_{max} versus shear strain curves were obtained from Li *et al.*. [6]

In both cases, a soil column of 100m was modeled using 100 elements of one meter of thickness each. The median V_s increases from 80m/sec below the mudline to 400m/sec at 100m of depth. The variability in the soil properties was included through a Monte Carlo approach by randomly varying the coefficient of permeability (π_0), the shear and the compression viscous damping ratios at 1Hz (ξ_s and ξ_c), the coefficient of lateral earth pressure at rest (K_0), the coefficient, G_0, which defines the elastic shear modulus G_{max} at very low strain levels, the friction angle, Φ_0, and the shear strain value, $\gamma_{64\%}$, at 64% of G_{max}. The seven basic RVs above were considered lognormally distributed with $\sigma_{\ln RV}$ equal to 0.25 for ξ_s, ξ_c, K_0 and G_0; to 0.1 for Φ_0; to 0.35 for $\gamma_{64\%}$, and to 0.7 for π_0. A distribution truncation at $2\sigma_{\ln RV}$ was included to prevent unrealistic parameter values.

The spatial correlation among layers was characterized by a first-order auto-regressive model, [9] with lag-one correlation coefficient equal to 0.58. The thickness of each layer is not considered random. *Within each layer* perfect positive correlation is assumed for Φ_0, G_0 and $\gamma_{64\%}$ and all three are considered to be perfectly negatively correlated with both ξ_s and ξ_c. K_0 and Φ_0 are assumed to be independent of all other RVs.

I.3.3 Amplification Study Results

For both soil deposits, each one of the 78 records was driven through a different realization of the soil column. The 78 amplification functions are displayed in Fig. 2. The two wide peaks (at f_{sc}=0.8Hz and 2Hz) identify the first two soil resonant frequencies. At f_{sc} the two soil columns amplify on average more than three and four times the spectral acceleration at the bedrock, $S_a^r(f_{sc})$, while PGA_r is amplified on average by 40% and 100%.

AF (f) displays a large variability particularly in the high frequency range (see solid lines in Fig. 4 to come). Some of the records induce a highly nonlinear behavior in the soil deposit with associated large deformations and the corresponding *AF (f)* do not exhibit the peaks mentioned above.

On the other hand, other records have *AF (f)* well above one for the entire frequency range. This discrepancy is due to the difference both in intensities of the input ground motions and in the "strengths" of different realizations of the soil column. When the intensity increases (i.e., increasing values of M, PGA_r, and $S_a^r(f)$, and decreasing values of R) the *AF (f)* tends to diminish in amplitude and to flatten out, and f_{sc} systematically decreases towards lower f values. The dependence of *AF (f)* on $S_a^r(f)$ (i.e., locally at the same frequency, f) can be appreciated from Fig. 3. The negative correlation is statistically significant at frequencies around f_{sc} and above. It is emphasized that nonlinear soil responses at frequencies above 2Hz have been recently observed.[3]

Fig. 4 shows the predictive power of different combinations of four bedrock ground motion intensity measures (M, R, $S_a^r(f)$, and PGA_r) in terms of the standard error of estimation, $\sigma_{\ln AF(f)}$. For comparison, we included the unconditional $\sigma_{\ln AF(f)}$ curve, which describes the total variation in *AF (f)* from Fig. 2 when no regression is done. The similarities between the two sites is remarkable. M and R, even when coupled with PGA_r, yield a higher error than $S_a^r(f)$ alone.

Hence to predict *AF (f)* it is more informative to know $S_a^r(f)$ than M, R and PGA_r. When $S_a^r(f)$ is already included in the regression function the extra explanatory power provided by M (which carries information about the spectral shape) is negligible (compare 3rd and 4th model). In different words, *AF (f) conditional* on $S_a^r(f)$ is virtually independent of M. The most important consequence, however, is that, given the low values of $\sigma_{\ln AF(f)|\ln S_a^r(f)}$, the median *AF (f)* can be estimated within 10% for *all frequencies* with the knowledge of $S_a^r(f)$ from only ten response analyses. Although record selection with no attention to M and R is always to be discouraged, these results show that there is no apparent predictive benefit in keeping the explicit dependence of M and R. During the selection more care should be devoted to ensure a wide range of $S_a^r(f)$ for f values of interest rather than in selecting records with the most appropriate M and R values for the region around the site. Finally results not shown here for brevity,[2] indicate that the portion of $\sigma_{\ln AF(f)}$ due to the uncertainty in the soil properties is of secondary importance with respect to that due to record-to-record variability.

I.3.4 PSHA Results

The two soil deposits were assumed to be located in the Santa Barbara Channel (SBC) (Fig. 5), Southern California, for which a seismotectonic model was readily available. The site hazard was

readily available. The site hazard was computed both by a conventional PSHA approach with the Abrahamson and Silva[1] attenuation law for generic soil conditions, and by the proposed convolution method applied to both soil deposits. The latter method makes use of the rock hazard curves found using the same attenuation relation[1]. The median *AF (f)* in Fig 3 and the $\sigma_{\ln AF(f)}$ values in Fig 4 where used to estimate $S_a^s(f)$. The UHS displayed in Fig. 6 show that using a generic soil attenuation law may lead to severe underestimation of the hazard for $S_a^s(f)$ below approximately f=2Hz at low MRP values. The hazard at high frequencies (here above 2Hz) is overestimated by the predictive equation for generic soil conditions especially at high MRP values. The gap at high frequencies between the UHS found by convolution and by conventional PSHA, however, may be partly due to the application of rock outcrop motions directly to the column base. These differences in hazard prediction are due to the significant nonlinear response (Fig. 3) of the two soil columns considered in this study.

I.4 Summary and Conclusions

Two applications of a practical soil- and site-specific PSHA method have been presented in this paper. Soil surface hazard estimates more precise than those provided by attenuation equations for generic soil conditions can be found by explicitly considering the nonlinear behavior of the deposit via an amplification function. The dynamic behavior of the soil at all oscillator frequencies can be accurately predicted with as few as ten ground motions which may be selected without particular attention to specific scenario events (i.e., M and R pairs) representing the hazard at the site. Each record is run through a different characterization of the soil column to account for uncertainty in the soil parameters. This effect is minor.

References

Abrahamson, N.A., W.J. Silva, "Empirical Response Spectra Attenuation Relations for Shallow Crustal Earthquakes," *Seism. Res. Lett.*, 68 (1), pp. 94-127, 1997.

Bazzurro, P., C.A. Cornell, "Efficient PSHA for Nonlinear Soil Sites with Uncertain Properties," submitted to *Journ. Of Geotech. And Geoenvironmental Engineering*, ASCE, 1999.

Beresnev, I.A, G.M. Atkinson, P.A. Johnson, E.H. Field, "Stochastic Finite-Fault Modeling of Ground Motions from the 1994 Northridge, California, Earthquake," *II. Widespread Nonlinear Response at Soil Sites, BSSA*, 88(6), pp 1402-1410, 1998.

Electric Power Research Institute (EPRI), "Guidelines for Site Specific Ground Motions," Rept. TR-102293, Vol. 1-5, Palo Alto, CA, November 1993.

Faccioli, E., "A Stochastic Approach to Soil Amplification," *BSSA*, 66(4), pp. 1277-1291, 1976.

Li, X.S., Z.L. Wang, C.K. Shen, "SUMDES - A Nonlinear procedure for Response Analysis of Horizontally-layered Sites Subjected to Multi-directional Earthquake Loading," Dept. of Civil Engineering, University of California, Davis, March 1992.

Schnabel, P., H.B. Seed, J. Lysmer, "Modification of Seismograph Records for Effect of Local Soil Conditions," *B.S.S.A.*, 62, pp. 1649-1664, 1972.

Steidl, J.H., A.G. Tumarkin, R.J. Archuleta, "What is a Reference Site?", *B.S.S.A.*, 86(6), pp. 1733-1748, 1996.

Toro, G. "Probabilistic model of soil-profile Variability-Guidelines for Determining Design Basis Ground Motions," ed. J.F. Schneider, Electric Power Research Institute, EPRI TR-102293, Vol. 2, App. 6A, 1993.

Whitman, R.V., J.N. Protonotarios, "Inelastic Response to Site-modified Ground Motions," *Journal of the Geotechnical Engineering Division*, ASCE, 103 (10), pp. 1037-1053, 1977.

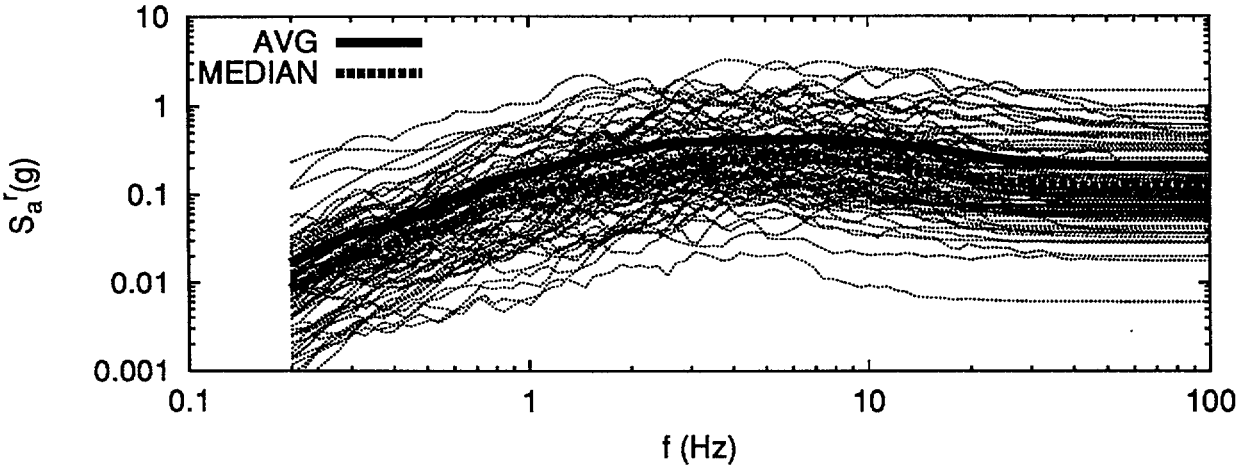

Figure I-1: Response spectra for 5% of damping of the selected records.

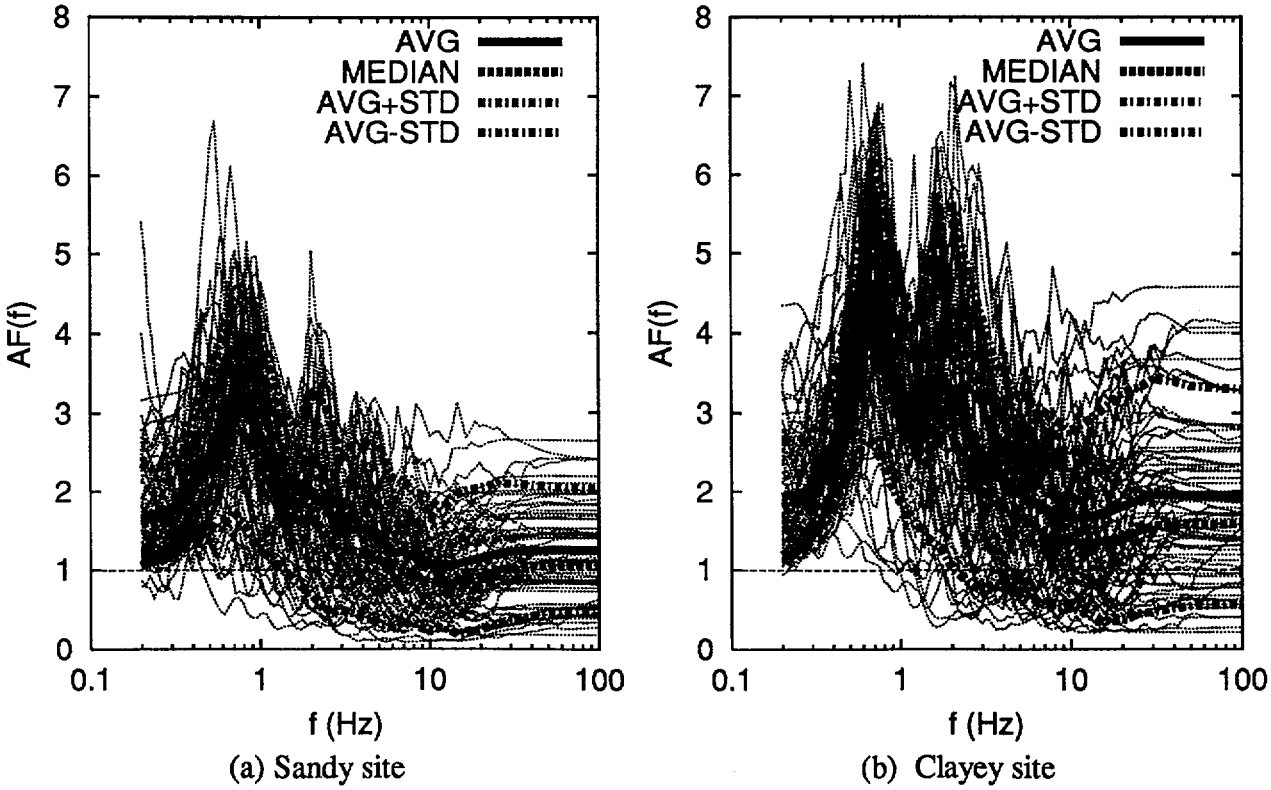

Figure I-2: Amplification function for both soil deposits.

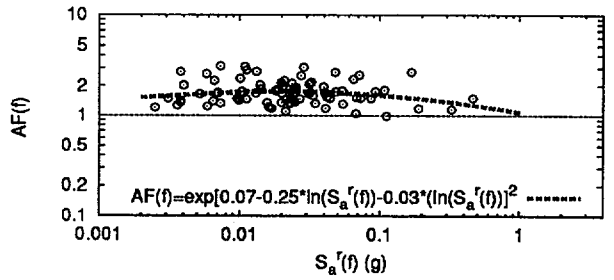

(a) Sand: f=0.33Hz

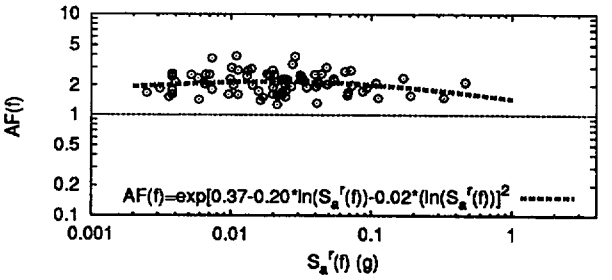

(b) Clay: f=0.33Hz

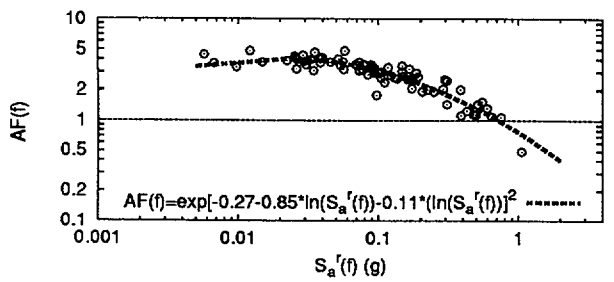

(c) Sand: f=1.0Hz

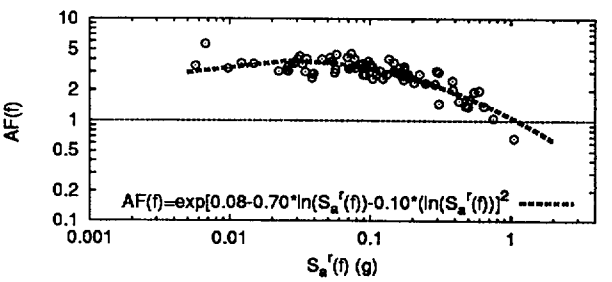

(d) Clay: f=1.0Hz

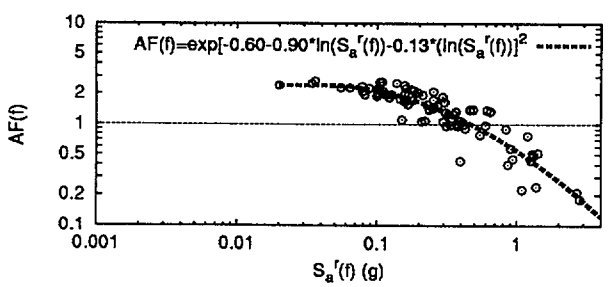

(e) Sand: f=5.0Hz

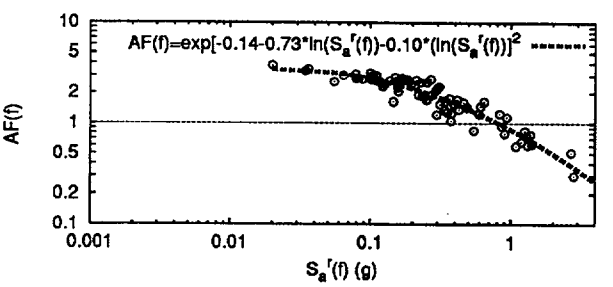

(f) Clay: f=5.0Hz

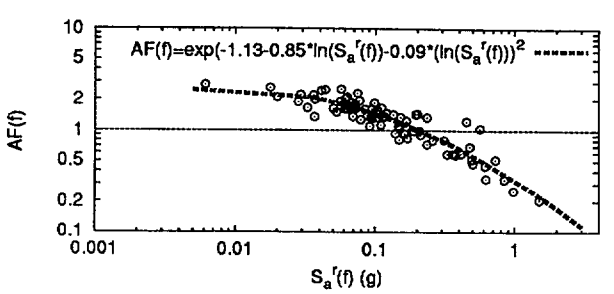

(g) Sand: PGA_r (100Hz)

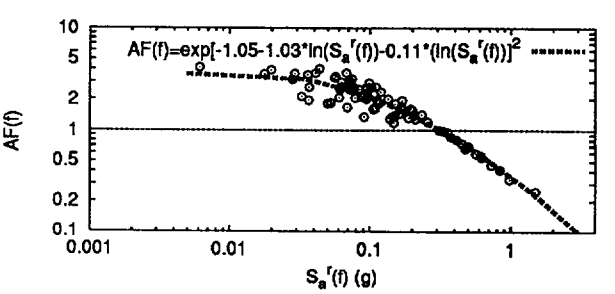

(h) Clay: PGA_r (100Hz)

Figure I-3: Regression of *AF (f)* on $S_a^r(f)$ at different f values for both soil deposits.

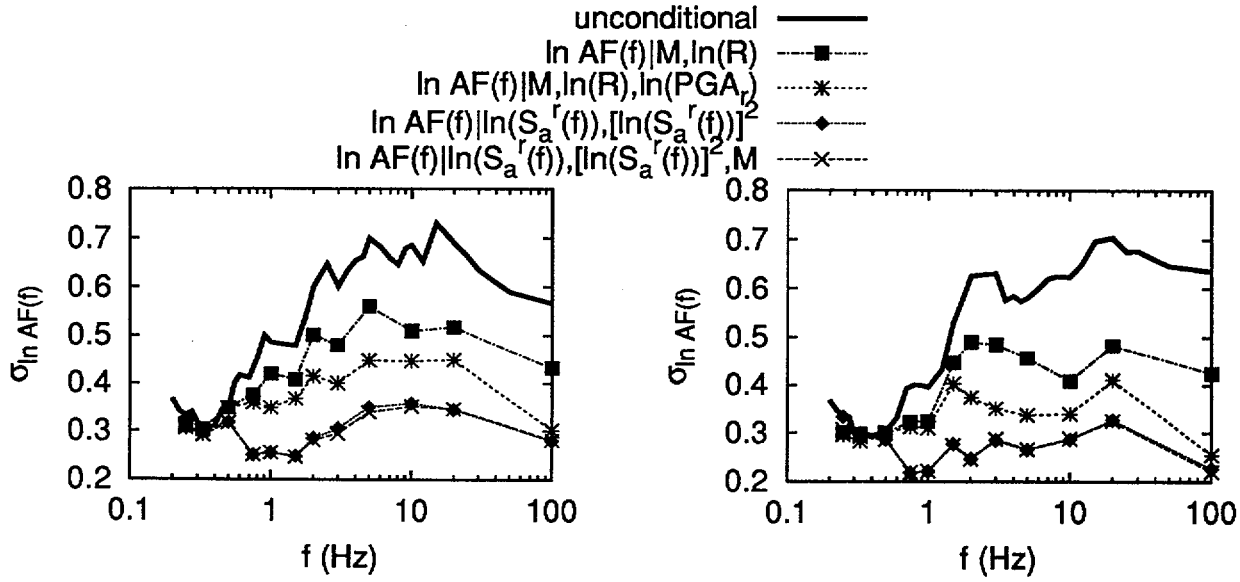

(a) Sandy deposit

(b) Clayey deposit

Figure I-4: Regression of $AF\ (f)$, on M, R, $S_a^r(f)$, and PGA_r.

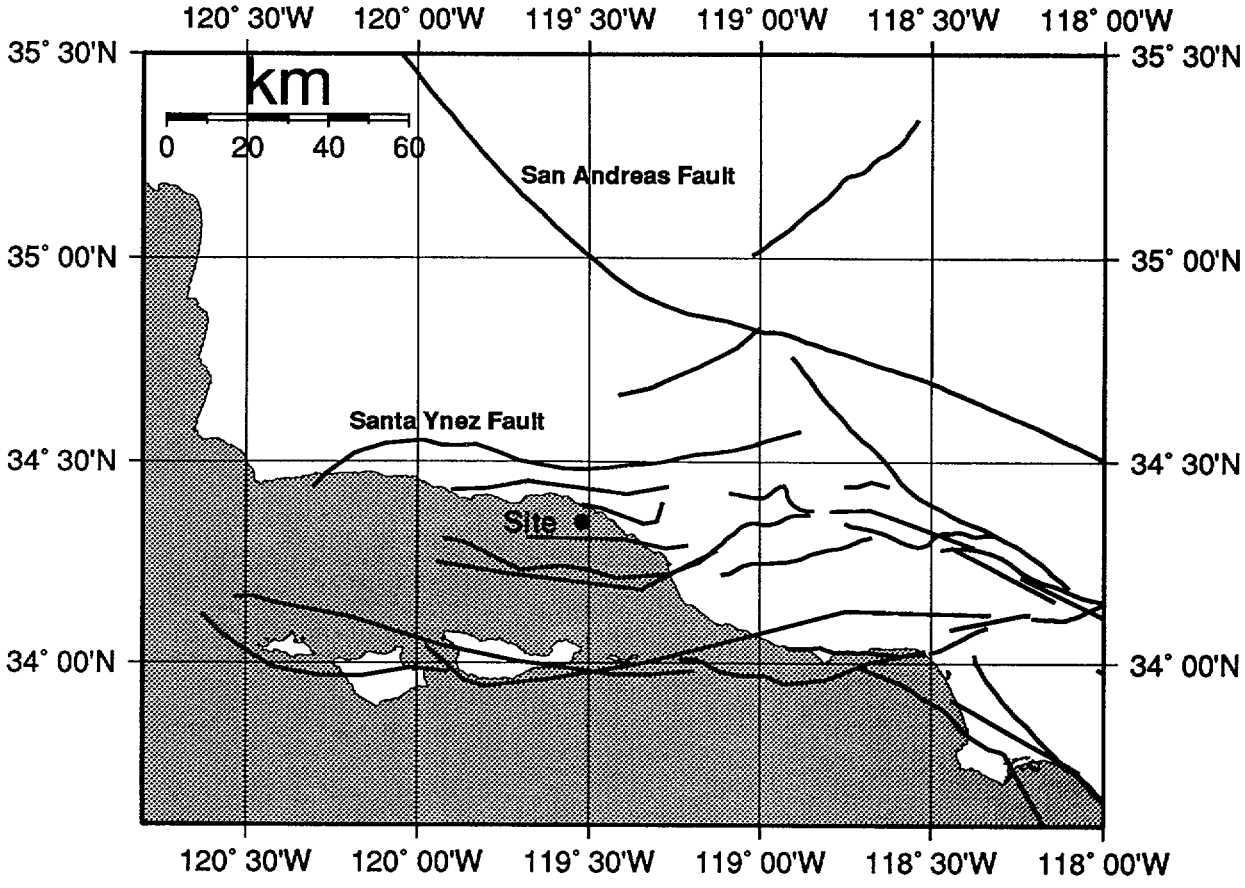

Figure I-5: Location of the site in the Santa Barbara Channel.

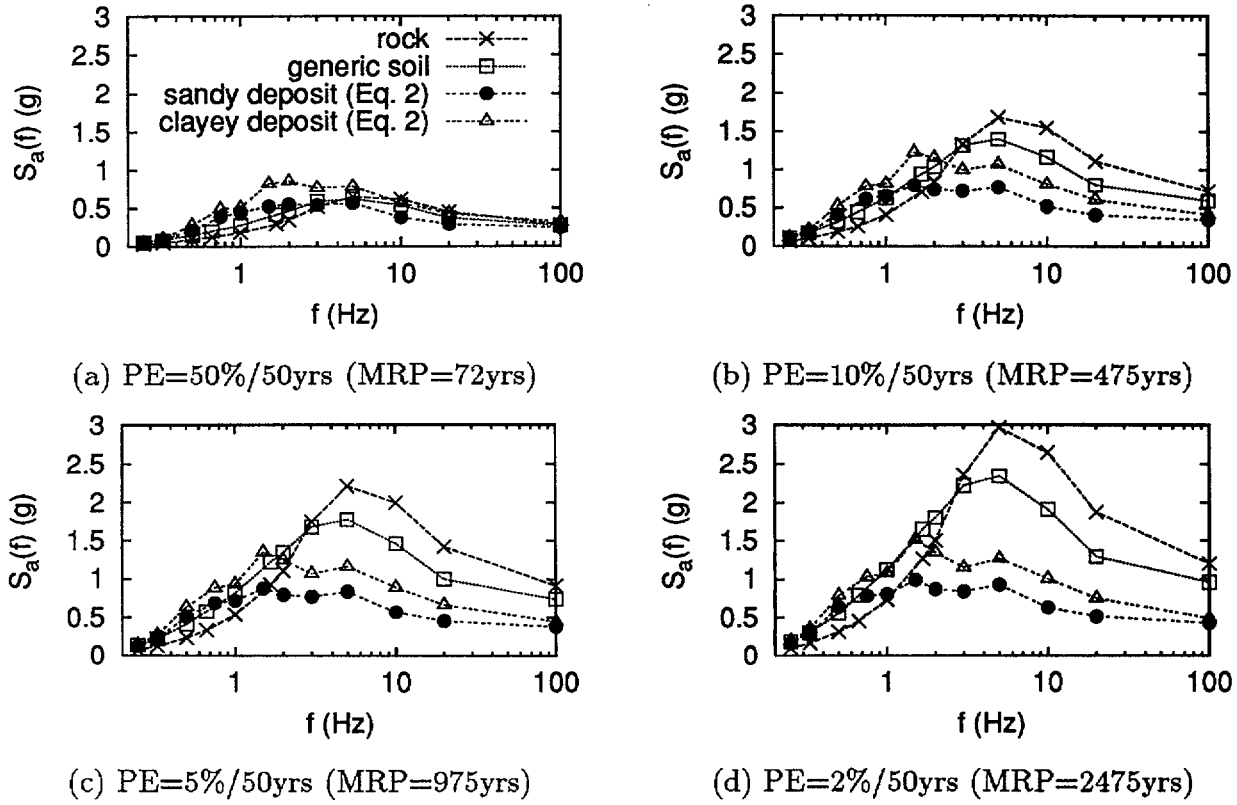

(a) PE=50%/50yrs (MRP=72yrs)

(b) PE=10%/50yrs (MRP=475yrs)

(c) PE=5%/50yrs (MRP=975yrs)

(d) PE=2%/50yrs (MRP=2475yrs)

Figure I-6: Uniform Hazard Spectra (UHS) for the SBC site. (PE=Probability of Exceedence; MRP=Mean Return Period.)

APPENDIX J CHARACTERISTICS OF VERTICAL STRONG GROUND MOTIONS FOR APPLICATIONS TO ENGINEERING DESIGN

J.1 Introduction

In the near-source region (distance R $\leq$ 10 to 15 km) of large earthquakes, the characteristics of strong ground motions change in stable and predictable ways. Durations become significantly shorter (Chang et al., 1996; Abrahamson and Silva, 1997), velocity and displacement time histories increase significantly in amplitude and become more pulse-like (depending upon rupture directivity effects), long period fault normal motions show a stable increase over fault parallel motions (Somerville et al., 1997), and short period vertical motions can exceed horizontal motions (Niazi and Bozorgnia, 1991; Bozorgnia et al., 1995) at both rock and soil sites (EPRI, 1993).

For vertical motions, the trends indicated above imply that the commonly adopted vertical-to-horizontal response spectral ratio of 2/3 (Newmark and Hall, 1978) may be significantly exceeded at short periods in the near-source distance range. The increase in near-source strong motion recordings at both rock and soil sites aid in constraining empirical attenuation relationships and provide direct empirical estimation of statistical spectral shapes for vertical and horizontal components. These data also make it possible to examine the dependencies of the vertical-to-horizontal response spectral ratio (V/H) on magnitude, distance, and site conditions.

An additional, important use of these data is to examine similarities and differences in the characteristics of the time histories between vertical and horizontal motions. For design motions, the relative phasing between horizontal and vertical motions can be an important issue, leading to different structural analyses and design decisions depending on whether or not significant energy is expected to occur both vertically and horizontally at nearly the same time.

J.2 Effects of Site Conditions on the Characteristics of Vertical and Horizontal Strong Ground Motions

The Geomatrix categorization criterion listed in Table J-1 is used to broadly classify strong motion recording sites into rock or soil. While the distinction between rock and soil is becoming less clear for Western United States (WUS) sites as more rock sites are drilled and velocities determined (EPRI, 1993; BNL, 1997), this largely qualitative classification scheme captures significant and stable differences in strong ground motions (Sadigh et al., 1997; Abrahamson and Silva, 1997; BNL, 1997).

J.3 Generic Rock and Soil Site Velocity Profiles

To demonstrate the compression- and shear-wave velocity profiles implied by the rock and soil categories (Table J-1), Figures J-1 and J-2 show median (lognormal distribution) and 1 σ velocity profiles computed for the two categories. The velocity profiles were computed from measured (downhole or crosshole) velocities at strong motion sites classified as Geomatrix A or B (Figure J-1) or C or D (Figure J-2). For the generic rock site, a strong velocity gradient is seen in the top 150 ft, with low near-surface shear- and compression-wave velocities (Vs and Vp, respectively) being

approximately 800 ft/sec and 1,600 ft/sec. The shear-wave velocity value of about 800 ft/sec departs significantly from the classically assumed value of about 2,500 ft/sec which is not reached, on average, until a depth of about 70 to 100 ft. With such low near- surface velocities, these rock sites can be expected to show some nonlinear effects under very high loading conditions (BNL, 1997).

The absolute variability of both the shear- and compression-wave velocities is high (COV 0.5 to 0.6) and there is little to suggest the presence of the water table at a compression-wave velocity of about 5,000 ft/sec. Contrasting the rock site profiles in Figure J-1 with those of the soil in Figure J-2, significant differences are immediately apparent. Interestingly, over the top 50 ft or so, the compression-wave velocities are very similar for both the rock and soil sites. For the soil site, the much lower shear-wave velocities imply a significantly higher Poisson's ratio, reflecting a larger Vp/Vs ratio for soil than for rock. Additionally for the soil site, the effect of the water table on the compression-wave velocity is apparent in the nearly constant velocity of the fluid phase at about 5,000 ft/sec at depths from around 100 ft to 250 ft. Beyond about 250 ft, the compression-wave velocity of the skeleton material exceeds that of the fluid phase, increasing Vp with depth.

The velocity variability at the soil sites is much less in absolute variation but similar to that of the rock sites in a relative sense ($\sigma_{ln} \approx 0.4$ to 0.5). The lower absolute variability suggests that strong ground motions are less variable at soil than at rock sites.

To contrast the dynamic material properties between rock and soil sites further, Figures J-3 and J-4 show Poisson's ratios computed from the compression- and shear-wave velocity profiles. The +1 σ values of Poisson's ratio greater than 0.5 are non-physical and result from a higher shallow ratio combined with a large variability. The higher variability in dynamic material properties for the rock versus the soil sites is reflected in the larger variation in Poisson's ratio for the rock site (Figure J-3 verses Figure J-4). Rock sites have lower overall Poisson's ratios, and they increase with depth to about 70 ft, remain nearly constant to a depth of about 200 ft, and then decrease to a value near 0.25 at a depth of 500 ft. Interestingly, Poisson's ratio for the soil sites (Figure J-4) show a similar trend but shifted nearly a constant amount to a depth of about 350 ft. Beyond about 350 ft, Poisson's ratio for the soil sites decreases less rapidly than for rock sites, remaining at a value of around 0.4 to a depth of 500 ft.

The dashed lines on Figures J-3 and J-4 represent smooth Poisson's ratio models and are shown in Figure J-5 for the generic rock and soil sites. The similar patterns and nearly constant shift to a depth of about 350 ft are quite apparent in the smooth models.

The differences in Poisson's ratio as well as the overall velocities between the rock and soil sites may have important implications for the differences in vertical and horizontal motions. At rock sites, even though the shallow shear-wave velocities are low, the steep velocity gradient results in shear-wave velocities exceeding 2,000 to 3,000 ft/sec at depths of 50 to 70 ft. As a result, for the same level of input motion, nonlinear effects are expected to be much less pronounced than at a corresponding soil site and are expected to be confined to the top 50 to 100 ft. The higher rock velocities and shallower potentially nonlinear zone will also tend to confine nonlinear effects to higher frequencies (BNL, 1997). If vertical motions are more linear than horizontal, perhaps because of lower strains for inclined SV-waves and contributions of P-waves, the magnitude dependence of the V/H ratio would

be expected to be less at rock sites than at soil sites. As earthquake magnitude increases, the higher loading levels induce more nonlinearity in the horizontal motions at soil sites than the rock sites. The vertical motions, remaining relatively linear, simply scale up and broaden in spectral content as magnitude increases. As a result, the magnitude scaling of the V/H ratios should be inversely proportional to the profile stiffness, and should be significantly larger for soil than for rock.

In addition to the effects of overall stiffness, the large jump in Poisson's ratio at the soil/rock interface (or steep gradient) at soil sites (Figure J-5) will have an important impact on incoming wavefields. For a generic California deep crustal model, the average shear- and compression-wave velocities at the surface are about 3,500 to 4,500 ft/sec and 6,500 to 8,000 ft/sec, respectively (BNL, 1997). For a deep generic soil site, Figure J-2 shows shear- and compression-wave velocities at a depth of 500 ft of about 2,000 ft/sec and 6,500 ft/sec respectively. Transition to rock at this depth then would likely involve a very steep shear-wave velocity gradient with a factor of 2 or more jump in velocity. For the compression wave, the transition is much less pronounced, a factor of only 1.0 to 1.2 on average. This consequence of the drop in Poisson's ratio between soil and rock, manifested as a large jump in shear-wave velocity, tends to refract (bend) incident shear-waves much more severely than incident compression-waves. In passing through the rock/soil transition zone, the incident shear-waves will become much more vertical than the incident compression-waves. For incident SV-waves, this will have the effect of converting vertical motions to horizontal motions while the compression-waves largely remain inclined until depths of 100 to 200 ft where they are amplified and refracted (bent to a more vertical incidence) by the shallow compression-wave gradient (Figure J-2).

Since earthquake sources emit much larger shear-wave amplitudes than compression-wave amplitudes, by the ratio of the source-region velocities cubed ($(Vp/Vs)^3 \approx 5$), incident inclined SV-waves may be expected to dominate vertical motions at close distances. At large distances, the SV-wave is beyond its critical angle and does not propagate to the surface very effectively (Kawase and Aki, 1990). At a source depth of 8 km and a generic California crustal model (Figure J-3), the SV-wave critical angle for geometrical ray theory occurs at an epicentral distance of about 5 km for a point-source. Crustal heterogeneity and source finiteness (vertical extent) tend to extend this distance somewhat. Also, geometrical ray theory is appropriate for high frequencies, and low frequency energy tend to be refracted less by the shallow velocity gradients, also resulting in extending the distance to the SV-wave critical angle. However, even considering these effects, the SV-wave is not likely to dominate the vertical component of rock motion at distances exceeding 10 to 20 km.

At soil sites, because of the large change in shear-wave velocity at the base of the profile and the accompanying wave refraction, compression-waves may be expected to dominate the vertical motions at near as well as far distances. Additionally, because of the large compression-wave velocity gradient from the surface to depths of about 100 to 200 ft, short period compression waves will be amplified, which will result in large short period vertical motions.

J.4 Short-Period Time Domain Characteristics of Vertical Motions

A series of plots from the CDMG initial earthquake data reports illustrate the effects of site conditions on acceleration time histories for vertical and horizontal components. These plots show all three components for each site in a convenient format for illustrative purposes.

As an illustration of close-in rock sites, Figure J-6 shows three component acceleration time histories at the Pacoima Dam (Downstream) and Corralitos sites for the 1994 **M** 6.7 Northridge and 1989 **M** 6.9 Loma Prieta earthquakes. Both sites are located about 8 km from the fault and both sets of records show very similar motions on the horizontal and vertical components. Structures founded on rock conditions at close distances may then be expected to experience simultaneous horizontal and vertical demands at similar levels and over a fairly broad period range.

For close-in soil sites, Figure J-7 shows distinctly different features in the Sylmar County Hospital and Arleta records for the Northridge earthquake. These soil sites are close-in recordings at fault distances of 6.1 km for Sylmar and 9.2 km for Arleta. Unlike the rock site recordings, the soil site records show strong short-period motion arriving significantly before the large horizontal motions. Structures founded on deep soil can be expected to experience vertical and horizontal demands significantly different from those on rock conditions. The vertical demands at close-in soil sites can be characterized as out-of-phase with the dominant horizontal motions and of much higher frequencies. The largest short period motions on the vertical component may arrive before those of the horizontal and will be larger than the short period horizontal motions. During the passage of the dominant horizontal component motions, the vertical demands on a structure could be characterized as random high-frequency chatter that may exceed 1g at short periods. This is markedly different from the vertical motions at close-in rock sites, which tend to show strong low-frequency coherence with the horizontal motions. (Further illustrations of this coherence are presented in the next section.)

For the more distant sites, Figure J-8 shows some interesting features across the Gilroy array for motions during the 1989 Loma Prieta earthquake. Rock sites Gilroy 6 and 7, at fault distances of 19.9 and 24.2 km respectively, show features similar to those at the close-in soil site: earlier arriving and high-frequency vertical motions out-of-phase with the dominant horizontal motions. At rock site Gilroy 1 however, at a fault distance of 11.2 km, the vertical motions display early arriving high frequency energy as well as low-frequency energy coherent with the dominant horizontal motions. A possible explanation for this behavior is that this site, at a fault distance of about 11 km, is in the transition region from close-in to more distant rock site characteristics.

An interesting and apparent contradiction to the expected close-in rock site characteristics are the recordings at Pacoima Kagel Canyon for the Northridge earthquake (Figure J-9). This rock site is at a fault distance of 8.2 km, about the same distance as the Pacoima Downstream site (Figure J-6), but displays soil site characteristics on the vertical component: early arriving high frequency energy and out-of-phase motions with the horizontal components. As part of a recent, Caltrans/NSF/EPRI-sponsored project to Resolve Site Response Issues associated with the Northridge Earthquake (ROSRINE project), the Pacoima Kugel Canyon site has recently been drilled and logged, as have been other sites. Based on the shear-wave velocity logging, the site is misclassified. With shear-wave velocities of just under 2,000 ft/sec from about 100 ft to the bottom of the hole at about 300 ft, the site is closer to a stiff soil than rock (Figures J-1 and J-2). This is not entirely unexpected, the site being underlain by the Saugus formation, a typically soft Los Angeles area sandstone.

For the distant ($R \geq 10$ to 15 km) soil sites, Figure J-10 shows the remaining sites across the Gilroy array that recorded the Loma Prieta earthquake. Site Gilroy 2 is at fault distance of 10.7 km and sites 3 and 4 are at fault distances of 14.4 and 16.1 km respectively. As with the close-in soil sites (Figure

J-7) and the distant rock sites (Figure J-8), the vertical motions show high-frequency early arriving energy and little coherence with the dominant horizontal motions.

These acceleration time history plots illustrate general trends in short period vertical and horizontal motions. For rock sites at close distances ($R \leq 10$ to 15 km) the plots show dominant SV motion on the vertical component with phasing similar to the horizontal components. At soil sites, compression-waves dominate the vertical motions, showing earlier-arriving and larger higher frequency energy content. For more distant sites, compressional-wave energy tends to dominate the vertical component at both rock and soil sites.

J.5 Response Spectral Characteristics of Vertical Motions

In order to illustrate the distance and site dependencies of vertical motions in more detail, over a broad frequency period range, Figures J-11 to J-18 show 5% damped pseudo-absolute acceleration response spectra and acceleration, velocity, and displacement time histories for selected sites. Cases examined are close-in and distant rock and soil sites. Acceleration, velocity, and displacement time histories are plotted to show that at close-in soil sites and at more distant rock and soil sites, long period coherence exists between vertical and horizontal components. This results in the dominant long period motions being "in-phase" in the sense that the largest long period motions occur at nearly the same time on both the vertical and horizontal components.

For the close-in rock site, Figure J-11 shows response spectra computed for the vertical and two horizontal component records at the Southern California Edison Lucerne site from the 1992 **M** 7.2 Landers earthquake. The fault distance is about 2 km and the vertical component slightly exceeds the horizontal components at periods shorter than about 0.1 sec. At long periods, beyond about 1 sec, the vertical is comparable to the smaller of the horizontal components, the fault-parallel motion. The period range of nearly constant spectral acceleration in the horizontal components, about 2 to 5 sec, is likely due to the effects of directivity.

The corresponding time histories are shown in Figure J-12 and reveal strong coherence among components. The maximum velocity and displacement of the vertical component exceed those of the fault-parallel component (labeled "345"). The maximum vertical displacement is about 15 cm (6 inches) occurring over a 2 sec period of time during which the fault-normal direction (labeled "260") moved about 60 cm (2 ft).

For the close-in soil site, Figures J-13 and J-14 show the response spectra and time histories at the Arleta site for the 1994 Northridge earthquake. The fault distance is 9.2 km and the vertical component greatly exceeds the horizontal components at periods shorter than about 0.2 sec. Beyond about 2 sec, as with the rock site Lucerne, the vertical component becomes comparable to the horizontals. The time histories are shown in Figure J-14 and indicate long period coherence and out-of-phase short period energy (as noted previously in Figure J-7).

For the more distant sites, Figures J-15 and J-16 show response spectra and time histories for the Gilroy array no. 6 rock site and Figures J-17 and J-18 show corresponding plots for the Gilroy array no. 4 soil site. These motions occurred during the 1989 Loma Prieta and the fault distances are 16.1

and 19.9 km for sites 4 and 6 respectively. For both sites, the short period vertical motions relative to the corresponding horizontal motions are significantly lower, as compared to the close-in sites. Interestingly, as with the close-in sites, the long period vertical motions approach the horizontal motions for periods beyond about 2 to 4 sec. This feature is not predicted by either empirical or numerical modeling and suggests that vertical motions are associated with high variability.

The corresponding time histories, Figures J-16 and J-18, show the usual pattern: early arriving short period energy on the verticals that is out-of-phase with the horizontal motions, and longer period motions that are more in-phase between the components.

J.6 Magnitude, Site, and Distance Dependencies of Horizontal and Vertical Component Response Spectral Shapes

To examine empirically the role of possible site nonlinearity in the V/H ratios, statistical spectral shapes (SA/PGA) were computed for magnitude bins centered on **M** 5.5 and **M** 6.5 for both rock and soil sites. The magnitude bins are one unit wide (**M** 5.5 = **M** 5 - 6, **M** 6.5 = **M** 6 - 7 for soil, **M** 6.5 = **M** 6-7+, for rock) to include enough records to produce smooth and stable shapes.

The distance range was truncated at 50 km to avoid the effects of distance dependencies on the shapes. Records were selected from a strong motion database that includes available strong motion data for $\mathbf{M} \geq 4.5$. For this application, only earthquakes occurring in tectonically active regions were selected (the 1995 **M** 6.9 Kobe earthquake is included).

To examine the effects of the level of motion on the vertical and horizontal component spectral shapes, two distance bins were selected: 0 to 10 km and 10 to 50 km. For **M** 5.5 rock sites, Figure J-19 shows the horizontal and vertical statistical shapes. To assess nonlinear effects, Figure J-19 shows shapes computed for the two distance bins: 0 to 10 km and 10 to 50 km. The vertical spectral shapes (dashed lines) show more short period energy than the horizontal shapes (solid and dotted lines) and about the same level of maximum spectral amplification. The vertical shapes have a maximum spectral amplification near 0.1 sec whereas the shapes for the horizontal component peak near 0.2 sec. This difference is likely due to differences in damping, with the vertical component showing significantly less damping than the horizontal. The lack of any significant distance dependency in this shift in peak spectral amplification between the vertical and horizontal components suggests that the difference in damping exists in the shallow portion of the path and that the sites behave in a linear manner. The shallow crustal damping is thought to occur in the top 1 to 2 km of the crust (Anderson and Hough 1984; Silva and Darragh, 1995) and is generally modeled as a frequency independent exponential damping term with a damping parameter termed kappa:

$$\kappa = \frac{H}{\overline{V_S}\,\overline{Q}}, \qquad \overline{Q} = \frac{1}{2\,\overline{\eta}} \tag{J-1}$$

where H is the depth of the damping zone (1 to 2 km), $\overline{V_S}$ and $\overline{Q}$ are the average shear-wave velocity and quality factor over the depth H, and $\overline{\eta}$ is the corresponding damping ratio (decimal).

Response spectral shapes depend strongly on kappa, shifting to shorter periods as kappa decreases (Silva and Darragh, 1995). To illustrate this effect, Figure J-20 shows response spectral shapes computed using a simple point-source model with kappa values ranging from 0.006 sec to 0.160 sec. The shift in shape with kappa is easily seen and a peak near 0.2 sec is consistent with a kappa value of about 0.04 sec while a factor of two shift in the peak to about 0.1 sec corresponds to a similar shift in kappa value to about 0.02 sec. Interestingly, the factor of 2 shift in kappa for the verticals ($\kappa_V \approx \kappa_H/2$; EPRI, 1993) was also found by Anderson (1991) in a detailed analysis of vertical and horizontal motions recorded at rock sites and may be a result of the contribution of compressional waves to vertical strong ground motions. The kappa or shallow crustal damping effect is the likely mechanism controlling the large shift in spectral shapes between soft rock WUS spectral shapes and hard rock CEUS spectral shapes (Silva and Darragh, 1995) and will impact hard rock vertical spectral shapes as well as horizontal shapes.

To continue the shape comparison for rock sites, Figure J-21 shows horizontal and vertical shapes computed for **M** 6.5 (**M** 6.0 - 7+) at the two distance ranges: 0 to 10 km and 10 to 50 km. As with the **M** 5.5 shapes, there is a distinct shift in the peak amplification frequency between vertical and horizontal spectra of nearly 2. Also there does not appear to be a strong distance or amplitude effect on either the vertical or horizontal shapes suggesting largely linear response at these ground motion levels.

To consider soil sites, Figures J-22 and J-23 show the vertical and horizontal response spectral shapes for **M** 5.5 (**M** 5.0 - 6.0) and **M** 6.5 (**M** 6.0 - 7+) earthquakes. As with the **M** 5.0 rock shapes, there is about a factor of two difference in the periods of maximum spectral amplification between the vertical (near 0.1 sec) and horizontal shapes (near 0.2 sec). Also there is no appreciable and stable shift in either the vertical or horizontal shapes with distance (0 - 10 km or 10 - 50 km) reflecting largely linear response. Similar periods of peak amplification between rock and soil of about 0.2 sec for the horizontal and 0.1 sec for the vertical suggests similar low strain damping values at both rock and soil sites.

For the **M** 6.5 (**M** 6.0 - 7+) soil records, shown in Figure J-23, the horizontal shapes show a well-defined and broad-band shift between 10 to 50 km and 0 to 10 km. The horizontal shape for 10 to 50 km peaks near 0.2 sec whereas the shape for 0 to 10 km peaks near 0.3 sec, crosses the 10 to 50 km shape at that period, remains above the 10-50 km shape out to nearly 10 sec. These characteristics are very similar to those shown in Figure J-20 which illustrated the effects of kappa on response spectral shapes. The Figure J-23 results suggest nonlinear response resulting in an overall increase in kappa from about 0.04 sec (linear soil response) to about 0.06 to 0.08 sec at the higher amplitude levels.

For the vertical component in Figure J-23, a slight shift appears to be present between the shapes computed for the 0 to 10 km and 10 to 50 km bins but the shift is in the wrong direction and is not stable with period, crossing at about 0.1 and again near 2.0 sec. This is likely due to a sampling problem with too few sites contributing to the close-in (0 to 10 km) shapes.

The analyses of response spectral shapes reveals several features of interest: (1) a consistent shift in shapes between vertical and horizontal components at both rock and soil sites indicating lower shallow crustal damping for vertical components by about a factor of about 2, (2) similar low-strain damping values for rock and soil sites, and 3) horizontal component soil shapes that show nonlinear response characterized by a stable and broad-band shift in shape to longer periods at higher amplitude levels. These features are important factors in understanding the effects of magnitude, distance, and site condition on vertical-to-horizontal response spectral ratios.

J.7 Empirical and Numerical Model Estimates of the Vertical-to-Horizontal Response Spectral Ratios

A combination of empirical attenuation relations and numerical modeling is used to estimate vertical-to-horizontal ratios as functions of magnitude, distance, and site conditions. While the empirical relations are reasonably well constrained for WUS (or other tectonically active regions), little data exist for **M** > 5.0 for CEUS conditions at distances of interest ($R \leq 20$ km).

The only large magnitude earthquake considered representative of the CEUS that generated close-in strong motion records is the **M** 6.8 1985 Nahanni earthquake. Strong motions were recorded at three sites, all hard rock and all within 20 km of the source. This earthquake, along with smaller magnitude CEUS hard rock recordings, clearly show significantly different spectral content between WUS and CEUS horizontal rock motions. This feature is illustrated in Figure J-24, which compares WUS and CEUS horizontal component rock site response spectral shapes for **M** around 6.5 and 4.0. The difference in short period spectral content between WUS and CEUS is significant and consistent between different magnitude earthquakes and is attributed to differences in shallow crustal damping or kappa values (Silva and Darragh, 1995). For CEUS rock site vertical components, an open question exists as to whether they show a shift to even shorter periods than the horizontal components (see Figure J-21 for WUS rock). The effective bandwidth of current recordings is not capable of resolving this issue, however if similar physical mechanisms control the motions at WUS and CEUS rock sites, some degree of shift would be expected and should be reflected in estimates of CEUS V/H ground motion ratios.

These differences in rock site spectral content have implications for soil motions since WUS and CEUS control motions (at depth), would be expected to have differences in spectral content, given the differences for rock outcrop motions. The differences in WUS and CEUS control motion spectral content may not result in significantly different deep soil horizontal motions due to the effects of material damping and nonlinearity. However, vertical component soil motions, if response remains largely linear in compression (constrained modulus), may have very high short period levels at close distances to large magnitude earthquakes (EPRI, 1993).

J.8 Applications to WUS Rock and Deep Soil Sites

For rock sites, the recommended V/H ratios reflect the average of Sadigh et al. (1997) and Abrahamson and Silva (1997) empirical relations, while for soil, because Sadigh et al. (1997) do not present a relationship for the vertical component, only the Abrahamson and Silva (1997) relation is used. Figure J-25 shows empirical vertical and horizontal spectra (5% damping) for **M** 6.5 at a

distance of 5 km for both rock and soil site conditions. A shift of the peak response of the vertical spectra to shorter periods than the horizontal is present showing a crossing in spectral levels at short periods. At this close distance (R = 5 km), response spectral ratios (V/H) exceed 1 at short periods and drop significantly at longer periods.

To examine the distance dependency of the V/H ratio for WUS, Figure J-26 shows empirical V/H ratios computed for both rock and soil sites. As expected, from the earlier examination of response spectra at individual sites (Figures J-11, J-13, J-15, and J-17), the maximum rock site V/H ratios are lower than the corresponding ratios for soil sites. For the rock sites, the distance dependency is considerably less than that for soil, a maximum of about 1.5 in the distance range 1 to 40 km. The larger distance dependence in the V/H ratios for soil sites may be due to nonlinear response of the soils: as distance increases, relatively less damping occurs in the soil column.

To examine the magnitude dependency of the V/H ratios, Figure J-27 shows empirical V/H ratios for rock and soil sites computed for distances of 1 and 20 km. The magnitude dependence of the V/H ratios is stronger for soil sites than for rock sites, again possibly reflecting effects of nonlinearity. Additionally, the magnitude dependence decreases with increasing distance for both rock and soil sites. For rock sites, this may be an artifact of the magnitude saturation built into the empirical relations, being different for rock and soil sites.

These empirical V/H ratios are reasonably well constrained and can provide the basis for developing smooth design ratios for WUS rock and deep moderately stiff soils. For applications to design motions, strong consideration should be given to adequate conservatism, which should reflect the higher uncertainty in vertical motions compared to horizontal motions, particularly for close distances to large magnitude ($\mathbf{M} \geq 7$) earthquakes.

J.9 Applications to CEUS Rock and Deep Soil Sites

Based on the comparisons of the spectral content between WUS and CEUS rock site spectral shapes shown in Figure J-24, differences in rock (and possibly soil) V/H ratios are expected between the two tectonic regions (EPRI, 1993).

As previously discussed, due to the paucity of recordings ($\mathbf{M} \geq 5$, $R \leq 50$ km) reflecting CEUS conditions, some form of modeling is necessary to assess the appropriateness of WUS V/H ratios for engineering design applications.

J.10 Computational Model

To model vertical motions, inclined P-SV waves from the stochastic point-source ground motion model (EPRI, 1993) are assumed and the P-SV propagators of Silva (1976) are used to model the crust and soil response to inclined P-SV wavefields. The angle of incidence at the top of the source layer is computed by two-point ray tracing through the crust and soil column (if present) assuming incident compression-waves.

To model soil response, a soil column is placed on top of the crustal structure and the incident inclined P-SV wavefield is propagated to the surface where the vertical (or radial) motions are computed.

J.11 Treatment of Soil Response for Vertical Motions

Commonly, equivalent-linear site response analyses for vertical motions have used strain-iterated shear moduli from a horizontal motion analysis to adjust the compression-wave velocities assuming either a strain-independent Poisson's ratio or bulk modulus. Some fraction (generally 30% to 100%) of the strain-iterated shear-wave damping is used to model the compression-wave damping, and a linear analyses is performed for vertically propagating compression waves using the horizontal control motions scaled by some factor near 2/3.

The equivalent-linear approach implicitly assumes some coupling between horizontal and vertical motions. This is necessitated by the lack of well determined M/M_{max} (constrained modulus over maximum constrained modulus) and damping curves for the constrained modulus. Ideally the strain dependency of the constrained modulus should be determined independently of the shear modulus. Also, the conventional approach assumes vertically-propagating compression waves and not inclined P-SV waves. Additionally, the use of some fraction of the horizontal control motion is an approximation and does not reflect the generally greater high-frequency content of vertical component motions at rock sites due to lower kappa values (EPRI, 1993).

Alternatively, fully nonlinear analyses can be made using two- or three-component control motions (Costantino, 1967; 1969; Li et al., 1992; EPRI, 1993). These nonlinear analyses require two- or three-dimensional soil models that describe plastic flow and yielding and the accompanying volume changes as well as coupling between vertical and horizontal motions through Poisson's effect. These analyses are important to examine expected dependencies of computed motions on material properties and may have applications to the study of soil compaction, deformation, slope stability, and component coupling. However, the models are very sophisticated and require specification of many parameters, at least some of which are poorly understood.

In the current implementation of the equivalent-linear approach to estimate vertical to horizontal response spectral ratios, the horizontal component analyses are performed for vertically propagating shear waves using an equivalent-linear random vibration theory (RVT) methodology coupled to the point-source stochastic ground motion model (EPRI, 1993; Schneider et al., 1993). To compute the vertical motions, a linear analysis is performed for incident inclined P-SV waves using low-strain, compression- and shear-wave velocities derived from the generic shear- and compression-wave velocity profiles (Figures J-1 and J-2). Compression-wave damping is assumed to be equal to the low strain shear-wave damping (Johnson and Silva, 1981). The horizontal component and vertical component analyses are assumed to be independent.

These approximations (linear analysis for the vertical component, and uncoupled vertical and horizontal components) have been checked by comparing results of fully nonlinear analyses at soil sites Gilroy 2 and Treasure Island to recorded vertical and horizontal motions from the 1989 Loma Prieta earthquake (EPRI, 1993). The nonlinear analyses indicate that little coupling exists between

the vertical and horizontal motions for the ranges in control motions analyzed (maximum about 0.5g). These assumptions will, if anything, result in conservative estimates of vertical motions since a higher degree of coupling implies degradation of constrained modulus and an accompanying increase in compression-wave damping.

The point-source computational model has been validated for horizontal motions with the Loma Prieta earthquake by comparing recorded motions with model predictions (Schneider et al., 1993) and more recently with 14 additional earthquakes (**M** 5.0 - 7.4) at about 500 sites (BNL, 1997). For vertical motions, current validation includes comparisons of recorded motions to model predictions for the 1989 **M** 6.9 Loma Prieta earthquake (20 rock and 16 soil sites), 1992 **M** 7.2 Landers earthquake (3 rock and 9 soil sites), and the 1994 **M** 6.7 Northridge earthquake (16 rock and 56 soil sites). The variability of vertical motions is not modeled as well as horizontal motions because observed vertical motions show more variation than the horizontal and the model is not able to capture the increased variability. The larger standard error associated with vertical motions is reflected in empirical relations (Abrahamson and Silva, 1997).

As an example of the comparison of model predictions to recorded motions, Figure J-28 shows recorded and computed vertical and horizontal motions for the **M** 7.2 Landers earthquake at the rock* site Lucerne ($R \approx 2$ km). The simple point-source, using the generic shallow rock profile with equivalent-linear analyses for the horizontal component and a linear analysis for the vertical appears to capture the general features of the recorded motions.

To generate V/H ratios based on numerical modeling, the shallow generic profiles (Figures J-1 and J-2) were placed on top of the generic California crust (Figure J-29). For equivalent-linear analyses, recently developed rock and cohesionless soil modulus curves (G/G_{max}) and hysteretic damping curves (BNL, 1997) were used. The point-source stress drop was 60 bars, based on inversions of the Abrahamson and Silva (1997) empirical attenuation (BNL, 1997), and the source depth was taken as 8 km (equivalent to the value used in the inversions).

Figures J-30 and J-31 compare simulated V/H ratios to empirical ratios for rock and soil sites for **M** 6.5, the best constrained magnitude for the empirical relations. In general the model captures the overall shapes and trends with distance of the empirical ratios but shows a stronger close-in distance effect. This strong distance effect is controlled by the incidence angle (top of source layer) increasing rapidly with increasing epicentral distance. As previously mentioned, crustal heterogeneity as well as source finiteness would tend to weaken this distance dependence. For the point-source model, crustal randomization to simulate uncertainty and randomness in the crustal structure would reduce the near-source distance dependency making it similar to the empirical. However, the simple point-source model, as implemented here, captures the general trends of the WUS empirical rock and soil V/H ratios well enough to provide guidance in assessing the appropriateness of applying WUS ratios to CEUS conditions.

---

*The Lucerne site is actually a shallow (15 ft) soil over very hard rock (unweathered granite).

To generate V/H ratios for the CEUS, a generic midcontinent crustal model was used (EPRI, 1993). The CEUS crustal model is considered appropriate for hard rock sites in the CEUS east of the Rocky Mountains with the possible exception of the Gulf Coast region. This region has a crustal structure somewhat intermediate between the WUS and the CEUS (EPRI, 1993). The large difference between the two generic crustal models shown in Figure J-31 gives rise to significantly different short-period strong ground motion characteristics at close-in distances (as depicted in Figure J-24) as well as different rates of attenuation with distance. These differences may be expected to impact the V/H ratios as well. For the WUS ratios, both the empirical and numerical model results showed that the stiffer profile (rock verses soil) resulted in lower short period ($\leq$ 0.3 sec) V/H ratios but larger long period ratios. For the hard rock CEUS crust, this trend is also expected, resulting in a lower maximum V/H ratio with perhaps a higher long period level. Because of the lower horizontal and vertical kappa values for the CEUS crust, the peak in the V/H ratio may be expected to occur at much shorter periods than in the CEUS rock ratios. These expected trends are reflected in the model prediction shown in Figure J-32 (top plot). Oscillations in the model V/H ratios are due to resonances in the vertical and horizontal spectra. These would be reduced if the profile were randomized and median spectra used in the V/H ratios. For CEUS hard rock sites, the peak V/H ratio is significantly lower and at a shorter period than soft rock sites and the long period level is higher as well. This difference between WUS and CEUS in the period range of 0.1 to 1.0 sec was also found by Atkinson and Boore (1997) in an empirical analysis of the H/V ratio of Fourier amplitude spectra at large distances ($R \geq 20$ km) in Western and Eastern Canada.

For deep soil sites, Figure J-32 (bottom) plot) suggests that the V/H ratio may be significantly higher in the CEUS than in WUS. This results primarily from nonlinear soil response in the horizontal component as well as assuming linear response for the verticals. The factors contributing to the higher degree of nonlinear response for the CEUS soil ratios are the higher levels of high frequency energy in the control motions (Figure J-24), the larger overall motions due to the higher stress drop (100 bars for CEUS and 60 bars for WUS), and the large jump in shear-wave velocity from the base of the soil to the top layer of the CEUS crust (Figure J-31). These results suggest that for both rock and soil CEUS V/H ratios, it is probably inappropriate to adopt WUS ratios for design purposes. A similar conclusion was reached in the EPRI (1993) project to estimate strong ground motion in the CEUS. In that project, design V/H ratios were developed for CEUS rock and stiff soil conditions based primarily on model simulations.

It should be emphasized that only a single and very simple model, which involves many assumptions, has been implemented here. However, the results may provide a useful contribution to developing design V/H ratios for CEUS conditions. Naturally, the most satisfying approach is to make use of multiple well-validated models to assess the range in uncertainty in the CEUS V/H ratios.

J.12 Conclusions

Characteristics of vertical and horizontal component strong ground motions have been examined to reveal general trends that may be of significance to structural analyses. Recordings at both rock and deep soil sites representative of WUS showed distinctly different behavior of vertical motions at rock and soil sites at close source distances ($R \leq 10$ to 15 km). At rock sites, the largest motions tend to occur on all three components at nearly the same time and "in-phase" motion is present on

acceleration, velocity, and displacement time histories. Vertical component response spectra can exceed those of the horizontal components at short periods (≤ 0.1 sec) by moderate amounts (20% on average) and at very close fault distances ($R \leq 5$ km).

At soil sites, short period (≤ 0.2 sec) vertical motions occur earlier in acceleration time histories than the largest motions on the horizontal components and are not in phase. For intermediate-to-long periods, however, near-source soil site velocity and displacement time histories are "in-phase", showing the dominant motion occurring at about the same time. At close source distances ($R \leq 5$ km) short period (≤ 0.1 sec) vertical motions may exceed horizontal motions by a factor of 2.

Analyses of vertical and horizontal component statistical response spectral shapes for both rock and soil sites at varying magnitudes and distances show significantly less damping at both rock and soil sites for vertical motions. These analyses also suggest that vertical motions are largely linear at both rock and soil sites. Horizontal motions, on the other hand show a broad-band shift in spectral shape to longer periods consistent with an increase in damping due to nonlinear site response, for earthquakes of **M** 6.0 to 7.0+ and at source distances within 10 km.

Response spectral V/H ratios were computed from median WUS empirical horizontal and vertical component response spectra at rock and soil sites for a suite of distances (Figure J-26). These empirical V/H ratios may be used to obtain ratios for applications to structural design for WUS conditions.

Nonlinear response in horizontal motions coupled with largely linear response for vertical motions at WUS soil sites is expected to result in larger V/H ratios and a stronger magnitude dependency for soil sites compared to rock sites at close distances. This trend is seen in V/H ratios computed using empirical attenuation relations, and at least part of this effect is attributable to nonlinear response involving horizontal motions at soil sites.

To estimate V/H ratios for CEUS hard rock and deep soil conditions, a simple point-source model is used to predict both rock and soil horizontal and vertical motions. The model treats vertical motions as inclined P-SV waves with a linear analysis and horizontal motions as vertically incident shear-waves using equivalent-linear analyses. Model predictions for WUS V/H ratios show generally favorable agreement with empirical V/H ratios. Application of the simple model to CEUS show generally higher V/H ratios for hard rock sites compared to soft rock sites at long periods (> 0.3 sec). At short periods, the peak in the V/H ratio is shifted from about 0.07 sec for soft rock to about 0.013 sec for hard rock. This shift results from the lower shallow crustal damping at the hard rock site.

For soil sites, the CEUS V/H ratio is predicted to be significantly larger than the corresponding WUS ratio. This is attributed to higher levels of nonlinear soil response for the horizontal motions caused by CEUS rock control motions being richer in short period energy, higher overall levels of control motions caused by higher CEUS stress drops (100 bars compared to 60 bars), and a larger impedance contrast at the base of the soil column. Because of the simplicity of the model and the number of significant assumptions, use of multiple well validated models is recommended in developing design V/H ratios for the CEUS.

A general conclusion is that the conventional V/H factor of 2/3 is not appropriate at CEUS rock and soil sites and may only be appropriate for WUS sites at periods longer than about 0.3 sec and for distances beyond about 50 km.

References

Abrahamson, N.A. and W.J. Silva (1997). "Empirical response spectral attenuation relations for shallow crustal earthquakes." *Seism. Soc. Am.*, 68(1), 94-127.

Anderson, J.G. (1991). "A preliminary descriptive model for the distance dependence of the spectral decay parameter in southern California." *Bull. Seism. Soc. Am.*, 81(6), 2186-2193.

Anderson, J. G. and S. E. Hough (1984). "A Model for the Shape of the Fourier Amplitude Spectrum of Acceleration at High Frequencies." *Bull. Seism. Soc. Am.*, 74(5), 1969-1993.

Atkinson, G.M. and D.M. Boore (1997). "Some comparisons between recent ground-motion relations." *Seism. Res. Lett.* 68(1), 24-40.

Bozorgnia, Y., M. Niazi, and K.W. Campbell (1995). "Characteristics of free-field vertical ground motion during the Northridge earthquake." *Earthquake Spectra,* 11(4), 515-525.

Brookhaven National Laboratory (1997). "Description and validation of the stochastic ground motion model." Submitted to Brookhaven National Laboratory, Associated Universities, Inc. Upton, New York.

Chang, S.W., J.D. Bray and R.B. Seed (1996). "Engineering implications of ground motions from the Northridge earthquake." *Bull. Seism. Soc. Am.*, 86(1B), S270-S288.

Costantino, C.J. (1967). "Finite element approach to wave propagation problems." *J. Engin. Mechanics Div.* Amer. Soc. Civil Engrs., vol. 93

Costantino, J.C. (1969). "Two dimensional wave propagation through nonlinear media." *J. Compt. Physics*, vol. 4.

Electric Power Research Institute (1993). "Guidelines for determining design basis ground motions." Palo Alto, Calif: Electric Power Research Institute, vol. 1-5, EPRI TR-102293.

Johnson, L.R. and W.J. Silva (1981). "The effects of unconsolidated sediments upon the ground motion during local earthquakes." *Bull. Seism. Soc. Am.*, 71, 127-142.

Li, X.S., Z.L. Wang, and C.K. Shen (1992). SUMDES: A nonlinear procedure for response analysis of horizontally-layered sites subjected to multi-directional earthquake loading. Dept. of Civil Eng. Univ. of Calif., Davis.

Niazi, M. and Y. Bozorgnia (1991). "Behavior of near-source peak horizontal and vertical ground motions over smart-1, array, Taiwan." *Bull. Seism. Soc. Am.,* 81(3), 715-732.

Newmark, N.M. and W.J. Hall (1978). "Development of criteria for seismic review of selected nuclear power plants." NUREG/CR-0098, Nuclear Regulatory Commission.

Kawase, H. and K. Aki (1990). "Topography effect at the critical SV-wave incidence: possible explanation of damage pattern by the Whittier Narrows, California, earthquake of 1 October 1987." *Bull. Seism. Soc. Am.,* 80(1), 1-30.

Sadigh, C.-Y. Chang, J.A. Egan, F. Makdisi, and R.R. Youngs (1997). "Attenuation relationships for shallow crustal earthquakes based on California strong motion data." *Seism. Soc. Am.,* 68(1), 180-189.

Schneider, J.F., W.J. Silva, and C.L. Stark (1993). "Ground motion model for the 1989 **M** 6.9 Loma Prieta earthquake including effects of source, path and site." *Earthquake Spectra,* 9(2), 251-287.

Silva, W.J. and R. Darragh (1995). "Engineering characterization of earthquake strong ground motion recorded at rock sites." Palo Alto, Calif:Electric Power Research Institute, TR-102261.

Silva, W.J. (1976). "Body Waves in a Layered Anelastic solid." *Bull. Seism. Soc. Am.*, 66(5), 1539-1554.

Somerville, P.G., N.F. Smith, R.W. Graves, and N.A. Abrahamson (1997). "Modification of empirical strong ground motion attenuation relations to include the amplitude and duration effects of rupture directivity." *Seism. Res. Lett.*, 68(1), 199-222.

Wald, D.J., and T.H. Heaton (1994). "Spatial and temporal distribution of slip for the 1992 Landers, California, earthquake." *Bull. Seism. Soc. Amer.*, 84(3), 668-691.

Table J-1

GEOMATRIX CONSULTANTS

STRONG-MOTION RECORDING STATIONS
CLASSIFICATION SYSTEM

Geotechnical Subsurface Characteristics

Designation	Description
A	Rock. Instrument is founded on rock material (V_S > 600 mps (1969 ft/sec) or a very thin veneer (less than 5m (16 ft)) of soil overlying rock material.
B	Shallow (stiff) soil. Instrument is founded in/on a soil profile up to 20m (66 ft) thick overlying rock material, typically in a narrow canyon, near a valley edge, or on a hillside.
C	Deep narrow soil. Instrument is founded in/on a soil profile at least 20m (66 ft) thick overlying rock material in a narrow canyon or valley no more than several kilometers wide.
D	Deep broad soil. Instrument is founded in/on a soil profile at least 20m (66 ft) thick overlying rock material in a broad canyon or valley.
E	Soft deep soil. Instrument is founded in/on a deep soil profile that exhibits low average shear-wave velocity (V_S < 150 mps (492 ft/sec)).

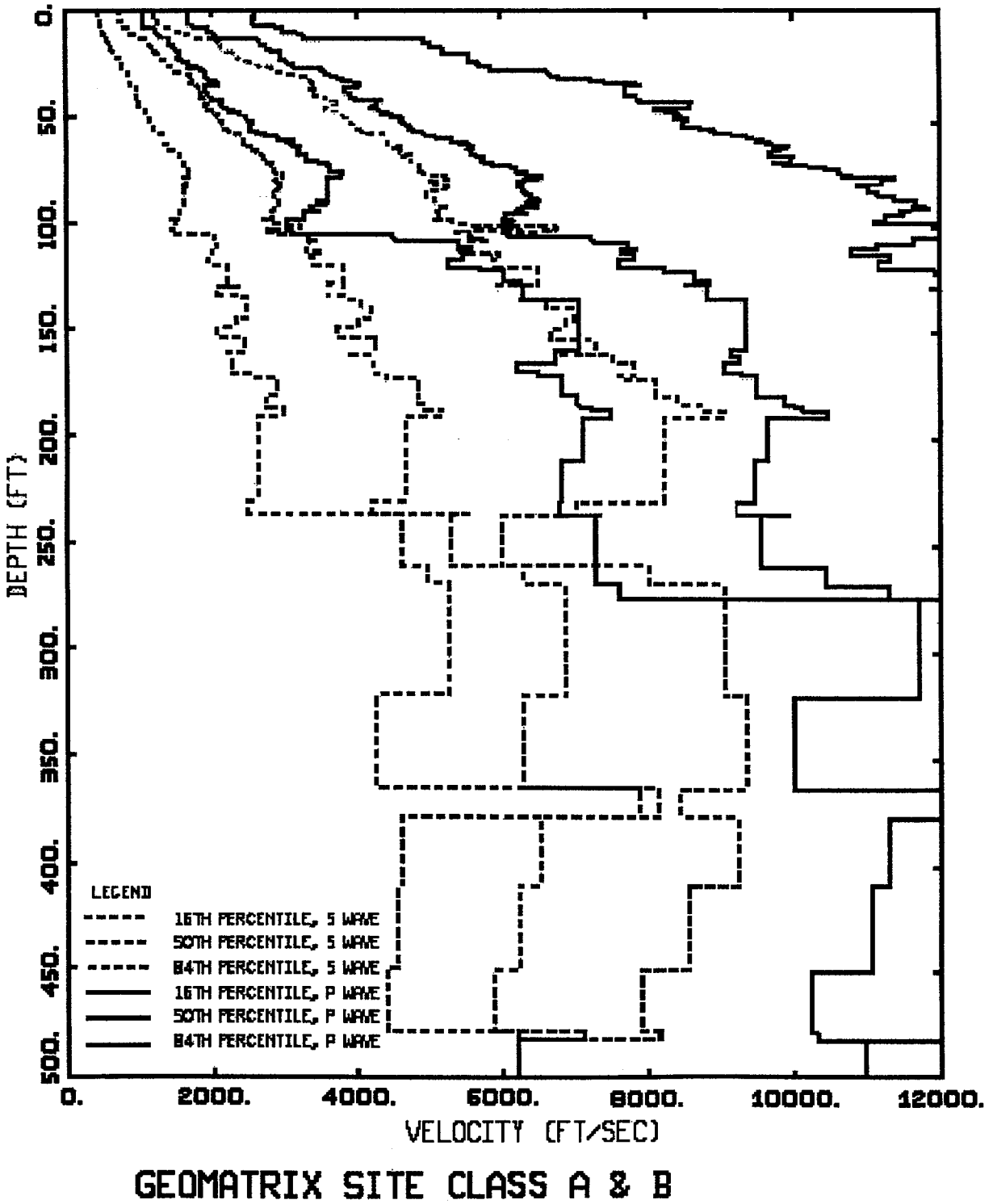

Figure J-1. Median and $\pm \sigma$ compression- and shear-wave velocity profiles for Geomatrix site class A plus B (soft rock, table J-1).

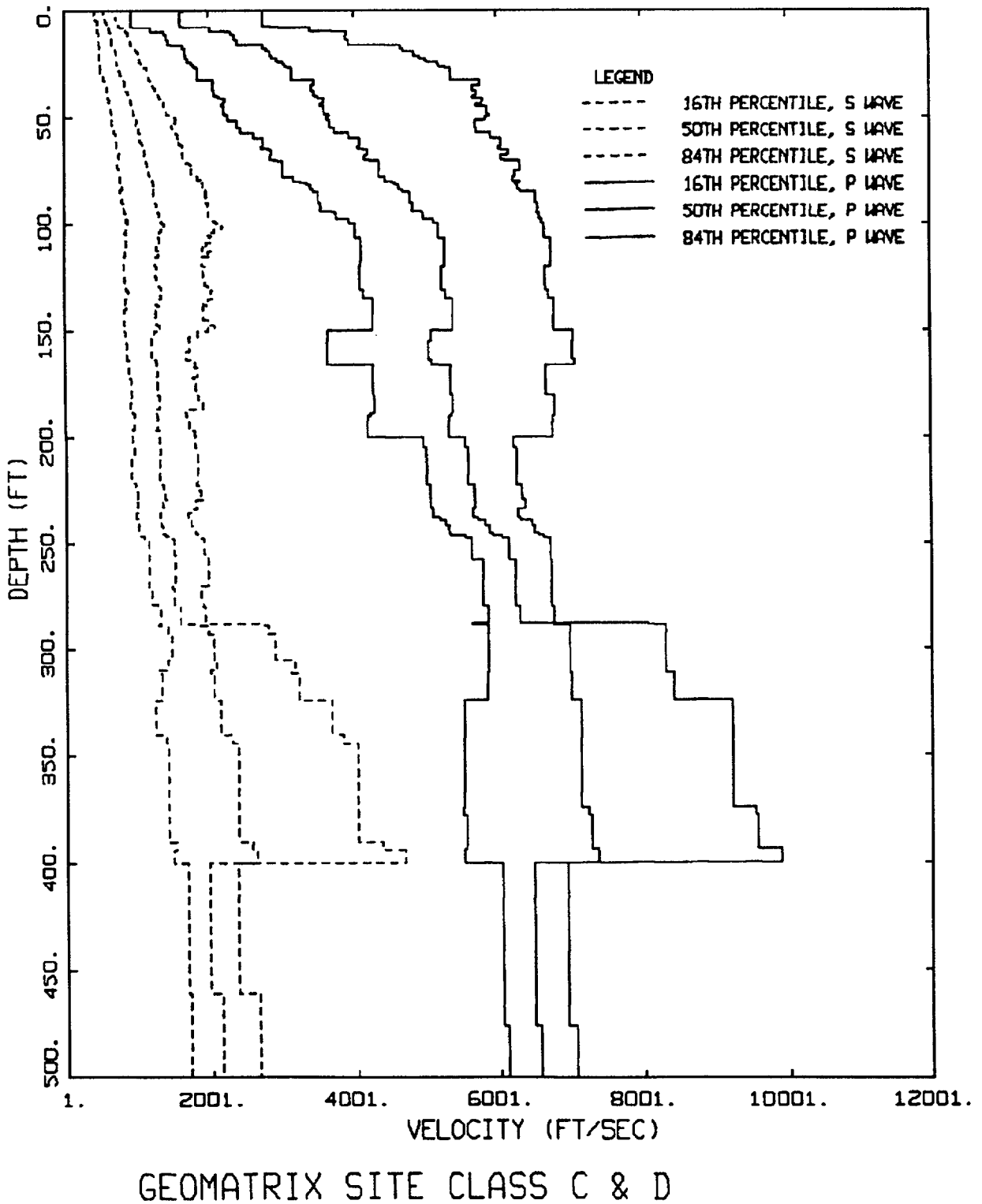

Figure J-2. Median and $\pm$ 1 σ compression- and shear-wave velocity profiles for Geomatrix site class C plus D (deep soil, Table J-1).

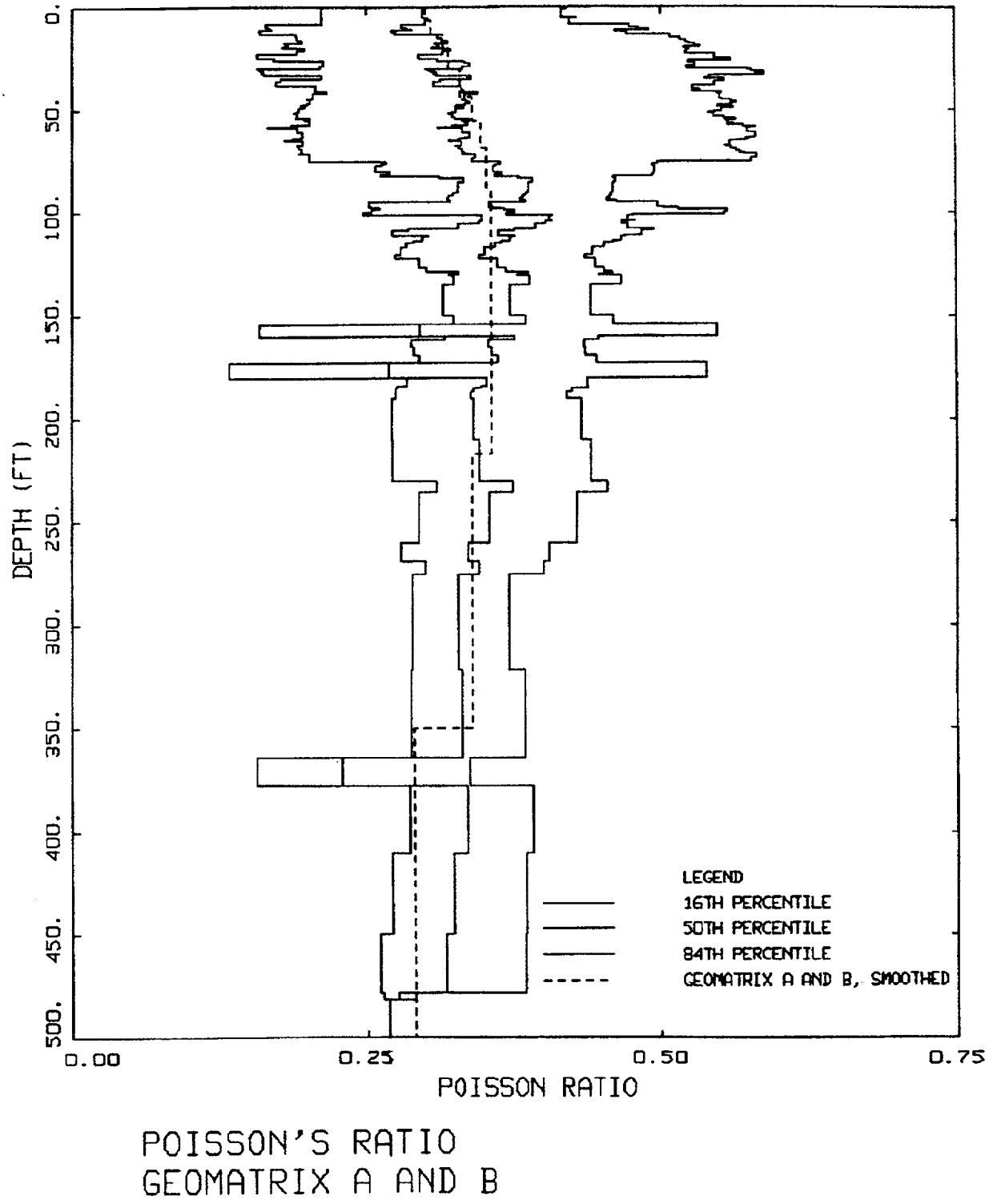

Figure J-3. Median and $\pm$ 1 σ Poisson's ratio profiles for Geomatrix site class A plus B (soft rock, Table J-1).

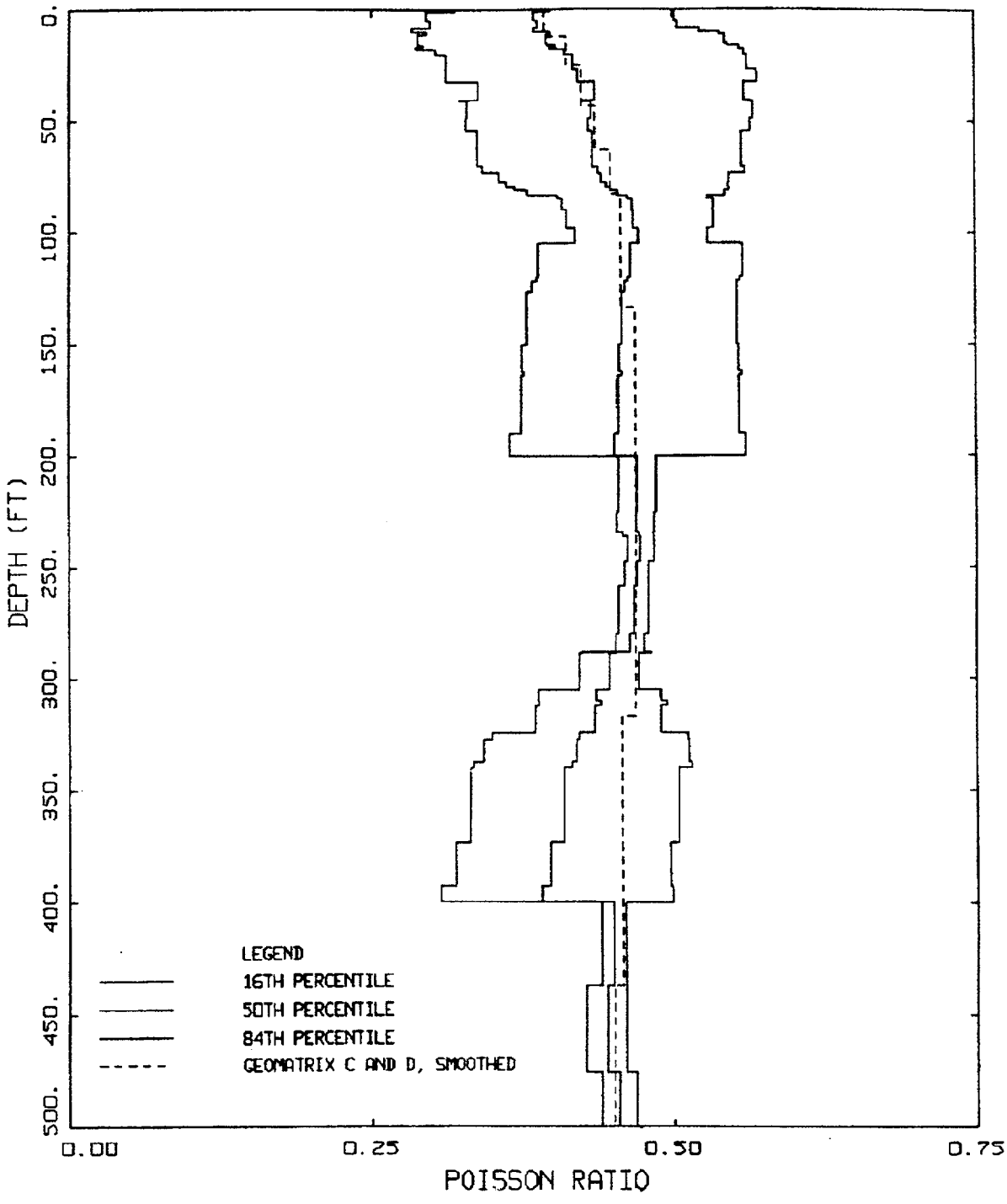

Figure J-4. Median and $\pm$ 1 σ Poisson's ratio profiles for Geomatrix site class C plus D (deep soil, Table J-1).

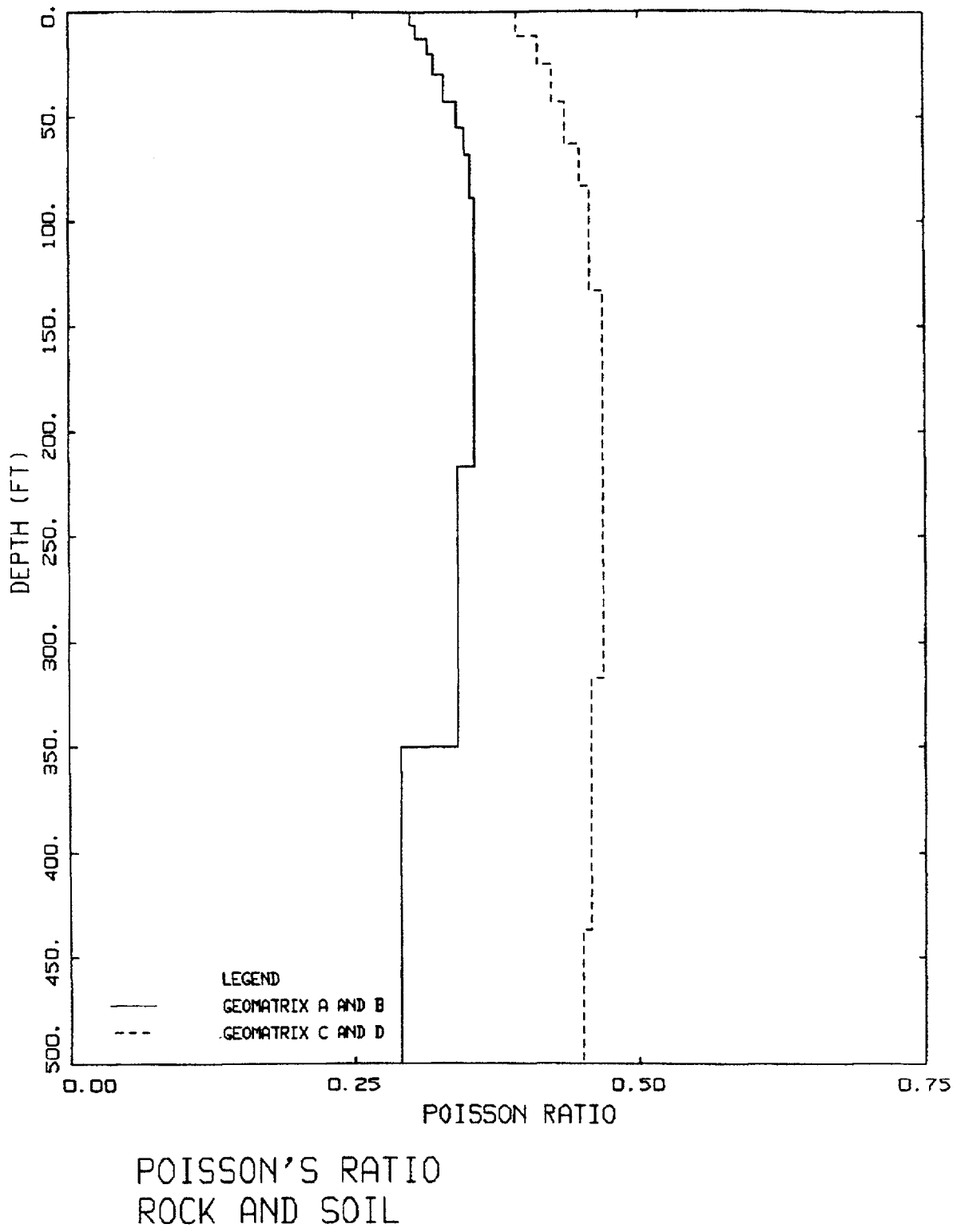

Figure J-5. Poisson's ratio profiles for Geomatrix site class A plus B and C plus D (soft rock, Table J-1).

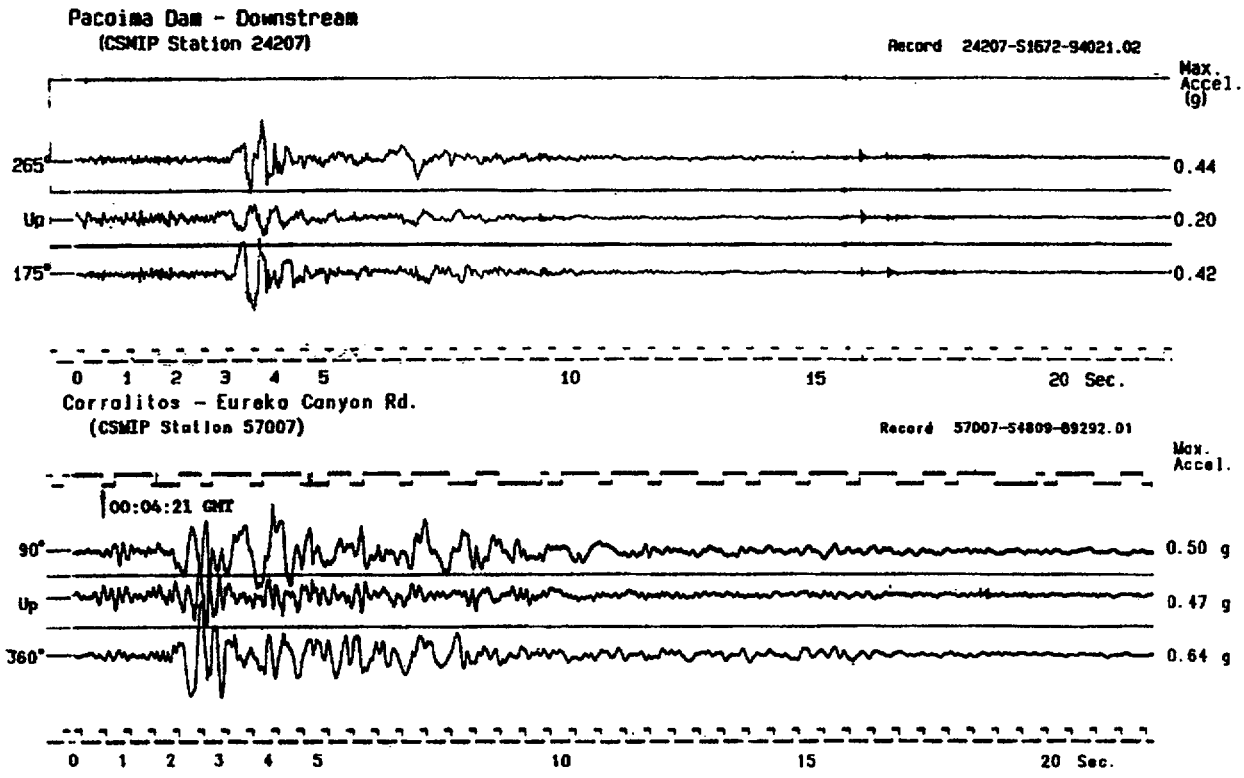

Figure J-6. Horizontal and vertical component acceleration time histories recorded at rock sites Pacoima Downstream for the 1994 **M** 6.7 Northridge earthquake (top) and Corralitos for the 1989 **M** 6.9 Loma Prieta earthquake (bottom). (Source: CDMG initial data reports).

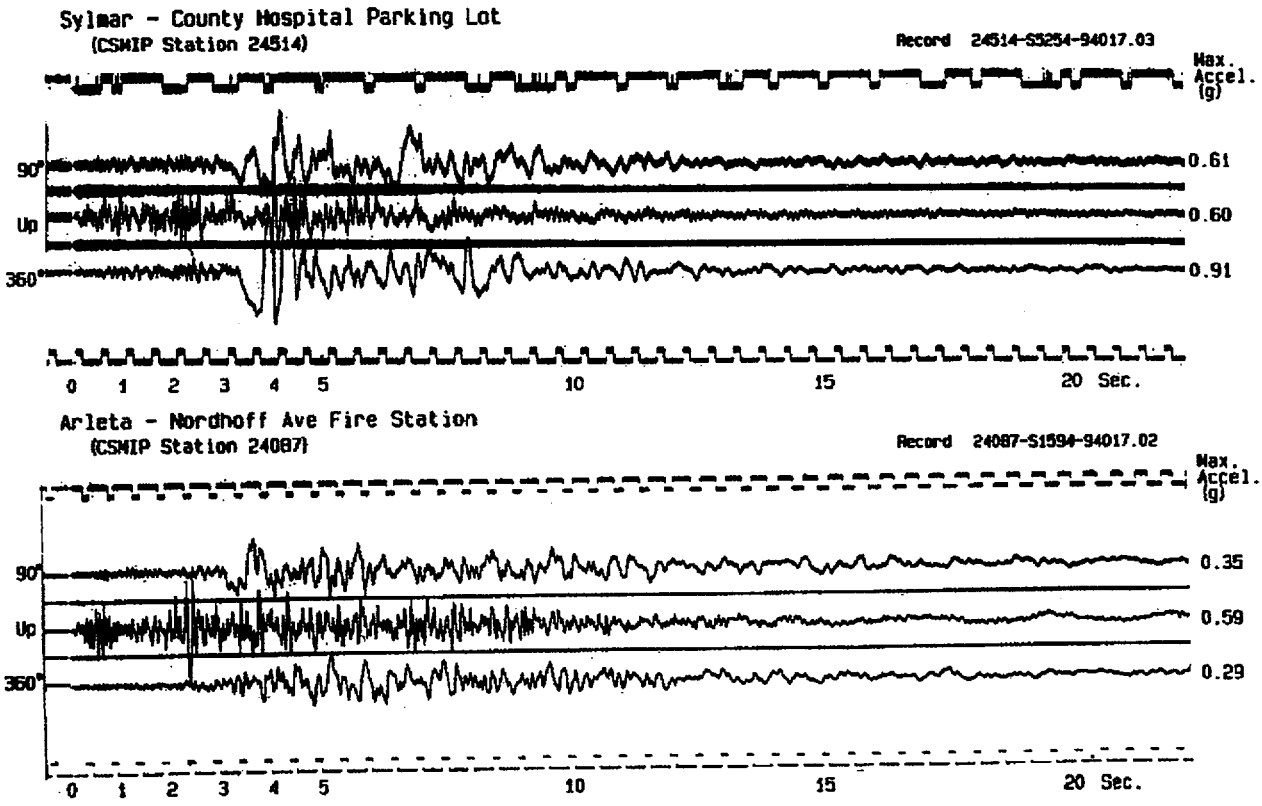

Figure J-7. Horizontal and vertical component acceleration time histories recorded at soil sites Sylmar (top) and Arleta (bottom) for the 1994 M 6.7 Northridge earthquake. (Source: CDMG initial data reports).

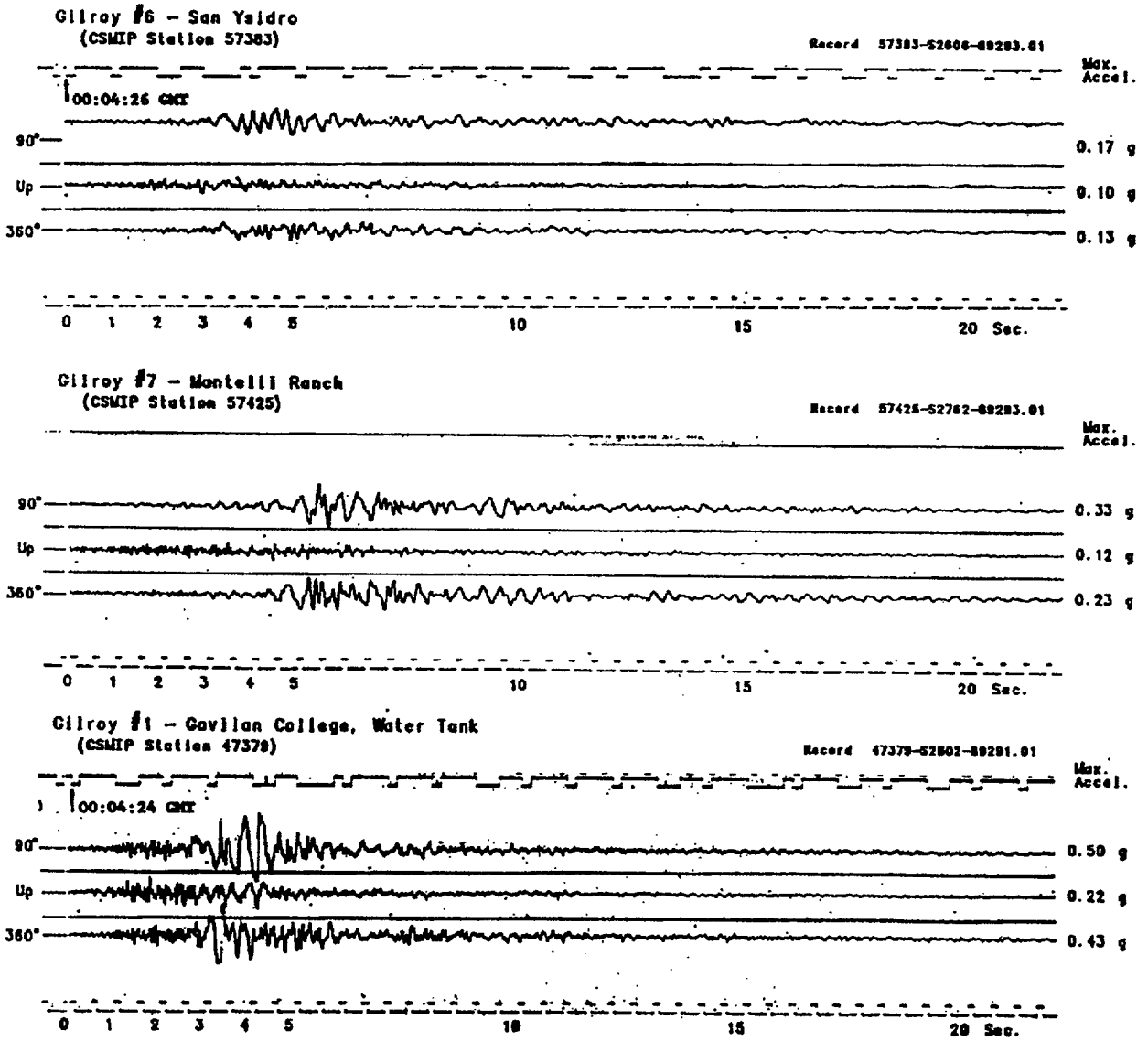

Figure J-8. Horizontal and vertical component acceleration time histories recorded at rock sites Gilroy 6, 7, and 1 (top, middle, and bottom) for the 1989 M 6.9 Loma Prieta earthquake. (Source: CDMG initial data reports)

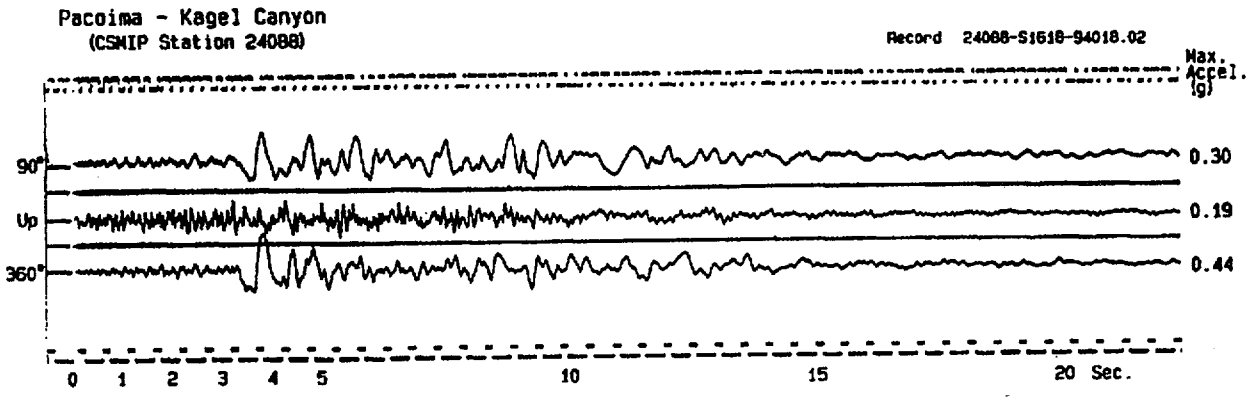

Figure J-9. Horizontal and vertical component acceleration time histories recorded at "rock" site Pacoima Kagel for the 1994 **M** 6.7 Northridge earthquake. (Source: CDMG initial data reports)

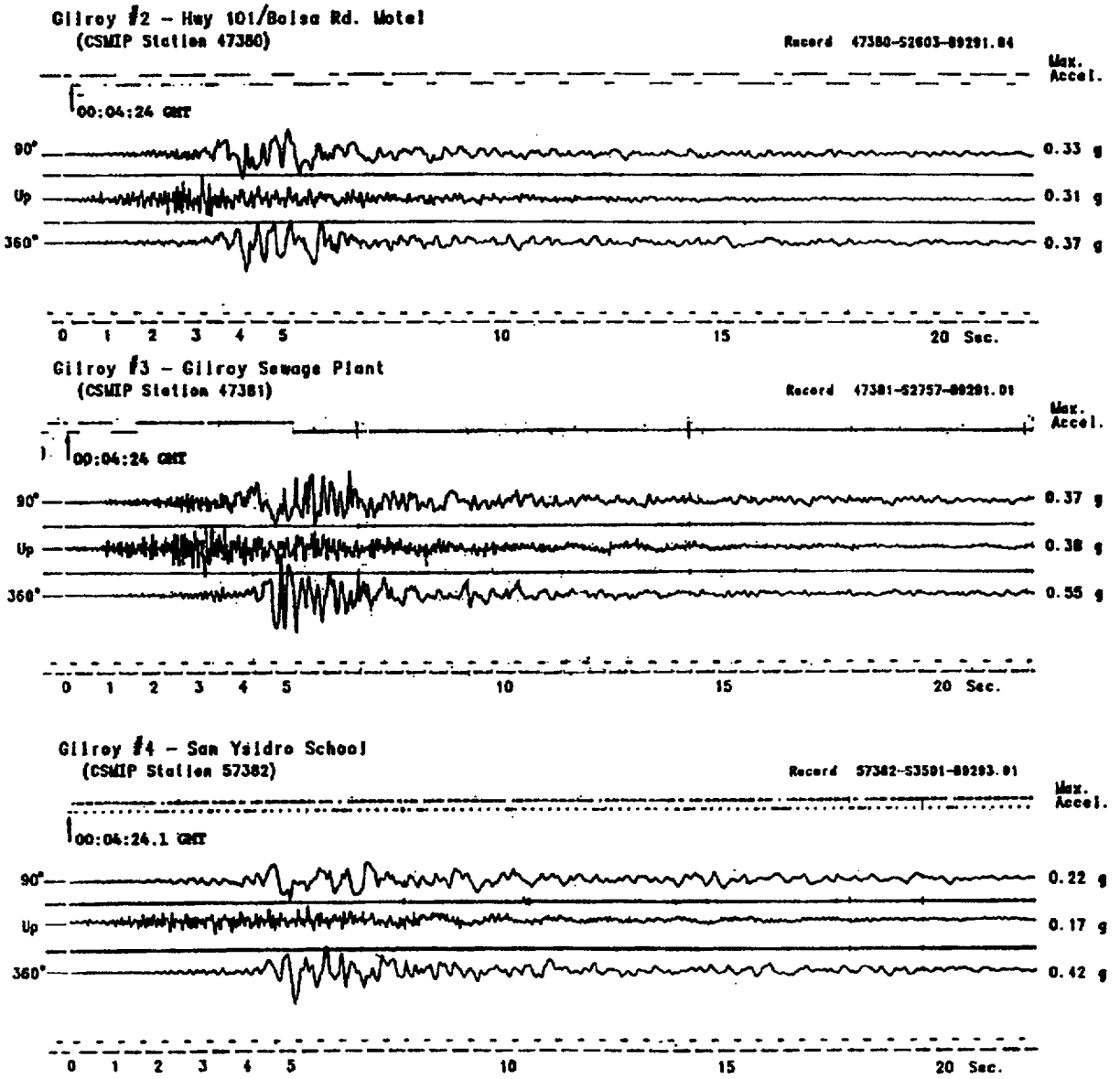

Figure J-10. Horizontal and vertical component acceleration time histories recorded at soil sites Gilroy 2, 3, and 4 (top, middle, and bottom) for the 1989 M 6.9 Loma Prieta earthquake. (Source: CDMG initial data reports)

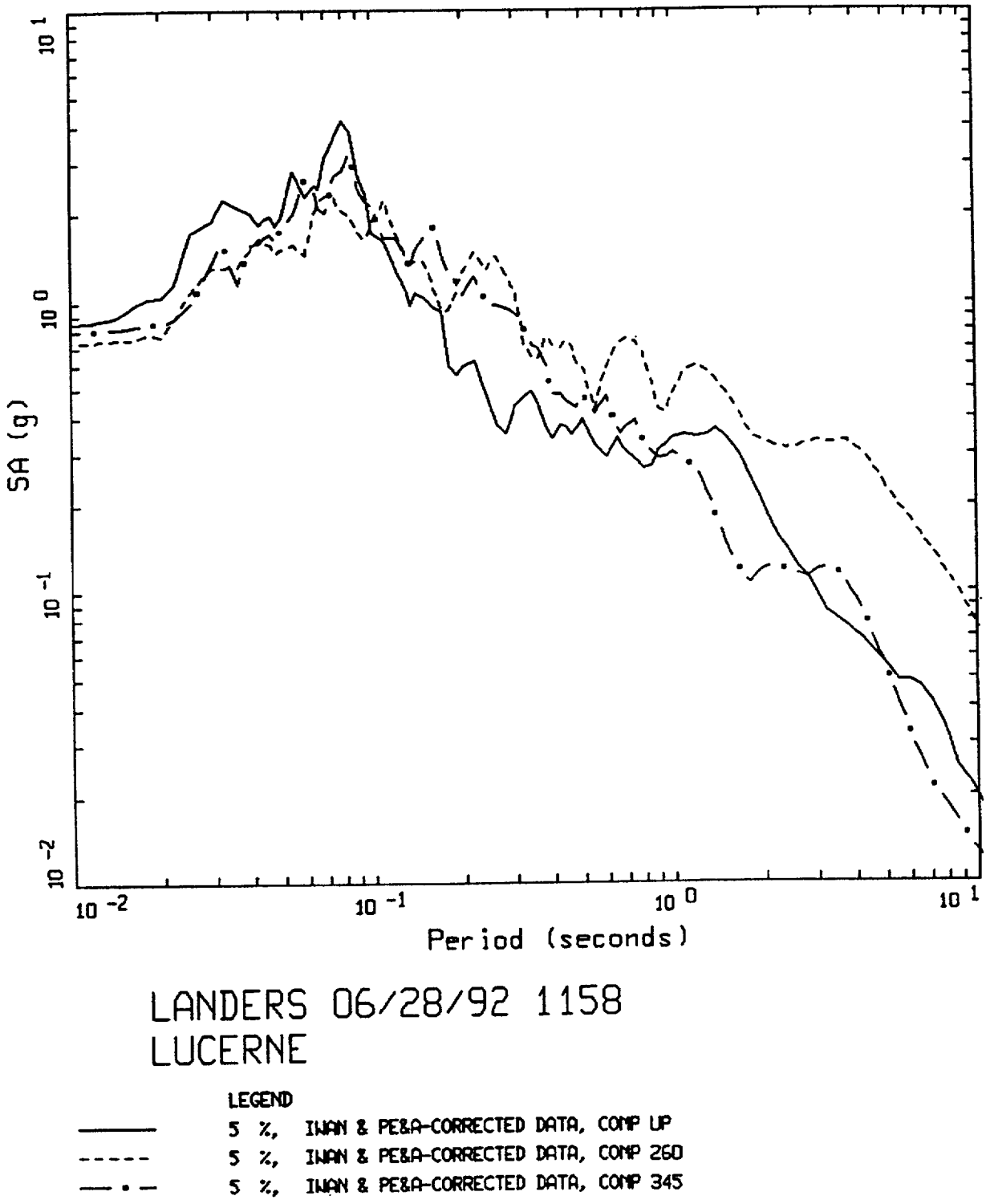

Figure J-11. 5% damped psuedo absolute response spectra at the SCE rock site Lucerne for the 1992 M 7.2 Landers earthquake. Fault distance is about 2 km.

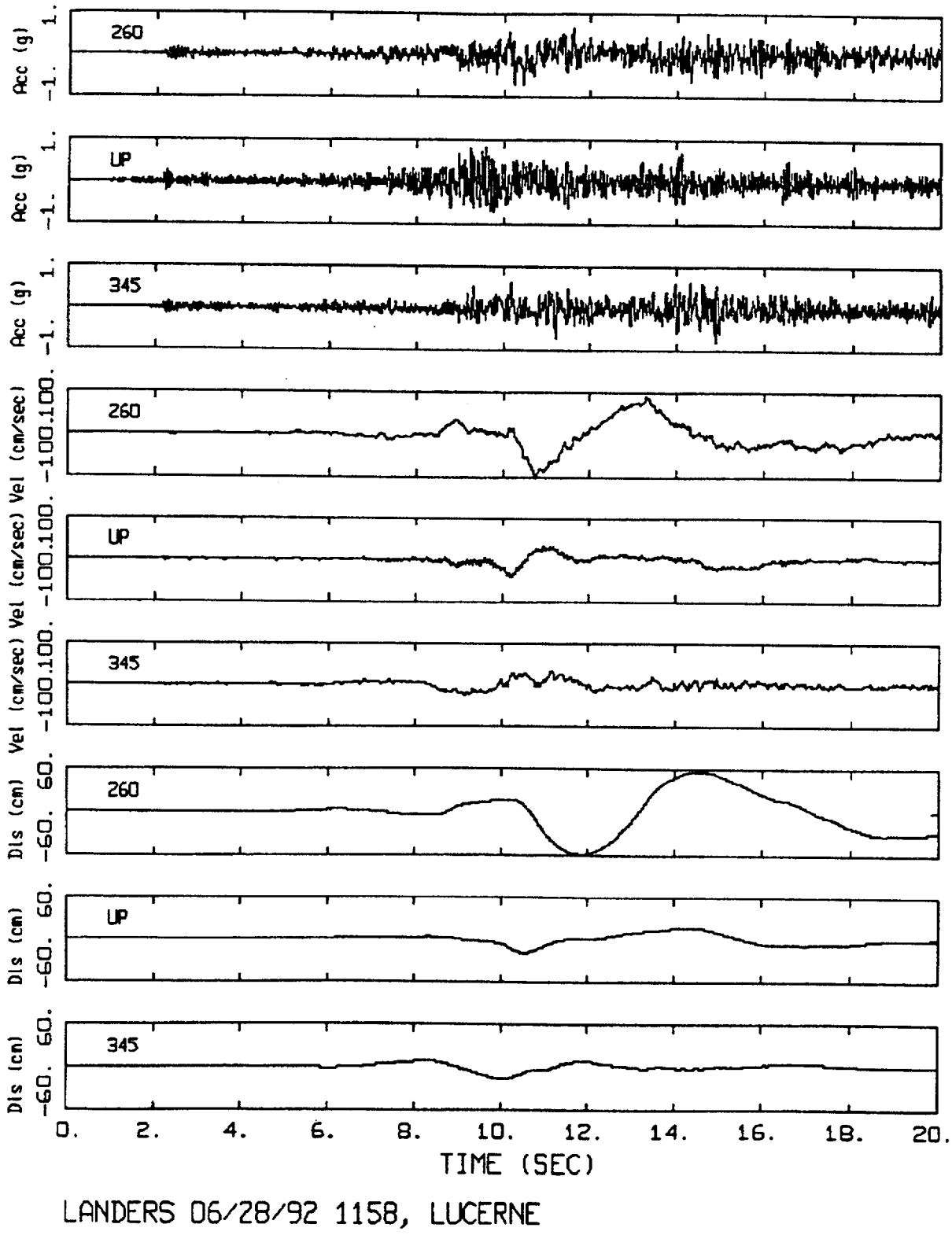

Figure J-12. Acceleration, velocity, and displacement time histories at the SCE rock site Lucerne for the 1992 M 7.2 Landers earthquake. Fault distance is about 2 km.

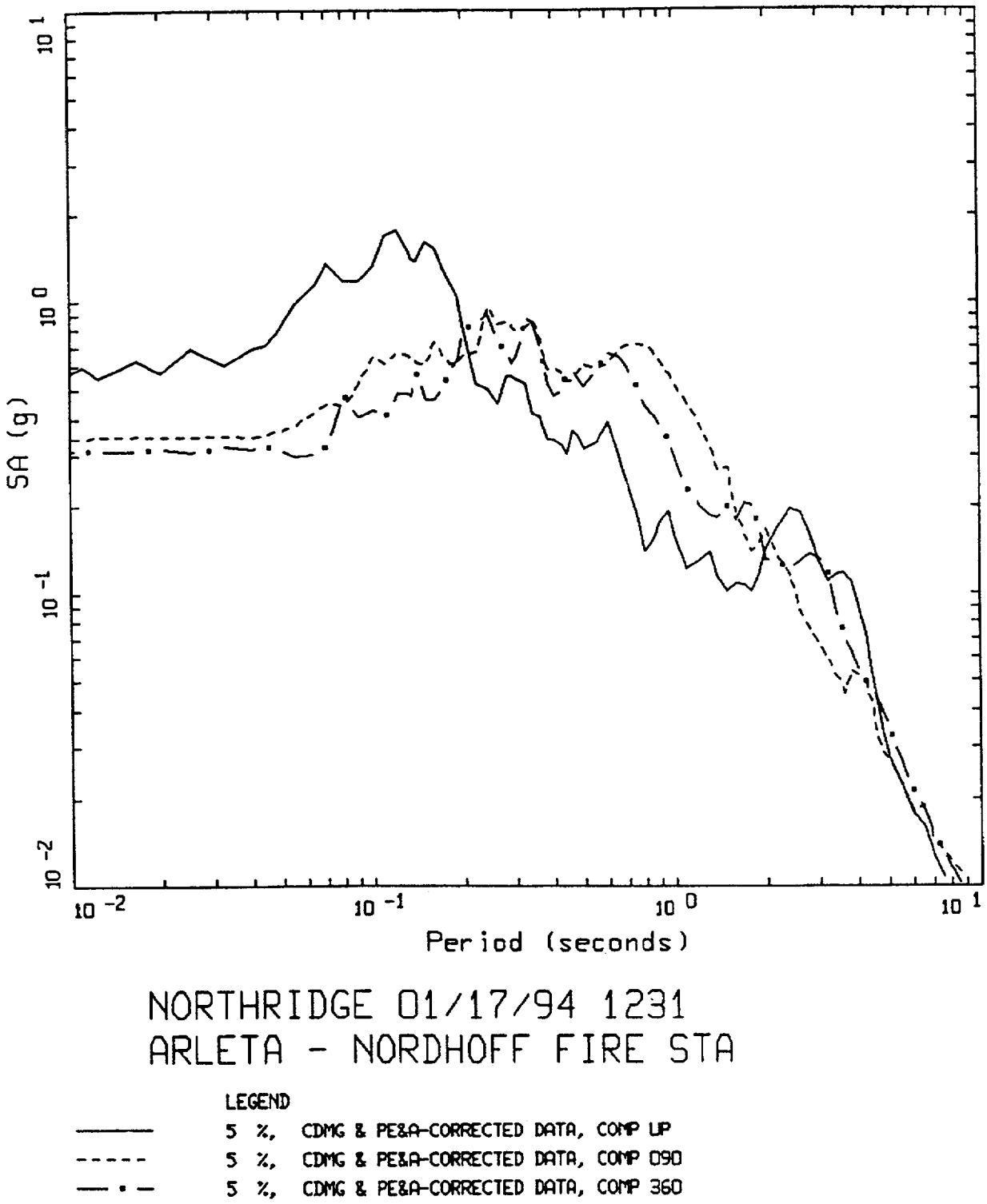

Figure J-13. 5% damped psuedo absolute response spectra at the soil site Arleta for the 1994 M 6.7 Northridge earthquake. Fault distance is about 9 km.

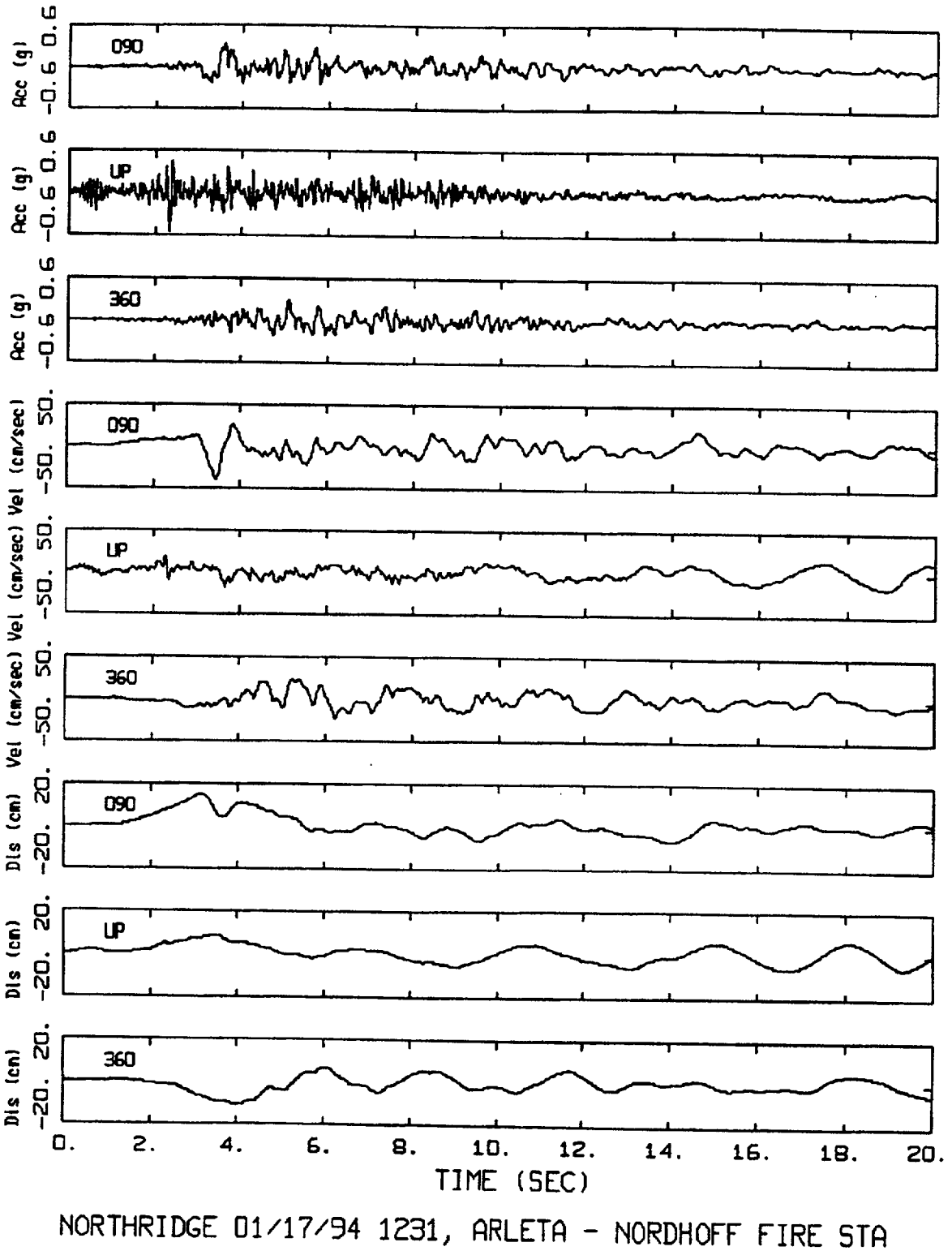

Figure J-14. Acceleration, velocity, and displacement time histories at the soil site Arleta for the 1994 M 6.7 Northridge earthquake. Fault distance is about 9 km.

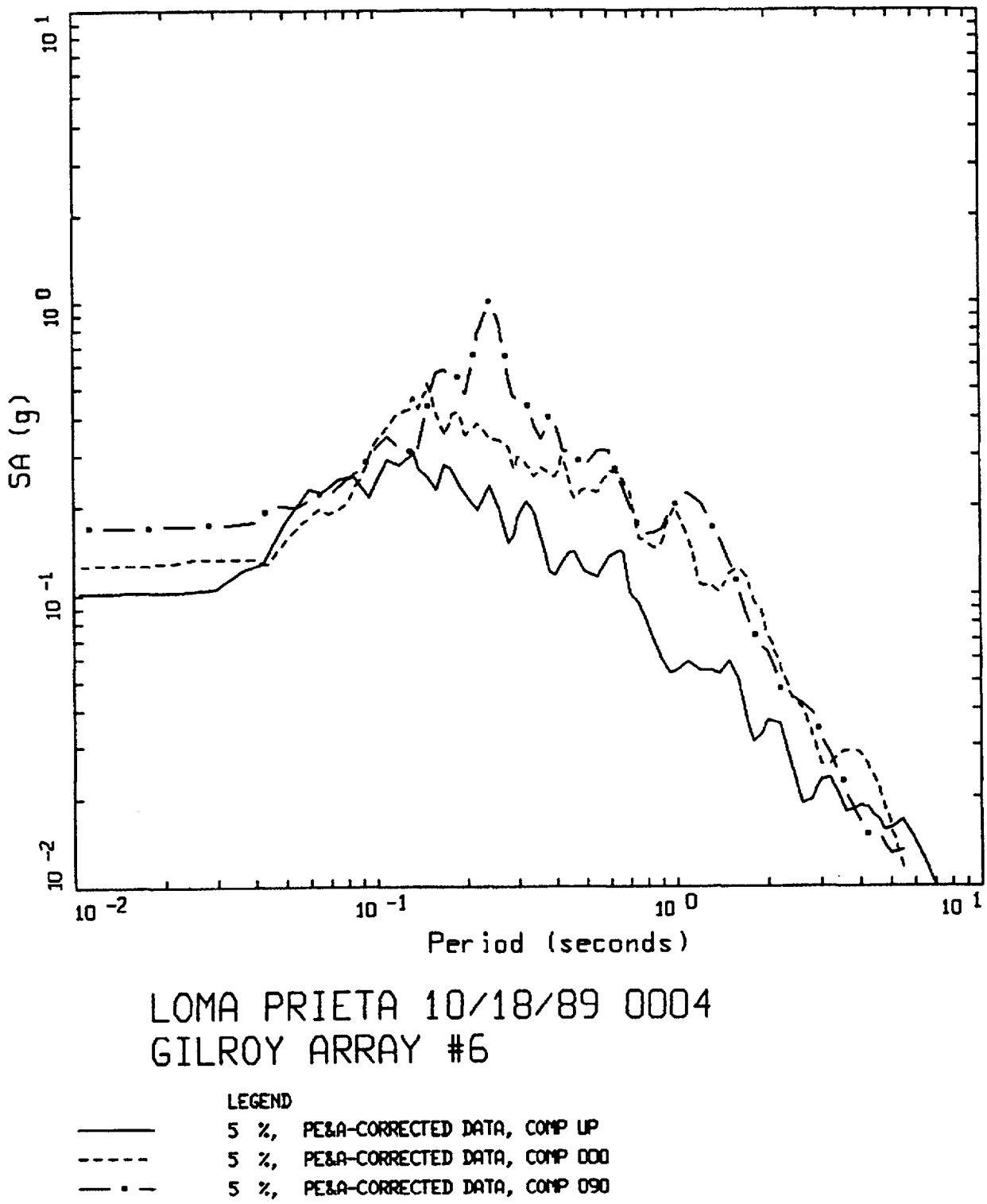

Figure J-15. 5% damped pseudo absolute response spectra at the rock site Gilroy 6 for the 1989 M 6.9 Loma Prieta earthquake. Fault distance is about 19 km.

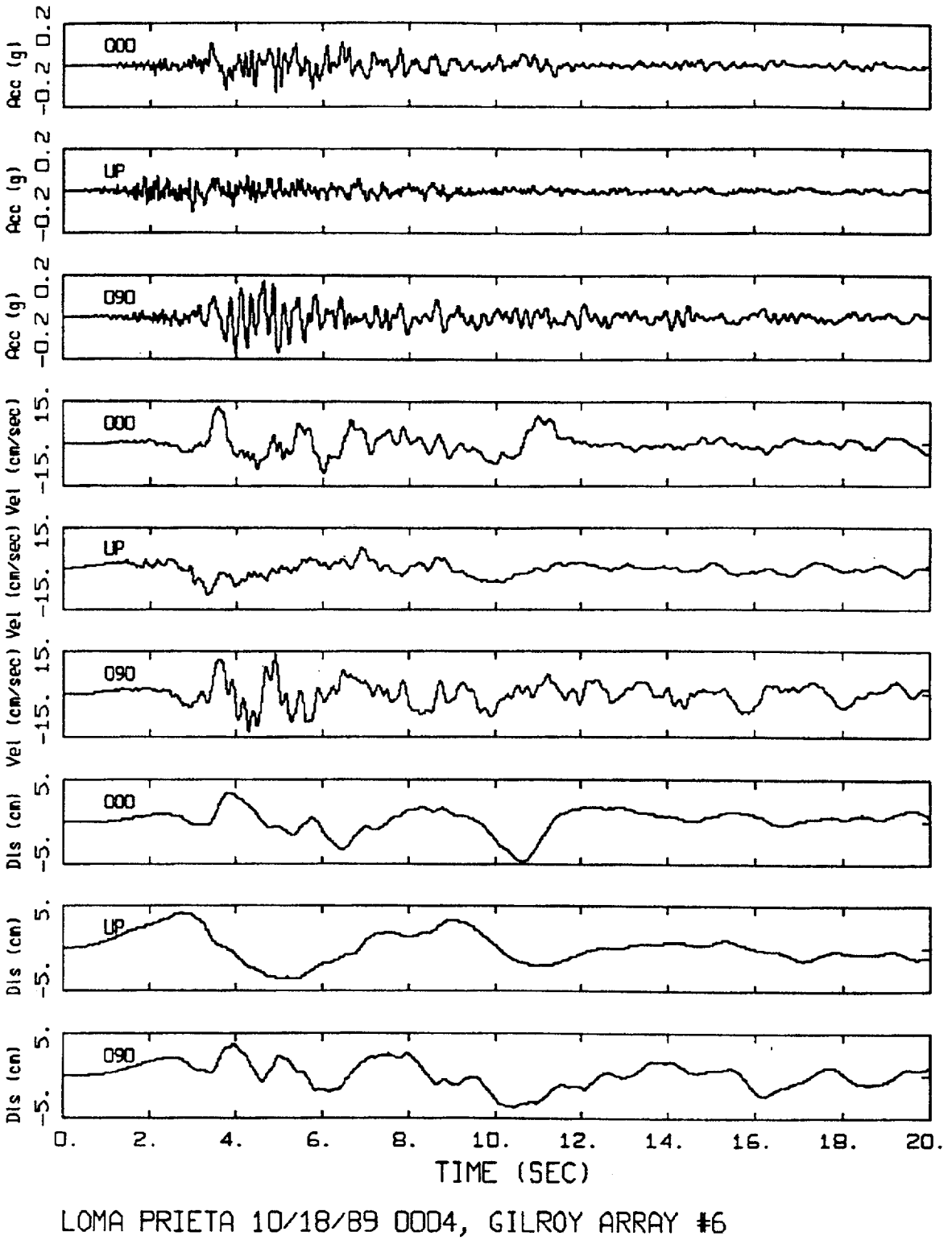

Figure J-16. Acceleration, velocity, and displacement time histories at the rock site Gilroy 6 for the 1989 M 6.9 Loma Prieta earthquake. Fault distance is about 19 km.

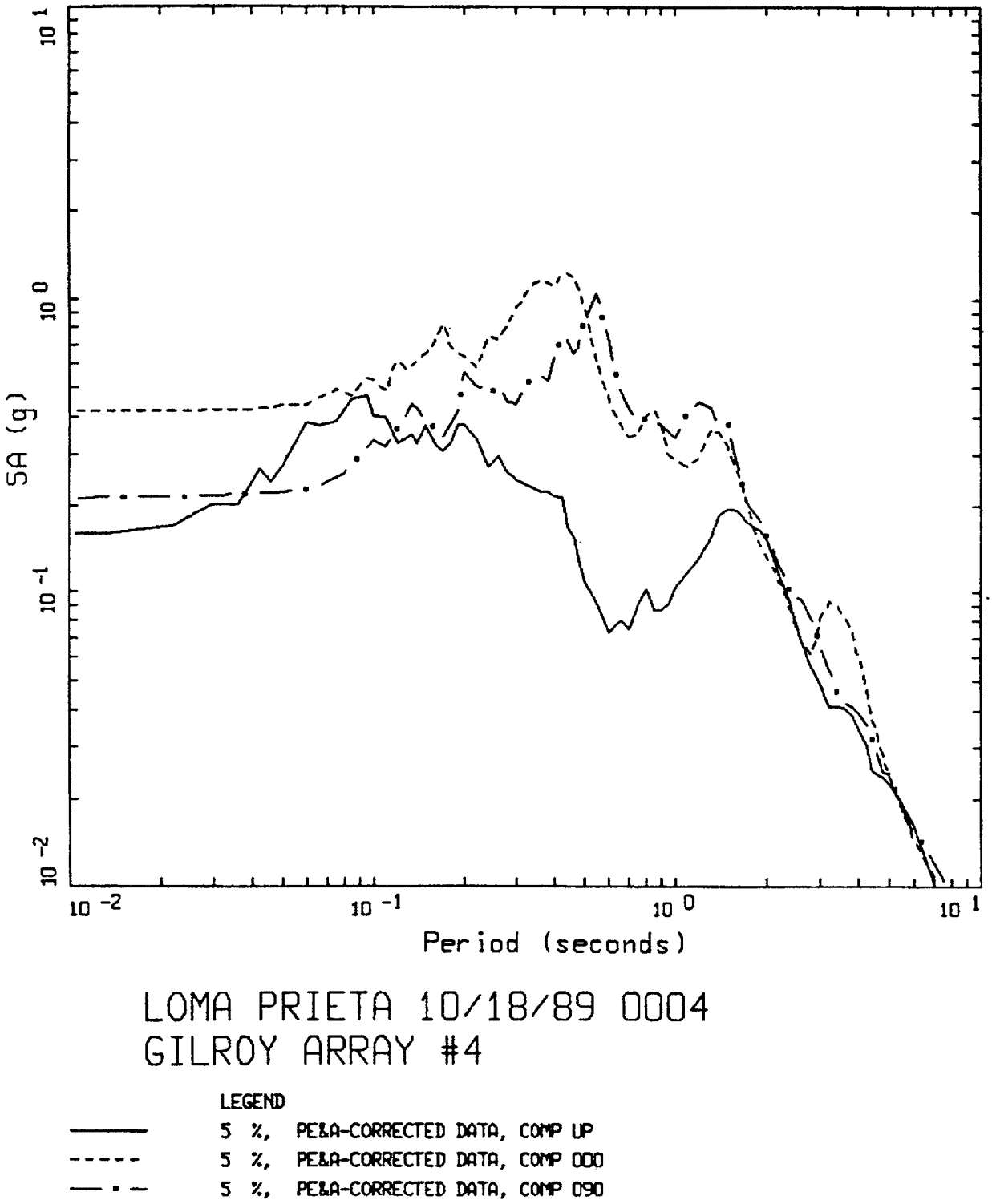

Figure J-17. 5% damped pseudo absolute response spectra at the soil site Gilroy 4 for the 1989 M 6.9 Loma Prieta earthquake. Fault distance is about 16 km.

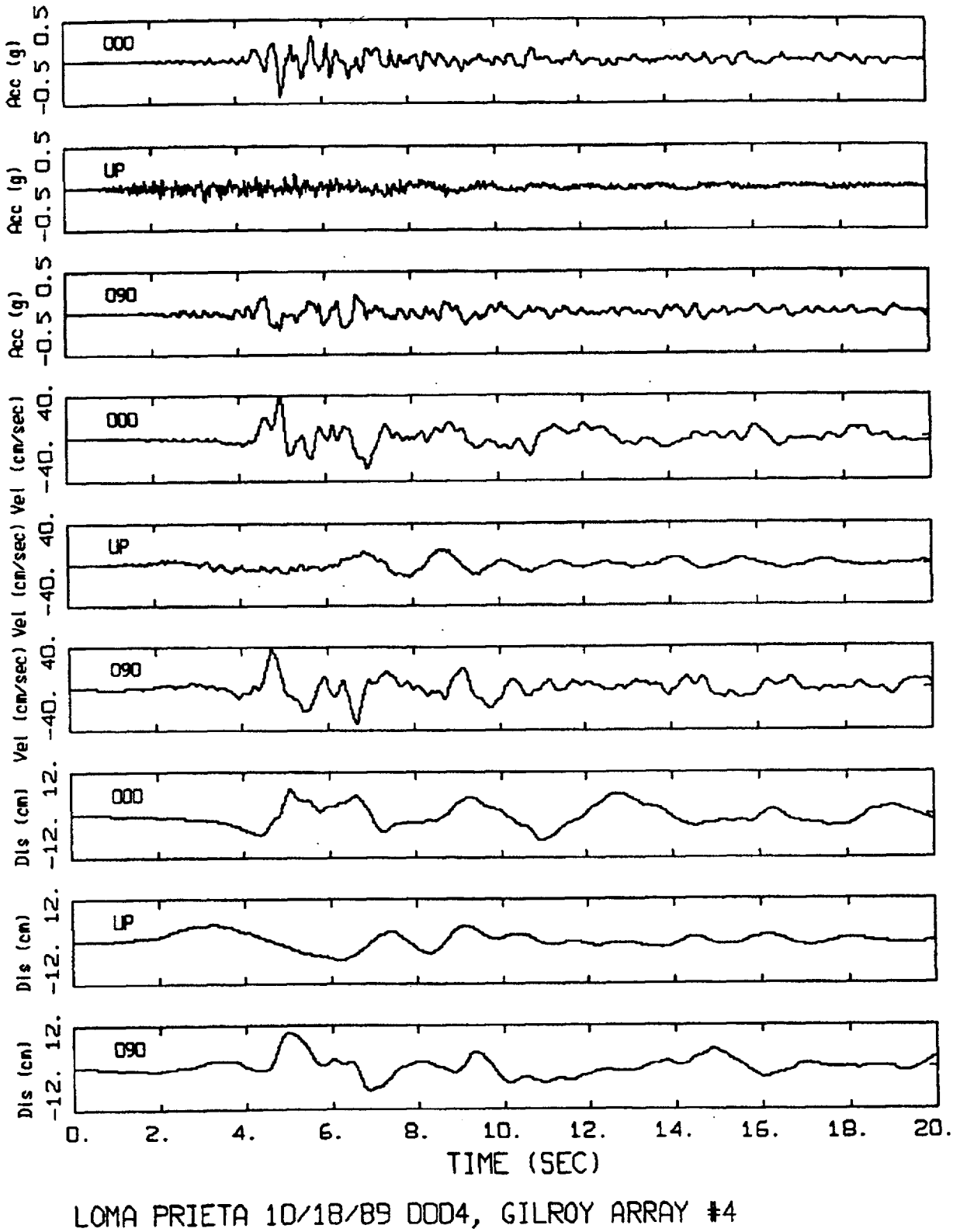

Figure J-18. Acceleration, velocity, and displacement time histories at the soil site Gilroy 4 for the 1989 M 6.9 Loma Prieta earthquake. Fault distance is about 16 km.

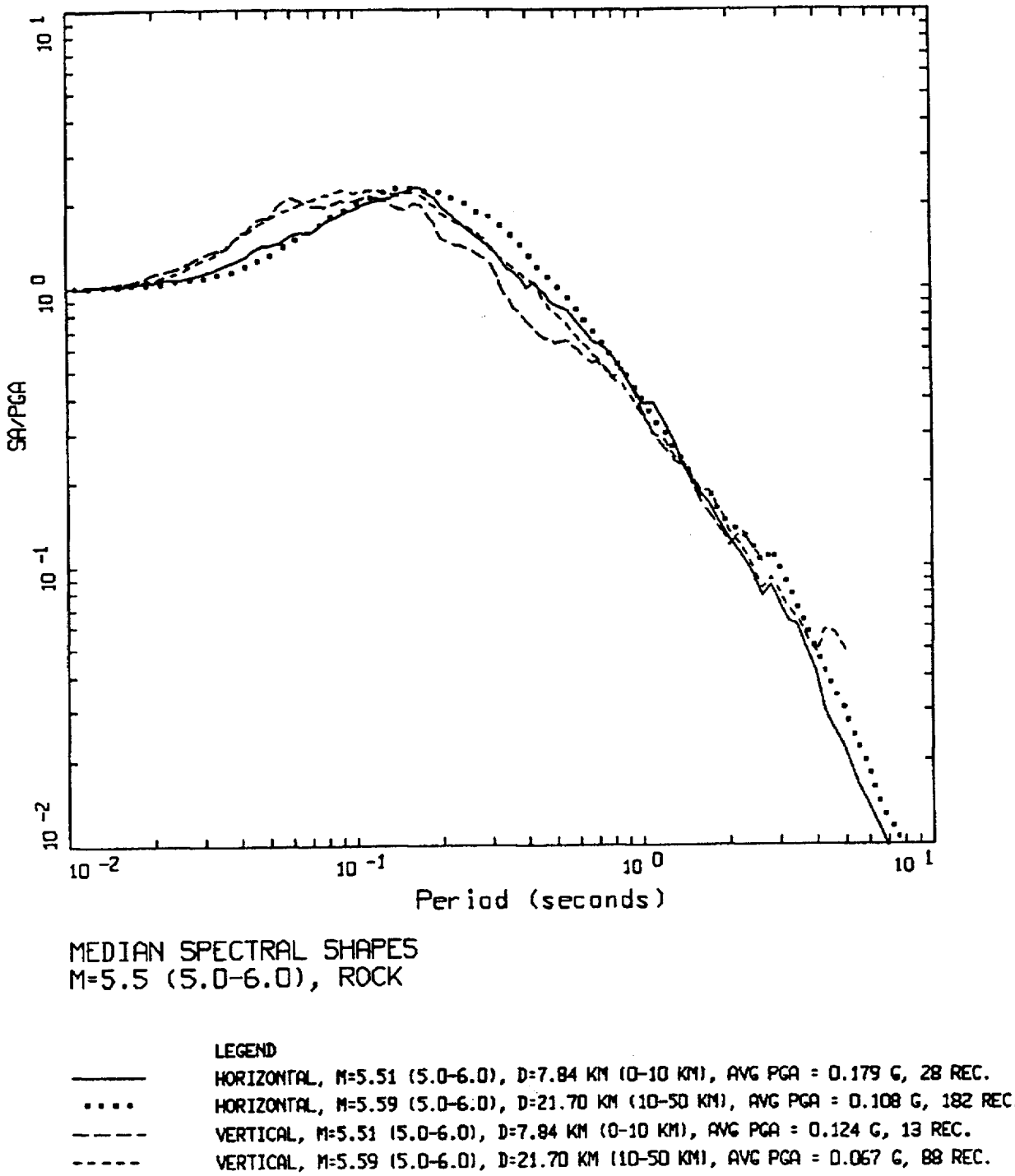

Figure J-19. Median statistical response spectral shapes (5% damping) computed from WUS data recorded at rock sites in the magnitude range of **M** 5 to **M** 6. Rupture distances range from 0 to 10 km and 10 to 50 km.

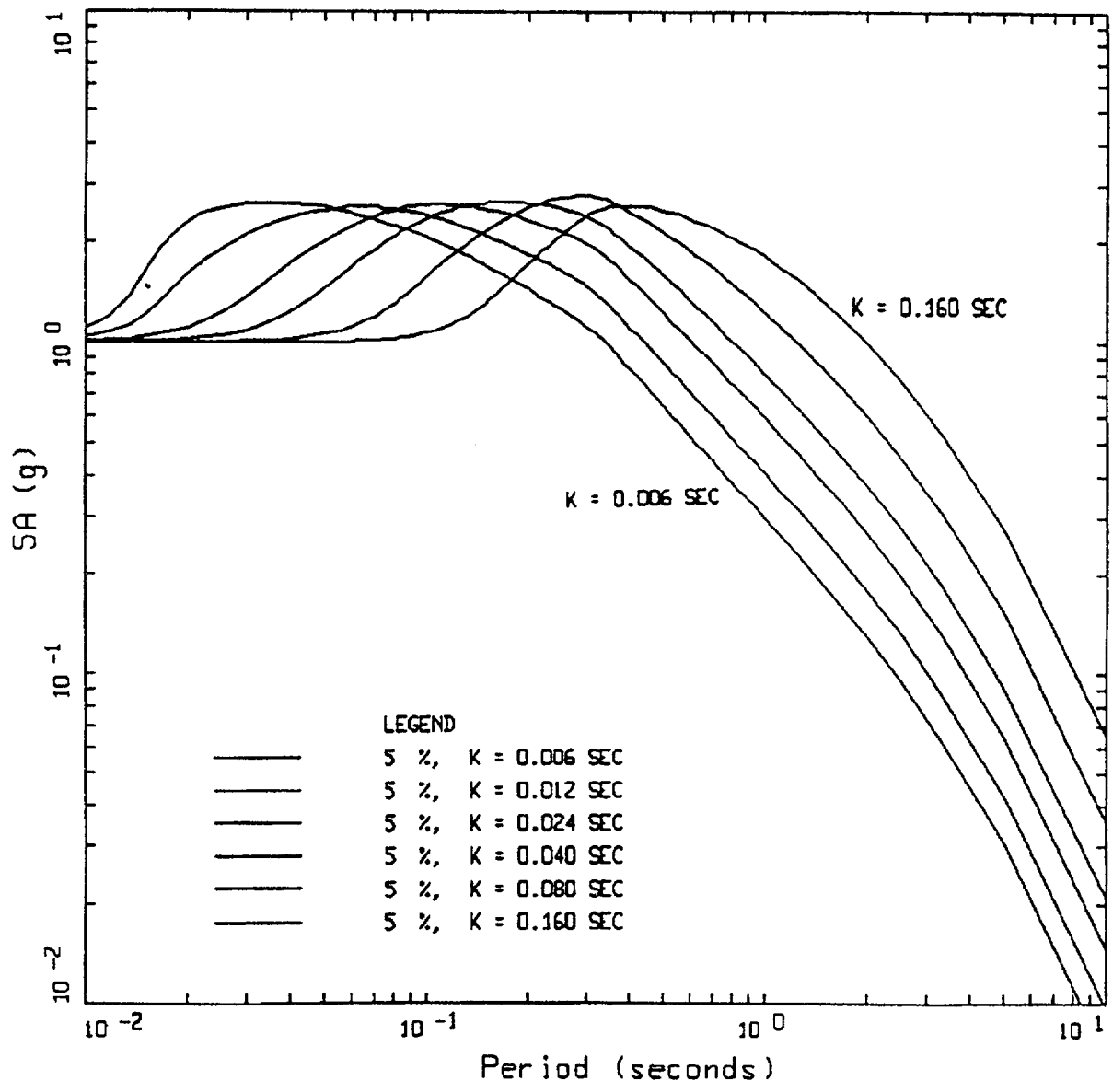

Figure J-20. The effects of kappa on 5% damped response spectral shapes computed for a M 6.5 earthquake at 10 km using WNA parameters. As kappa increases, the peak shifts to longer periods and remains essentially constant in amplitude.

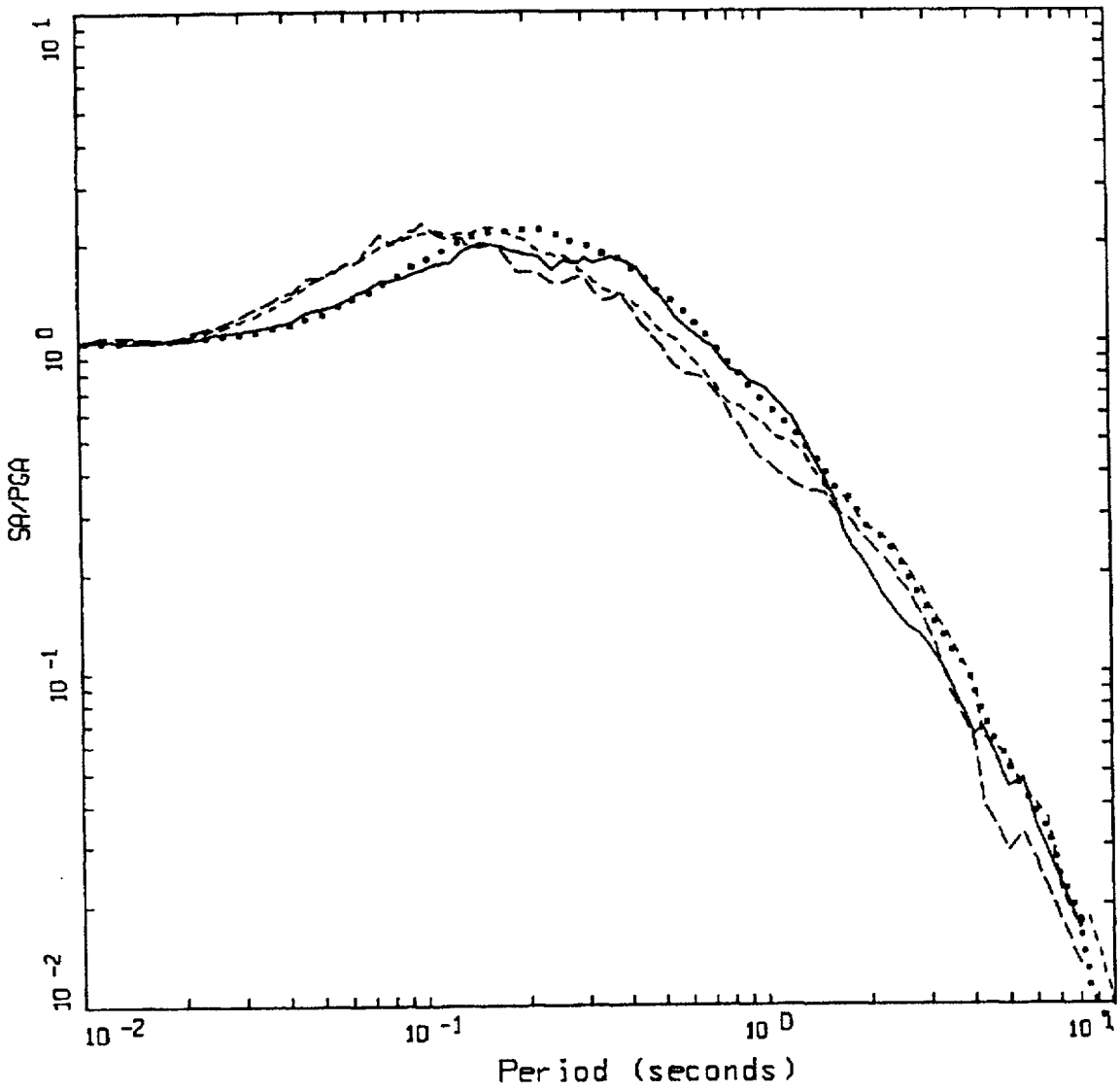

MEDIAN SPECTRAL SHAPES
M=6.5 (6.0-7+), ROCK

LEGEND

——— HORIZONTAL, M=6.52 (6.0-7+), D=6.09 KM (0-10 KM), AVG PGA = 0.456 G, 28 REC.

• • • • HORIZONTAL, M=6.36 (6.0-7+), D=26.47 KM (10-50 KM), AVG PGA = 0.124 G, 206 REC.

— — — — VERTICAL, M=6.52 (6.0-7+), D=6.09 KM (0-10 KM), AVG PGA = 0.457 G, 11 REC.

- - - - - VERTICAL, M=6.36 (6.0-7+), D=26.47 KM (10-50 KM), AVG PGA = 0.074 G, 103 REC.

Figure J-21. Median statistical response spectral shapes (5% damping) computed from WUS data recorded at rock sites in the magnitude range of **M** 6 to **M** 7+. Rupture distances range from 0 to 10 km and 10 to 50 km.

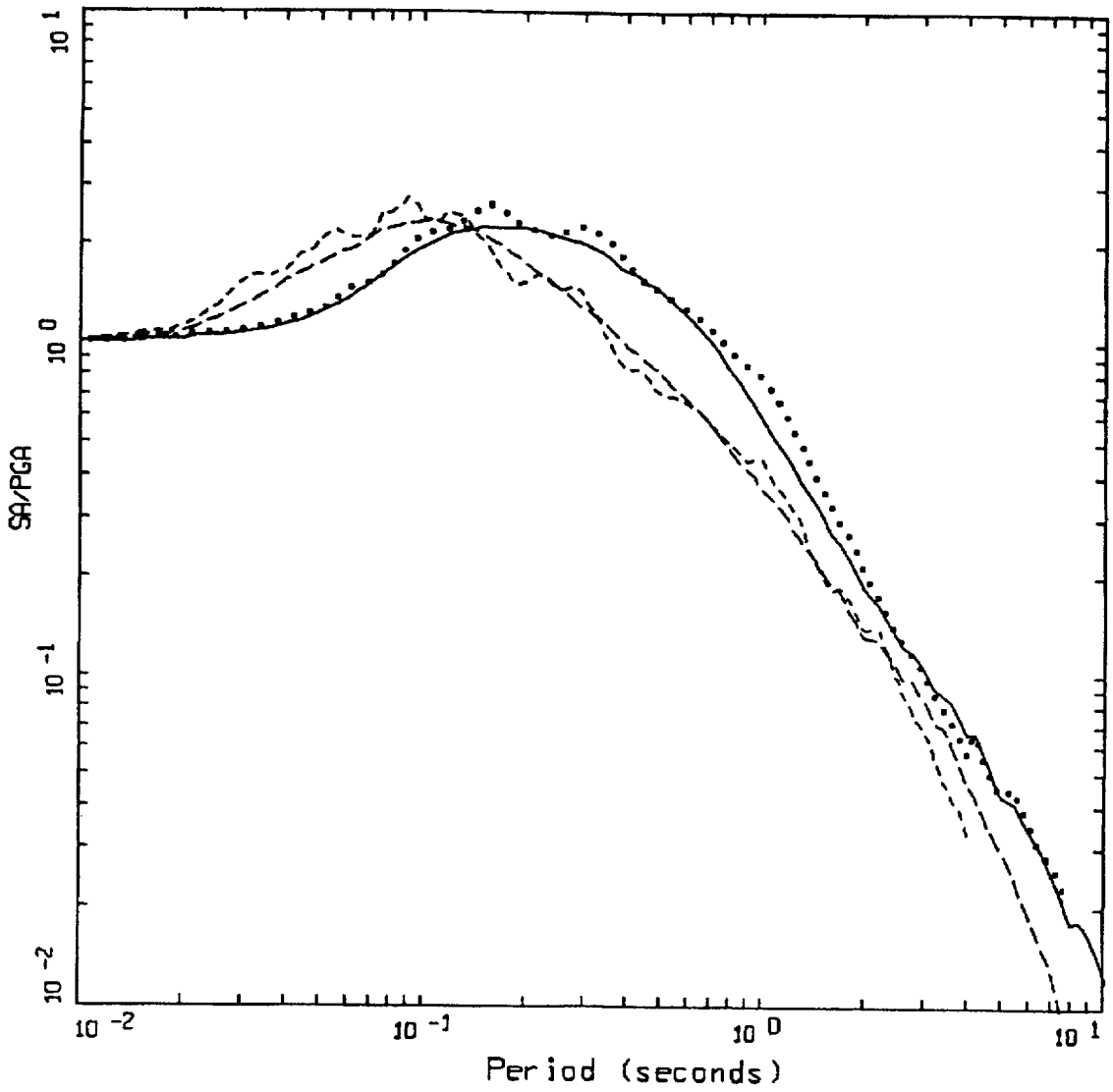

Figure J-22. Median statistical response spectral shapes (5% damping) computed from WUS data recorded at soil sites in the magnitude range of **M** 5 to **M** 6. Rupture distances range from 0 to 10 km and 10 to 50 km.

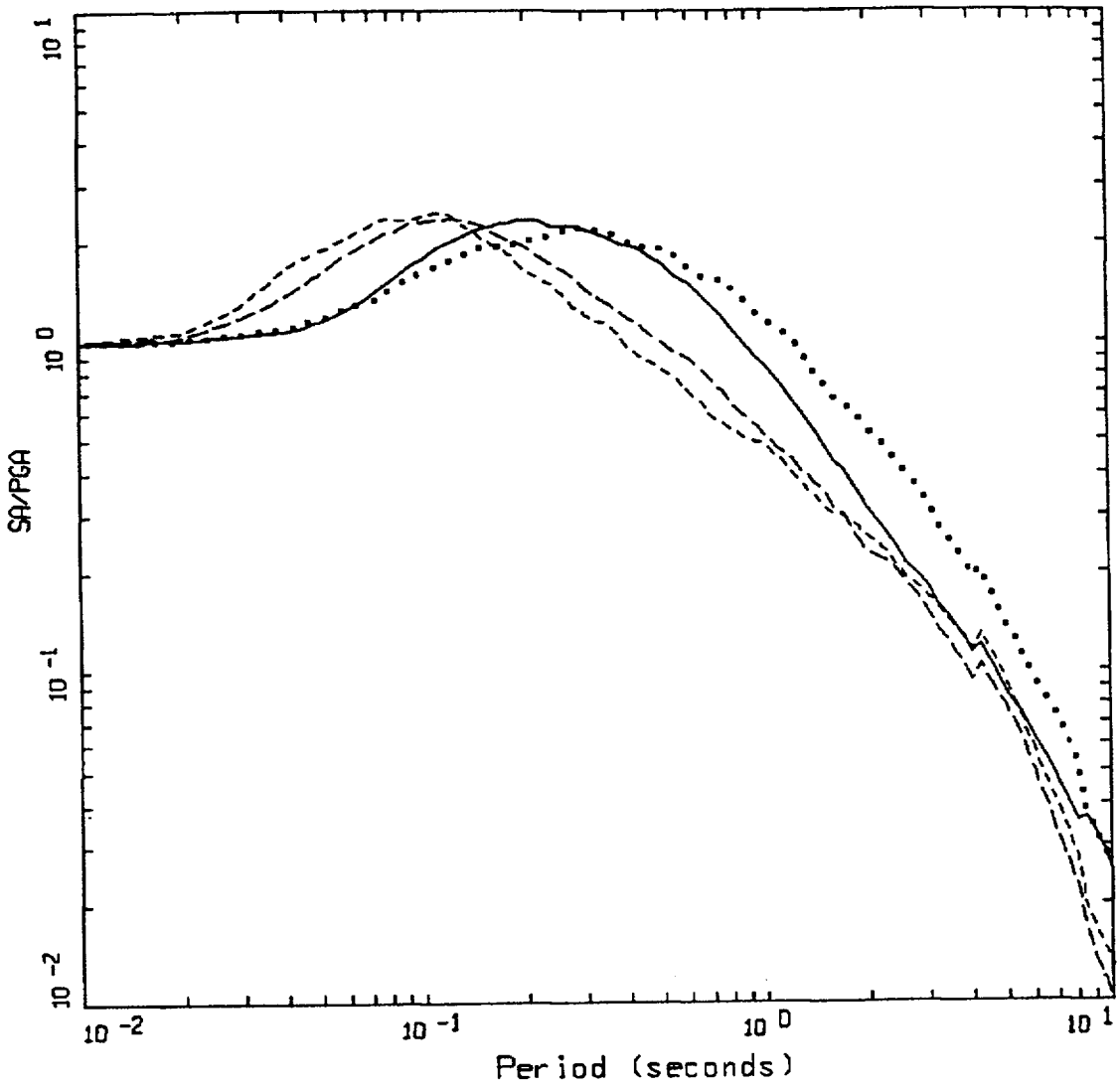

MEDIAN SPECTRAL SHAPES
M=6.5 (6.0-7.0), SOIL

LEGEND

• • • •	HORIZONTAL, M=6.51 (6.0-7.0), D=5.56 KM (0-10 KM), AVG PGA = 0.381 G, 87 REC.
———	HORIZONTAL, M=6.33 (6.0-7.0), D=28.49 KM (10-50 KM), AVG PGA = 0.136 G, 505 REC.
- - - - -	VERTICAL, M=6.51 (6.0-7.0), D=5.56 KM (0-10 KM), AVG PGA = 0.315 G, 42 REC.
— — — —	VERTICAL, M=6.33 (6.0-7.0), D=28.49 KM (10-50 KM), AVG PGA = 0.089 G, 247 REC.

Figure J-23. Median statistical response spectral shapes (5% damping) computed from WUS data recorded at soil sites in the magnitude range of M 6 to M 7+. Rupture distances range from 0 to 10 km and 10 to 50 km.

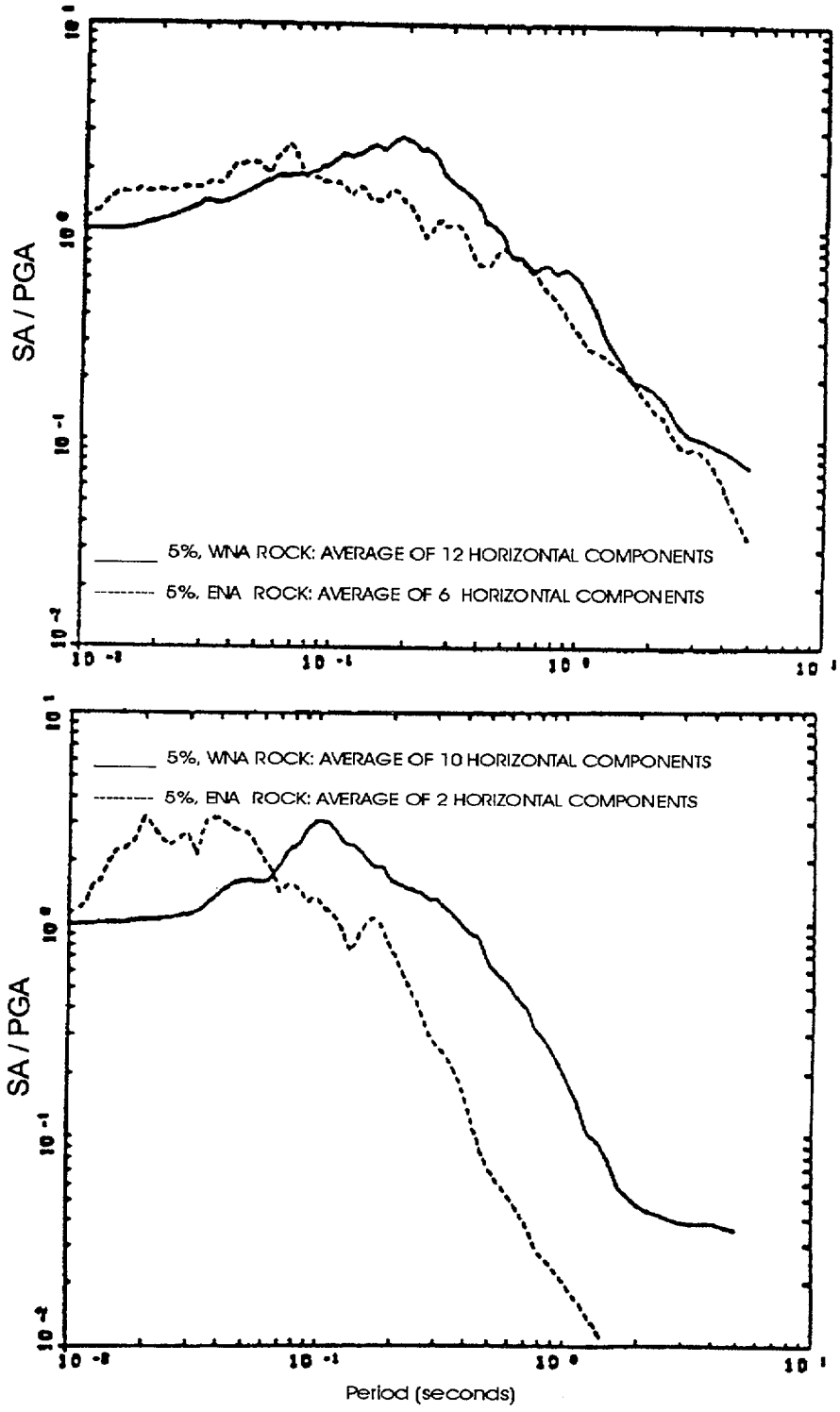

Figure J-24. Average 5% damping response spectral shapes (SA/PGA) computed from motions recorded on rock sites at close distances to **M** = 6.4 earthquakes (top figure) and **M** = 4.0 earthquakes (bottom figure). In each figure the solid line corresponds to motions recorded in WNA, dashed line to motions recorded in ENA.

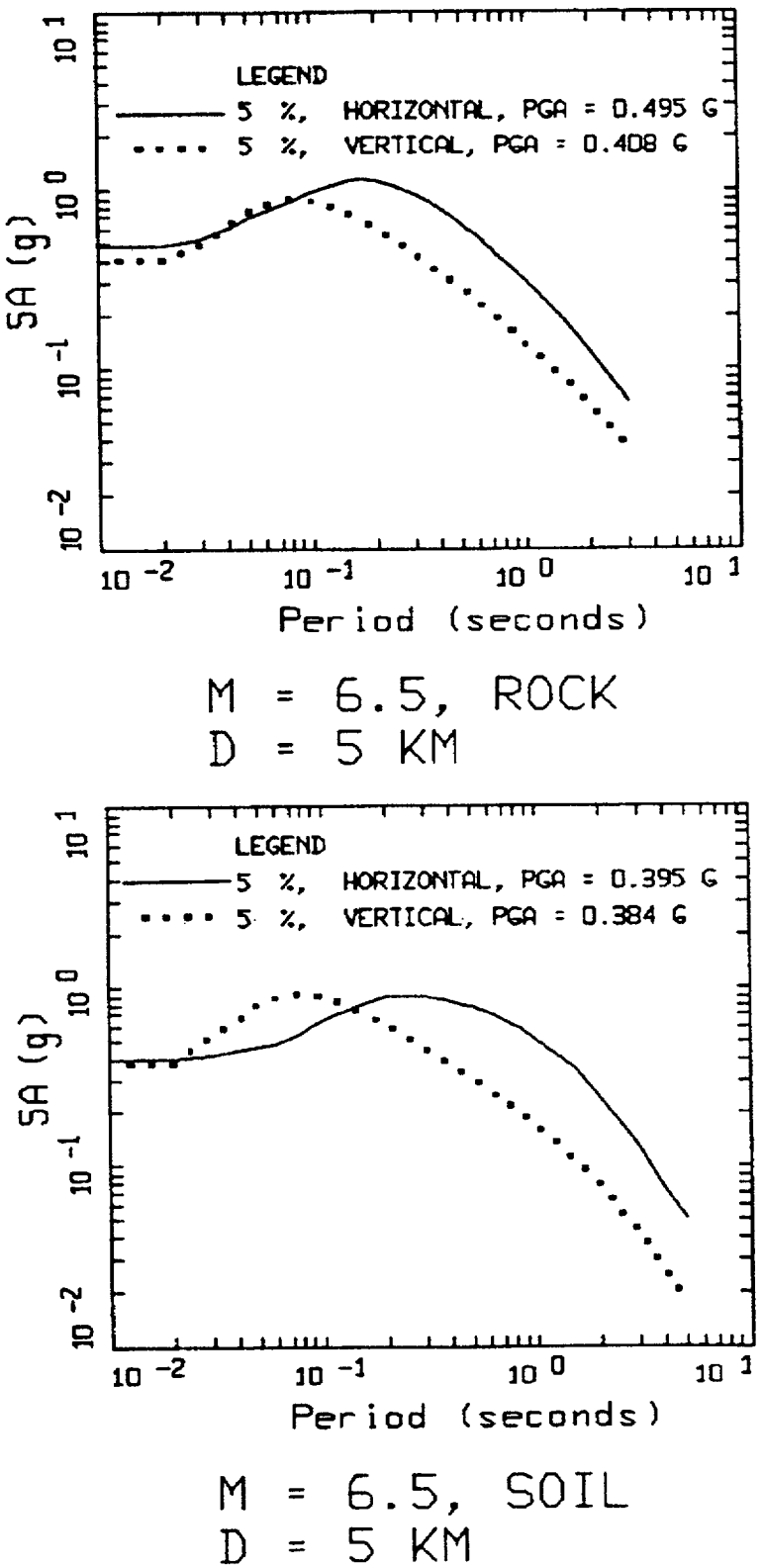

Figure J-25. Median empirical response spectra (5% damped) computed at rock and soil sites for **M** 6.5 at fault distance of 5 km.

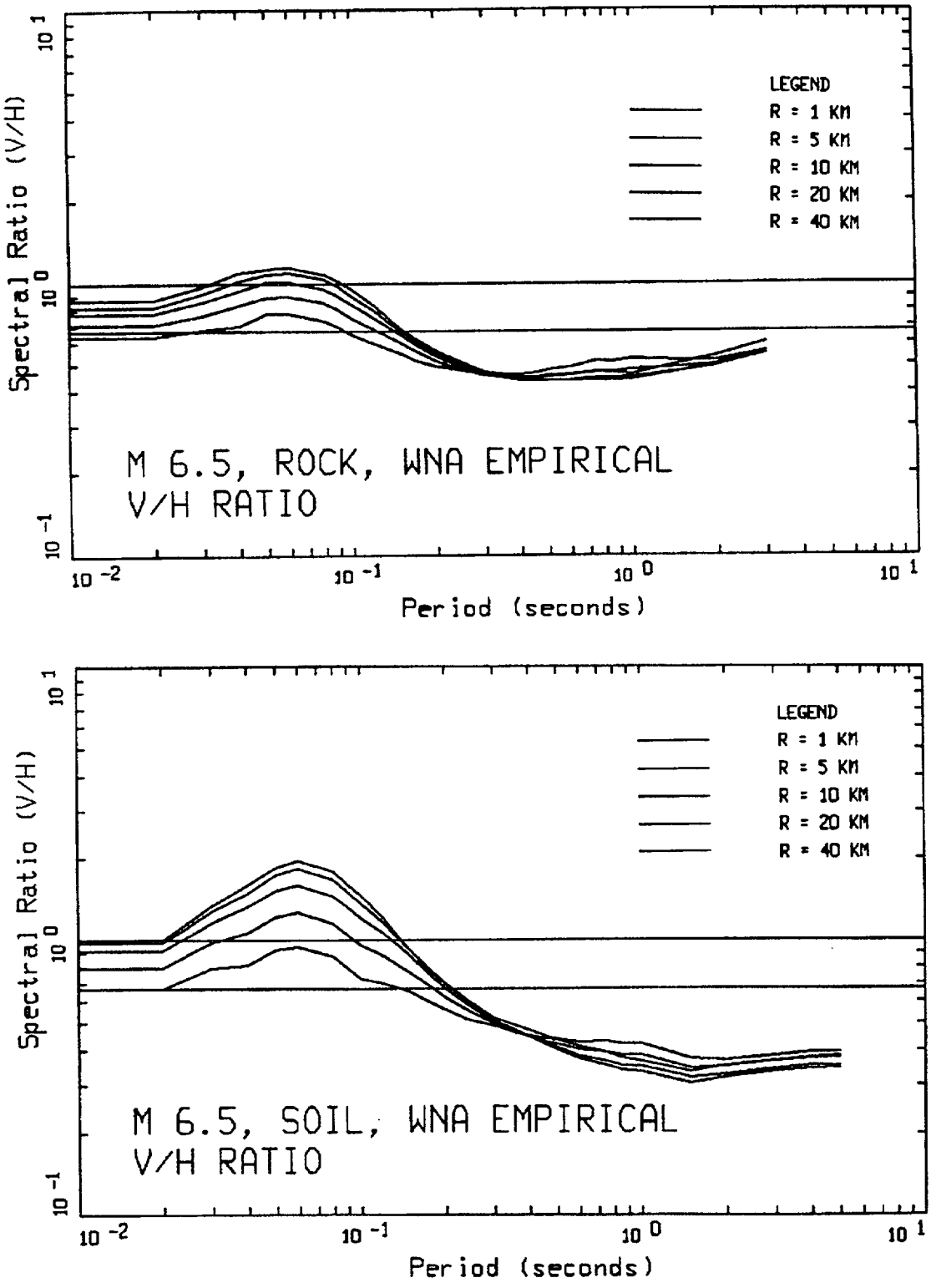

Figure J-26. Distance to fault dependency of response spectral ratios (V/H) for **M** 6.5 at rock and soil sites. Line at 0.66 indicates the constant ratio of 2/3. The R=1 km line is the highest on each plot at 0.05 sec.

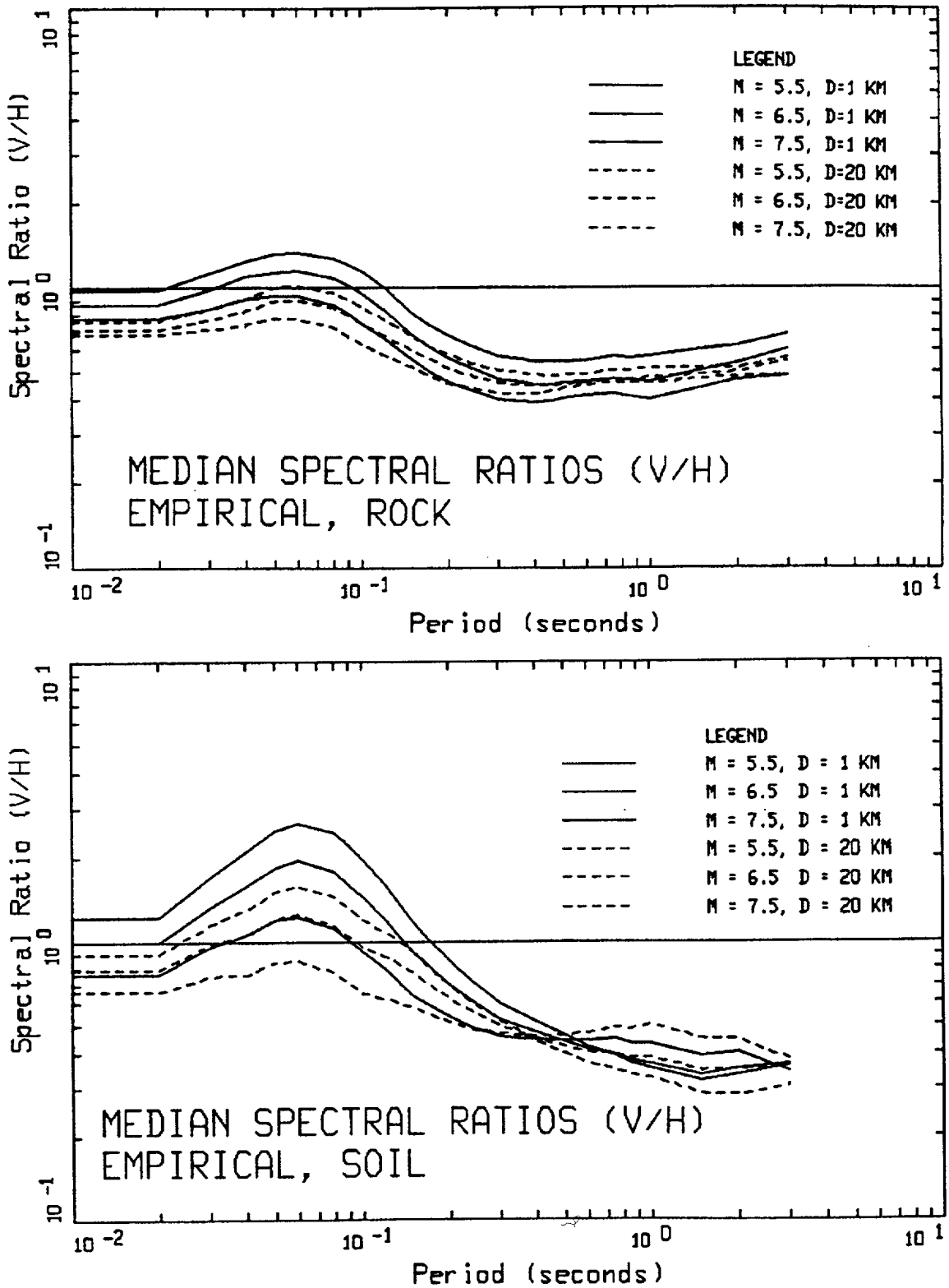

Figure J-27. Magnitude dependency of response spectral ratios (V/H) at fault distances 1 and 20 km. **M** 7.5 shows the highest amplification at 0.05 sec., **M** 5.5 shows the lowest.

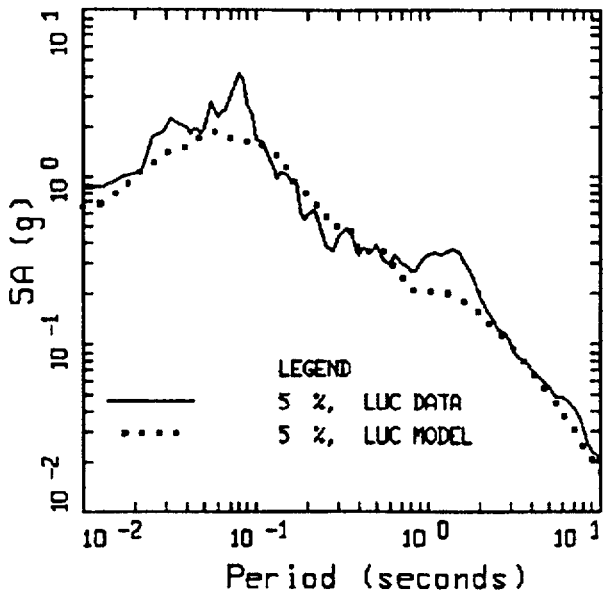

LANDERS, VERTICAL
LUC

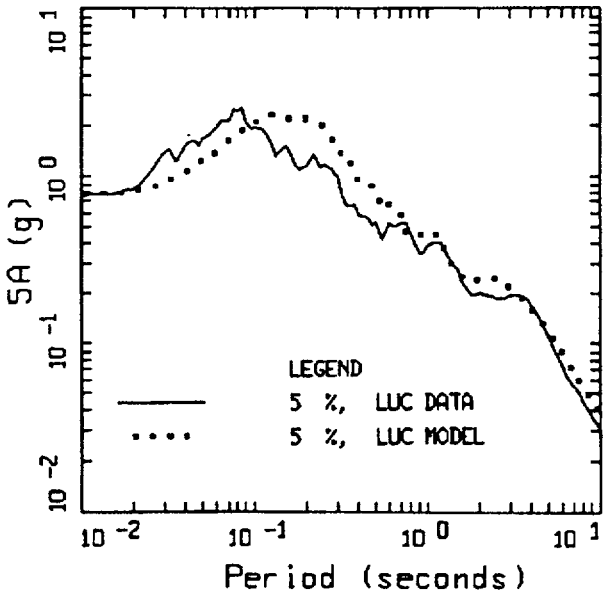

LANDERS, HORIZONTAL
LUC

Figure J-28. Comparison of simulations to recorded motions for vertical and horizontal (average) components at the SCE rock site Lucerne for the 1992 M 7.2 Landers earthquake. The site is at a fault distance of about 2 km. A point-source model is used with the generic rock compression- and shear-wave velocity profiles (Figure J-1) over the regional crustal model (Wald and Heaton, 1994).

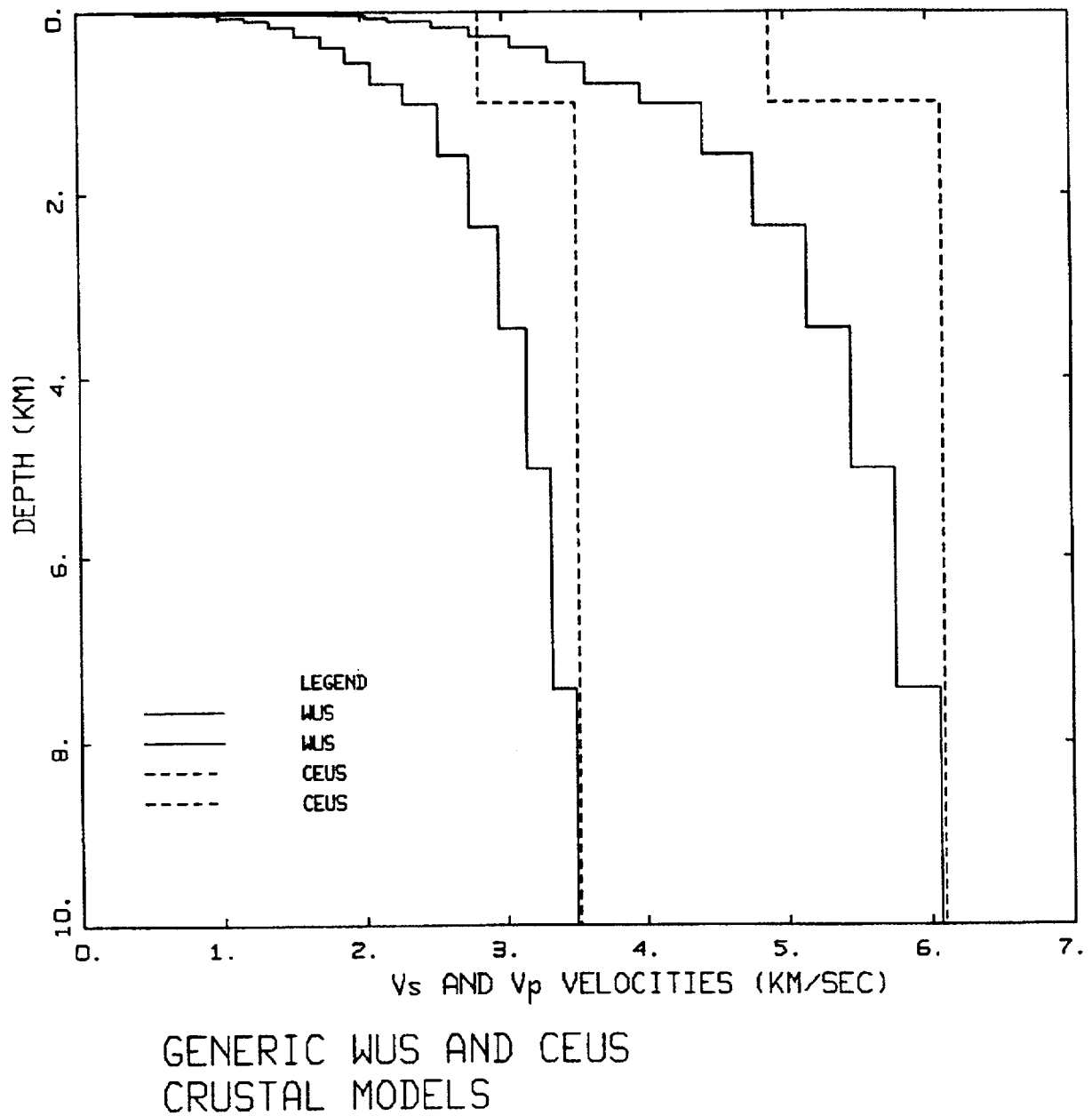

Figure J-29. Comparison of generic compression- and shear-wave velocity profiles for WUS and CEUS crustal conditions.

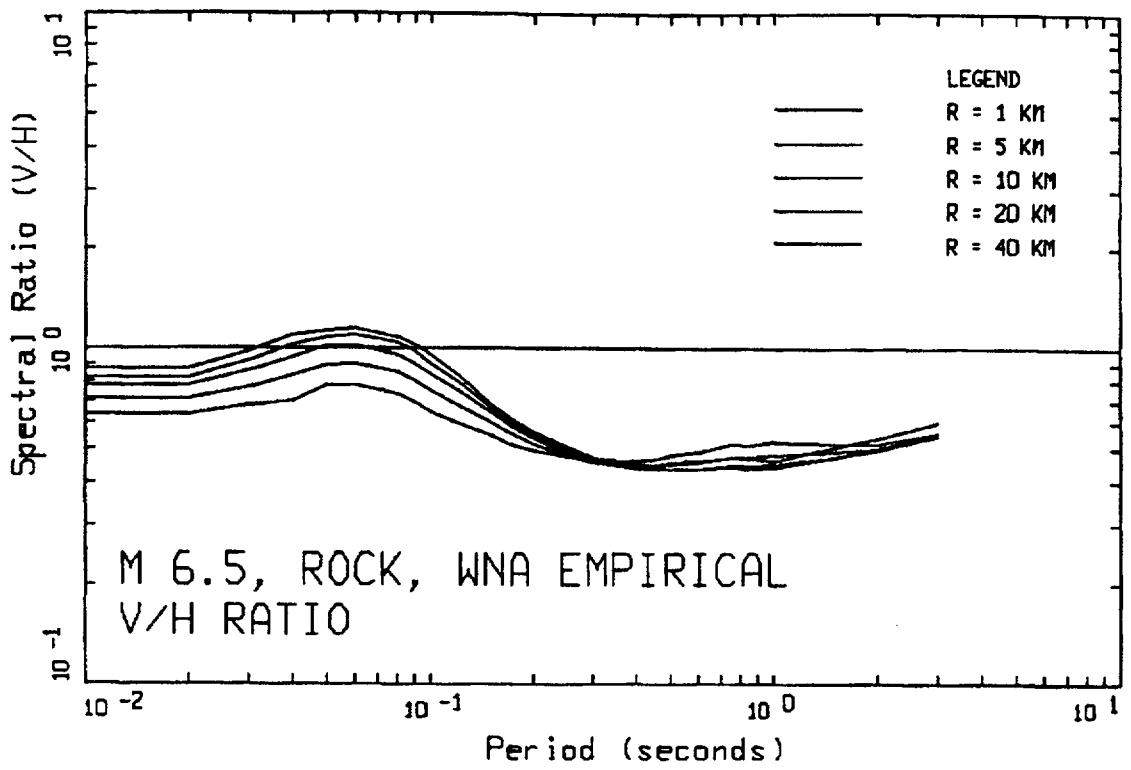

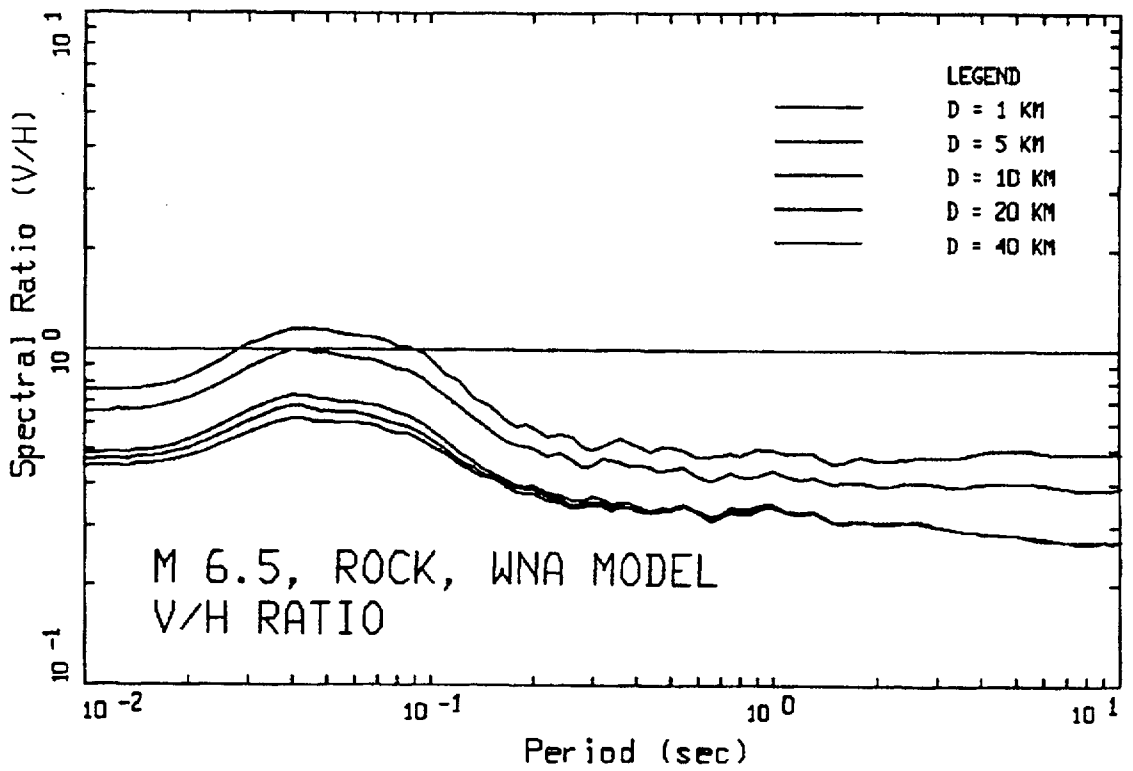

Figure J-30. Comparison of empirical and model response spectral ratios (V/H) at rock sites for M 6.5. The R=1 km line is the highest on each plot at 0.05 sec.

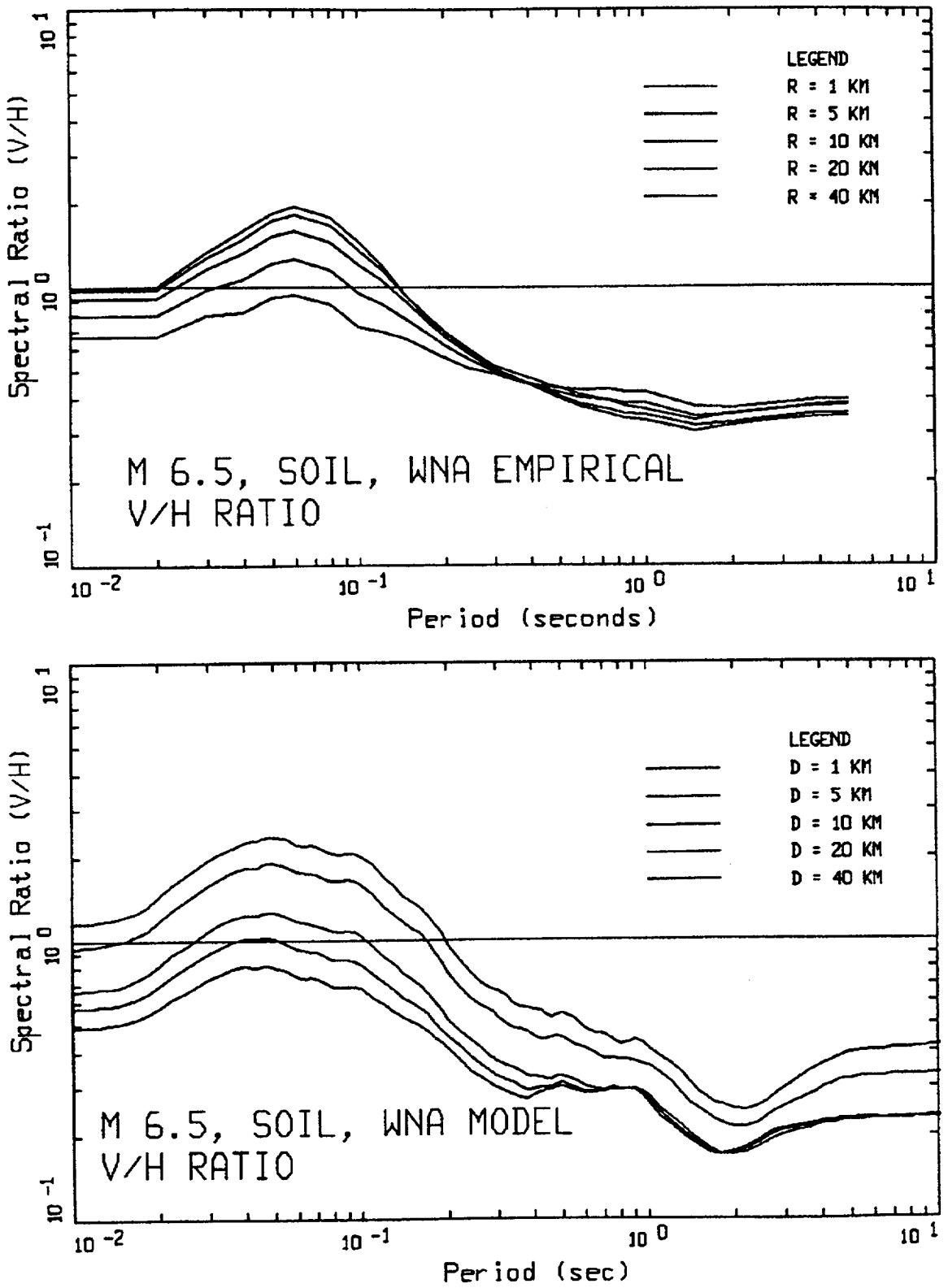

Figure J-31. Comparison of empirical and model response spectral ratios (V/H) at soil sites for M 6.5. The R=1 km line is the highest on each plot at 0.05 sec.

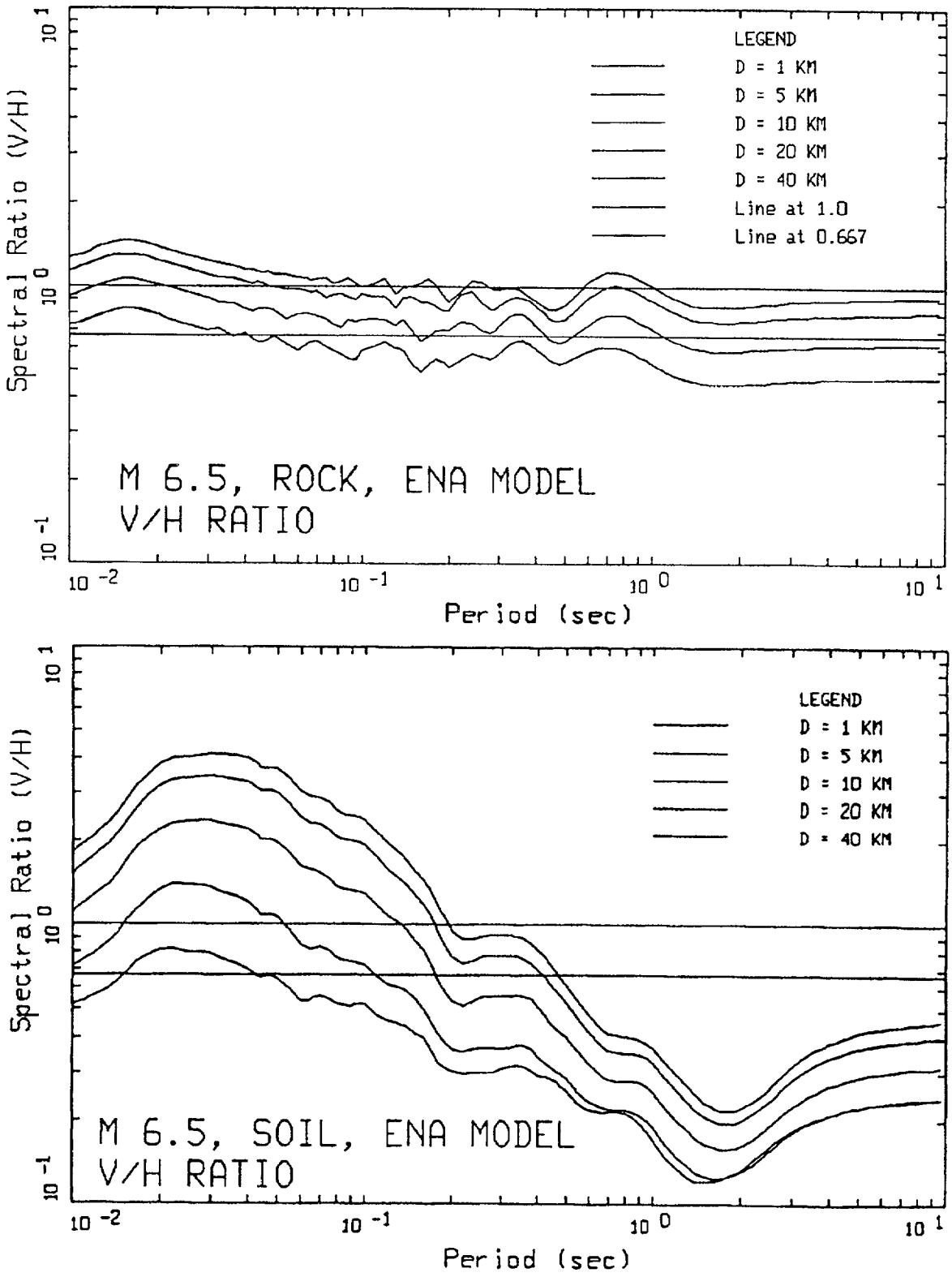

Figure J-32. Response spectral ratios (V/H) computed for CEUS rock and soil sites for **M** 6.5 at a suite of distances. The CEUS crustal model (Figure J-29) is used for rock sites with the generic soil profile (Figure J-2) placed on top to model soil sites.

APPENDIX K COMPARISON OF WUS RECOMMENDED RESPONSE SPECTRAL SHAPES TO RECORDINGS OF THE CHI-CHI, TAIWAN AND TURKEY EARTHQUAKES

The recent September 20, 1999, **M** 7.6 Chi-Chi, Taiwan and August 17, 1999, **M** 7.4 Kocaeli and November 12, 1999, **M** 7.1 Duzce, Turkey earthquakes resulted in over 400 strong motion recordings, greatly increasing the number of data available for large earthquakes. While the number of rock sites is fewer than 400 (a total of 214) and site conditions are not as well determined as most WUS and CEUS sites, the available data reflect a unique opportunity to evaluate the recommended spectral shapes. Although neither Turkey nor Taiwan are within the conterminous US, they both reflect active tectonics and are expected to have ground motions due from shallow crustal sources with similar characteristics to WUS, those being soft rock conditions and a dominantly single-corner frequency source spectrum (Atkinson and Silva; 1997, 2000).

To provide a basis for comparing the Taiwan and Turkey statistical response spectral shapes to the recommended shapes, the data were parceled into the standard distance bins (see Section 4): 0 to 10 km, 10 to 50 km, 50 to 100 km, 100 to 200 km, and 0 to 50 km. Tables K-1 and K-2 indicate bin statistics from the Chi-Chi and Turkey earthquakes, respectively, and Table K-3 lists the bin statistics for the combined data set. The tables show significantly larger motions for the Chi-Chi earthquake than for the Turkey earthquakes. Part of this likely results from the differences in magnitude and source mechanism (thrust verses strike slip, Abrahamson and Silva, 1997) but examination of PGV, PGV/PGA, and $PGA \cdot PGD/PGV^2$ suggests large differences in absolute motion over a wide frequency range.

For the combined data set (Chi-chi and Turkey earthquakes), Figures K-1 to K-5 compare the statistical shapes to the recommended spectral shapes computed for the bin average magnitudes and distances. Records are weighted such that each earthquake has equal weight in the bin shapes. The figures show a difference in shapes between the statistical and the recommended shapes, with the recommended shapes higher at high frequency and generally lower at low frequency. At the largest distance bin, 100 to 200 km, Figure K-4 shows a very large frequency shift. In this case the recommended shape peak is near 3 Hz while the peak in the statistical shape is shifted to 1 to 2 Hz. These trends suggest the effects of shallow crustal damping, (kappa) within about 50 km and a combination of kappa and deep crustal damping (Q(f)) beyond 50 km (Silva and Green, 1989; Silva and Darragh, 1995; McGuire et al., 2000). To see this more clearly, Figure K-6 shows the effects of kappa on response spectral shapes computed for **M** 6.5 (McGuire et al., 2000). The shift in shape to lower frequency as kappa increases is evident. Figure K-6 shows that for large kappa values (about 0.04, the value for soft WUS rock [(Silva and Darragh, 1995; McGuire et al., 2000)], a factor of two increase in kappa results in a frequency shift of nearly a factor of two. For sites within 50 km, Figure K-5 shows a slight shift to lower frequency for the combined data set, suggesting a small increase in kappa over that for WUS. However, Figure K-4 (100 to 200 km) shows a dramatic frequency shift, nearly a factor of two. Since this distance bin is populated entirely by Chi-Chi data, the shift in spectral shape suggests major differences in kappa and Q(f) between Taiwan and WUS.

To see this more clearly, Figures K-7 to K-11 show spectral comparisons for the Chi-Chi earthquake only, and Figures K-12 to K-15 show comparisons for the Turkey earthquakes only. For the Chi-Chi earthquake sufficient data are available for each bin to adequately define stable shapes (Table K-2). For the Turkey earthquakes (Table K-3) only the 10 to 50 km and 0 to 50 km bins have sufficient data from which to discern trends.

For the Chi-Chi earthquake, Figures K-7 to K-9 and Figure K-11 (0 to 50 km) show about a 30% shift in the spectra to lower frequency relative to WUS. From Figure K-6 this shift suggests an increase in kappa of about 20 to 30% over the soft rock WUS value of about 0.04 sec (Silva and Darragh, 1995; McGuire et al., 2000) to about 0.05 sec. Figure K-10, which plots the 100 to 200 km bin, shows a larger shift, about a factor of two, suggesting a much lower Q(f) for Taiwan than WUS (Silva and Green, 1989).

Data from recent Turkey earthquakes that have sufficiently populated bins show shapes generally consistent with the WUS empirical (recommended) shapes. These shapes are illustrated in Figure K-13 for the 10 to 50 km bin, and in Figure K-15 for the 0 to 50 km bin.

Results of these comparisons indicate that Turkey data appear to be representative of WUS soft rock conditions. However, because of possibly higher crustal damping in Taiwan, care should be taken in decisions to include the Chi-Chi data with the WUS data set, or alternatively, to use WUS empirical relations for applications in Taiwan as larger crustal damping will result in lower absolute levels at high frequency (Section 3). Analyses of the larger aftershock data will likely resolve the issue of crustal damping (Kappa and Q(f)). Both the Chi-Chi and Turkey data sets are considered appropriate for use as inputs to scaling or spectral matching procedures, so they are included in the time history analysis data set.

REFERENCES

Abrahamson, N.A. and Silva, W.J. (1997). "Empirical response spectral attenuation relations for shallow crustal earthquakes." *Seism. Res. Lett.*, 68(1), 94-127.

Atkinson, G.M and W.J. Silva (1997). "An empirical study of earthquake source spectra for California earthquakes." *Bull. Seism. Soc. Am.* 87(1), 97-113.

Atkinson, G.M and W.J. Silva (2000). "Stochastic modeling of California ground motions." *Bull. Seism. Soc. Am.* 90(2), 255-274.

Silva, W.J. and R. Darragh (1995). "Engineering characterization of earthquake strong ground motion recorded at rock sites." Palo Alto, Calif: Electric Power Research Institute, TR-102261.

Silva, W.J., and Green, R.K. (1989). "Magnitude and distance scaling of response spectral shapes for rock sites with applications to North American tectonic environment." Earthquake Spectra, 5(3), 591-624.

Table K-1
WUS STATISTICAL SHAPE BINS
CHI CHI

Magnitude Bins (M)

Range	Bin Center
5 - 6	5.5
6 - 7	6.5
7+	7.5

Distance Bin (km)	$\overline{M}$	$\overline{D}$ (km)	Number of Spectra	PGA[1](g), σ_{ln}	PGV*(cm/sec), σ_{ln}	PGD*(cm), σ_{ln}	$\frac{PGV^*}{PGA}$ ($\frac{cm/sec}{g}$), σ_{ln}	$\frac{PGA \cdot PGD^*}{PGV^2}$, σ_{ln}
0 - 10, rock	7.60	4.93	20	0.42, 0.55	61.92, 0.50	37.56, 0.83	145.87, 0.49	4.08, 0.39
10 - 50, rock	7.60	33.42	38	0.14, 0.90	20.49, 0.81	13.87, 0.82	143.71, 0.52	4.62, 0.54
50 - 100, rock	7.60	76.29	116	0.05, 0.47	8.68, 0.59	7.81, 0.80	162.08, 0.39	5.44, 0.45
100 - 200, rock	7.60	126.85	40	0.03, 0.66	6.19, 0.63	5.60, 0.80	218.66, 0.37	4.06, 0.30
0 - 50, rock	7.60	24.08	56	0.20, 0.94	29.37, 0.90	19.88, 0.96	146.30, 0.51	4.54, 0.48

[1]Median values

Table K-2
WUS STATISTICAL SHAPE BINS
TURKEY

Magnitude Bins (M)

Range
5 - 6
6 - 7
7+

Bin Center
5.5
6.5
7.5

Distance Bin (km)	$\overline{M}$	$\overline{D}$ (km)	Number of Spectra	PGA[1](g), σ_{ln}	PGV*(cm/sec), σ_{ln}	PGD*(cm), σ_{ln}	$\frac{PGV^*}{PGA}$ ($\frac{cm/sec}{g}$), σ_{ln}	$\frac{PGA \cdot PGD^*}{PGV^2}$, σ_{ln}
0 - 10, rock	7.40	5.50	3	0.26, 0.51	45.42, 0.79	30.23, 1.20	173.22, 0.28	3.77, 0.12
10 - 50, rock	7.27	27.50	14	0.12, 1.09	15.94, 0.87	7.42, 1.24	128.21, 0.61	3.56, 0.42
50 - 100, rock	7.40	62.30	2	0.06, -----	5.79, -----	3.88, -----	96.49, -----	6.81, -----
100 - 200, rock	------	--------	----------	----------	----------	----------	----------	----------
0 - 50, rock	7.30	22.61	17	0.15, 1.02	20.11, 0.93	10.14, 1.31	137.07, 0.55	3.60, 0.37

[1]Median values

Table K-3
WUS STATISTICAL SHAPE BINS
CHI CHI AND TURKEY

Magnitude Bins (**M**)

Range	Bin Center
5 - 6	5.5
6 - 7	6.5
7+	7.5

Distance Bin (km)	$\overline{M}$	$\overline{D}$ (km)	Number of Spectra	PGA[2](g), σ_{ln}	PGV*(cm/sec), σ_{ln}	PGD*(cm), σ_{ln}	$\frac{PGV^*}{PGA}$ ($\frac{cm/sec}{g}$), σ_{ln}	$\frac{PGA \cdot PGD^*}{PGV^2}$, σ_{ln}
0 - 10, rock	7.57	5.03	23	0.39, 0.56	58.80, 0.52	36.22, 0.83	150.10, 0.45	4.02, 0.36
10 - 50, rock	7.51	31.82	52	0.14, 0.93	19.15, 0.82	11.72, 0.97	139.36, 0.54	4.31, 0.52
50 - 100, rock	7.60	76.05	118	0.05, 0.47	8.62, 0.59	7.72, 0.80	160.66, 0.39	5.46, 0.45
100 - 200, rock	7.60	126.85	40	0.03, 0.66	6.19, 0.63	5.60, 0.80	218.66, 0.37	4.06, 0.30
0 - 50, rock	7.53	23.72	73	0.19, 0.96	26.79, 0.91	16.88, 1.07	144.00, 0.51	4.29, 0.46

[2]Median values

Table K-4

CHI-CHI, TAIWAN AND TURKEY STRONG-MOTION CATALOG (09/05/00)

Earthquake	Date & Time			Magnitude (2)			Station (3)			Closest Dist (km)(4)	Site Codes (5)	Comp.	Filter HP (hz)	Corners LP (hz)	PGA (g)	PGV (cm/s)	PGD (cm)
No. Location, Mech. Dip (1)	YEAR	MODY	M	ML	MS	OTH	No.	Description	H/F								
0141 Kocaeli, Turkey	1999	0817	7.4	0.0	7.8	6.7	KOERI	99999	Arcelik	17.0	--B	UP	1.50	80.0	0.086	2.6	0.22
00								99		17.0	-	000	0.80	70.0	0.180	10.5	0.90
												270	0.90	70.0	0.108	6.2	0.63
							ERD	99999	Cekmece	76.1	--D	UP	0.60	20.0	0.046	3.4	0.34
								99		76.1	-	000	0.30	20.0	0.114	12.1	1.41
												270	0.40	20.0	0.105	6.4	0.84
							ERD	99999	Duzce	14.2	--D	UP	0.08	20.0	0.229	20.4	17.01
								99		14.2	-	180		20.0	0.312	58.8	44.11
												270	0.08	15.0	0.358	46.4	17.61
							ERD	99999	Eregli	999.9	---	UP	1.00	20.0	0.047	2.9	0.21
								99		999.9	-	180	0.40	20.0	0.121	13.3	2.75
												090	0.40	20.0	0.090	10.2	1.23
							ERD	99999	Gebze	17.0	--B	UP	1.00	40.0	0.151	6.3	0.59
								99		17.0	-	000	0.06	25.0	0.244	50.3	42.74
												270	0.08	30.0	0.137	29.7	27.54
							ERD	99999	Goynuk	35.5	--B	UP	0.10	30.0	0.114	11.5	7.59
								99		35.5	-	000	0.15	30.0	0.132	8.8	3.05
												090	0.10	25.0	0.119	10.5	3.94
							ERD	99999	Izmit	7.7	--B	UP	2.00	30.0	0.149	11.9	4.99
								99		7.7	-	180	0.10	30.0	0.152	22.6	9.81
												090	0.10	30.0	0.220	29.8	17.12
							ERD	99999	Iznik	29.7	--B	UP	0.30	30.0	0.083	7.7	1.70
								99		29.7	-	180	0.15	25.0	0.103	16.5	7.00
												090	0.07	25.0	0.136	28.8	17.44
							ITU	99999	Mecidiyekoy	62.3	--B	UP	1.10	60.0	0.028	1.3	0.16
								99		62.3	-	000	0.20	50.0	0.053	3.8	1.49
												270	0.05	60.0	0.068	8.83	10.11
							ERD	99999	Sakarya	3.3	--B	UP			0.259	41.84	31.32
								99		3.3	-	XXX	-99.				
												090	0.04	40.0	0.376	79.5	70.52
							ERD	99999	Tekirdag	999.9	--A	UP	0.10	20.0	0.011	1.2	0.74

Table K-4

CHI-CHI, TAIWAN AND TURKEY STRONG-MOTION CATALOG (09/05/00)

Earthquake	Date & Time			Magnitude (2)			Station (3)			Closest Dist (km)(4)	Site Codes (5)	Comp.	Filter HP (hz)	Corners LP (hz)	PGA (g)	PGV (cm/s)	PGD (cm)
No. Location, Mech, Dip (1)	YEAR	MODY	M	ML	MS	OTH		No.	Description H/F								
								99		999.9	-	180	0.60	30.0	0.033	2.6	0.35
												090	0.10	30.0	0.035	2.8	1.29
							KOERI	99999	Yarimca	4.4	B-D	UP			0.242	30.8	29.55
								99		4.4	-	000	0.10	80.0	0.292	62.3	44.91
												270	0.1	80.0	0.340	68.2	35.86
0142 Chi-Chi, Taiwan 02	1999	0920	7.6	7.3	7.6	0.0	CWB	99999	ALS	15.29	--1	V	0.14	40.0	0.073	14.2	6.13
								99		12.27	A	E	0.10	30.0	0.183	39.3	10.37
												N	0.14	40.0	0.163	21.9	8.64
							CWB	99999	ESL	44.94	--1	V	0.04	50.0	0.057	7.4	7.33
								99		40.24	C	E	0.15	25.0	0.068	6.2	2.31
												N	0.05	25.0	0.077	7.9	5.55
							CWB	99999	NST	36.95	--1	V	0.06	24.0	0.108	17.5	11.82
								99		36.95	A	E	0.03	50.0	0.309	22.7	21.38
												N	0.05	50.0	0.388	26.9	16.05
							CWB	99999	STY	52.06	--1	V	0.10	30.0	0.018	2.7	1.94
								99		50.58	A	E	0.10	30.0	0.033	4.8	2.29
												N	0.1	30.0	0.040	4.0	1.98
							CWB	99999	WNT	1.18	--1	V	0.05	50.0	0.311	34.2	17.06
								02		1.18	C	E	0.03	50.0	0.958	68.8	31.11
												N	0.05	50.0	0.626	42.0	18.83
							CWB	99999	WSF	45.71	--1	V	0.05	30.0	0.035	6.9	5.36
								99		45.71	D	E	0.06	50.0	0.066	14.8	12.72
												N	0.05	30.0	0.073	11.1	8.92
							CWB	99999	CHK	67.90	--1	V	0.40	20.0	0.016	2.4	0.45
								99		64.88	C	E	0.20	20.0	0.040	5.1	1.34
												N	0.14	20.0	0.051	7.1	2.13
							CWB	99999	ENA	77.75	--1	V	0.20	30.0	0.046	6.2	1.61
								99		75.14	A	E	0.30	30.0	0.070	5.9	0.90
												N	0.30	22.0	0.060	5.1	1.18
							CWB	99999	ILA027	94.73	--1	V	0.03	20.0	0.022	5.6	6.17
								99		92.59	C	E	0.06	20.0	0.101	17.8	8.02
												N	0.10	20.0	0.062	14.4	9.16

Table K-4

CHI-CHI, TAIWAN AND TURKEY STRONG-MOTION CATALOG (09/05/00)

Earthquake No. Location, Mech. Dip (1)	Date & Time YEAR	MOD Y	M	Magnitude (2) ML	MS	OTH	Station (3)	No.	Description H/F	Closest Dist (km)(4)	Site Codes (5)	Comp.	Filter HP (hz)	Corners LP (hz)	PGA (g)	PGV (cm/s)	PGD (cm)
							CWB	99999	ILA032	95.77	--1	V	0.33	20.0	0.025	2.6	0.80
								99		92.59	C	E	0.03	20.0	0.056	11.7	5.05
												N	0.13	20.0	0.049	8.6	2.09
							CWB	99999	ILA035	104.77	--1	V	0.20	20.0	0.011	2.1	0.61
								99		103.19	C	E	0.05	20.0	0.070	10.5	5.51
												N	0.13	20.0	0.052	9.9	3.32
							CWB	99999	ILA039	97.56	--1	V	0.20	14.0	0.020	3.2	1.18
								99		95.76	C	E	0.03	20.0	0.058	12.1	13.71
												N	0.15	20.0	0.062	12.1	4.66
							CWB	99999	ILA043	88.86	---	V	0.30	30.0	0.034	2.9	0.59
								99		86.58	A	E	0.40	20.0	0.063	5.2	0.61
												N	0.30	14.0	0.052	5.8	1.06
							CWB	99999	NCU	78.90	--1	V	0.05	12.0	0.036	8.1	6.19
								99		78.90	B	E	0.04	20.0	0.075	16.7	19.86
												N	0.10	20.0	0.086	16.1	8.36
							CWB	99999	NSK	64.51	--1	V	0.20	50.0	0.034	5.1	1.12
								99		63.95	A	E	0.02	30.0	0.070	6.9	4.22
												N	0.20	33.0	0.065	5.1	1.20
							CWB	99999	PNG	114.21	--1	V	0.40	30.0	0.013	1.2	0.21
								99		114.21	A	E	0.24	40.0	0.028	1.6	0.52
												N	0.22	30.0	0.035	2.4	0.75
							CWB	99999	SSD	99.30	--1	V	0.30	20.0	0.014	1.5	0.35
								99		98.47	C	E	0.20	20.0	0.018	1.7	0.48
												N	0.30	20.0	0.026	1.6	0.27
							CWB	99999	TAW	136.58	--1	V	0.10	14.0	0.003	0.6	0.27
								99		135.11	C	E	0.40	14.0	0.005	0.7	0.18
												N	0.20	14.0	0.007	0.9	0.30
							CWB	99999	TAP042	108.19	--1	V	0.02	30.0	0.025	9.2	8.73
								99		108.19	B	N	0.02	30.0	0.100	15.5	11.46
												W	0.02	30.0	0.085	19.1	19.06
							CWB	99999	TCU018	63.81	--1	V		50.0	0.032	18.7	17.55
								99		63.81	C	N	0.02	30.0	0.057	22.3	28.27

Table K-4

CHI-CHI, TAIWAN AND TURKEY STRONG-MOTION CATALOG (09/05/00)

Earthquake No. Location, Mech, Dip (1)	Date & Time YEAR	MOD Y	M	Magnitude (2) ML	MS	OTH	Station (3)	No.	Description H/F	Closest Dist (km)(4)	Site Codes (5)	Comp.	Filter HP (hz)	Corners LP (hz)	PGA (g)	PGV (cm/s)	PGD (cm)
												W	0.02	30.0	0.054	34.5	52.36
							CWB	99999	KAU082	183.97	---	V	0.02	12.0	0.009	2.8	2.60
								99		182.87	A	N	0.02	15.0	0.019	4.8	4.58
												W	0.02	12.0	0.017	7.8	6.77
							CWB	99999	TAP059	125.93	--1	V	0.02	20.0	0.018	5.7	6.82
								99		125.89	A	N	0.02	30.0	0.039	6.5	4.80
												W		15.0	0.030	7.6	8.11
							CWB	99999	TAP060	128.49	--1	V	0.02	24.0	0.014	5.0	7.02
								99		128.41	A	N	0.02	20.0	0.036	7.6	6.05
												W		20.0	0.036	11.0	8.80
							CWB	99999	TAP035	96.88	--1	V	0.02	24.0	0.028	7.6	9.01
								99		96.68	A	N	0.02	24.0	0.085	8.3	8.00
												W	0.02	24.0	0.067	8.4	12.78
							CWB	99999	TCU096	51.96	--1	V	0.02	50.0	0.037	15.0	14.59
								99		51.96	C	N	0.04	40.0	0.107	27.0	26.11
												W	0.02	22.0	0.059	39.5	41.34
							CWB	99999	TCU007	88.39	--1	V	0.03	30.0	0.028	8.5	9.98
								99		88.39	B	N	0.02	20.0	0.071	18.0	15.45
												W	0.02	22.0	0.060	23.6	37.22
							CWB	99999	TCU025	54.36	---	V	0.05	50.0	0.034	13.8	18.29
								99		54.36	A	N	0.05	50.0	0.058	10.5	10.17
												W	0.03	50.0	0.075	19.0	22.00
							CWB	99999	ILA046	91.45	--1	V	0.04	40.0	0.028	8.0	11.80
								99		89.23	C	N	0.04	40.0	0.055	9.8	7.66
												W	0.04	40.0	0.068	13.3	10.59
							CWB	99999	TCU014	92.42	--1	V	0.03	22.0	0.018	6.2	8.05
								99		92.42	B	N	0.02	25.0	0.075	13.5	15.04
												W	0.02	20.0	0.058	24.2	37.42
							CWB	99999	TCU015	47.35	--1	V	0.02	50.0	0.068	17.2	14.85
								99		47.35	B	N	0.03	50.0	0.114	29.5	24.14
												W	0.02	50.0	0.119	49.8	49.79
							CWB	99999	TAP043	93.73	--1	V	0.02	20.0	0.026	8.4	9.53

Table K-4

CHI-CHI, TAIWAN AND TURKEY STRONG-MOTION CATALOG (09/05/00)

Earthquake No.	Location, Mech, Dip (1)	Date & Time YEAR	MOD Y	M	Magnitude (2) ML	MS	OTH	Station (3)	No.	Description H/F	Closest Dist (km)(4)	Site Codes (5)	Comp.	Filter HP (hz)	Corners LP (hz)	PGA (g)	PGV (cm/s)	PGD (cm)
									99		93.73	C	N	0.02	20.0	0.082	17.3	13.10
													W	0.02	20.0	0.065	18.4	2.61
								CWB	99999	TAP032	98.79	--1	V	0.02	50.0	0.059	9.6	8.76
									99		98.79	C	N	0.03	50.0	0.115	18.0	11.46
													W	0.02	40.0	0.107	24.2	21.13
								CWB	99999	KAU034	122.84	--1	V	0.02	12.0	0.009	2.3	3.08
									99		121.84	A	N	0.04	12.0	0.009	2.1	2.42
													W	0.05	14.0	0.009	2.1	2.56
								CWB	99999	TCU026	54.61	--1	V	0.02	50.0	0.061	17.1	18.12
									99		54.61	B	N	0.02	50.0	0.091	27.5	29.95
													W	0.02	50.0	0.120	39.4	43.09
								CWB	99999	ILA036	101.55	--1	V	0.03	30.0	0.026	12.8	9.59
									99		99.79	C	N	0.05	40.0	0.068	17.0	8.86
													W	0.04	30.0	0.055	15.2	10.41
								CWB	99999	KAU038	157.43	--1	V	0.03	20.0	0.006	2.0	2.69
									99		156.16	B	N	0.03	15.0	0.010	2.4	2.56
													W	0.30	12.0	0.007	1.2	0.39
								CWB	99999	KAU018	87.76	--1	V	0.02	20.0	0.016	6.2	5.41
									99		87.71	A	N	0.02	22.0	0.026	7.9	6.97
													W	0.02	20.0	0.035	6.2	7.12
								CWB	99999	TAP053	98.33	---	V	0.03	20.0	0.035	10.4	9.77
									99		98.24	A	N	0.03	20.0	0.086	12.2	7.62
													W	0.02	24.0	0.082	11.3	15.70
								CWB	99999	TAP046	127.26	--1	V	0.02	30.0	0.018	4.5	6.17
									99		126.99	C	N	0.02	30.0	0.054	6.6	4.93
													W	0.02	24.0	0.084	12.6	7.08
								CWB	99999	TAP052	99.92	---	V	0.03	50.0	0.039	8.2	10.24
									99		99.92	B	N	0.02	50.0	0.127	23.6	14.06
													W	0.02	30.0	0.066	16.6	25.29
								CWB	99999	KAU007	117.13	--1	V	0.02	20.0	0.014	6.8	5.13
									99		117.13	C	N	0.02	20.0	0.024	9.0	9.31
													W	0.04	15.0	0.025	7.4	6.92

Table K-4

CHI-CHI, TAIWAN AND TURKEY STRONG-MOTION CATALOG (09/05/00)

Earthquake No. Location, Mech, Dip (1)	Date & Time YEAR	MOD Y	M	Magnitude (2) ML	MS	OTH		Station (3) No.	Description H/F	Closest Dist (km)(4)	Site Codes (5)	Comp.	Filter HP (hz)	Corners LP (hz)	PGA (g)	PGV (cm/s)	PGD (cm)
							CWB	99999	CHY063	78.12	--1	V	0.03	24.0	0.025	5.3	5.42
								99		78.12	B	N	0.03	24.0	0.068	9.4	8.27
												W	0.02	22.0	0.060	7.9	6.92
							CWB	99999	TCU009	80.14	--1	V	0.02	30.0	0.022	11.8	11.19
								99		80.14	C	N	0.02	30.0	0.069	19.5	24.70
												W	0.02	30.0	0.070	26.5	41.45
							CWB	99999	KAU012	92.08	--1	V	0.03	20.0	0.022	7.7	7.48
								99		92.08	C	N		20.0	0.047	9.8	10.83
												W	0.05	20.0	0.086	9.9	7.82
							CWB	99999	TCU006	71.05	--1	V	0.02	22.0	0.036	15.2	14.26
								99		71.05	B	N	0.02	17.0	0.081	19.3	21.23
												W	0.02	20.0	0.057	36.2	56.14
							CWB	99999	CHY065	90.23	--1	V	0.02	50.0	0.031	5.1	7.56
								99		90.23	C	N	0.03	40.0	0.097	12.5	8.25
												W	0.02	33.0	0.118	15.8	8.44
							CWB	99999	TCU011	76.22	--1	V	0.03	30.0	0.031	9.3	14.51
								99		76.22	C	N	0.03	30.0	0.074	24.6	14.39
												W		30.0	0.065	24.6	32.14
							CWB	99999	TAP086	101.12	---	V	0.02	22.0	0.034	8.0	9.62
								99		100.93	A	N	0.02	30.0	0.050	7.9	5.70
												W	0.02	22.0	0.038	8.5	11.86
							CWB	99999	TAP036	95.60	--1	V	0.02	30.0	0.017	6.9	9.15
								99		95.33	A	N		30.0	0.039	6.1	5.83
												W	0.02	20.0	0.030	7.6	10.69
							CWB	99999	TAP034	98.81	--1	V	0.02	30.0	0.023	9.3	9.57
								99		98.69	C	N	0.02	30.0	0.066	12.6	6.79
												W	0.02	30.0	0.055	9.8	14.06
							CWB	99999	TCU092	96.44	---	V	0.02	30.0	0.028	10.3	10.11
								99		96.44	B	N	0.02	24.0	0.066	17.2	15.60
												W	0.02	20.0	0.086	23.0	36.91
							CWB	99999	TCU008	83.68	--1	V	0.02	30.0	0.025	9.6	9.64
								99		83.68	B	N	0.02	30.0	0.062	17.5	13.38

Table K-4

CHI-CHI, TAIWAN AND TURKEY STRONG-MOTION CATALOG (09/05/00)

Earthquake No. Location, Mech, Dip (1)	Date & Time YEAR	MOD Y	M	Magnitude (2) ML	MS	OTH	Station (3)	No.	Description H/F	Closest Dist (km)(4)	Site Codes (5)	Comp.	Filter HP (hz)	Corners LP (hz)	PGA (g)	PGV (cm/s)	PGD (cm)
												W	0.02	30.0	0.071	29.8	42.50
							CWB	99999	KAU040	154.59	--1	V	0.02	18.0	0.007	1.8	1.99
								99		153.29	C	N		10.0	0.008	2.1	3.20
												W	0.04	12.0	0.008	2.2	2.67
							CWB	99999	ILA031	94.77	--1	V		50.0	0.030	7.3	9.75
								99		92.63	A	N		30.0	0.076	9.1	10.68
												W		50.0	0.057	10.0	9.94
							CWB	99999	TCU010	80.42	--1	V	0.02	20.0	0.026	13.7	12.95
								99		80.42	B	N	0.02	20.0	0.074	19.3	23.89
												W	0.03	20.0	0.088	31.8	46.68
							CWB	99999	KAU078	102.85	--1	V	0.03	50.0	0.015	2.6	2.44
								99		101.92	C	N	0.02	50.0	0.024	2.2	3.17
												W	0.02	50.0	0.046	2.6	3.64
							CWB	99999	KAU077	97.20	--1	V	0.03	20.0	0.012	3.4	3.01
								99		95.65	A	N	0.03	20.0	0.023	2.5	3.76
												W	0.02	20.0	0.022	3.2	2.68
							CWB	99999	TAP069	135.31	--1	V	0.04	20.0	0.013	5.2	6.49
								99		133.93	A	N	0.05	20.0	0.033	5.8	4.58
												W	0.04	20.0	0.026	5.0	8.69
							CWB	99999	TTN024	70.58	--1	V	0.03	30.0	0.022	4.0	3.35
								99		67.69	A	N	0.02	30.0	0.027	3.9	3.50
												W	0.02	20.0	0.030	3.8	5.32
							CWB	99999	TTN018	86.15	--2	V	0.02	20.0	0.014	2.9	3.17
								99		83.80	A	N	0.02	20.0	0.024	4.1	3.55
												W	0.02	20.0	0.035	3.8	5.56
							CWB	99999	TTN027	87.62	--1	V	0.03	22.0	0.015	3.6	2.64
								99		85.31	B	N	0.03	30.0	0.039	6.1	3.68
												W	0.03	20.0	0.031	6.6	5.69
							CWB	99999	ILA050	77.75	--1	V	0.02	40.0	0.055	8.6	8.92
								99		75.14	A	N		40.0	0.064	9.9	16.41
												W	0.04	40.0	0.065	7.3	6.69
							CWB	99999	TAP065	130.91	--1	V	0.03	20.0	0.013	5.6	6.37

Table K-4

CHI-CHI, TAIWAN AND TURKEY STRONG-MOTION CATALOG (09/05/00)

Earthquake No. Location, Mech, Dip (1)	Date & Time YEAR MOD Y M	Magnitude (2) ML MS OTH		Station (3) No.	Description H/F	Closest Dist (km)(4)	Site Codes (5)	Comp.	Filter HP (hz)	Corners LP (hz)	PGA (g)	PGV (cm/s)	PGD (cm)
				99		130.75	A	N	0.04	20.0	0.023	7.7	5.28
								W	0.03	18.0	0.040	9.9	6.98
			CWB	99999	TTN028	90.63	--1	V	0.03	20.0	0.016	3.0	3.14
				99		88.39	A	N	0.02	20.0	0.016	3.1	2.79
								W	0.02	18.0	0.019	3.2	4.93
			CWB	99999	KAU051	139.70	--1	V	0.03	12.0	0.007	3.3	3.60
				99		138.52	A	N	0.02	22.0	0.008	2.9	2.69
								W	0.10	14.0	0.009	2.4	2.12
			CWB	99999	KAU069	83.58	--1	V	0.03	24.0	0.019	2.2	3.05
				99		82.75	A	N	0.10	30.0	0.036	3.1	0.859
								W	0.02	22.0	0.039	3.3	3.69
			CWB	99999	ILA051	90.37	---	V	0.02	24.0	0.024	8.4	10.13
				99		88.49	A	N	0.02	22.0	0.033	7.3	9.19
								W	0.02	22.0	0.080	12.3	9.66
			CWB	99999	TCU085	64.51	--1	V	0.03	50.0	0.042	9.4	12.32
				99		63.95	A	N		40.0	0.054	6.4	7.38
								W		40.0	0.063	7.5	13.88
			CWB	99999	TTN036	90.48	--1	V	0.02	14.0	0.018	8.4	6.97
				99		88.24	B	N	0.02	12.0	0.030	6.8	4.79
								W	0.02	12.0	0.025	7.6	8.65
			CWB	99999	TTN016	136.58	--1	V	0.03	14.0	0.006	2.5	2.80
				99		135.11	C	N	0.03	14.0	0.010	2.6	4.05
								W	0.04	14.0	0.009	2.9	3.38
			CWB	99999	KAU083	123.04	--1	V	0.02	14.0	0.011	4.9	4.97
				99		122.87	D	N	0.02	14.0	0.024	8.4	5.81
								W	0.02	14.0	0.030	8.9	7.18
			CWB	99999	HWA022	71.45	--1	V		30.0	0.040	7.9	7.62
				99		68.60	A	N		30.0	0.082	11.0	17.16
								W	0.02	30.0	0.123	12.0	11.01
			CWB	99999	TTN025	81.68	--1	V	0.02	30.0	0.024	3.7	3.11
				99		79.19	C	N	0.02	30.0	0.050	5.0	2.60
								W	0.02	30.0	0.034	3.9	5.08

Table K-4

CHI-CHI, TAIWAN AND TURKEY STRONG-MOTION CATALOG (09/05/00)

Earthquake No. Location, Mech, Dip (1)	Date & Time YEAR	MOD Y	M	Magnitude (2) ML	MS	OTH	Station (3)	No.	Description H/F	Closest Dist (km)(4)	Site Codes (5)	Comp.	Filter HP (hz)	Corners LP (hz)	PGA (g)	PGV (cm/s)	PGD (cm)
							CWB	99999	TAP067	104.27	--1	V	0.03	20.0	0.037	8.4	10.40
								99		104.11	A	N	0.02	20.0	0.042	9.6	8.18
												W	0.02	20.0	0.039	11.5	12.16
							CWB	99999	TAP066	117.50	--1	V	0.02	22.0	0.022	4.1	6.23
								99		117.50	B	N	0.03	20.0	0.074	12.7	7.78
												W	0.02	22.0	0.050	9.1	15.81
							CWB	99999	ILA052	96.68	--1	V	0.04	24.0	0.017	6.4	8.32
								99		94.59	A	N	0.04	22.0	0.039	5.7	9.33
												W	0.04	22.0	0.027	7.3	9.66
							CWB	99999	TTN026	81.76	--1	V	0.03	22.0	0.014	3.2	3.22
								99		79.28	A	N	0.02	20.0	0.040	4.1	2.88
												W	0.02	20.0	0.027	4.2	5.63
							CWB	99999	KAU057	121.39	---	V	0.50	24.0	0.010	1.0	0.27
								99		121.39	A	N	0.03	20.0	0.016	4.6	5.55
												W	0.02	20.0	0.017	6.0	11.22
							CWB	99999	TCU083	78.90	--1	V	0.02	30.0	0.034	9.4	11.66
								99		78.90	B	N	0.02	20.0	0.111	23.6	13.27
												W	0.02	20.0	0.089	31.9	48.44
							CWB	99999	CHY006	14.93	---	V	0.03	50.0	0.202	25.0	11.63
								99		14.93	C	E	0.03	50.0	0.364	55.4	25.59
												N	0.03	50.0	0.345	42.8	15.18
							CWB	99999	CHY010	25.39	---	V	0.03	20.0	0.125	10.6	5.16
								99		25.39	C	E	0.02	20.0	0.227	19.2	7.26
												N	0.03	50.0	0.173	21.9	11.07
							CWB	99999	CHY014	41.49	---	V	0.03	40.0	0.101	11.5	5.16
								99		41.46	C	E	0.02	50.0	0.229	24.3	6.21
												N	0.03	50.0	0.263	21.9	6.57
							CWB	99999	CHY019	57.08	---	V	0.03	40.0	0.024	4.6	5.02
								99		57.08	C	E	0.02	50.0	0.052	6.3	6.66
												N	0.03	50.0	0.064	6.4	4.22
							CWB	99999	CHY022	71.64	--1	V	0.03	30.0	0.024	3.9	5.79
								99		71.64	A	E	0.00	40.0	0.065	6.9	7.12

Table K-4

CHI-CHI, TAIWAN AND TURKEY STRONG-MOTION CATALOG (09/05/00)

Earthquake No. Location, Mech. Dip (1)	Date & Time YEAR	MOD Y	M	Magnitude (2) ML	MS	OTH		Station (3) No.	Description H/F	Closest Dist (km)(4)	Site Codes (5)	Comp.	Filter HP (hz)	Corners LP (hz)	PGA (g)	PGV (cm/s)	PGD (cm)
												N	0.03	40.0	0.044	5.1	5.47
							CWB	99999	CHY034	20.23	---	V	0.03	30.0	0.091	15.0	8.37
								99		20.23	C	E	0.03	30.0	0.248	38.8	11.46
												N	0.03	30.0	0.310	48.5	16.54
							CWB	99999	CHY047	29.36	---	V	0.03	50.0	0.086	15.4	8.55
								99		29.36	C	E	0.03	50.0	0.168	21.1	10.27
												N	0.03	50.0	0.186	22.2	13.65
							CWB	99999	CHY052	45.00	--1	V	0.03	40.0	0.039	6.6	5.45
								99		45.00	A	E	0.03	50.0	0.086	9.6	6.91
												N	0.03	50.0	0.154	12.1	9.40
							CWB	99999	HWA002	53.85	---	V	0.03	40.0	0.033	7.0	7.18
								99		49.99	C	E	0.06	20.0	0.049	6.1	4.58
												N	0.06	40.0	0.094	11.9	6.80
							CWB	99999	HWA003	56.07	--2	V	0.00	30.0	0.053	9.3	5.34
								99		52.38	A	E	0.04	20.0	0.050	10.5	5.45
												N	0.00	20.0	0.138	19.1	8.92
							CWB	99999	HWA046	59.26	---	V	0.03	40.0	0.049	5.7	8.73
								99		55.78	A	E	0.02	50.0	0.076	9.8	18.09
												N	0.02	50.0	0.087	9.0	14.01
							CWB	99999	KAU001	54.58	---	V	0.02	30.0	0.041	5.9	6.65
								99		54.21	A	E	0.03	30.0	0.043	5.4	3.68
												N	0.03	30.0	0.022	5.9	6.21
							CWB	99999	TTN040	55.01	---	V	0.03	30.0	0.021	4.1	5.13
								99		51.25	A	E	0.03	33.0	0.030	7.2	7.37
												N	0.04	30.0	0.032	5.4	4.39
							CWB	99999	TTN041	54.16	---	V	0.03	30.0	0.041	4.7	4.39
								99		50.33	A	E	0.03	40.0	0.079	6.8	6.50
												N	0.03	40.0	0.066	4.6	4.02
							CWB	99999	ILA007	95.52	--1	V	0.03	30.0	0.036	6.7	10.54
								99		93.40	A	N	0.02	30.0	0.089	10.6	12.90
												W	0.02	30.0	0.062	9.5	9.27
							CWB	99999	ILA008	96.54	--1	V	0.03	30.0	0.037	9.2	11.36

Table K-4

CHI-CHI, TAIWAN AND TURKEY STRONG-MOTION CATALOG (09/05/00)

Earthquake No. Location, Mech, Dip (1)	Date & Time YEAR	MOD Y	M	Magnitude (2) ML	MS	OTH		Station (3) No.	Description H/F	Closest Dist (km)(4)	Site Codes (5)	Comp.	Filter HP (hz)	Corners LP (hz)	PGA (g)	PGV (cm/s)	PGD (cm)
								99		94.45	D	N	0.04	30.0	0.057	15.8	11.42
												W	0.02	30.0	0.082	19.8	17.27
							CWB	99999	ILA010	92.19	---	V	0.03	30.0	0.023	7.8	10.77
								99		90.00	A	N	0.02	30.0	0.039	7.2	11.60
												W	0.02	30.0	0.059	7.9	9.76
							CWB	99999	ILA014	92.32	--1	V	0.03	24.0	0.030	7.3	11.85
								99		90.17	C	N	0.03	30.0	0.067	13.4	8.17
												W	0.02	30.0	0.063	12.4	14.24
							CWB	99999	ILA015	96.59	--1	V	0.03	40.0	0.020	8.4	9.88
								99		95.04	C	N	0.05	40.0	0.050	10.1	6.88
												W	0.04	33.0	0.038	6.3	6.64
							CWB	99999	ILA021	88.11	--1	V	0.03	33.0	0.027	8.1	11.82
								99		86.28	A	N	0.04	33.0	0.067	9.0	9.18
												W	0.02	40.0	0.061	11.7	9.96
							CWB	99999	ILA024	79.01	--1	V	0.03	40.0	0.024	7.8	10.86
								99		76.88	A	N	0.02	40.0	0.033	8.5	9.41
												W	0.02	40.0	0.040	9.6	9.14
							CWB	99999	ILA063	71.61	---	V	0.04	50.0	0.031	7.3	9.44
								99		69.63	A	N	0.02	50.0	0.091	8.1	12.98
												W	0.02	50.0	0.082	12.6	8.81
							CWB	99999	KAU003	122.15	---	V	0.04	20.0	0.010	5.4	7.18
								99		122.15	B	N	0.02	20.0	0.018	6.5	9.02
												W	0.02	20.0	0.020	5.4	10.82
							CWB	99999	TAP072	110.06	---	V	0.03	30.0	0.018	7.5	9.54
								99		109.77	A	N	0.04	30.0	0.050	11.4	6.59
												W	0.03	50.0	0.029	7.5	8.67
							CWB	99999	TAP075	118.44	---	V	0.03	30.0	0.024	6.3	8.90
								99		118.05	A	N	0.02	50.0	0.050	9.7	6.49
												W	0.02	30.0	0.083	10.3	11.98
							CWB	99999	TAP077	129.35	---	V	0.02	30.0	0.024	5.6	6.87
								99		128.74	A	N	0.02	30.0	0.036	6.8	6.03
												W	0.02	30.0	0.031	12.0	9.08

Table K-4

CHI-CHI, TAIWAN AND TURKEY STRONG-MOTION CATALOG (09/05/00)

Earthquake No. Location, Mech. Dip (1)	Date & Time YEAR	MOD Y	M	Magnitude (2) ML	MS	OTH	Station (3)	No.	Description H/F	Closest Dist (km)(4)	Site Codes (5)	Comp.	Filter HP (hz)	Corners LP (hz)	PGA (g)	PGV (cm/s)	PGD (cm)
							CWB	99999	TAP078	131.02	---	V	0.03	33.0	0.018	5.4	8.02
								99		130.29	A	N	0.04	40.0	0.042	8.6	5.60
												W	0.02	40.0	0.043	6.9	8.98
							CWB	99999	TAP081	135.55	---	V	0.03	20.0	0.012	6.0	8.01
								99		134.22	A	N	0.02	20.0	0.021	4.9	5.44
												W	0.02	50.0	0.031	7.9	8.78
							CWB	99999	TTN002	76.01	--1	V	0.03	20.0	0.016	5.2	4.77
								99		73.33	A	N	0.03	20.0	0.026	5.4	4.57
												W	0.03	20.0	0.026	5.4	6.40
							CWB	99999	TTN004	77.41	--1	V	0.04	20.0	0.026	3.9	4.07
								99		74.78	C	N	0.04	20.0	0.046	8.3	4.57
												W	0.03	20.0	0.039	7.4	5.69
							CWB	99999	TTN042	72.62	---	V	0.03	20.0	0.019	5.4	5.05
								99		69.82	A	N	0.03	20.0	0.059	5.9	4.55
												W	0.03	22.0	0.059	5.4	5.97
							CWB	99999	TTN044	68.22	---	V	0.03	22.0	0.033	6.0	4.44
								99		65.23	B	N	0.02	22.0	0.055	10.2	6.66
												W	0.03	30.0	0.048	9.7	7.12
							CWB	99999	TTN046	74.49	---	V	0.03	22.0	0.020	5.0	5.04
								99		71.76	A	N	0.03	22.0	0.067	7.4	3.18
												W	0.03	20.0	0.113	11.2	6.13
							CWB	99999	TTN047	74.90	---	V	-99.				
								99		82.51	B	N	0.03	20.0	0.027	5.7	4.78
												W	0.03	20.0	0.026	6.2	6.44
							CWB	99999	TCU078	7.50	--1	V	0.02	50.0	0.176	18.8	14.19
								01		0.00	B	N	0.15	50.0	0.292	29.8	9.17
												W	0.04	50.0	0.444	39.2	31.24
							CWB	99999	TCU089	8.22	--1	V	0.03	50.0	0.191	22.3	24.36
								01		0.00	B	N	0.04	50.0	0.248	31.0	32.37
												W	0.07	50.0	0.333	30.9	18.48
							CWB	99999	TCU079	10.04	--1	V	0.03	50.0	0.388	25.3	12.59
								01		0.01	B	N	0.07	50.0	0.393	48.8	13.78

Table K-4

CHI-CHI, TAIWAN AND TURKEY STRONG-MOTION CATALOG (09/05/00)

Earthquake No. Location, Mech, Dip (1)	Date & Time YEAR	MOD Y	M	Magnitude (2) ML	MS	OTH	Station (3)	No.	Description H/F	Closest Dist (km)(4)	Site Codes (5)	Comp.	Filter HP (hz)	Corners LP (hz)	PGA (g)	PGV (cm/s)	PGD (cm)
												W	0.20	50.0	0.742	61.2	11.11
							CWB	99999	TCU084	10.39	--1	V	0.09	50.0	0.340	25.3	11.94
								01		0.01	B	N	0.10	50.0	0.417	45.6	21.27
												W	0.20	30.0	1.157	114.7	31.43
							CWB	99999	TCU071	4.94	--1	V	0.10	50.0	0.449	34.8	31.32
								01		1.01	B	N	0.04	50.0	0.655	69.4	49.06
												W	0.20	50.0	0.567	44.4	13.76
							CWB	99999	TCU072	7.36	--1	V	0.05	50.0	0.279	35.8	27.28
								99		0.24	B	N	0.05	50.0	0.400	56.3	41.28
												W	0.05	50.0	0.488	71.7	38.64
							CWB	99999	CHY024	9.06	--1	V	0.03	50.0	0.152	44.8	34.80
								02		9.06	D	N	0.02	50.0	0.175	48.9	31.04
												W	0.02	50.0	0.278	52.9	43.62
							CWB	99999	TCU120	8.10	--1	V	0.03	50.0	0.162	32.1	22.34
								02		8.10	C	N	0.03	50.0	0.192	36.9	33.30
												W	0.02	50.0	0.225	63.1	54.09
							CWB	99999	TCU065	0.98	--1	V	0.02	50.0	0.272	77.0	53.70
								02		0.98	B	N	0.06	50.0	0.603	78.8	60.74
												W	0.03	50.0	0.814	126.2	92.57
							CWB	99999	TCU067	0.33	--1	V	0.04	50.0	0.225	42.7	28.48
								02		0.33	B	N	0.03	50.0	0.325	66.6	45.95
												W	0.02	50.0	0.503	79.5	93.09
							CWB	99999	CHY080	6.95	---	V	0.03	50.0	0.724	49.0	27.82
								99		6.79	B	N	0.05	50.0	0.902	102.4	3.97
												W	0.10	50.0	0.968	107.5	18.60
							CWB	99999	CHY028	7.31	--1	V	0.04	50.0	0.337	36.4	13.56
								02		7.31	C	N	0.10	50.0	0.821	67.0	23.28
												W	0.12	50.0	0.653	72.8	14.68
							CWB	99999	TCU109	13.09	--1	V	0.03	50.0	0.137	26.6	20.27
								02		13.09	C	N	0.04	50.0	0.155	53.1	34.74
												W	0.05	50.0	0.156	50.8	46.49
							CWB	99999	TCU107	20.35	--2	V	0.03	50.0	0.088	27.8	21.70

Table K-4

CHI-CHI, TAIWAN AND TURKEY STRONG-MOTION CATALOG (09/05/00)

Earthquake No. Location, Mech, Dip (1)	Date & Time YEAR	MOD Y	M	Magnitude (2) ML	MS	OTH	Station (3)	No.	Description H/F	Closest Dist (km)(4)	Site Codes (5)	Comp.	Filter HP (hz)	Corners LP (hz)	PGA (g)	PGV (cm/s)	PGD (cm)
								02		20.35	C	N	0.03	50.0	0.158	47.4	32.79
												W	0.03	50.0	0.124	36.8	39.81
							CWB	99999	TCU052	0.24	--1	V	0.04	50.0	0.241	110.5	163.51
								01		0.06	B	N	0.04	50.0	0.419	118.4	246.15
												W	0.04	50.0	0.348	159.0	184.42
							CWB	99999	CHY074	82.49	--1	V	0.03	40.0	0.094	15.6	9.40
								99		82.49	B	N	0.02	40.0	0.158	23.6	11.74
												W	0.02	40.0	0.234	28.1	19.04
							CWB	99999	TCU056	11.11	--1	V	0.05	50.0	0.115	41.4	27.07
								02		11.11	D	N	0.03	50.0	0.134	42.9	54.55
												W	0.04	40.0	0.134	42.5	50.77
							CWB	99999	CHY029	15.28	--1	V	0.04	50.0	0.155	18.7	9.82
								02		15.28	C	N	0.03	50.0	0.238	35.2	29.10
												W	0.03	50.0	0.277	30.3	14.73
							CWB	99999	TCU048	14.38	--1	V	0.04	50.0	0.098	20.8	21.64
								02		14.38	C	N	0.04	50.0	0.184	48.3	53.55
												W	0.02	50.0	0.123	32.6	52.18
							CWB	99999	TCU113	31.49	--1	V	0.03	50.0	0.077	16.0	17.03
								02		31.49	E	N	0.03	50.0	0.074	23.4	27.12
												W	0.04	50.0	0.070	27.8	22.21
							CWB	99999	CHY035	18.12	--1	V	0.08	50.0	0.099	14.4	5.99
								99		180.12	C	N	0.04	50.0	0.246	37.6	16.86
												W	0.04	40.0	0.252	45.6	12.03
							CWB	99999	TCU104	13.64	---	V	0.03	50.0	0.083	23.3	20.60
								02		13.64	B	N	0.03	50.0	0.085	47.2	52.70
												W	0.03	50.0	0.106	36.6	51.97
							CWB	99999	TCU070	19.10	---	V	0.03	50.0	0.085	31.0	30.93
								02		19.10	B	N	0.03	50.0	0.169	62.3	56.67
												W	0.02	50.0	0.255	52.1	48.09
							CWB	99999	TCU068	1.09	--1	V	0.02	50.0	0.486	187.3	266.55
								01		0.50	D	N	0.02	50.0	0.462	263.1	430.00
												W	0.03	50.0	0.566	176.6	324.11

Table K-4

CHI-CHI, TAIWAN AND TURKEY STRONG-MOTION CATALOG (09/05/00)

Earthquake	Date & Time	Magnitude (2)				Station (3)			Closest	Site	Comp.	Filter	Corners	PGA	PGV	PGD
No. Location, Mech. Dip (1)	YEAR MOD Y M	ML	MS	OTH		No.	Description H/F		Dist (km)(4)	Codes (5)		HP (hz)	LP (hz)	(g)	(cm/s)	(cm)
					CWB	99999 02	TCU105	18.10	---	V	0.02	40.0	0.064	21.4	18.40
								18.10	C	N	0.03	30.0	0.129	38.9	45.59
										W	0.03	40.0	0.112	34.6	48.59
					CWB	99999 99	TCU103	4.01	--1	V	0.02	50.0	0.149	64.3	42.36
								4.01	C	N	0.05	50.0	0.162	26.8	15.97
										W	0.02	50.0	0.134	61.9	87.54
					CWB	99999 99	CHY041	25.96	--1	V	0.03	50.0	0.123	9.8	6.37
								25.96	D	N	0.03	50.0	0.639	39.5	11.25
										W	0.04	50.0	0.302	20.4	8.62
					CWB	99999 99	TCU059	17.84	---	V	0.05	40.0	0.057	18.6	12.06
								17.84	C	N	0.03	30.0	0.172	56.2	53.52
										W	0.03	30.0	0.165	59.4	63.65
					CWB	99999 99	TCU087	3.18	--1	V	0.02	30.0	0.108	61.5	51.32
								3.18	B	N	0.05	30.0	0.122	37.1	25.54
										W	0.02	30.0	0.128	40.8	62.62
					CWB	99999 99	CHY046	29.49	--1	V	0.03	50.0	0.079	8.6	6.21
								29.49	C	N	0.04	50.0	0.182	21.0	11.90
										W	0.03	50.0	0.142	20.6	10.28
					CWB	99999 99	CHY042	34.91	--1	V	0.04	30.0	0.061	9.0	4.72
								34.90	B	N	0.03	30.0	0.067	12.3	7.97
										W	0.06	30.0	0.099	15.5	6.50
					CWB	99999 99	CHY087	34.46	--1	V	0.03	40.0	0.056	6.4	5.77
								34.46	D	N	0.03	50.0	0.126	11.9	8.11
										W	0.02	50.0	0.136	10.2	7.18
					CWB	99999 99	CHY086	35.43	--1	V	0.04	30.0	0.050	8.2	4.78
								35.41	B	N	0.03	30.0	0.204	17.8	7.89
										W	0.10	30.0	0.115	14.2	6.66
					CWB	99999 99	TCU128	9.70	--1	V	0.02	40.0	0.097	46.0	34.77
								9.70	D	N	0.05	30.0	0.170	68.8	41.87
										W	0.02	30.0	0.139	73.0	90.62
					CWB	99999 99	HWA020	44.94	--1	V	0.02	50.0	0.056	8.0	12.44
								40.24	D	N	0.02	50.0	0.069	7.9	8.80

Table K-4

CHI-CHI, TAIWAN AND TURKEY STRONG-MOTION CATALOG (09/05/00)

Earthquake No. Location, Mech, Dip (1)	Date & Time YEAR	MOD Y	M	Magnitude (2) ML	MS	OTH	Station (3)	No.	Description H/F	Closest Dist (km)(4)	Site Codes (5)	Comp.	Filter HP (hz)	Corners LP (hz)	PGA (g)	PGV (cm/s)	PGD (cm)
												W	0.02	50.0	0.061	10.3	18.07
							CWB	99999	KAU054	40.50	--1	V	0.03	50.0	0.030	5.9	4.66
								99		39.64	B	N	0.03	50.0	0.080	5.2	3.56
												W	0.04	50.0	0.085	8.5	6.00
							CWB	99999	TCU036	16.69	--1	V	0.02	40.0	0.064	23.9	22.50
								99		16.69	D	N	0.02	40.0	0.131	50.2	42.17
												W	0.02	20.0	0.139	59.6	63.60
							CWB	99999	TCU046	14.34	--1	V	0.03	30.0	0.104	32.3	37.74
								99		14.34	D	N	0.06	30.0	0.116	30.9	23.18
												W	0.03	30.0	0.133	39.8	37.37
							CWB	99999	CHY088	42.82	--1	V	0.04	40.0	0.040	7.4	4.93
								99		42.82	D	N	0.04	33.0	0.216	20.5	14.21
												W	0.04	33.0	0.144	21.0	8.06
							CWB	99999	HWA038	42.91	--2	V	0.02	33.0	0.041	5.5	5.25
								99		37.97	C	N	0.03	30.0	0.059	7.4	7.51
												W	0.04	30.0	0.035	8.8	4.97
							CWB	99999	TCU039	16.70	--1	V	0.02	50.0	0.136	50.7	45.98
								99		16.70	C	N	0.02	50.0	0.145	54.0	44.54
												W	0.02	50.0	0.206	50.0	76.78
							CWB	99999	CHY102	46.17	--1	V	0.03	30.0	0.025	6.5	5.06
								99		45.99	B	N	0.03	33.0	0.050	6.3	4.15
												W	0.04	30.0	0.044	7.1	5.35
							CWB	99999	CHY081	47.74	--1	V	0.03	30.0	0.025	7.2	4.86
								99		47.74	B	N	0.03	30.0	0.045	9.8	7.66
												W	0.02	30.0	0.052	11.0	7.18
							CWB	99999	HWA024	44.32	--2	V	0.03	40.0	0.025	4.5	5.43
								99		39.55	B	N	0.03	30.0	0.024	4.8	5.02
												W	0.03	30.0	0.023	7.5	7.36
							CWB	99999	HWA017	53.91	--1	V	0.03	50.0	0.049	9.4	11.67
								99		50.06	D	N	0.02	50.0	0.084	9.4	7.23
												W	0.02	50.0	0.082	10.8	21.83
							CWB	99999	HWA043	54.90	--1	V	0.02	40.0	0.031	10.2	9.99

Table K-4

CHI-CHI, TAIWAN AND TURKEY STRONG-MOTION CATALOG (09/05/00)

Earthquake No. Location, Mech. Dip (1)	Date & Time YEAR	MOD Y	M	Magnitude (2) ML	MS	OTH	Station (3)	No.	Description H/F	Closest Dist (km)(4)	Site Codes (5)	Comp.	Filter HP (hz)	Corners LP (hz)	PGA (g)	PGV (cm/s)	PGD (cm)
								99		51.13	D	N	0.02	40.0	0.070	7.7	9.31
												W	0.05	40.0	0.056	8.9	7.04
							CWB	99999	CHY050	50.07	--1	V	0.03	50.0	0.028	4.9	5.29
								99		50.07	B	N	0.03	50.0	0.069	8.3	7.73
												W	0.04	50.0	0.106	9.8	4.51
							CWB	99999	TCU045	24.06	---	V	0.02	50.0	0.361	21.4	22.95
								99		24.06	B	N	0.04	50.0	0.512	39.0	14.34
												W	0.02	50.0	0.474	36.7	50.66
							CWB	99999	HWA016	54.73	--1	V	0.02	50.0	0.053	10.1	10.39
								99		50.95	D	N	0.05	50.0	0.080	12.7	5.65
												W	0.05	50.0	0.102	13.3	12.88
							CWB	99999	KAU050	52.06	--1	V	0.02	30.0	0.023	5.2	4.13
								99		50.58	B	N	0.03	40.0	0.040	6.4	3.28
												W	0.02	30.0	0.042	5.2	6.98
							CWB	99999	TCU029	24.71	--1	V	0.02	50.0	0.063	23.2	26.81
								99		24.71	D	N	0.04	50.0	0.200	54.0	40.19
												W	0.03	50.0	0.166	38.6	44.57
							CWB	99999	TCU031	26.78	--1	V	0.02	30.0	0.065	26.8	29.00
								99		26.78	C	N	0.02	30.0	0.122	43.4	31.11
												W	0.02	20.0	0.110	51.1	47.95
							CWB	99999	HWA056	48.75	---	V	0.02	50.0	0.062	7.1	10.35
								99		44.46	B	N	0.03	50.0	0.107	10.8	10.36
												W	0.02	50.0	0.107	11.7	17.64
							CWB	99999	CHY079	54.97	---	V	0.03	25.0	0.029	5.2	4.77
								99		54.96	B	N	0.03	23.0	0.050	6.7	4.18
												W	0.02	30.0	0.043	5.6	5.62
							CWB	99999	HWA023	57.06	--2	V	0.03	50.0	0.026	7.6	10.14
								99		53.44	B	N	0.04	40.0	0.037	6.6	9.03
												W	0.04	40.0	0.037	8.6	13.88
							CWB	99999	TCU047	33.01	---	V	0.02	50.0	0.270	26.9	17.88
								99		33.01	B	N	0.03	50.0	0.413	40.2	22.22
												W	0.02	50.0	0.301	41.6	51.08

Table K-4

CHI-CHI, TAIWAN AND TURKEY STRONG-MOTION CATALOG (09/05/00)

Earthquake No. Location, Mech. Dip (1)	Date & Time YEAR	MOD Y	M	Magnitude (2) ML	MS	OTH	Station (3)	No.	Description H/F	Closest Dist (km)(4)	Site Codes (5)	Comp.	Filter HP (hz)	Corners LP (hz)	PGA (g)	PGV (cm/s)	PGD (cm)
							CWB	99999	TTN031	57.00	--1	V	0.03	40.0	0.043	14.2	5.59
								99		53.38	D	N	0.03	50.0	0.086	12.8	7.83
												W	0.03	30.0	0.074	13.3	6.66
							CWB	99999	TCU034	32.97	--1	V	0.02	50.0	0.074	12.9	14.93
								99		32.97	B	N	0.04	50.0	0.108	23.1	21.66
												W	0.02	50.0	0.250	42.1	46.07
							CWB	99999	HWA026	58.80	---	V	0.02	50.0	0.038	6.7	9.93
								99		55.30	B	N	0.03	50.0	0.058	9.1	9.74
												W	0.02	50.0	0.071	11.2	18.17
							CWB	99999	CHY057	62.81	--1	V	0.03	30.0	0.022	5.2	5.10
								99		62.81	D	N	0.03	30.0	0.056	6.2	4.90
												W	0.02	30.0	0.038	7.1	6.10
							CWB	99999	CHY062	64.07	--1	V	0.04	50.0	0.019	4.1	4.77
								99		64.07	D	N	0.18	50.0	0.053	4.7	2.09
												W	0.20	15.0	0.053	4.5	1.60
							CWB	99999	TTN032	59.11	--1	V	0.02	40.0	0.030	7.1	5.95
								99		55.62	B	N	0.02	40.0	0.078	12.6	6.60
												W	0.03	40.0	0.053	10.0	5.53
							CWB	99999	TCU033	38.19	--1	V	0.03	50.0	0.079	15.6	15.15
								99		38.19	D	N	0.03	50.0	0.180	24.5	21.00
												W	0.02	50.0	0.156	47.2	51.72
							CWB	99999	CHY061	66.91	--1	V	0.04	30.0	0.021	4.5	4.54
								99		66.89	B	N	0.07	30.0	0.042	3.7	3.13
												W	0.02	30.0	0.029	6.0	6.04
							CWB	99999	TTN033	61.68	--1	V	0.02	22.0	0.018	5.5	4.81
								99		58.34	D	N	0.02	30.0	0.040	7.0	4.63
												W	0.03	30.0	0.031	6.4	5.83
							CWB	99999	TCU095	43.44	--1	V	0.02	50.0	0.255	21.8	21.95
								99		43.44	D	N	0.04	50.0	0.712	49.1	24.45
												W	0.02	50.0	0.378	62.0	51.75
							CWB	99999	TCU098	45.02	--1	V	0.02	50.0	0.050	14.8	14.36
								99		45.02	D	N	0.03	50.0	0.107	34.9	25.1

Table K-4

CHI-CHI, TAIWAN AND TURKEY STRONG-MOTION CATALOG (09/05/00)

Earthquake No. Location, Mech, Dip (1)	Date & Time YEAR	MOD Y	M	Magnitude (2) ML	MS	OTH	Station (3)	No.	Description H/F	Closest Dist (km)(4)	Site Codes (5)	Comp.	Filter HP (hz)	Corners LP (hz)	PGA (g)	PGV (cm/s)	PGD (cm)
												W	0.02	50.0	0.100	42.0	51.93
0143 Duzce, Turkey 00	1999	1112	7.1	7.2	7.3	6.5	ERD	99999	Bolu	16.0	--B	UP	0.05		0.203	17.3	14.29
								99		16.0	-	000	0.05		0.728	56.4	23.07
												090	0.05		0.822	62.1	13.55
							ERD	99999	Duzce	6.7	--D	UP	0.06	50.0	0.357	22.6	19.40
								99		6.7	-	180	0.06	50.0	0.348	60.0	42.09
												270	0.08	50.0	0.535	83.5	51.59
							ERD	99999	Mudurnu	34.6	--A	UP	0.08		0.060	10.6	7.33
								99		34.6	-	000	0.08		0.120	9.3	7.63
												090	0.08		0.056	16.3	15.37
							ERD	99999	Sakarya	42.7	--B	UP	0.05	40.0	0.011	3.2	4.00
								99		42.7	-	180	0.05	40.0	0.023	5.5	5.80
												090	0.05	40.0	0.016	5.5	7.34

Notes:

(1) Source mechanism: 00 = strike slip, 01 = normal, 02 = reverse, 03 = reverse-oblique, 04 = normal-oblique, 99 = unknown.
Dip is the dip of rupture surface.

(2) M is moment magnitude, UNK = Magnitude type unknown. Missing magnitudes have the value of zero.

(3) Station numbers were assigned as 99999 where not available.
H/F is the designation for the site being on the hanging wall (01) or foot wall (02), or unknown/not applicable (99).

(4) Distances are closest distances. Values of 999.9 indicate unknown distances.
Second distance is to the surface projection of the fault plane (i.e., JB Distance).

(5) Site codes definitions are from three sources: 1) Geomatrix (3 letter), 2) USGS (1 letter), 3) CWB (1 number), described below.

GEOMATRIX 3-LETTER SITE CLASSIFICATIONS

FIRST LETTER: Instrument housing

- = Unknown

I = Free-field instrument or instrument shelter. Instrument is located at or within several feet of the ground surface.

A = One-story structure of lightweight construction. Instrument is located at the lowest level and within several feet of the ground surface.

B = Two- to four-story structure of lightweight construction. Instrument is located at the lowest level and within several feet of the ground surface.

C = Two- to four-story structure of lightweight construction. Instrument is located at the lowest level in a basement and below the ground surface.
D = Five or more story structure of heavy construction. Instrument is located at the lowest level and within several feet of the ground surface.
E = Five or more story structure of heavy construction. Instrument is located at the lowest level in a basement and below the ground surface.
F = Structure housing instrument is buried below the ground surface, eg. tunnel.
G = Structure of light or heavyweight construction, instrument not at lowest level.
H = Earth dam.
I = Concrete Dam

SECOND LETTER: Mapped local geology

Sedimentary or metasedimentary:

- = Unknown
H = Holocene (Recent) Quaternary (< 15000y bp).
Q = Pleistocene Quaternary (< 2my bp).
P = Pliocene Tertiary (< 6my bp).
M = Miocene Tertiary (< 22my bp).
O = Oligicene Tertiary (< 36my bp).
E = Eocene Tertiary (< 58my bp).
L = Paleocene Tertiary (< 63my bp).
K = Cretaceous (< 145my bp).
F = Franciscan Formation (Cretaceous/Late Jurrassic).
J = Jurassic (< 210my bp).
T = Triassic (<255my bp).
Z = Permian or older (> 255my bp).

Igneous or meta-igneous:

V = Volcanic (extrusive).
N = Intrusive.
G = Granitic.

THIRD LETTER: Geotechnical subsurface characteristics for the Turkey earthquakes

A = Rock. Instrument on rock (Vs > 600 mps) or < 5m of soil over rock.
B = Shallow (stiff) soil. Instrument on/in soil profile up to 20m thick overlying rock.
C = Deep narrow soil. Instrument on/in soil profile at least 20m thick overlying rock, in a narrow canyon or valley no more than several km wide.
D = Deep broad soil. Instrument on/in soil profile at least 20m thick overlying rock, in a broad valley.
E = Soft deep soil. Instrument on/in deep soil profile with average Vs < 150 mps.
- = Unknown

THIRD LETTER: Geotechnical subsurface characteristics for the Chi-Chi, Taiwan earthquake from the Central Weather Bureau of Taiwan.

1 = Hard site.
2 = Medium site.
3 = Soft soil site.
- = Unknown

USGS 1-LETTER SITE CLASSIFICATIONS

Average shear-wave velocity to a depth of 30m is:

A = > 750 m/s
B = 360 - 750 m/s
C = 180 - 360 m/s
D = < 180 m/s

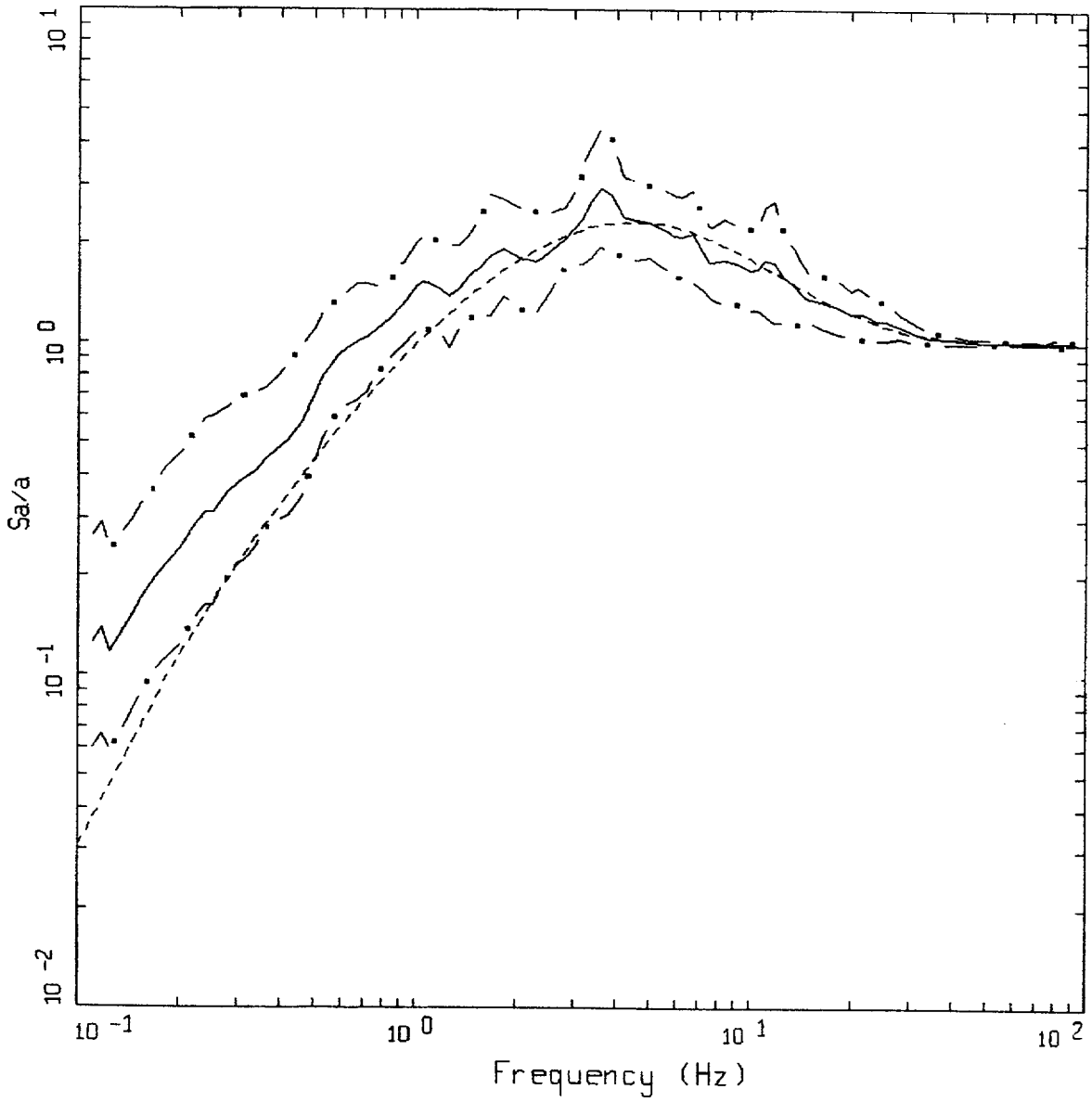

Figure K-1. Comparison of statistical response spectral shapes computed for the Chi Chi, Taiwan and Turkey earthquakes with recommended shape: bin **M** 7+ and $D = 0$ to 10 km.

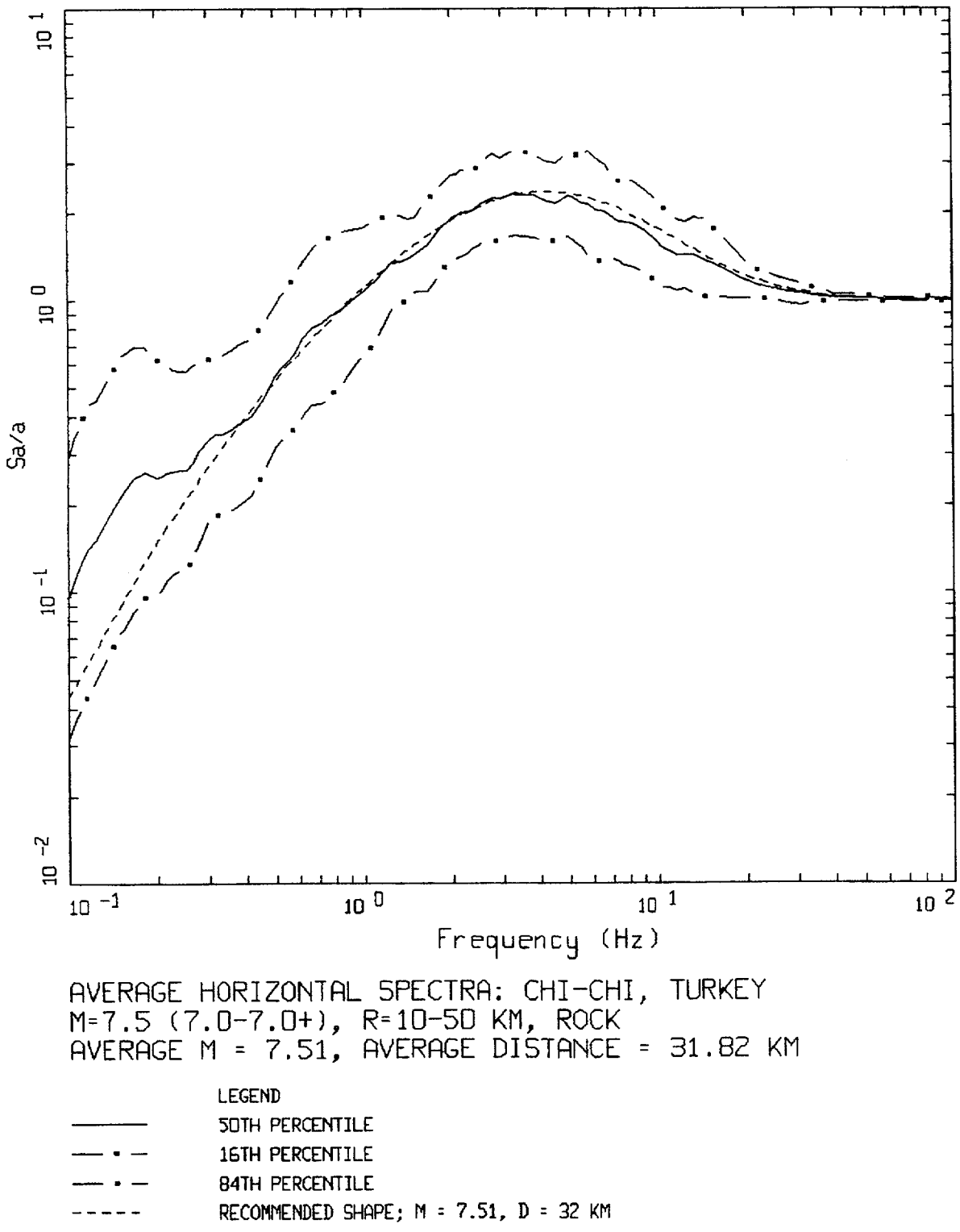

Figure K-2. Comparison of statistical response spectral shapes computed for the Chi Chi, Taiwan, and Turkey earthquakes with recommended shape: bin **M** 7+ and D =10 to 50 km.

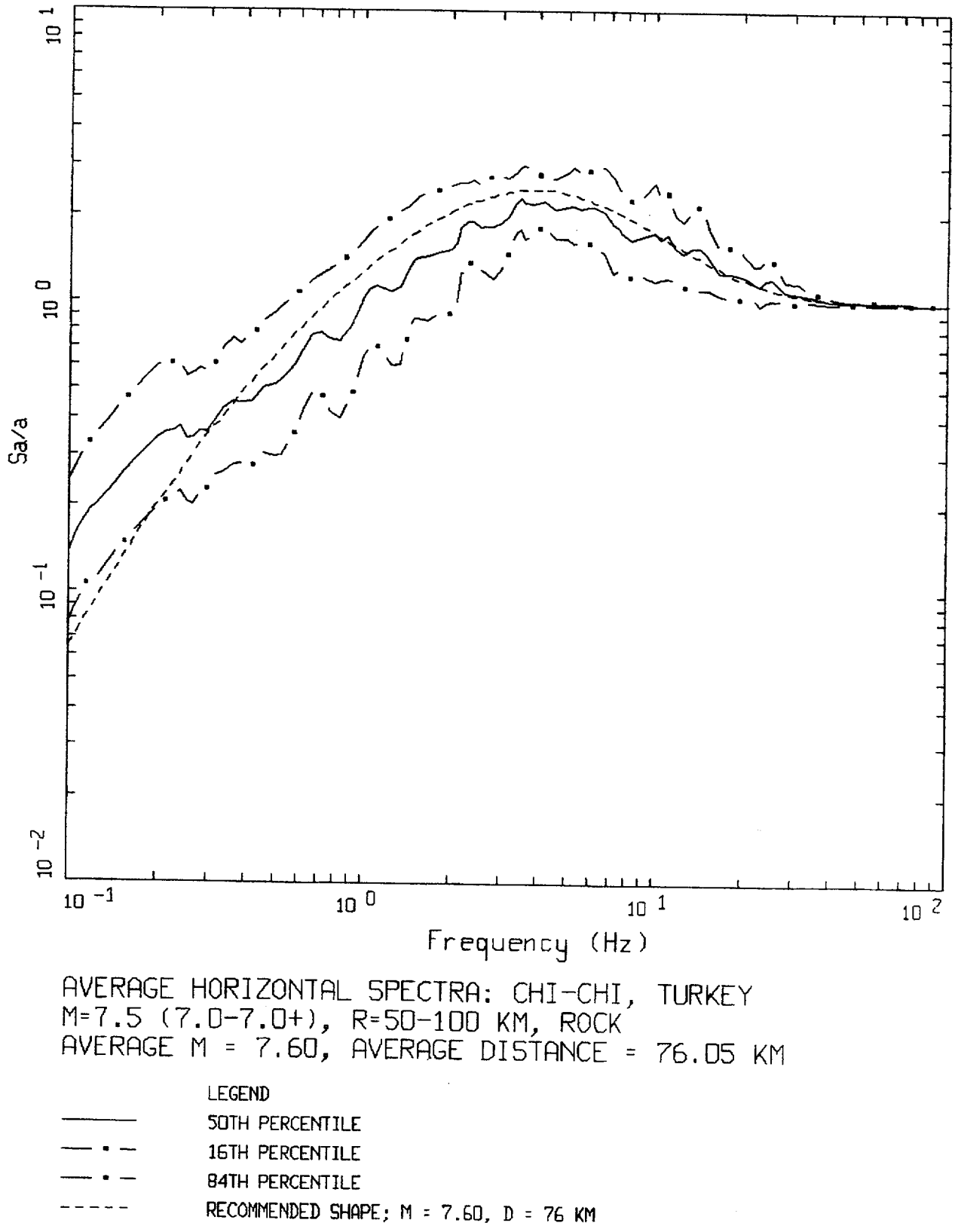

Figure K-3. Comparison of statistical response spectral shapes computed for the Chi Chi, Taiwan and Turkey earthquakes with recommended shape: bin **M** 7+ and $D = 50$ to 100 km.

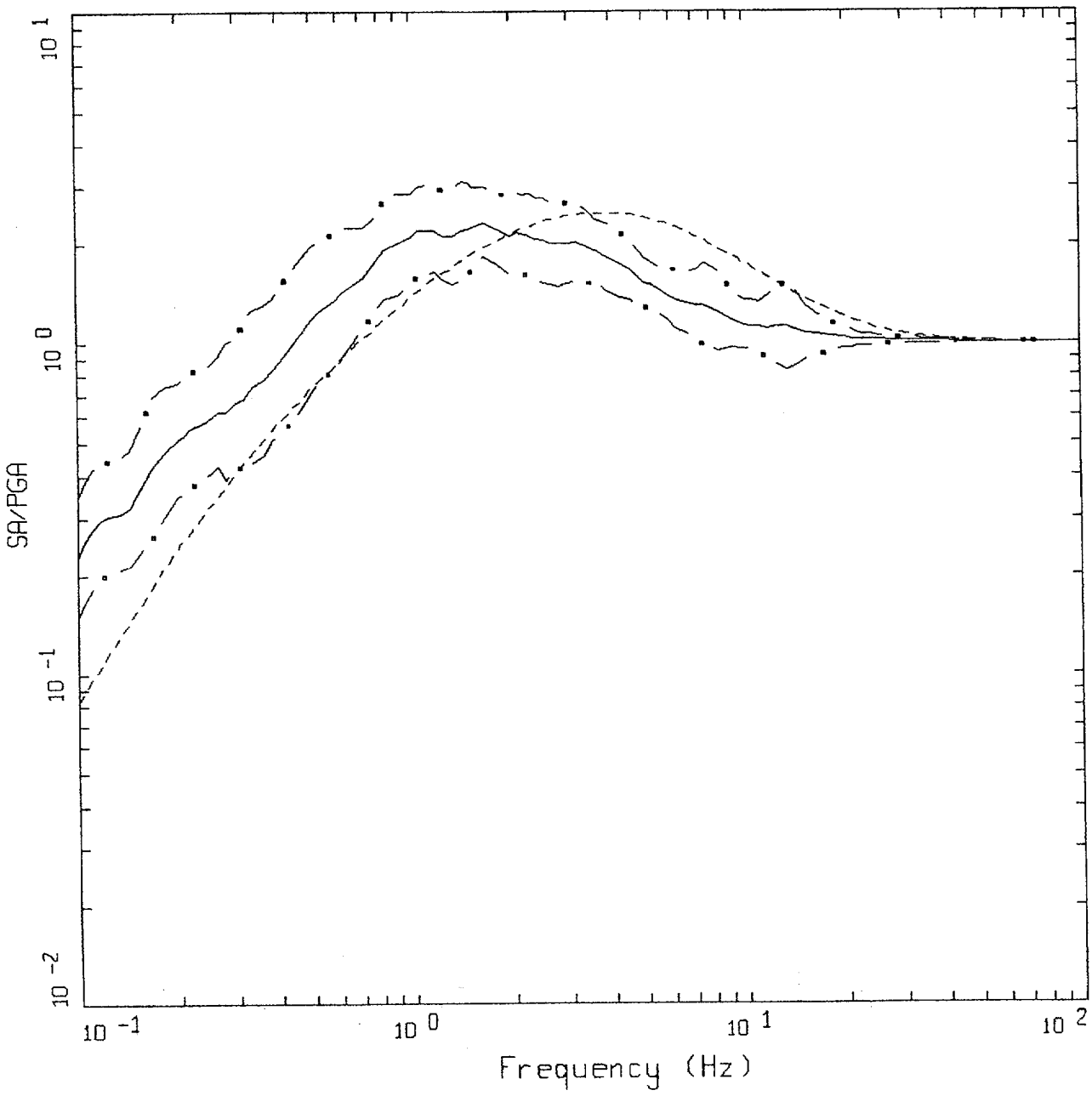

Figure K-4. Comparison of statistical response spectral shapes computed for the Chi Chi, Taiwan and Turkey earthquakes with recommended shape: bin **M** 7+ and $D = 100$ to 200 km.

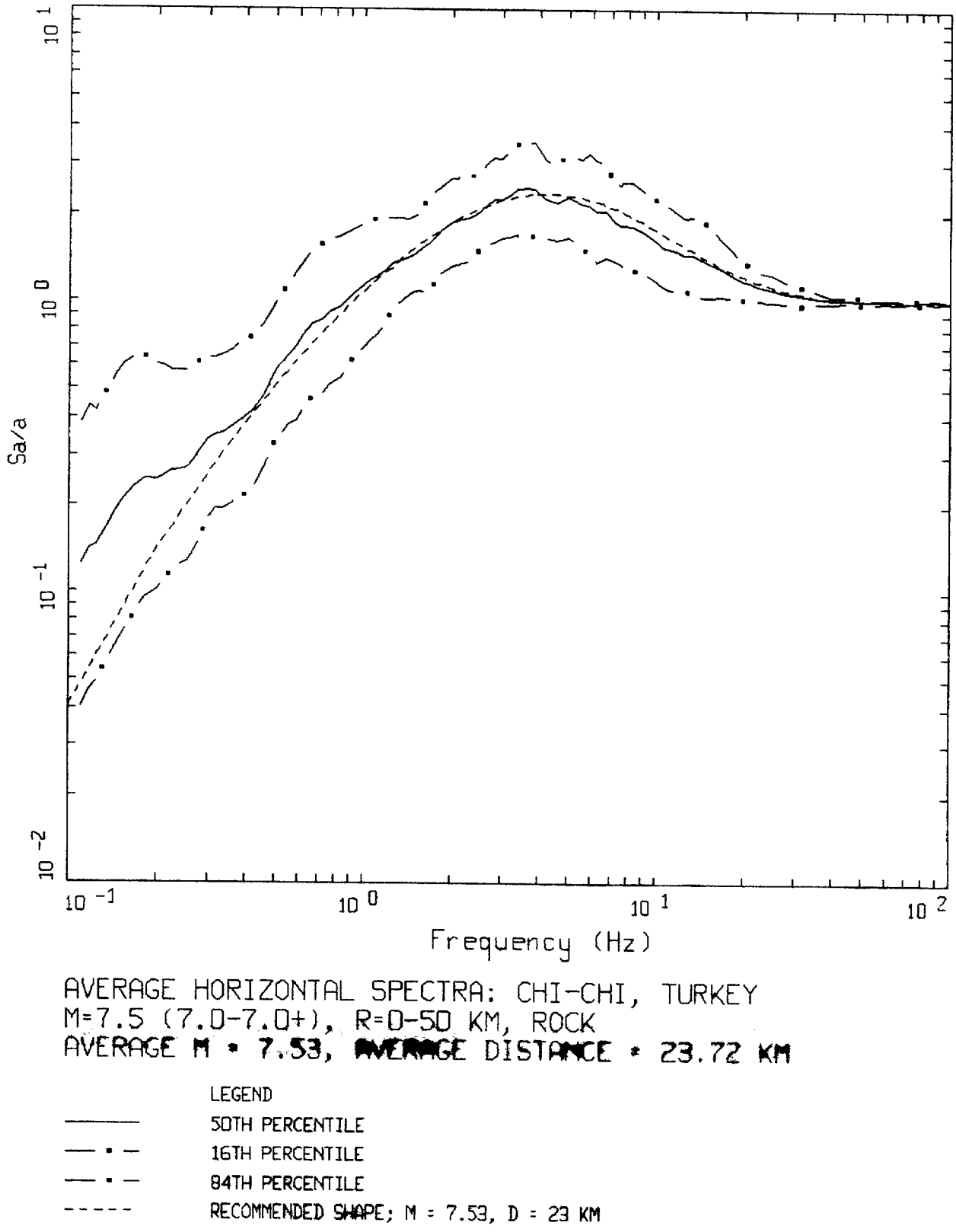

Figure K-5. Comparison of statistical response spectral shapes computed for the Chi Chi, Taiwan and Turkey earthquakes with recommended shape: bin **M** 7+ and $D = 0$ to 50 km.

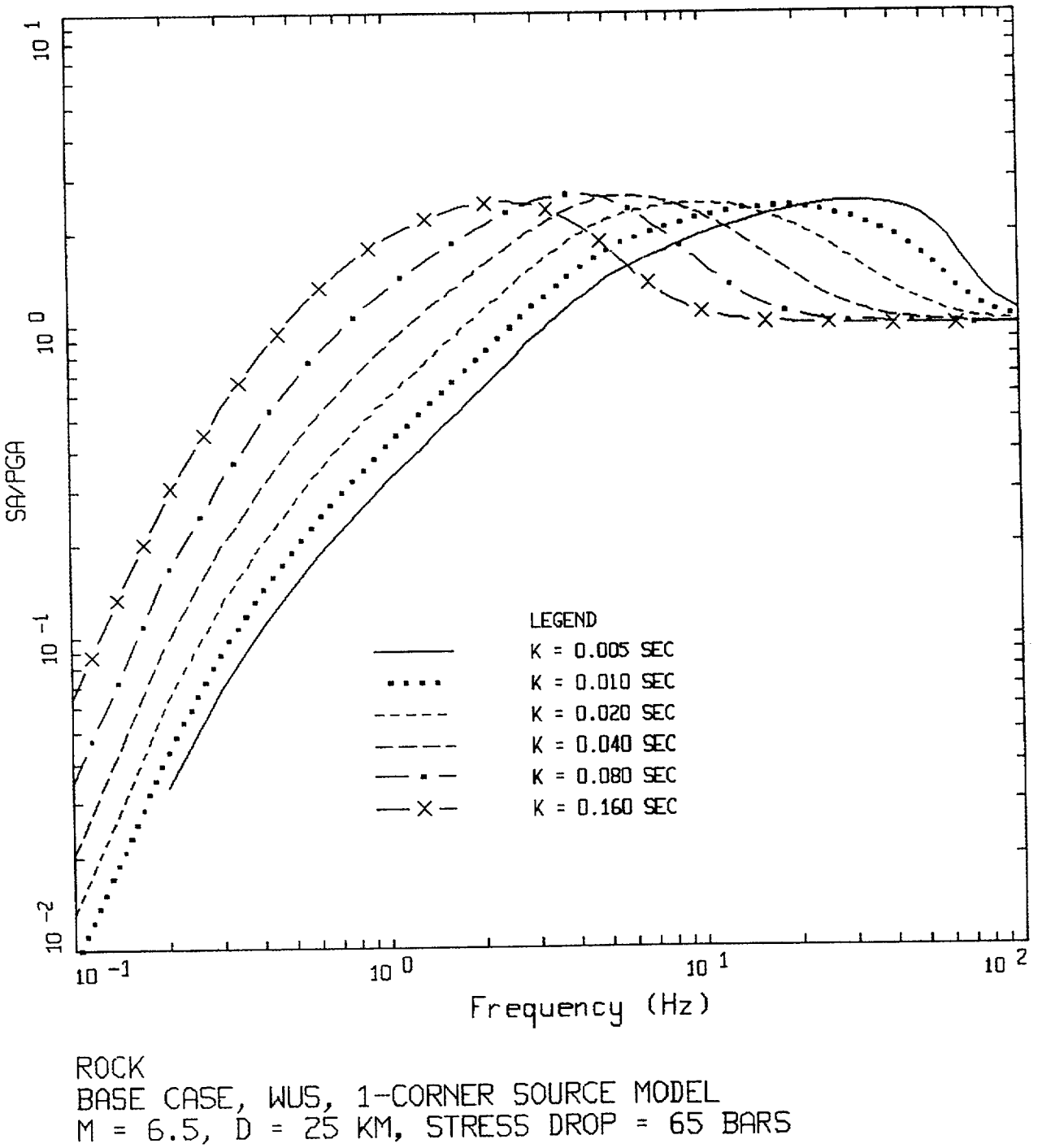

Figure K-6. Response spectral shapes computed for M 6.5 at a distance of 25 km for a suite of kappa values using WUS parameters.

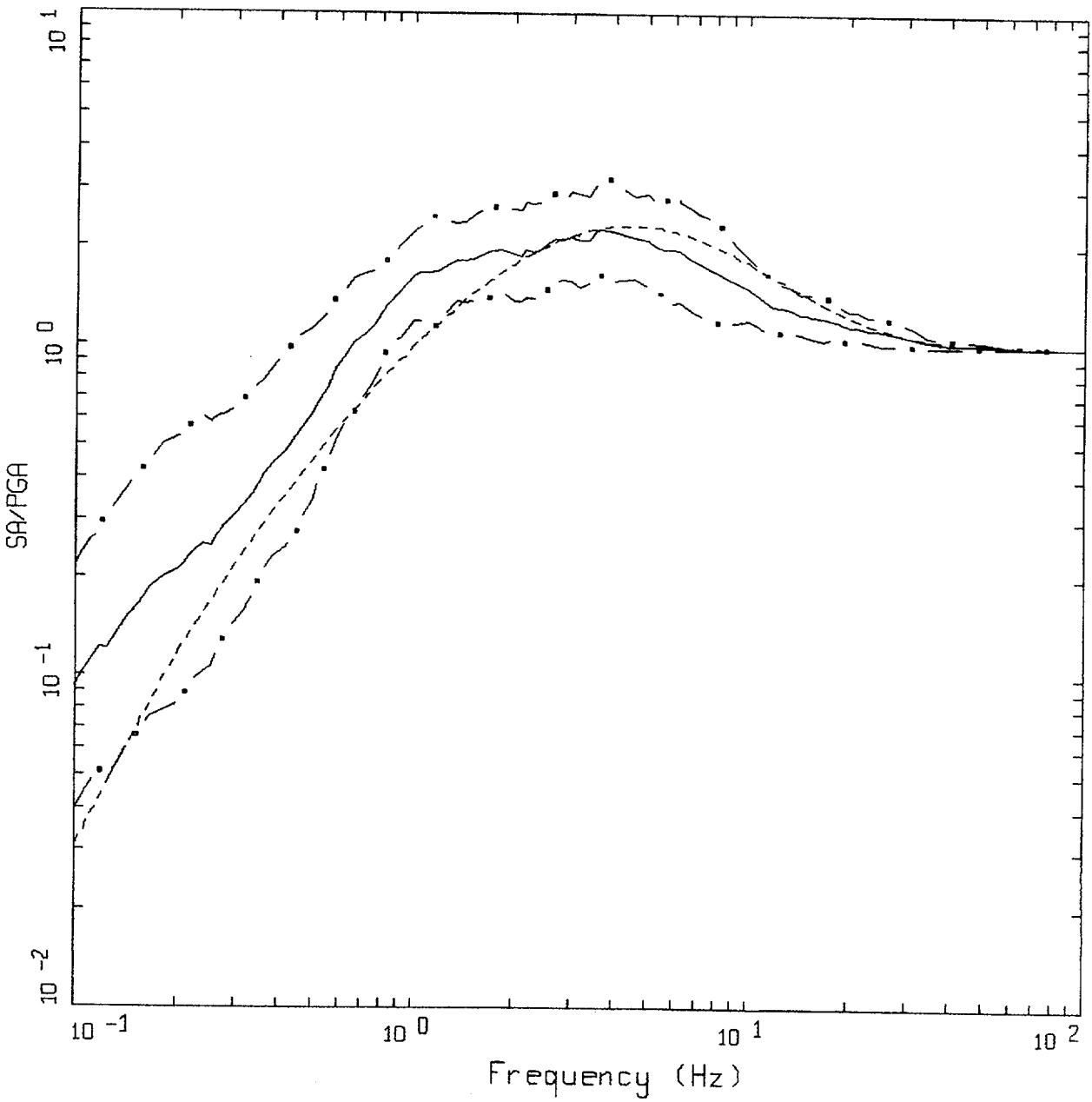

Figure K-7. Comparison of statistical response spectral shapes computed for the Chi Chi, Taiwan earthquake with recommended shape: bin **M** 7+ and $D = 0$ to 10 km.

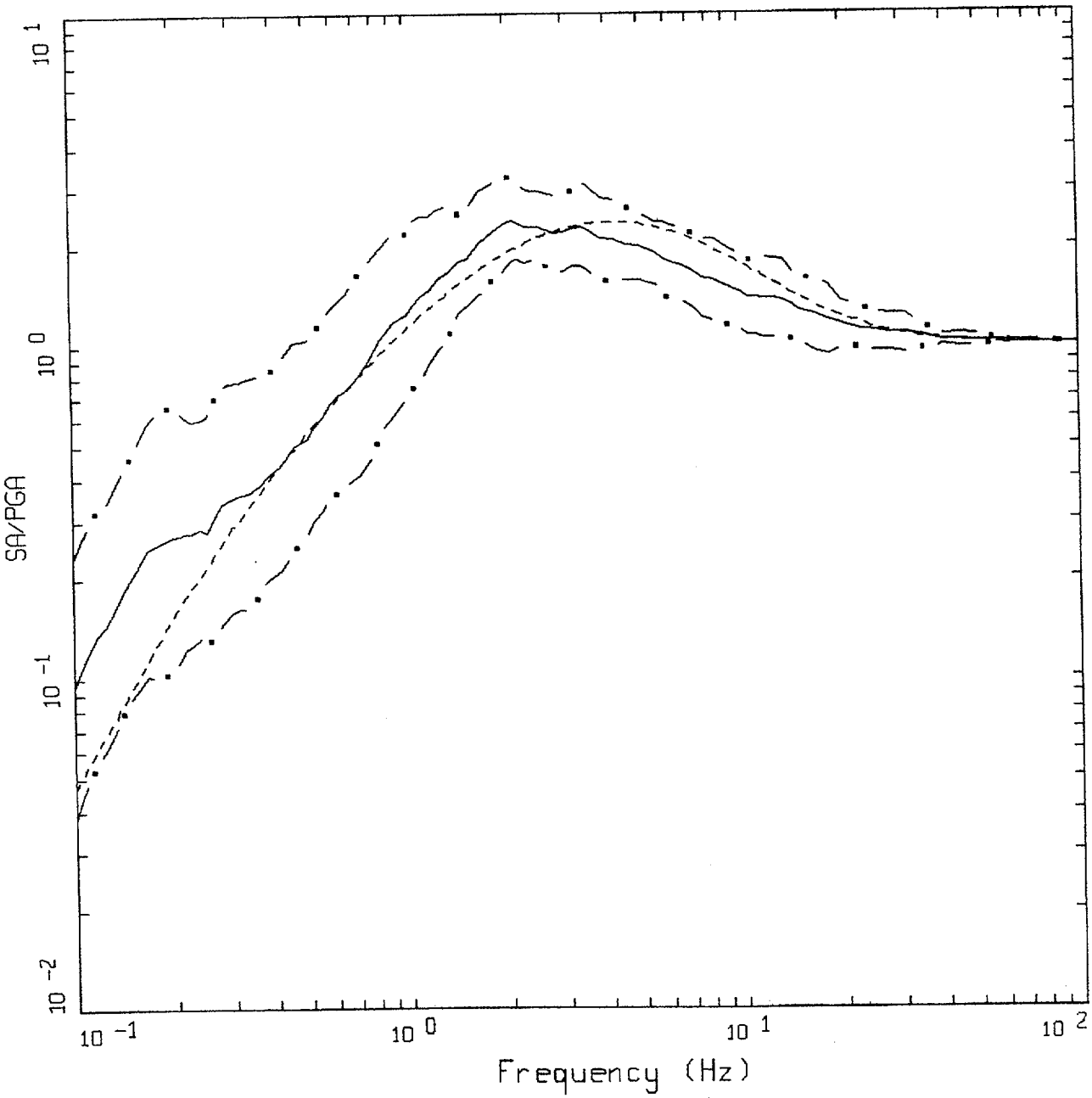

Figure K-8. Comparison of statistical response spectral shapes computed for the Chi Chi, Taiwan earthquake with recommended shape: bin **M** 7+ and $D = 10$ to 50 km.

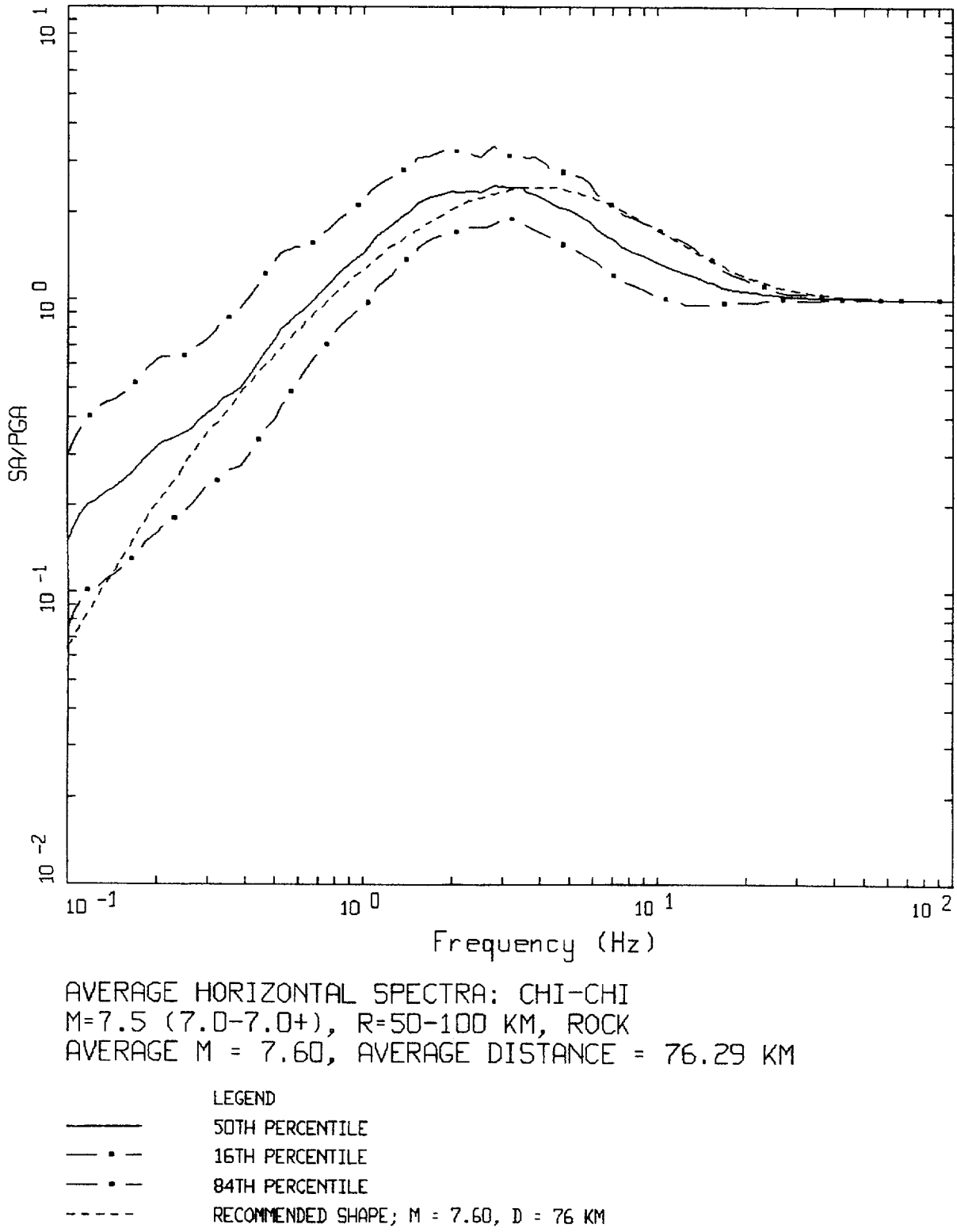

Figure K-9. Comparison of statistical response spectral shapes computed for the Chi Chi, Taiwan earthquake with recommended shape: bin **M** 7+ and D = 50 to 100 km.

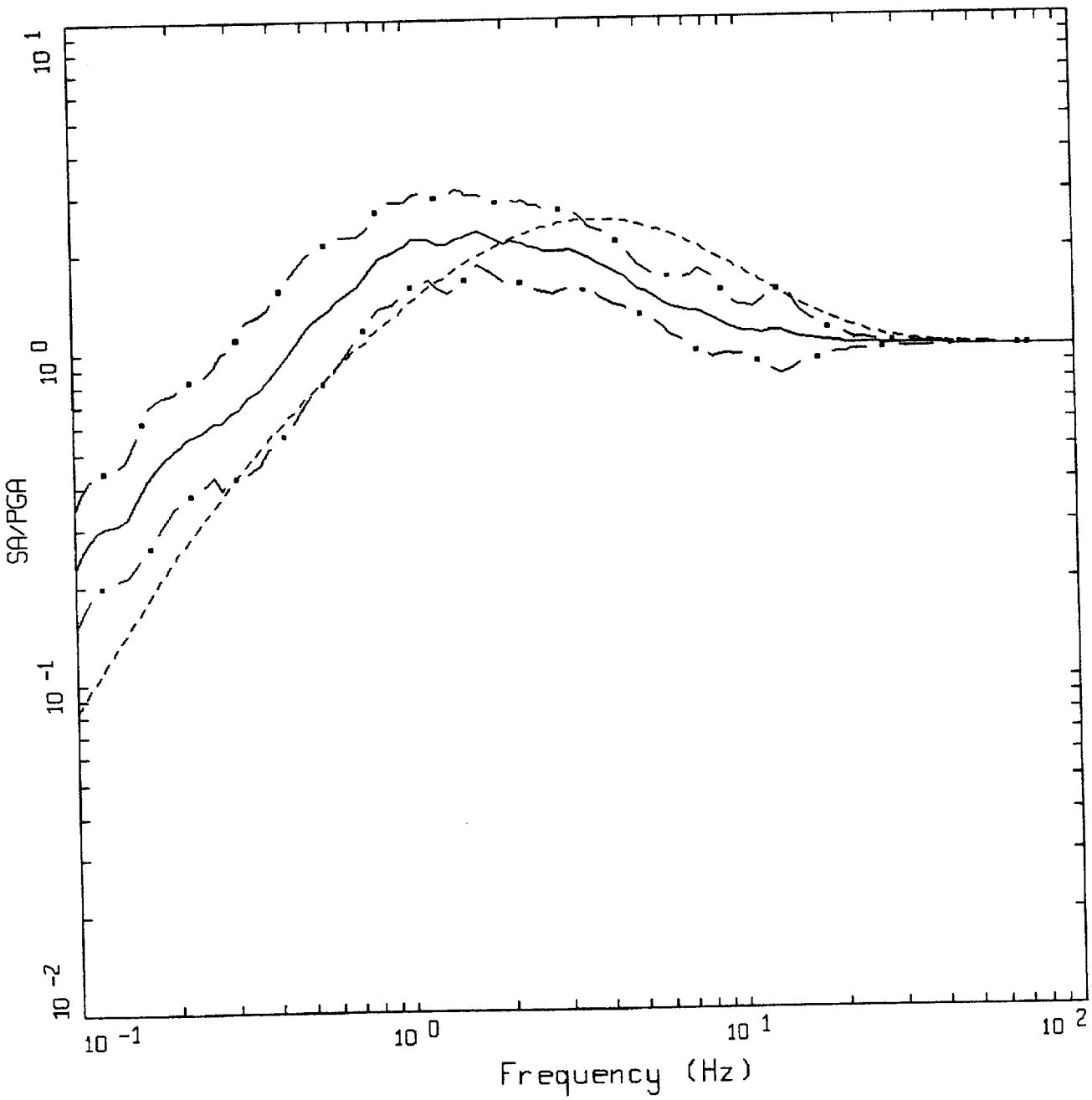

Figure K-10. Comparison of statistical response spectral shapes computed for the Chi Chi, Taiwan earthquake with recommended shape: bin **M** 7+ and D = 100 to 200 km.

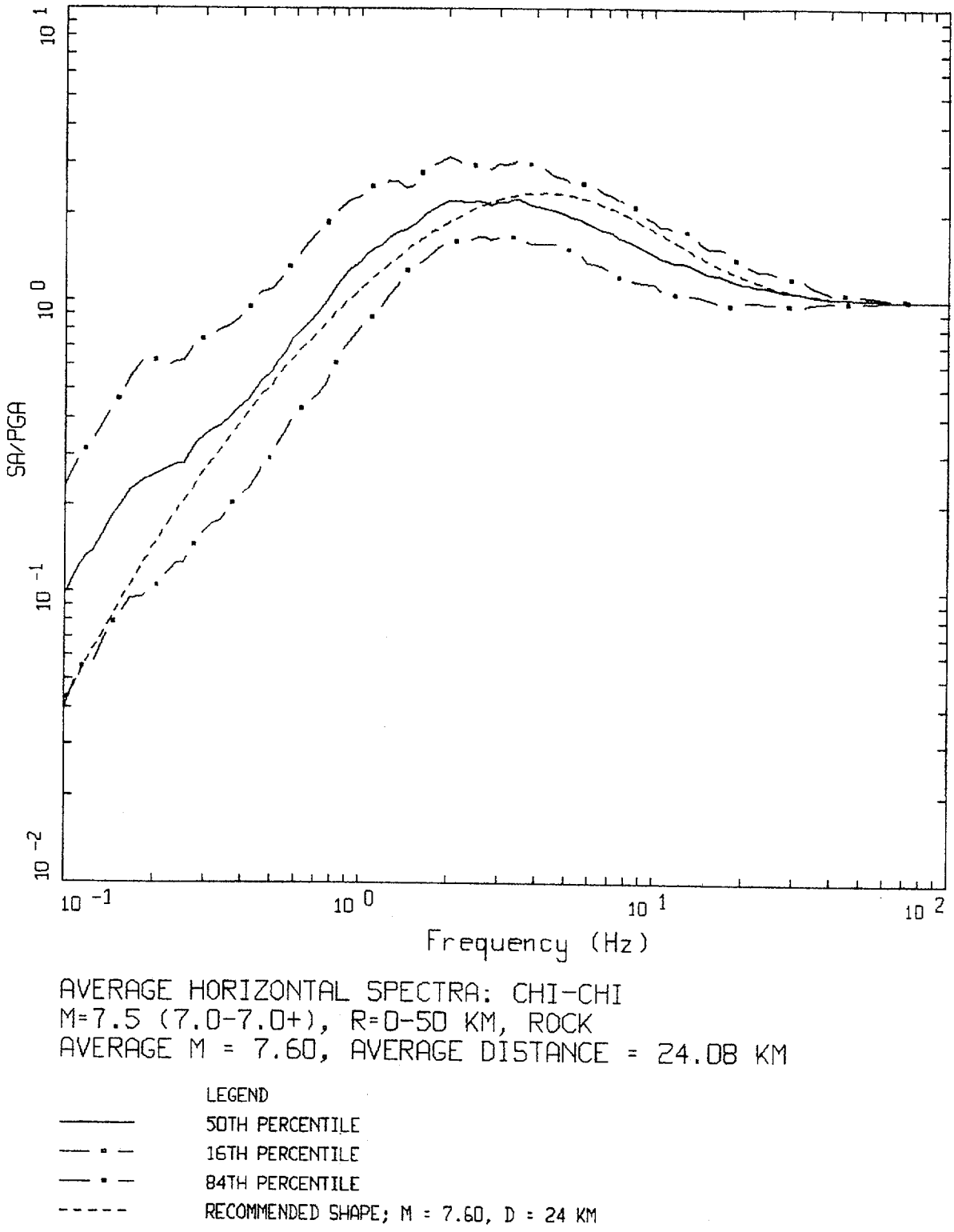

Figure K-11. Comparison of statistical response spectral shapes computed for the Chi Chi, Taiwan earthquake with recommended shape: bin **M** 7+ and $D = 0$ to 50 km.

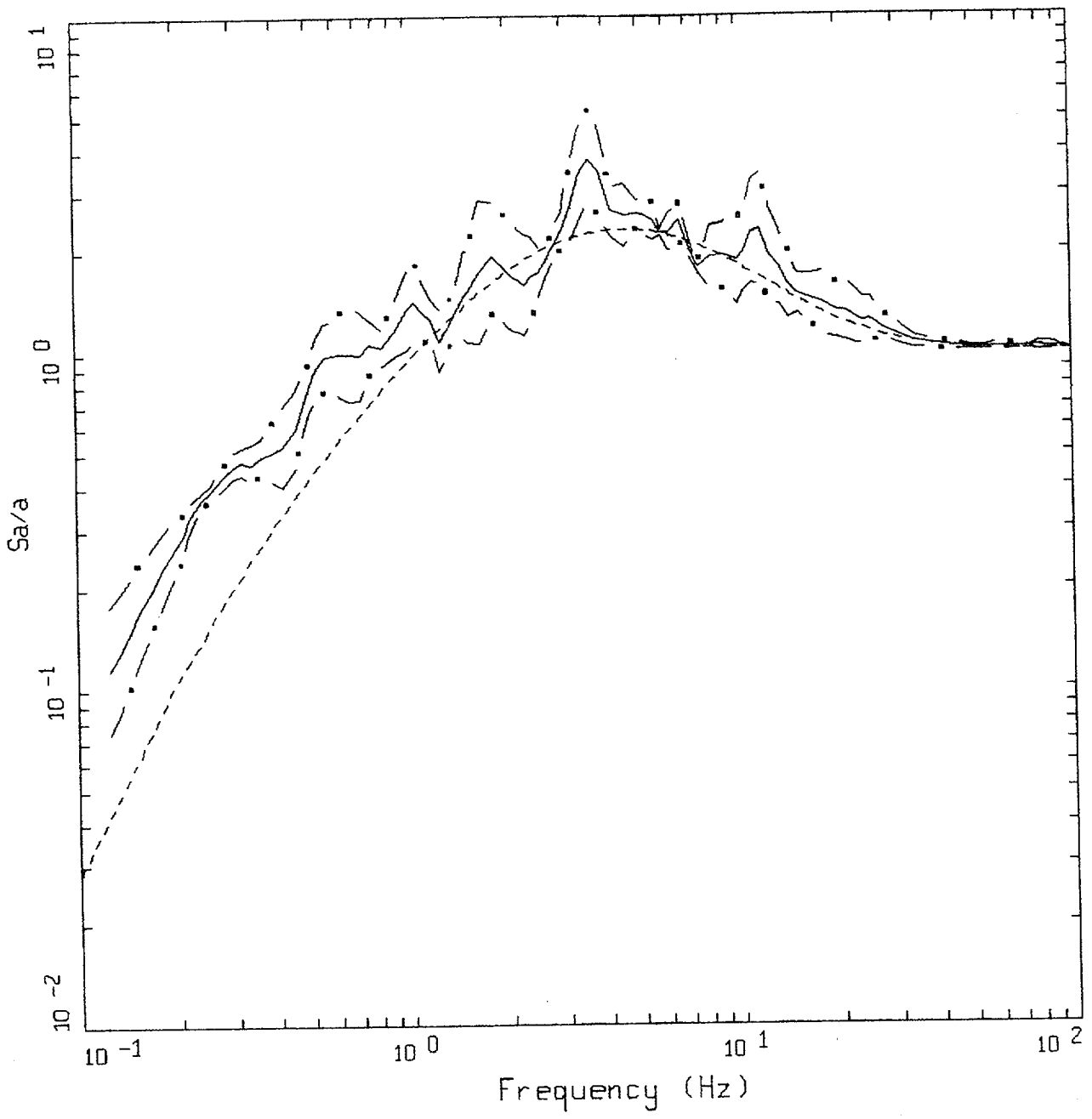

Figure K-12. Comparison of statistical response spectral shapes computed for the Turkey earthquakes with recommended shape: bin **M** 7+ and $D = 0$ to 10 km.

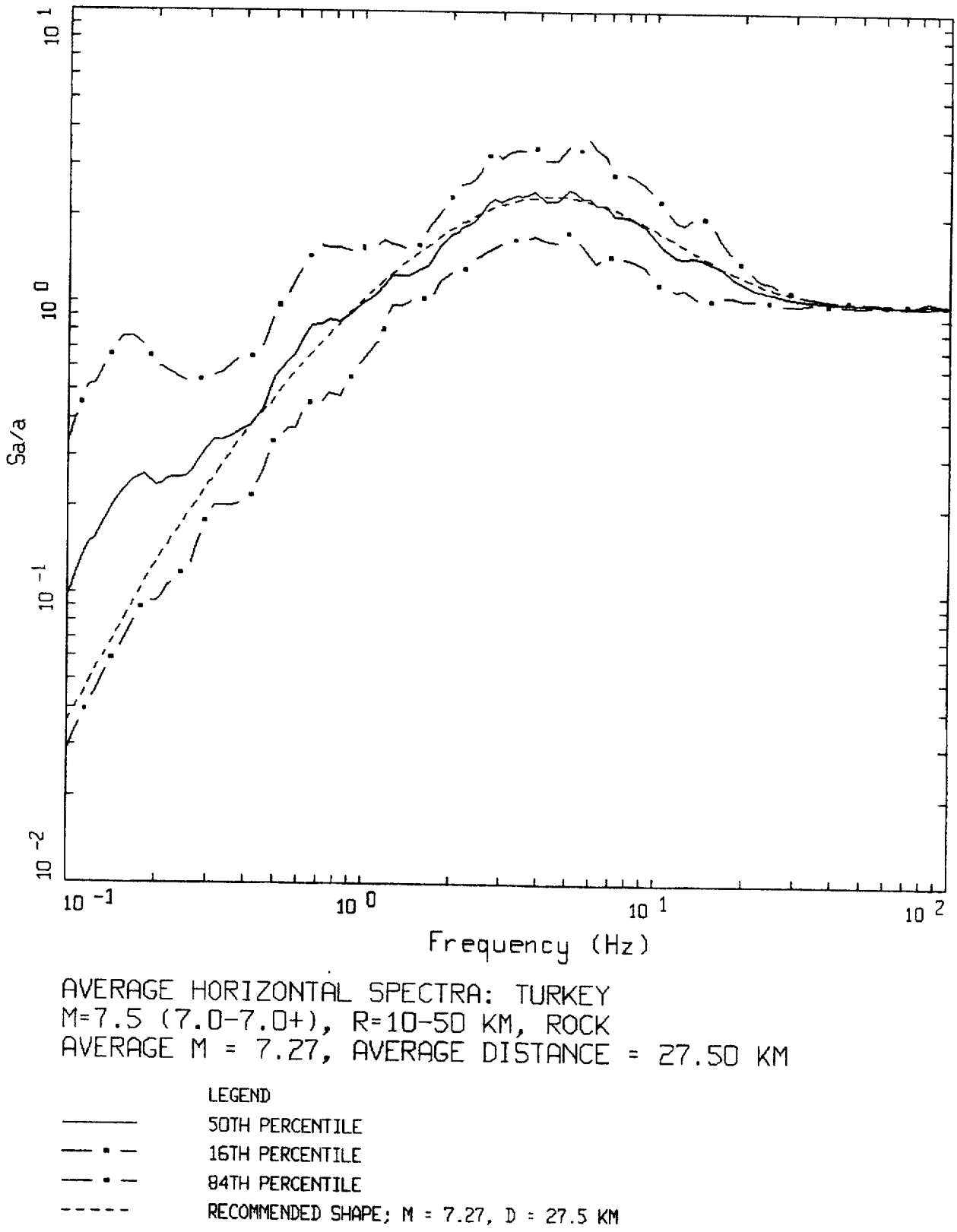

Figure K-13. Comparison of statistical response spectral shapes computed for the Turkey earthquakes with recommended shape: bin **M** 7+ and $D = 10$ to 50 km.

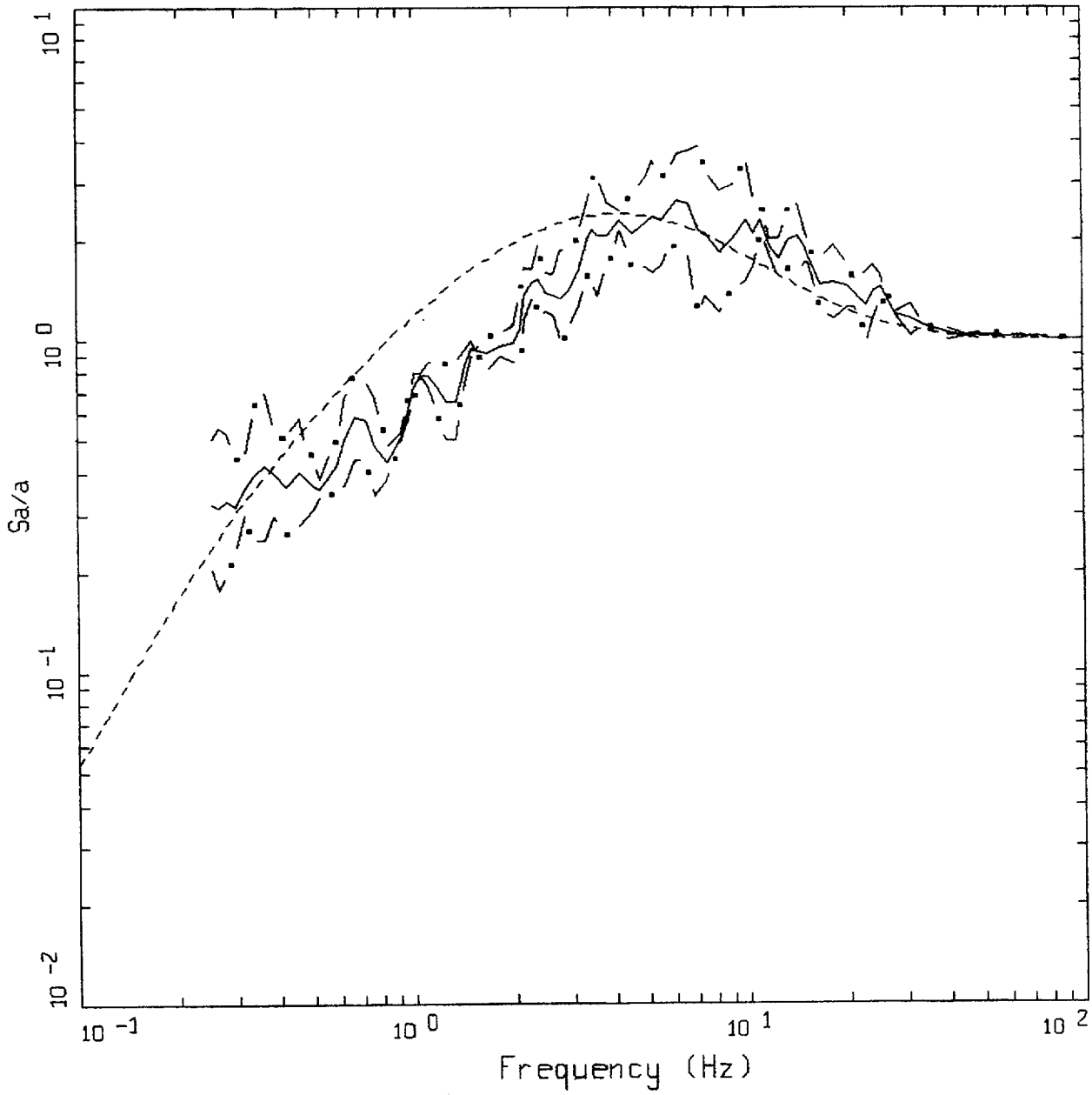

Figure K-14. Comparison of statistical response spectral shapes computed for the Turkey earthquakes with recommended shape: bin **M** 7+ and D = 50 to 100 km.

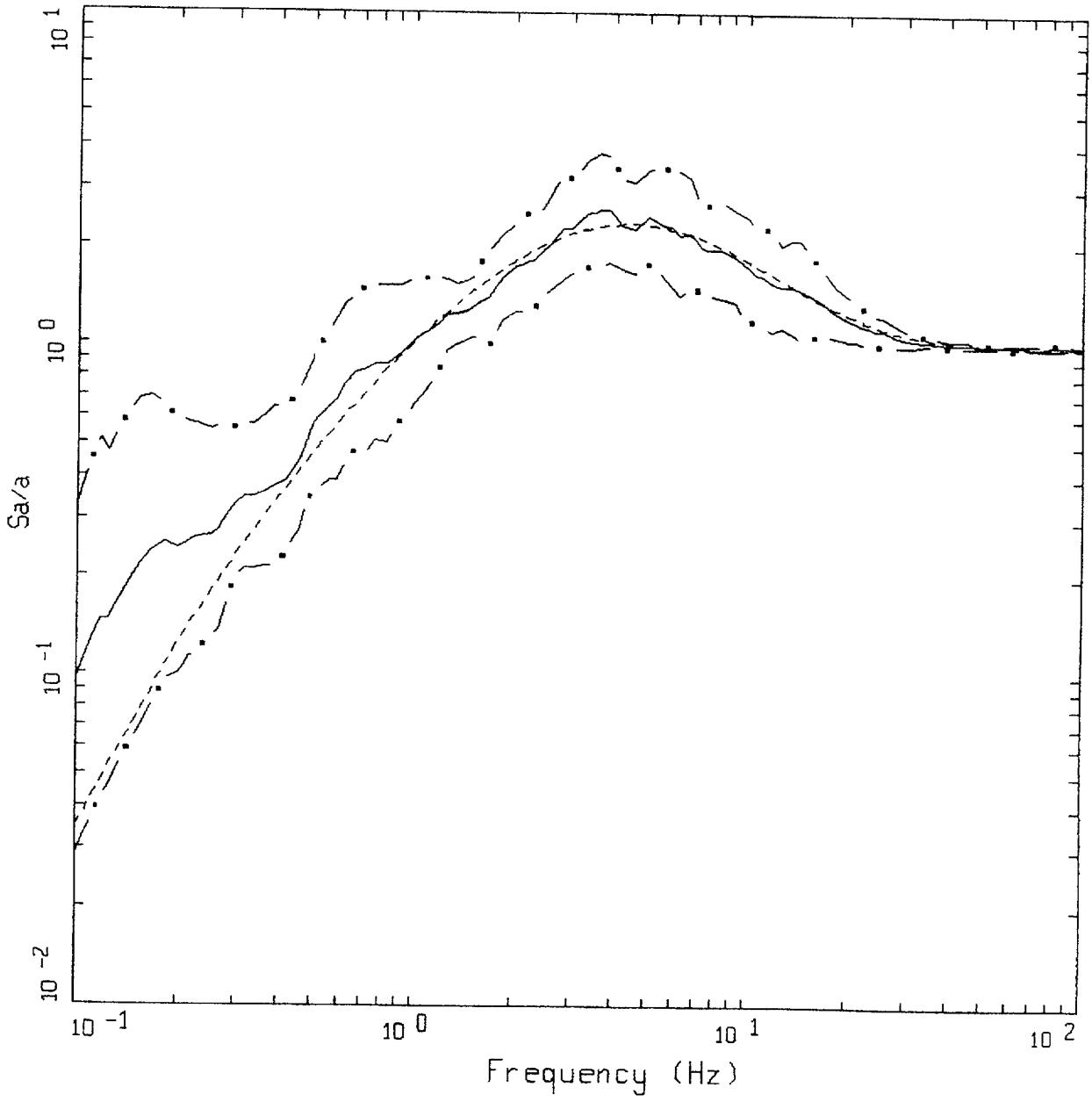

Figure K-15. Comparison of statistical response spectral shapes computed for the Turkey earthquakes with recommended shape: bin **M** 7+ and $D = 0$ to 50 km.

NRC FORM 335 (2-89) NRCM 1102, 3201, 3202

U.S. NUCLEAR REGULATORY COMMISSION

BIBLIOGRAPHIC DATA SHEET

(See instructions on the reverse)

1. REPORT NUMBER (Assigned by NRC, Add Vol., Supp., Rev., and Addendum Numbers, if any.)

NUREG/CR-6728

2. TITLE AND SUBTITLE

Technical Basis for Revision of Regulatory Guidance on Design Ground Motions: Hazard- and Risk-consistent Ground Motion Spectra Guidelines

3. DATE REPORT PUBLISHED

MONTH: October YEAR: 2001

4. FIN OR GRANT NUMBER

W6248

5. AUTHOR(S)

(1) R.K. McGuire, (2) W.J. Silva, and (3) C.J. Costantino

6. TYPE OF REPORT

Technical

7. PERIOD COVERED *(Inclusive Dates)*

04/1996 - 03/2001

8. PERFORMING ORGANIZATION - NAME AND ADDRESS *(If NRC, provide Division, Office or Region, U.S. Nuclear Regulatory Commission, and mailing address; if contractor, provide name and mailing address.)*

(1) Risk Engineering, Inc., 4155 Darley Avenue, Suite A, Boulder, CO 80305
(2) Pacific Engineering & Analysis, 311 Pomona Avenue, El Cerrito, CA 94530
(3) Carl J. Costantino, 4 Rockingham Road, Spring Valley, NY 10977

9. SPONSORING ORGANIZATION - NAME AND ADDRESS *(If NRC, type "Same as above"; if contractor, provide NRC Division, Office or Region, U.S. Nuclear Regulatory Commission, and mailing address.)*

Division of Engineering Technology
Office of Nuclear Regulatory Research
U.S. Nuclear Regulatory Commission
Washington, DC 20555-0001

10. SUPPLEMENTARY NOTES

R.M. Kenneally, NRC Project Manager

11. ABSTRACT *(200 words or less)*

Recommendations for seismic design ground motions for nuclear facilities require a consistency with both observed strong motion data and with seismological theory on the characteristics of strong shaking. A database of recorded time histories forms the foundation of empirical recommendations for spectral shapes. For the central and eastern US (CEUS), a well-validated, simple model of strong motion allows quantification of the difference between western US (WUS) and CEUS motions. For design recommendations, the uniform hazard spectrum (UHS) is modified by a scale factor to a Uniform Reliability Spectrum (URS). Spectral shapes are scaled to the 10 Hz and 1 Hz URS amplitudes. We recommend criteria to match artificial motions to the target (scaled) spectra. We demonstrate the procedures for developing design spectra for rock conditions and for four soil profiles in the WUS and in the CEUS, using as example sites at a location in the Mojave desert, California, and Columbia, South Carolina. Results indicate that the URS, as calculated here, provides reliability-consistent designs over a range of site locations and structural frequencies.

12. KEY WORDS/DESCRIPTORS *(List words or phrases that will assist researchers in locating the report.)*

Seismic Effects
Regulatory Guides
Design Ground Motion
Response Spectra for Seismic Design

13. AVAILABILITY STATEMENT

unlimited

14. SECURITY CLASSIFICATION

(This Page) unclassified

(This Report) unclassified

15. NUMBER OF PAGES

16. PRICE

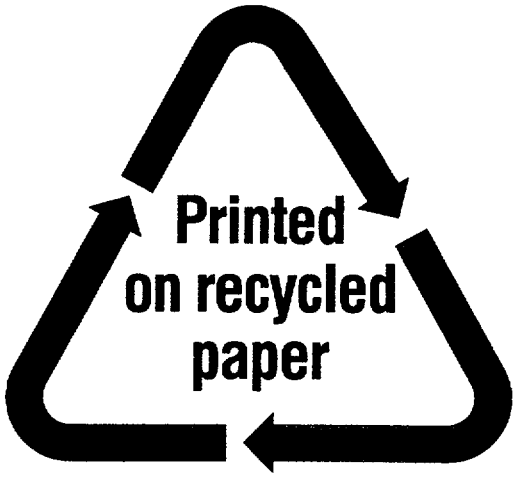

Federal Recycling Program

UNITED STATES
NUCLEAR REGULATORY COMMISSION
WASHINGTON, DC 20555-0001
